

1973

Wind Response Of Hyperbolic Cooling Towers

Mahmoud Galal Hashish

Follow this and additional works at: <https://ir.lib.uwo.ca/digitizedtheses>

Recommended Citation

Hashish, Mahmoud Galal, "Wind Response Of Hyperbolic Cooling Towers" (1973). *Digitized Theses*. 689.
<https://ir.lib.uwo.ca/digitizedtheses/689>

This Dissertation is brought to you for free and open access by the Digitized Special Collections at Scholarship@Western. It has been accepted for inclusion in Digitized Theses by an authorized administrator of Scholarship@Western. For more information, please contact tadam@uwo.ca, wlsadmin@uwo.ca.

The author of this thesis has granted The University of Western Ontario a non-exclusive license to reproduce and distribute copies of this thesis to users of Western Libraries. Copyright remains with the author.

Electronic theses and dissertations available in The University of Western Ontario's institutional repository (Scholarship@Western) are solely for the purpose of private study and research. They may not be copied or reproduced, except as permitted by copyright laws, without written authority of the copyright owner. Any commercial use or publication is strictly prohibited.

The original copyright license attesting to these terms and signed by the author of this thesis may be found in the original print version of the thesis, held by Western Libraries.

The thesis approval page signed by the examining committee may also be found in the original print version of the thesis held in Western Libraries.

Please contact Western Libraries for further information:

E-mail: libadmin@uwo.ca

Telephone: (519) 661-2111 Ext. 84796

Web site: <http://www.lib.uwo.ca/>



**NATIONAL LIBRARY
OF CANADA**

**CANADIAN THESES
ON MICROFILM**

**BIBLIOTHÈQUE
NATIONALE
DU CANADA**

**THÈSES CANADIENNES
SUR MICROFILM**

1 6 4 1 9

WIND RESPONSE OF HYPERBOLIC COOLING TOWERS

by

Mahmoud Galal Hashish

Faculty of Engineering

Submitted in partial fulfillment
of the requirements for the degree of
Doctor of Philosophy

Faculty of Graduate Studies
The University of Western Ontario

London, Canada

September 1973

© Mahmoud Galal Hashish 1973

ABSTRACT

Two approaches are developed for the analysis of the dynamic response of hyperbolic cooling towers to turbulent wind loading. The first, a simplified one, is based on the assumption that the resonant response is small and can be neglected. The analysis is then carried out on a quasi-static basis. The second is a rigorous dynamic approach which takes resonance into account. Both approaches were deduced from the general theory of the linear response of shells of revolution to turbulent wind loading. Applications for two sample problems are given in detail.

An experimental program aimed at defining the statistical properties on a 1/200 cooling tower model was carried out in the U.W.O. Boundary Layer Wind Tunnel. Comparisons of experimental and analytical results indicate that the *rms* of the pressure fluctuations could be predicted using a two-dimensional quasi-steady theory if the mean wind pressure distribution is known. The pressure spectra in the windward region show similar behaviour to the velocity spectra at low frequencies, but decay more rapidly at high frequencies. The vortices shed in the wake region were found to be weak, disorganized and spread over a broad range of frequencies. Some representative results showing the general behaviour of the cross-correlations and cross-spectral density functions are described. For meridional separations, they were found to display similar behaviour to line-like structures. For

circumferential separations, their behaviour is more complex, especially in the windward region. No significant correlation was detected between the pressure fluctuations acting in the windward and wake regions.

Experimental results for the statistical properties of the shell response and its constituent modal components were obtained from wind tunnel measurements on a 1/400 aeroelastic cooling tower model. Experimental and predicted results indicate that most of the quasi-static response, similar to the mean response resides in modes with low harmonic wave number m ; in particular $m = 1, 2$ and 3 . On the other hand, most of the resonant response resides in modes with lowest natural frequencies. For the sample problem analyzed, these were found to be the fundamental modes of harmonics $m = 4, 5$ and 6 . The *rms* of resonant response varies with the reduced velocity $\frac{\bar{U}}{fd}$ to a power of about 3.5, while the *rms* of the quasi-steady response varies with \bar{U}^2 .

A sensitivity analysis of shell effective stiffness and its static and dynamic response to wind was carried out. It is found that the angle of flow separation and the variation of the pressure characteristics in the circumferential direction are the most important parameters of the wind pressure. Response of modes of vibration associated with $m = 2$ are particularly sensitive to variations in these quantities. Constraints on the meridional displacement at base are necessary for the predominance of the membrane action. Out of all geometric ratios, the curvature parameter is the

most important one. Increased meridional curvature gives rise to increased membrane action.

ACKNOWLEDGEMENTS

The author is greatly indebted to Prof. S.H. Abu-Sitta, chief advisor, for his invaluable advice, encouragement, constructive criticism and continuous interest throughout the course of this work.

The author wishes to thank Prof. A.G. Davenport and Prof. M. Novak, members of the advisory committee for their advice and interest in the research program.

Thanks are extended to Dr. N. Isyumov, Dr. B.J. Vickery, Dr. T. Jandali, Dr. D. Surry and Dr. T.E. Base for useful discussions and to Messrs. K. McNamara and J. Gransden for reading parts of the manuscripts.

The experimental phase of this study was carried out at the Boundary Layer Wind Tunnel Laboratory of the University of Western Ontario. Thanks are due to the wind tunnel technical staff for their assistance; in particular, Messrs. R. Allen and P. Langford. Thanks are also extended to other members of the Faculty of Engineering Science technical staff; in particular, Messrs. H. Edney, D. Woytowich, R. Geadah, J. Vandenbrink and P. Teunissen for their help in the construction and instrumentation of the cooling tower models.

Typing of manuscripts was done carefully in a short space of time by Mrs. B. Town and Mrs. C. DuCharme. Their co-operative effort is appreciated.

Financial support from the University of Western Ontario

and the National Research Council of Canada is gratefully acknowledged.

The investigations reported in this thesis were carried out while the author was on a study leave from Ain Shams University, Cairo, Egypt. The co-operation and kind assistance of the members of the Faculty of Engineering, Ain Shams Univ. and the Missions Executive Committee are highly appreciated.

Supporting Technical Papers

The following papers are submitted in support of this thesis:

1. Hashish, M.G., "Free vibration of Hyperbolic Cooling Towers", Faculty of Engineering Science Research Report No. ST-1-70, The Univ. of Western Ontario, London, Canada, August, 1970.
2. Hashish, M.G. and Abu-Sitta, S.H., "Free Vibration of Hyperbolic Cooling Towers", Journal of Eng. Mech. Div., ASCE, Vol. 97, No. EM2, Proc. Paper No. 8037, April 1971.
3. Hashish, M.G. and Abu-Sitta, S.H., "Ring-Stiffened Hyperbolic Cooling Towers", Proceedings, Third Canadian Congress of Applied Mech., Calgary, Canada, May 1971.
4. Hashish, M.G. and Abu-Sitta, S.H., "Ring-Stiffened Hyperbolic Cooling Towers Under Wind Loading", Build. Sc., Vol. 7, 175 - 181, Pergamon Press, 1972.
5. Abu-Sitta, S.H. and Hashish, M.G., *Discussion on*, "The Influence of Meridional Cracking on the Vibration of Cylindrical Shells", Proc., Inst. of Civil Eng., Vol. 53, Part 2, 1972.
6. Hashish, M.G. and Abu-Sitta, S.H., "Mixed and Displacement Finite Difference Schemes For Hyperbolic Cooling Towers", Proceedings, Fourth Canadian

Congress of Applied Mech., Montreal, Canada 1973.

7. Abu-Sitta, S.H. and Hashish, M.G., "Dynamic Wind Stresses in Hyperbolic Cooling Towers", Accepted for publication in the ASCE Proc., Structural Div., 1973.
8. Abu-Sitta, S.H. and Hashish, M.G., "Dynamic Response of Shells of Revolution to Wind", submitted for possible presentation at the 5th International Conference on Experimental Stress Analysis.

TABLE OF CONTENTS

CERTIFICATE OF EXAMINATION	ii
ABSTRACT	iii
ACKNOWLEDGEMENTS	iv
SUPPORTING TECHNICAL PAPERS.	viii
TABLE OF CONTENTS.	x
LIST OF TABLES	xvi
LIST OF FIGURES.	xviii
NOMENCLATURE	xxvii
CHAPTER 1. INTRODUCTION	1
1.1 General Review	1
1.2 Wind Loads	12
1.3 Shell Response	15
1.4 Scope of Study	18
CHAPTER 2. STATIC WIND STRESSES.	20
2.1 Introduction	20
2.2 Analytical Procedure	24
2.2.1 Notation.	24
2.2.2 Shell Equations	24
2.2.3 The Modified Finite	27
Difference Method	
2.3 Static Wind Pressure	30
2.3.1 General	30
2.3.2 Wind Pressure on Circular Cylinders in Uniform Flow	31

	2.3.3	Static Wind Pressure on Cooling Towers	38
	2.4	Static Wind Stresses	49
	2.4.1	Description of Sample Problem	49
	2.4.2	Numerical Results	51
	2.5	Dependence of Static Wind Stresses on Various Parameters	60
	2.5.1	Mean Wind Pressure Distribution	61
	2.5.2	Variation of Wind Pressure with Height.	66
	2.5.3	Meridional Curvature.	68
CHAPTER 3		THEORY OF COOLING TOWERS RESPONSE	72
	3.1	Introduction	72
	3.2	Assumptions	73
	3.3	Modal Representation	74
	3.4	Equations of Motion	75
	3.5	Statistical Properties of Generalized Forces	82
	3.6	Statistical Properties of the Generalized Co-ordinates	89
	3.7	Statistical Description of Total Response	91
	3.7.1	Standard Deviation	91
	3.7.2	Power Spectral Density Function	92
	3.7.3	Peak Response	92

CHAPTER 4	VIBRATION CHARACTERISTICS	94
	4.1 Introduction	94
	4.2 Natural Frequencies and Mode Shapes of a Typical Tower	96
	4.2.1 Natural Frequencies	97
	4.2.2 Mode Shapes	100
	4.3 Dependence of Vibration Characteristics on Various Parameters.	104
CHAPTER 5	EXPERIMENTAL INVESTIGATION OF WIND PRESSURE .	113
	5.1 Introduction	113
	5.2 Experimental Set-up	117
	5.3 Flow Properties	119
	5.4 Mean Wind Pressures.	123
	5.5 Statistical Properties of Pressure Fluctuations	131
	5.5.1 Standard Deviation.	131
	5.5.2 Co-variance	136
	5.5.3 Power Spectral Density.	146
	5.5.4 Cross-Correlations and Cross-Spectra	156
CHAPTER 6	EXPERIMENTAL INVESTIGATION OF RESPONSE. . . .	171
	6.1 Introduction	171
	6.2 Aeroelastic Model.	174
	6.2.1 Principles of Aeroelastic Modelling	174

6.2.2	Model Geometry and Material Properties	176
6.3	Separation of Modes	178
6.4	Model Vibration Characteristics	181
6.5	Flow Properties and Experimental Set-up	190
6.6	Mean Response	193
6.7	Dynamic Response	199
6.7.1	Standard Deviation	200
6.7.2	Power Spectral Density	201
CHAPTER 7	APPROACHES TO THE PREDICTION OF DYNAMIC RESPONSE	
7.1	Introduction	223
7.2	Quasi-Static Approach	226
7.2.1	Theory	226
7.2.2	Application of Quasi-Static Approach	231
7.2.2.1	Model I	231
7.2.2.2	Model II	248
7.2.3	Parameteric Study	254
7.2.4	Comments on the Adequacy of the Quasi-Static Approach	263
7.3	Rigorous Dynamic Approach	266
7.3.1	Theory	266
7.3.2	Application	272
7.3.2.1	Statistical Properties of Generalized Forces	273

	7.3.2.2 Dynamic Response	283
	7.3.3 Comments	290
CHAPTER 8	CONCLUSIONS AND DESIGN CONSIDERATIONS	294
	8.1 General.	294
	8.2 Conclusions.	296
	8.3 Design Consideration	303
	8.4 Suggestions for Future Research.	313
APPENDIX I	SHELL EQUATIONS	314
	I.1 Shell Geometry	314
	I.2 Displacement and Mixed Formulations of the Fundamental Shell Equations	315
	I.2.1 Assumptions	316
	I.2.2 Fourier Representation of Shell Variables	316
	I.2.3 Force-Displacement Relations.	318
	I.2.4 Equilibrium Equations	320
	I.2.5 Displacement Scheme	321
	I.2.6 Mixed Scheme.	323
	I.3 Boundary Conditions.	326
	I.3.1 Free Edge	327
	I.3.2 Simply-Supported Edge	327
	I.3.3 Fixed Edge.	327
	I.3.4 Ring-Stiffened Edge	327
	I.3.5 Column Supported Edge	331

APPENDIX II	COMPARISONS WITH PREVIOUS RESULTS	333
II.1	Static Response	333
II.2	Free Vibration	336
APPENDIX III	1/400 AEROELASTIC MODEL	341
III.1	Model Material	341
III.2	Model Construction.	342
REFERENCES	345
VITA	368

LIST OF TABLES

Table	Description
1.1	Unit costs of cooling water systems
1.2	Numbers of plants projected to use various types of cooling
2.1	Power law exponent of wind profile for some typical terrains
2.2	Harmonic coefficients for various Pressure Distributions
5.1	Check on the decomposition of the Correlation Coefficient $C(s, \phi, s', \phi')$ to $C_y(s, s') \times C_h(\phi, \phi')$
6.1	Expressions for the outputs of Circuits A, B and C
6.2	Natural frequency of cooling tower model
6.3	Critical damping ratio for various harmonics (mechanical damping only)
6.4	Critical damping ratio for harmonics $m = 1$ to 3 (Mechanical and Aerodynamic)
7.1	Physical properties of Model I material
7.2	Natural frequencies of Model I
7.3	$\frac{p_{m,i}(t) p_{n,j}(t)}{s_o^4 \sigma_p^2(s_1, \phi_1)}$
7.4	$\frac{p'_{m,i}(t) p'_{n,j}(t)}{s_o^4 \sigma_p^2(s_1, \phi_1)}$
7.5	$\frac{p_{m,i}(t) p_{n,j}(t)}{s_o^4 \sigma_p^2(s_1, \phi_1)}$

- 7.6 $\overline{p'_{m,i}(t) p'_{n,j}(t)} / s_o^2 \sigma_p^2(s_1, \phi_1)$
- 7.7 Convergence of the contribution of $m = 2$ vs. mode number i
- 7.8 Convergence of the contribution of $m = 1 + 3$ vs. mode number
- 7.9 Variations in B_1 due to small variations in details of $C_{\tilde{n}}(\phi, \phi')$
- 7.10 Variations in B_2 due to small variations in the details of $C_{\tilde{n}}(\phi, \phi')$
- 7.11 Dependence of B_1 and B_2 on the st. dev. of the pressure fluctuations
- II.1 Natural Frequencies for a Sample Cooling Tower
- II.2 Influence of Top Ring Beam on the Natural Frequency

LIST OF FIGURES

Figure	Description
1.1	Diagrammatic Representation of Different Cooling Methods
1.2	Mechanical Draft Tower
1.3	Natural Draft Tower
1.4	Number of Hyperbolic Cooling Towers in Operation or under Construction in the U.S.A.
1.5	Largest Height of Towers Built in the U.S.A.
1.6	Distribution of k_0 for Towers in the U.S.A.
1.7	Distribution of k_1 for Towers in the U.S.A.
1.8	Distribution of k_2 for Towers in the U.S.A.
1.9	Distribution of (Throat Radius/Shell Thickness) Ratio for Towers in the U.S.A.
2.1	Geometry and Notations
2.2 & 2.3	Flow around Cylinders at Low and High R_e
2.4	Pressure Distribution around Long Circular Cylinders - After Roshko with Additions
2.5	Variation of Drag Coefficient for Long Circular Cylinders with Reynolds Number, Shell Surface Roughness and Turbulence Intensity
2.6	Influence of Turbulence and Shell Surface Roughness on the Pressure Distribution around Long Circular Cylinders - After Batham
2.7	Pressure Distribution around Hyperbolic Cooling Towers

- 2.8 Relation Between Peak Suction and its
Position - After Niemann
- 2.9 Relationship between the Difference between Peak
Suction and Base Pressure, and the Angle of
Flow Separation
- 2.10 Variation of Base Pressure Coefficient with
Reynolds Number
- 2.11 & 2.12 Effect of Turbulence and Surface Roughness
on the Pressure Distribution around Hyperbolic
Cooling Towers
- 2.13 Variation of Peak Suction with Surface
Roughness Reynolds Number R_k
- 2.14 Influence of Base Venting on the Pressure
Distribution
- 2.15 Geometry of the Sample Tower
- 2.16 to 2.19 Variation of Forces and Moments with
Height
- 2.20 Positive Directions of Forces and Moments
Acting on the Ring Beam
- 2.21 & 2.22 Distribution of Internal Forces and
Moments in the Ring Beam
- 2.23 Wind Pressure Distribution
- 2.24 & 2.25 Dependence of T_1 and M_2 on the Wind Pressure
Distribution
- 2.26 & 2.27 Influence of Wind Shear on T_1 and M_2
- 2.28 & 2.29 Influence of Meridional Curvature on T_1 and M_2

- 4.1 & 4.2 Dependence of Natural Frequencies on Curvature
Parameter k_o and on Boundary Conditions
- 4.3 Natural Frequencies for Harmonics $m = 0$ to 9
- 4.4 Mode Shapes of Normal Displacement for
Harmonics $m = 1$ to 9
- 4.5 to 4.13 Influence of Geometric Ratios on the
Fundamental Frequencies of $m = 1, 2$ and 3
- 4.14 to 4.16 Dependence of Mode Shapes for Harmonics
 $m = 1$ to 3 on Geometric Ratios
- 5.1 & 5.2 Influence of Turbulence and Shell Surface
Roughness on the Pressure Fluctuations
around the Tower
- 5.3 Pressure Model
- 5.4 Experimental Set-up
- 5.5 Variation of Mean Wind Speed with Height
- 5.6 Variation of Turbulence Intensity with
Height
- 5.7 to 5.9 Spectra of Velocity Fluctuations in BLWT
and in Natural Wind
- 5.10 to 5.15 Mean Pressure Distribution
- 5.16 Variation of Pressure Coefficients b_m with
Height
- 5.17 to 5.24 Distributions of the Standard Deviation
of the Pressure Fluctuations
- 5.25 Variation of the St. Dev. of the Pressure
Fluctuations with Height
- 5.26 to 5.28 Correlation Coefficient for Vertical

- Separations $C_v(l, l')$
- 5.29 Correlation Coefficient for Circumferential Separations in Windward Region $C_f(\phi, \phi')$
- 5.30 Correlation Coefficient for Circumferential Separations in Wake Region $C_r(\phi, \phi')$
- 5.31 Values of $C_f(\phi, \phi')$ near the Shell Boundaries
- 5.32 Values of $C_r(\phi, \phi')$ near the Shell Boundaries
- 5.33 Values of $C_f(\phi, \phi')$ at Throat; Base Vented
- 5.34 Values of $C_r(\phi, \phi')$ at Throat; Base Vented
- 5.35 to 5.38 Power Spectra of Pressure at Various Points along the Upstream Stagnation Line
- 5.39 to 5.45 Power Spectra of Pressure at Various Points around Shell Circumference at Throat
- 5.46 Values of the Transfer Function $X(s, \phi, f)$ at Different Points Along the Upstream Stagnation Line.
- 5.47 Cross-spectra of Velocity and Pressure Fluctuations for a Rectangular Prism, after Kao
- 5.48 Values of the Transfer Function $X(s, \phi, f)$ at Different Points around the Shell at Throat
- 5.49 to 5.52 Cross-Correlation of Pressures at Different Points along the Upstream Stagnation Line
- 5.53 to 5.58 Cross-Correlation of Pressures at Different Points around the Shell Circumference at Throat
- 5.59 to 5.62 Cross-Spectra of Pressures at Different Points along the Upstream Stagnation Line

- 5.63 to 5.70 Cross-Spectra of Pressures at Different Points around the Shell Circumference at Throat
- 5.71 Normalized Co-Spectrum $R_{\nu}(s, s', f)$
- 5.72 Normalized Co-spectrum $R_f(\phi, \phi', f)$
- 5.73 Normalized Co-Spectrum $R_r(\phi, \phi', f)$
- 6.1 1/400 Cooling Tower Model
- 6.2 Strain Gauge Circuits Employed For Modal Separation of Shell Response
- 6.3 Mode Shapes for Normal Displacement
- 6.4 & 6.5 Mode Shapes for Meridional and Circumferential Strains on the Inside Surface of the Model
- 6.6 Experimental Set-up for Frequency Measurements
- 6.7 Total Response of Cooling Tower Model to Acoustic Excitation
- 6.8 Output of Circuit A at Level 3, $\phi_0 = 0$
- 6.9 Output of Circuit B at Level 3, $\phi_0 = 0$
- 6.10 Output of Circuit C at Level 3, $\phi_0 = 0$
- 6.11 Arrangement of Testing Instruments
- 6.12 & 6.13 Mean Meridional Strain-Circuit A
- 6.14 & 6.15 Mean Circumferential Strain-Circuit A
- 6.16 & 6.17 Mean Meridional Strain-Circuit B
- 6.18 & 6.19 Mean Circumferential Strain-Circuit B

- 6.20 Total Mean Meridional Strain on the Inside
Surface of the Model
- 6.21 & 6.22 RMS Meridional Strain-Circuit A
- 6.23 & 6.24 Variance of Meridional Strain-Circuit A
- 6.25 to 6.27 RMS Meridional Strain-Circuit B
- 6.28 to 6.29 Total RMS Meridional Strain on Inside
Surface of Model
- 6.30 to 6.33 Power Spectra of Modal Strain-Circuit A
Output
- 6.34 to 6.37 Power Spectra of Modal Strain-Circuit B
Output
- 6.38 to 6.41 Power Spectra of Total Meridional Strain
- 6.42 Power Spectrum of the Symmetric Component
of the Generalized Force for Harmonic $m = 2$
- 6.43 Power Spectrum of the Anti-Symmetric Component
of the Generalized Force for Harmonic $m = 2$
- 7.1 Geometry of Model I
- 7.2 Modal Displacement for Harmonics $m = 1$ to 6
- 7.3 to 7.5 Variation of the Modal Response of Harmonics
 $m = 1, 2$ and 3
- 7.6 & 7.7 Variation of the Total Shell Response with
Height at $\phi = 0$ and 90°
- 7.8 Variation of Total Shell Response around Shell
Circumference at Level 1 ($0.27H$)
- 7.9 Variation of Total Shell Response around Shell
Circumference at Level 2 ($0.50H$)
- 7.10 Variation of Total Shell Response around Shell

- Circumference at Level 3 ($0.75H$)
- 7.11 Variation of Total Shell Response around Shell Circumference at Level 4 ($0.94H$)
- 7.12 & 7.13 Variation of Modal Response of Harmonic $m = 2$ around Shell Circumference
- 7.14 to 7.16 Variation of Combined Modal Response of Harmonics $m = 1, 3$ around Shell Circumference
- 7.17 Dependence of B_1 on ϕ_s
- 7.18 Dependence of B_2 on ϕ_s
- 7.19 Values of Correlation Coefficients $C_f(\phi, \phi')$, $C_p(\phi, \phi')$
- 7.20 **RMS Pressure Distributions**
- 7.21 Dependence of A_1 on β
- 7.22 Values of $J_0(f)$ for Harmonics $m = 1$ to 3
- 7.23 Values of $J_0(f)$ for Harmonics $m = 4$ to 6
- 7.24 Variation of $J_1(f)$ and $J_2(f)$ with Frequency for Harmonic $m = 2$
- 7.25 Variation of $J_1(f)$ and $J_2(f)$ with Frequency for the Cross-Product of Harmonics $m = 1$ and 2
- 7.26 Variation of $J_1(f)$ and $J_2(f)$ with Frequency for the Cross-Product of Harmonics $m = 2$ and 3
- 7.27 Power - Spectra of the Generalized Forces For Harmonic $m = 2$
- 7.28 Power - Spectra of the Cross - Product of the Generalized Forces for Harmonics $m = 1$ and 2
- 7.29 Power - Spectra of the Cross - Product of the Generalized Forces for Harmonics $m = 2$ and 3

- 7.30 Power Spectrum of Shell Response at Level 4,
 $\phi = 0$
- 7.31 Power Spectrum of Shell Response at Level 3,
 $\phi = 0$
- 7.32 Power Spectrum of Shell Response at Level 2,
 $\phi = 0$
- 7.33 Power Spectrum of Shell Response at Level 1,
 $\phi = 0$
- 7.34 Power Spectrum of Shell Response at Level 1,
 $\phi = 120^\circ$
- 7.35 Power Spectrum of Shell Response at Level 1,
 $\phi = 180^\circ$
- 7.36 Resonance Proportion of Shell Dynamic Response
at Level 1
- 8.1 Power Spectra of the Generalized Forces for
Model I
- 8.2 Power Spectra of the Response of the Funda-
mental Mode of Harmonic $m = 2$
- 8.3 Power Spectra of the Response of the Funda-
mental Mode of Harmonic $m = 3$
- 8.4 Power Spectra of the Response of the Funda-
mental Mode of Harmonic $m = 4$
- 8.5 Power Spectra of the Response of the Funda-
mental Mode of Harmonic $m = 5$
- 8.6 Geometry of a Typical Full-Scale Cooling Tower
- 8.7 Variation of Net Tensile Stress with Wind Speed

- I.1 Forces and Moments Acting on a Typical Shell Element
- I.2 Forces and Moments Acting on a Typical Beam Element
- II.1 Geometry of Sample Problem
- II.2 to II.5 Meridional and Circumferential Forces and Moments
- II.6 Convergence of Modified and Conventional Finite Difference Solutions

NOMENCLATURE

a	= shell radius at throat
A_1	= function defined by equation (7.10)
A_b	= beam cross-sectional area
b	= curvature constant ($b = \sqrt{-r_2 r_1}$ at throat)
b_m	= Fourier coefficient of mean pressure distribution for harmonic m
B	= frequency bandwidth at half resonant peak
B_1, B_2, B_3	= functions defined by equations (7.11 to 7.13)
e	= damping parameter
C_0	= shell extensional stiffness
$C(\ell, \phi, \ell', \phi')$	= correlation coefficient of pressure fluctuations
C_f, C_h, C_n, C_v	= shape functions for correlation coefficient
$C_p(s, \phi)$	= wind pressure coefficient
$C_{p_m, i p_n, j}, C_{p'_m, i p'_n, j}, C_{\tilde{p}_m, i \tilde{p}'_n, j}$	= normalized co-variance functions for the generalized forces
$\tilde{C}_{p_m, i p_n, j}, \tilde{C}_{p'_m, i p'_n, j}, \tilde{C}_{\tilde{p}_m, i \tilde{p}'_n, j}$	= co-variance functions for the generalized forces

d	= shell diameter at throat = $2a$
D_o	= shell bending stiffness
E	= Young's modulus of shell Material
E_b	= Young's modulus of beam material
f	= natural frequency in cps
\tilde{f}	= non-dimensional frequency parameter
\tilde{f}_1	= $\frac{f \Delta s}{\bar{U}}$
\tilde{f}_2	= $\frac{f r \Delta \phi}{\bar{U}}$
f_p, f_1, f_2	= shape functions for the st. dev. of the pressure fluctuations $\sigma_p(s, \phi)$
g	= gravitational acceleration
$g_{m,i}$	= peak factor for mode (m, i)
$G(s, \phi, s', \phi', f)$	= co-spectrum of the pressure fluctuations
h	= shell thickness = $h_o \times \bar{h}$
h_o	= reference shell thickness
i	= $\sqrt{-1}$
i	= mode number in the meridional direction
I_y, I_z	= beam flexural moments of inertia

j	= mode number in the meridional direction
J_0 to J_4	= functions defined by equations (7.29 to 7.33)
J_b	= effective torsional moment of inertia of the beam
k_0	= curvature parameter = a/b
k_1	= throat radius to height ratio = a/H
k_2	= height above throat to total height ratio $k_2 = z_t/H$
k_3	= shell thickness to height ratio = h/H
k_s	= shell surface roughness parameter
l	= meridional coordinate
$L_u(z)$	= a scale length of turbulence
m	= harmonic wave number
M_1, M_2	= meridional and circumferential bending moments
M_{12}, M_{21}	= twisting moments
\tilde{M}_1	= $r M_1 / E \epsilon_0^3$
$M_{m,i}$	= generalized mass of mode (m, i) equation (3.16)
M_y, M_z	= normal bending moments in the beam
n	= harmonic wave number

\bar{N}_1	= effective transverse shear force at boundary
\tilde{N}_1	= $r\bar{N}_1/E s_0^2$
$p(s, \phi, t)$	= fluctuating component of wind pressure
$\bar{p}(s, \phi)$	= mean wind pressure
p_1, p_2, p_3	= components of wind pressure in meridional, circumferential and normal directions
$\tilde{p}_1, \tilde{p}_2, \tilde{p}_3$	= non-dimensional pressure components, equation I.31
$p_{m,i}(t), p'_{m,i}(t)$	= symmetric and anti-symmetric components of the generalized force for mode (m,i) , equations (3.19 & 3.20)
p	= axial force in ring beam
$q_{m,i}, q'_{m,i}$	= symmetric and anti-symmetric components of the generalized coordinates for mode (m,i) , equation (3.23 & 3.24)
$Q(s, \phi, s', \phi', f)$	= quadrature spectrum of pressure fluctuations
r	= radius of a parallel circle at a distance z from throat
r_1, r_2	= meridional and circumferential radii of curvature

r_b	= radius of ring beam
r_t	= value of r at top edge of shell
$R(\tau)$	= auto-correlation function
R_e	= Reynolds number
R_f, R_v, R_r	= shape functions for the co-spectrum of pressure fluctuations
$R_p(\ell, \phi, \ell', \phi', \tau)$	= cross-correlation of pressure fluctuations
$R_{p_{m,i} p_{n,j}}(\tau)$	= cross-correlation of generalized forces
$R_{q_{m,i} q_{n,j}}(\tau)$	= cross-correlation of generalized coordinates
s	= meridional coordinate
s_o	= total meridional length
S	= $T_{12} - \frac{M_{21}}{r_2} = T_{21} - \frac{M_{12}}{r_1}$
S_1 to S_{10}	= ratios introduced to allow for variations in shell stiffnesses
\bar{S}	= $S + 2H/r_2$
\tilde{S}	= $r \bar{S}/E s_o^2$
$S(f)$	= power-spectral density function
$S_p(s, \phi, f)$	= power-spectrum of pressure fluctuations
$S_p(s, \phi, s', \phi', f)$	= cross-spectrum of pressure fluctuations
$S_{p_{m,i} p_{n,j}}(f)$	= cross-spectrum of generalized forces

$S_{q_{m,i} q_{n,j}}(f)$	= cross-spectrum of generalized coordinates
$S_w(s, \phi, f)$	= power-spectrum of normal displacement
$S_y(\varepsilon, \phi, f)$	= power-spectrum of $y(s, \phi, t)$
t	= time
T	= averaging period
T_1, T_2	= meridional and circumferential forces
T_{12}, T_{21}	= in-plane shear forces
\tilde{T}_1	= $r T_1 / E s_o^2$
$U(Z, t)$	= longitudinal component of wind velocity
$\bar{U}(Z)$	= mean wind velocity at height Z above ground
u, v, w	= meridional, circumferential and normal displacement components respectively
U, V, W	= non-dimensional displacement components; $U = u/s_o, V = v/s_o$ & $W = w/s_o$
$u_{m,i}, v_{m,i}, w_{m,i}$	= mode shapes of u, v and w for mode (m, i)
\bar{w}	= mean component of normal displacement
\hat{w}	= peak value of normal displacement
$W_{m,i}(\tau)$	= weighing function defined by equation (3.25)

$X(s, \phi, f)$	= transfer function defined by equation (5.14)
$y(s, \phi, t)$	= response function
y_A, y_B, y_C	= output of circuits A, B and C, Table 6.1
$y_{m,i}(s)$	= modal configuration of $y(s, \phi, t)$ for mode (m, i)
z	= axial coordinates measured from the shell throat downwards
z_t, z_b	= values of z at top and bottom edges respectively
Z	= height above ground
α	= power law exponent of mean wind profile
β	= rotation
β_1, \dots, β_7	= non-dimensional functions describing the geometric and material properties of the ring beam, Appendix I
$\gamma_0, \dots, \gamma_4$	= geometric ratios defined by equation (I.2)
$\gamma_5, \dots, \gamma_8$	= geometric ratios defined by equation (I.32)
ϵ_1, ϵ_2	= meridional and circumferential strains respectively
$\epsilon_{1i}, \epsilon_{2i}$	= meridional and circumferential strains on the inside surface

θ	= meridional angle, Fig. 2.1
κ_1, κ_2	= change of curvature in the meridional and circumferential directions respectively
μ	= Poisson's ratio
ν	= air viscosity
$\xi_{m,i}$	= damping parameter, equation (3.17)
η	= critical damping ratio, equation (3.27)
$\bar{v}_{m,i}$	= rate of zero-crossing with positive slope, equation (3.62)
ρ	= air density
ρ_b	= density of beam material
ρ_s	= density of shell material
$\bar{\sigma}_{1,i}, \bar{\sigma}_{2,i}$	= meridional and circumferential stresses on the inside surface of the shell
$\sigma_p(s, \phi)$	= standard deviation of pressure fluctuations
$\sigma_u(Z), \sigma_v(Z)$	= standard deviations of the longitudinal and lateral components of turbulence respectively
$\sigma_w(s, \phi)$	= standard deviation of normal displacement $w(s, \phi, t)$
$\sigma_y(s, \phi)$	= standard deviation of $y(s, \phi, t)$
τ	= time-delay

ϕ	= circumferential angle measured from the upstream stagnation line, clockwise
ϕ_s	= angle of flow separation
$\chi_{m,i}(f)$	= mechanical admittance function, equation (3.57)
ω	= frequency (<i>rad/sec</i>)
$\bar{\omega}$	= natural frequency of a damped- system
Ω	= non-dimensional frequency ratio = $\frac{4\pi^2 f^2 \rho_s H^2}{E}$
Δs	= separation in meridional direction
$\Delta\phi$	= angular separation

CHAPTER 1

INTRODUCTION

1.1 General Review

On November 1, 1965, three of the eight cooling towers constructed at the Ferrybridge C Power Station collapsed during strong wind conditions (1). The maximum mean hourly wind speed of 40 to 44 mph at 33 ft. above ground, recorded at time of collapse, is estimated to have an expected recurrence of at least once in five years (1). The impact of such incident resulted in an extensive review of the conventional methods used in the design of reinforced concrete cooling towers. Doubts arose about the structural design philosophy. Uncertainties in the definition of the design wind speed, the character of the wind pressures experienced by the tower, methods of analysis and the appropriate shell geometry, reinforcement, and wall thickness were among the problems that required reliable answers.

The natural draft cooling towers along with other cooling systems are in common use in modern industry. In large industries and power plants, vast quantities of waste heat are generated that cannot, economically, be put into good use. In fossil-fueled plants, for example,

40% of the heat energy input is converted into electricity and the remaining 60% is rejected; 15% is lost in the plant, and 45% have to be dissipated safely to the atmosphere (2). In nuclear plants, about 35% of the heat input is converted into electricity, 5% is lost in the plant and 60% of waste heat has to be discharged to the atmosphere (2).

Cooling systems are, therefore, very essential for the safe disposal of waste heat. During the past 50 years or so there has been considerable improvement in cooling methods and as a result, there are many alternative cooling systems available at present (3,4). The most commonly used methods are outlined in Fig. 1.1.

In once through cooling, water from a nearby water resource (e.g. lake, river,..) is pumped once through the system and is discharged back to the water resource; generally 25 to 30^oF warmer. Once through cooling is the most economical, but it is undesirable from an environmental point of view because of the possible effect of warm water on biological life.

A second alternative is cooling ponds. It consists of a large pond in which cooling takes place by air contact with the water surface. Cold water is drawn from one end of the pond and is pumped through the system. The heated water is, then, discharged at the other end of the pond and the cycle continues. This cooling process is economical when land is available at reasonable prices. It is,

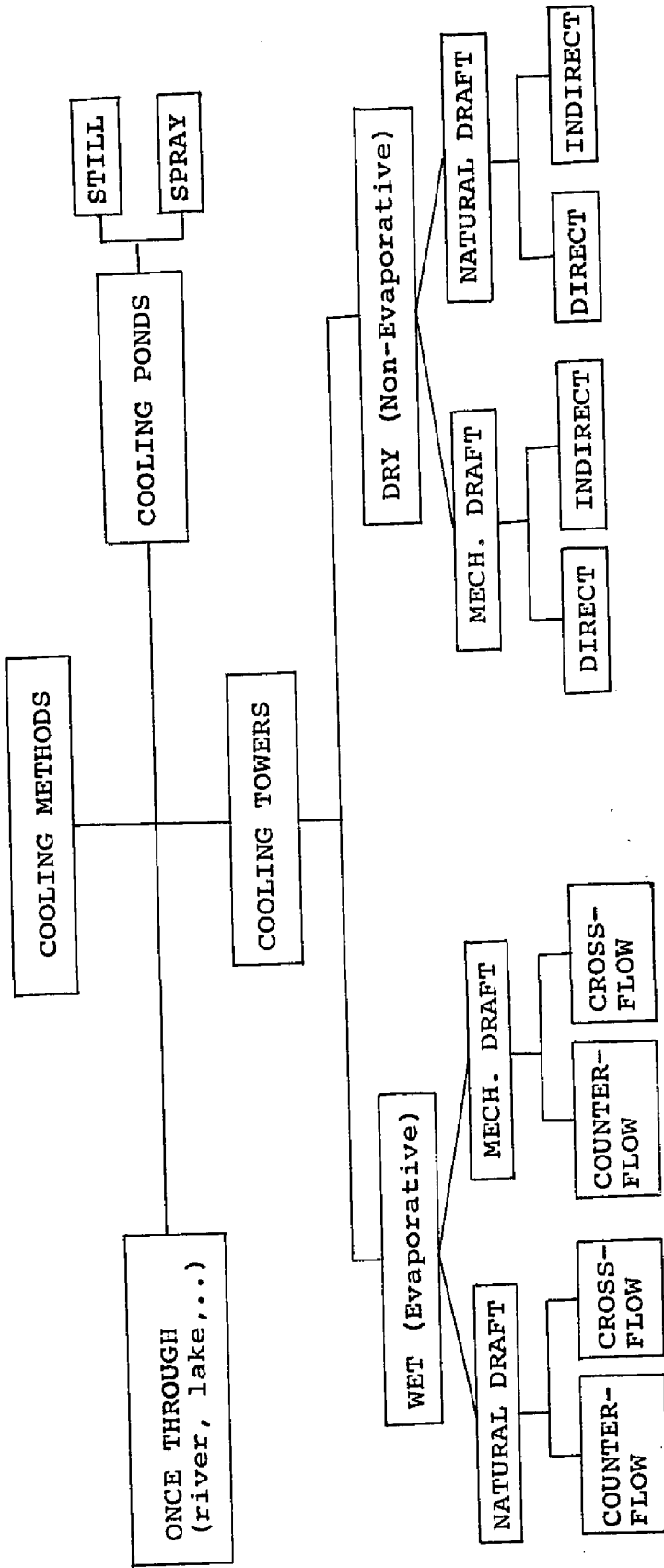


FIG. 1.1 DIAGRAMATIC REPRESENTATION OF DIFFERENT COOLING METHODS

however, the most inefficient cooling method. The efficiency of the cooling pond could be improved by using a spray system located few feet above a large pond or basin and the water is sprayed upwards. They are commonly referred to as spray ponds.

A third alternative for the disposal of waste heat is that which utilizes cooling towers. A cooling tower is merely a heat exchanger in which the heat gained by the cooling water is lost by contact with the air draft passing through the tower. The cold water is then recirculated back to the system and so on. If in the cooling process, the water comes into direct contact with the air, the unit is referred to as a wet cooling tower. On the other hand, if the cooling water is contained within a tubular system and does not come into direct contact with the air passing through the tower, the unit is referred to as a dry cooling tower.

If the air draft passing through the tower is caused by mechanical means, the unit is known as a mechanical draft tower, Fig. 1.2. When the draft of air is produced solely by means of a chimney action above the packing, the cooling unit is referred to as a natural draft cooling tower. Such cooling units are of two types; counterflow and cross-flow units depending on the passage of air through the packing. A counter flow tower, Fig. 1.3a, provides an upward air movement against downward water droplets movement. A cross-flow tower, Fig. 1.3b,

MECHANICAL DRAFT TOWERS

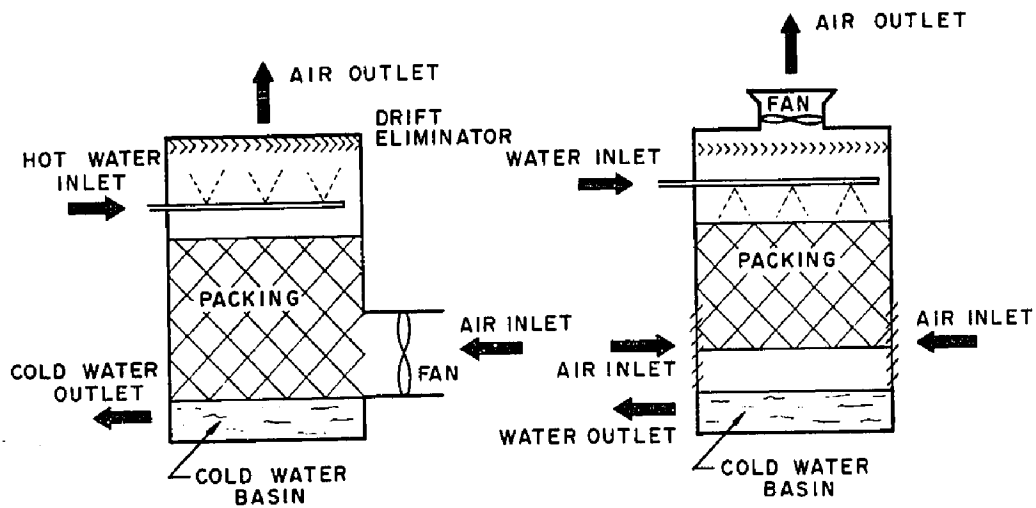


FIG. 1.2a FORCED DRAFT TOWER

FIG. 1.2b INDUCED DRAFT TOWER

NATURAL DRAFT TOWERS

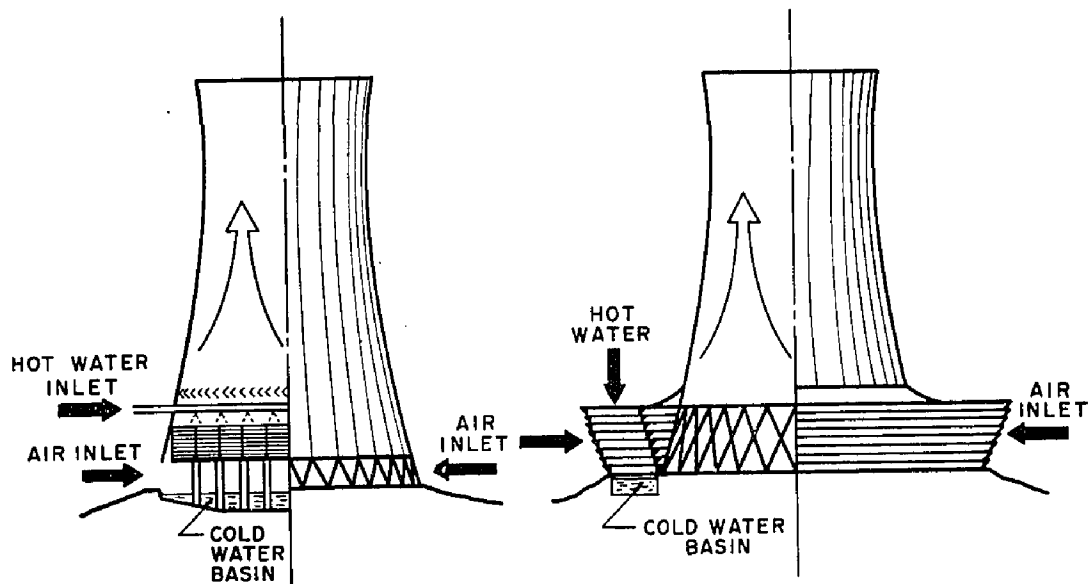


FIG. 1.3a COUNTERFLOW TOWER

FIG. 1.3b CROSSFLOW TOWER

provides a horizontal air flow through the packing while the cooling water falls vertically.

In addition, there are other systems used at present; for example, the hybrid cooling tower in which the air stream is generated both by natural and mechanical means by utilizing a chimney stack over the packing as well as fans located at the air intake (4). Detailed descriptions of the advantages and disadvantages of various cooling systems are covered extensively in the literature (e.g. Refs. 3,4).

The selection of one cooling method over others will rest largely on the individual industrial requirements of the plant, local site conditions, regulations on quality of environment, costs of materials, labour, power, and maintenance. Comparative cost can only be meaningful in a given case; however, some typical trends were indicated by Jameson and Adkins (2) and are given in Table 1.1.

Over the years, natural draft cooling towers have gone through a process of slow development. The first towers were built of wood (3). Later, steel was introduced as an alternative material for construction (3). However, for heights greater than 100 ft., it became uneconomical to use either wood or steel and there was a gradual change over to reinforced concrete as a suitable building material.

As for shape, towers with circular cross section were obviously more favourable than those with rectangular or

<u>Type of System</u>	<u>Investment Cost, \$/k.w.</u>	
	<u>Fossil-Fueled Plant*</u>	<u>Nuclear-Fueled Plant*</u>
Once-through**	2.00 - 3.00	3.00 - 5.00
Cooling ponds+	4.00 - 6.00	6.00 - 9.00
Evaporative cooling towers:		
Mechanical draft	5.00 - 8.00	8.00 - 11.00
Natural draft	6.00 - 9.00	9.00 - 13.00
Non-evaporative cooling towers:		
Mechanical draft	18.00 - 20.00	26.00 - 28.00
Natural draft	20.00 - 24.00	28.00 - 32.00

*Based on unit sizes of 600 Mw and larger.

**Circulation from lake, stream, or sea and involving no investment in pond or reservoir.

+Artificial impoundments designed to dissipate entire heat load to the air. Cost data are for ponds capable of handling 1,200 to 2,000 Mw of generating capacity.

TABLE 1.1 UNIT COSTS OF COOLING WATER SYSTEM (2)

square cross sections. First attempts with circular cylindrical towers were not satisfactory in regard to their structural strength and to some extent their cooling performance. They were soon abandoned in favour of hyperbolic cooling towers which have proved to be superior due to their structural resistance and their improved cooling performance.

The possibility of using towers with a hyperbolic profile was first investigated by Van Iterson in 1910 (5,6). A few years later, the first towers of this shape were built at the Emma Pit, Heerlen in the Netherlands. They

were soon to become one of the dominant features of power stations and industrial plants in England, France, Belgium, India, Germany, Egypt, Rumania, and many other countries.

The natural draft hyperbolic cooling tower was a late comer to the Northern American continent. Construction of the first unit of this type in the United States started in September 1960 at the Big Sandy station of Kentucky Power Co. (4). Their use, however, has been increasing ever since because of the rapid growth of power plants on dry sites, the increased cooling demands for large size power plants, and the opposition to thermal pollution of the natural water resources at both the regional and federal levels of government. In the past decade, the number of cooling towers in operation in U.S. has been steadily increasing as illustrated in Fig. 1.4.

Forecasts of the number of cooling towers that would have to be in operation in the U.S. in 1980 and 1990 to meet the expected cooling demands were given by Jameson and Adkins (2) and are shown in Table 1.2. The number of cooling towers expected to be in operation in 1990 could be as many as four times and possibly eight times the present number.

As the number of cooling units was growing, the heights of the towers were steadily increasing. This trend is clearly shown in Fig. 1.5 for cooling towers built or under construction in U.S. during the past decade. The

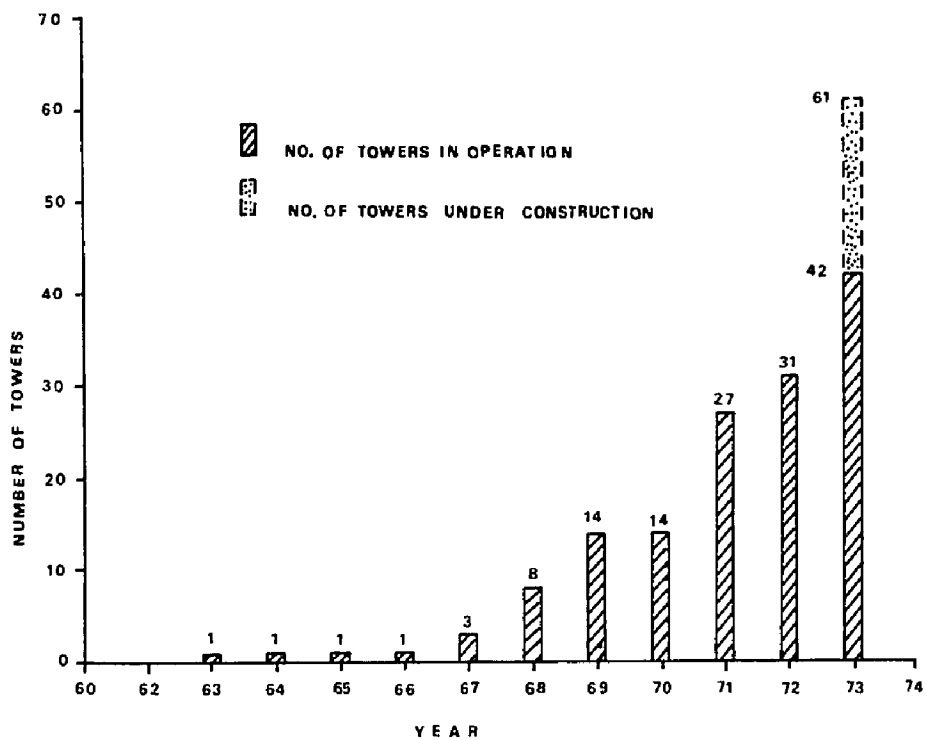


FIG.1.4 NUMBER OF HYPERBOLIC COOLING TOWERS IN OPERATION OR UNDER CONSTRUCTION IN U.S.A

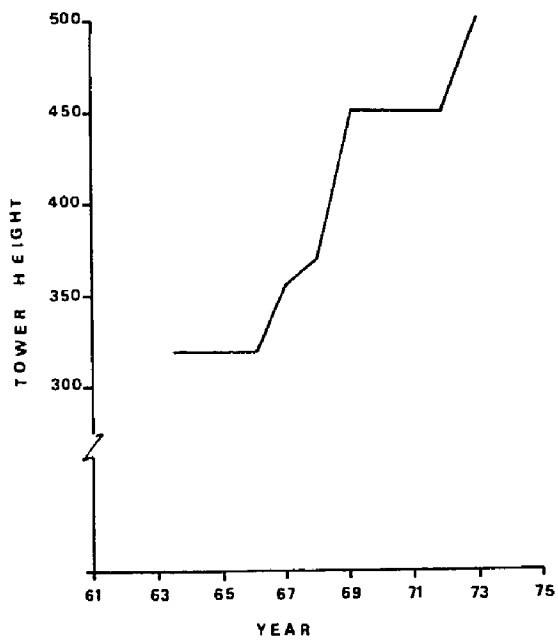


FIG.1.5 INCREASE OF LARGEST HEIGHT VS. YEAR

YEAR	ONCE-THROUGH	COOLING PONDS	COOLING TOWERS	TOTAL
1970	204	23	43	270
1980	251-44	59-126	123-263	433
1990	303-48	76-154	181-348	560

TABLE 1.2 NUMBERS OF PLANTS PROJECTED TO USE VARIOUS TYPES OF COOLING (2)

modern cooling tower is some 500 ft. high, 400 ft. base diameter, and a nominal wall thickness of 8 in, thus standing amongst the thinnest civil engineering shell structures ever built.

A survey of the geometric dimensions of cooling towers in U.S. conducted by Cole (7) indicate that there is not as yet a typical tower profile. Based on his survey, the ranges of variations of the various geometric ratios of the shell were computed and plotted in Figs. 1.6 to 1.9. The most common ratios are: a - meridional curvature parameter $k_o = 0.4$ (ranging from 0.33 to 0.47), b - throat radius/height = 0.2 (ranging from 0.18 to 0.28), c - height above throat/total height = 0.24 (ranging from 0.17 to 0.28), and d - shell radius/wall thickness at throat = 150 (ranging from 90 to 200). It is interesting to note that most of the towers built in Europe before the collapse of the Ferrybridge towers have a ratio of throat radius/wall thickness of about 200 or more.

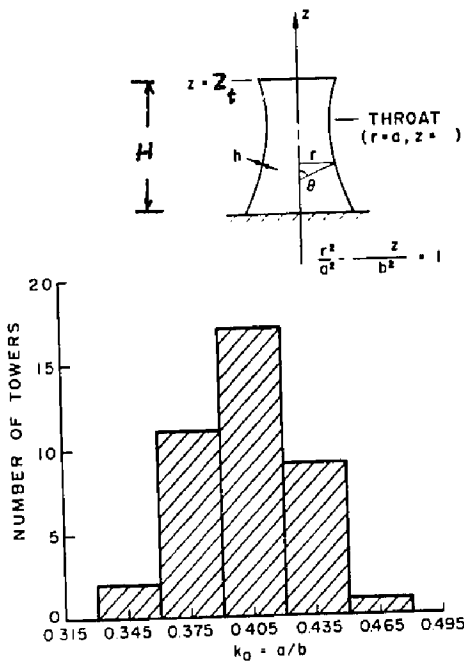


FIG. 1.6 DISTRIBUTION OF k_0 FOR TOWERS IN THE U.S.A.

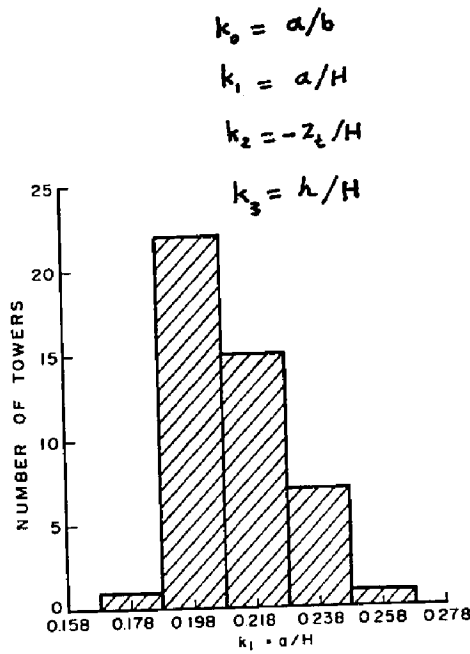


FIG. 1.7 DISTRIBUTION OF k_1 FOR TOWERS IN THE U.S.A.

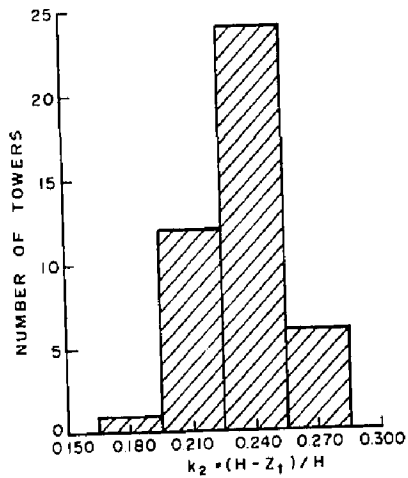


FIG. 1.8 DISTRIBUTION OF k_2 FOR TOWERS IN THE U.S.A.

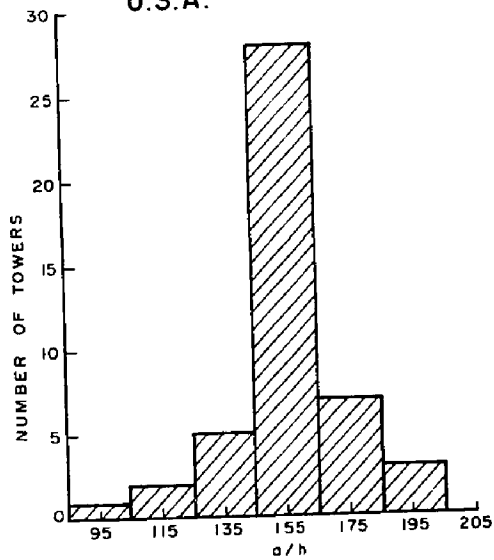


FIG. 1.9 DISTRIBUTION OF (THROAT RADIUS / SHELL THICKNESS) RATIO FOR TOWERS IN THE U.S.A.

1.2 Wind Loads

The most important stresses experienced by natural draft cooling towers are generated by wind loads and self weight of the shell. Others are, earthquake, temperature, shrinkage, settlement, ...etc. The wind loads produce meridional tensile stresses in the windward region of the shell while the self weight of the tower generates meridional uniform compressive stresses.

Early designers of reinforced concrete cooling towers were not mainly concerned with the wind action (6) because of the low height (up to 100 ft.). The nominal wall thickness of 5 in. was selected solely on practical grounds. Van Iterson (6), the first designer of such towers points out that:

The meridional compression stresses due to own weight are the only charges of some importance.

The steady increase in cooling demands was accompanied by rapid increases in the sizes of cooling towers. But the nominal wall thickness of about 5 in. remained almost unchanged. As a result, there were situations in which the uplift forces in strong wind conditions could easily offset and possibly surpass the compressive stresses due to self weight. Unless there is adequate reinforcement to resist the net tensile forces, this could lead to failure. This fact was dramatized by the collapse of the Ferrybridge towers in England in 1965 due to underestima-

tion of wind forces.

Since the net tensile stress is the difference between two almost equal quantities, small variations in the estimates of the design wind stresses could lead to large variations in the net tensile stresses. Therefore, the need for accurate and reliable approach to the prediction of the design wind stresses becomes evident. This, of course, have to take into account the random nature of wind, the uncertainties in the estimation of the design wind speed, and the dynamic characteristics of the shell structure. The treatment of wind loading as being static, a practice commonly regarded as adequate before the Ferrybridge incident, could lead to a substantial under-estimation of the actual wind stresses induced in the shell.

The wind loading is unsteady. It could be considered as composed of a mean (static) component upon which is superimposed a fluctuating (dynamic) component. Both components of the wind loads on hyperbolic cooling towers are influenced by many factors. The most important of which are Reynolds number, turbulence in the incoming flow, shell surface roughness, interference of surrounding structures to the wind flow, shell geometrical profile, and venting at base of tower.

Recently, some wind tunnel experiments have been conducted to define the distribution of the mean wind pressures around the shell circumference (8,9,10). The

reported measurements differ considerably owing to the strong dependence of the wind pressure on flow conditions and the difficulties of simulating high Reynolds number effects in the laboratory. Until now, the only reported full scale measurements of the mean wind pressure have been conducted by Niemann (11).

On the other hand, little attention was given to the study of the fluctuating component of the wind pressure. The first investigation of the nature of the wind pressure and response fluctuations was carried out in 1966 at the Boundary Layer Wind Tunnel Laboratory of The University of Western Ontario by Davenport and Isyumov (12). Their measurements emphasized the importance of the shell dynamic response and showed that the dynamic wind stresses are of the same order as the mean wind stresses. The interest created by this work initiated the study reported in this thesis.

The prediction of the dynamic wind stresses in cooling towers requires a comprehensive knowledge of the following statistical properties of the wind pressure fluctuations:

- a - Standard deviation
- b - Power spectral density functions
- c - Cross-spectral density functions

While the first two quantities describe the character of the wind pressure fluctuations at a single point on the shell surface, the last one provides a measure of their effectiveness on the overall shell response.

1.3 Shell Response

The wind stresses in hyperbolic cooling towers have been the subject of numerous investigations in recent years. Most of the work, however, was mainly concerned with the static component of the wind stresses and little attention was given to the dynamic component.

Until recently, the analysis of wind stresses in cooling towers was based on the membrane theory of thin shells of revolution (14,15,16). This theory neglects bending moments and out-of-plane shear forces and is only concerned with the in-plane forces acting on the shell. The membrane solutions were considered adequate.

Following the collapse of the Ferrybridge towers, however, the adequacy of the membrane theory was challenged. The need for a more refined analysis became evident. This was made possible, in part, by the advent of high speed digital computers and the subsequent development of efficient and fairly sophisticated numerical techniques. Numerical solutions to the bending theory of thin shells are now available in many forms (17 to 22).

While the accuracy of numerical solutions could be verified by theoretical means (e.g. comparisons with other numerical solutions, convergence, ..etc.), their adequacy to real situations could only be established on the basis of comparisons with experimental results. Very little work has been done in this field, especially measurements

of the response of full scale structures. On the basis of wind tunnel tests, Davenport and Isyumov (9) have reported good agreement between numerical solutions and experimental measurements.

On the other hand, the dynamic component of shell response has received far less attention in spite of the common awareness of their significance as demonstrated by the Ferrybridge incident and by recent evidence from experimental measurements. Wind tunnel measurements in turbulent flow by Davenport and Isyumov (9) have shown that the peak dynamic response is about 80% of the mean response in regions of largest stress. It was further found (12) that, in these regions, the proportion of resonant response relative to the total dynamic response is very small, thus suggesting that the response fluctuations follows closely a quasi-static behaviour.

Other measurements of the shell dynamic response were reported recently by Armit (13). The experiments were carried out on a scale model of the Ferrybridge C power station. It was found that the resonant response becomes predominant at high wind speeds. The results obtained confirm, beyond doubt, the significance of considering the dynamic component in estimating the wind induced stresses in cooling towers. Moreover, they provide an excellent example of situations where resonance could be a serious problem. The Ferrybridge towers are of

the cone-toroid profile and as such their stiffness is considerably less than that of a hyperboloid tower with same overall dimensions. Their lowest natural frequency of 0.6 (1) is almost half of that of the equivalent hyperboloid. This in turn explains the predominance of resonance as reported by Armitt.

Contrasting the results of Armitt (13) with those of Refs. (9,12), an important conclusion emerges. That is, with a clear understanding of their dynamic behaviour and the nature of wind loading, cooling towers could be designed in such a way as to avoid any unfavourable resonant response.

On the theoretical side, Yeh (23) developed a step by step numerical solution for the response of cooling towers to a prescribed time-dependent loading. Langhaar and Boreni (24) have described the means to determine the response of cooling towers to transient loads. Both approaches, however, are unrealistic in view of the random and complex nature of wind loading on cooling towers in both the time and space domains. With the exception of published experimental measurements, an extensive review of the available literature has revealed that neither rigorous nor practically reliable attempts have been made as yet towards the prediction of the shell dynamic response. The lack of such attempts could be attributed to many reasons. Some of these are: a - the lack of sufficient information about the relevant characteristics of the

wind pressure fluctuations, b - the complex, as well as the random, nature of wind loads and wind response of cooling towers, c - the fact that the importance of dynamic wind stresses has only been realized recently.

1.4 Scope of Study

The previously cited state of knowledge of the wind response of hyperbolic cooling towers leads, naturally to the objectives of this thesis.

The primary objective is to develop a rationale for the prediction of the wind induced stresses in hyperbolic cooling towers taking into consideration the random nature of wind and the dynamic characteristics of the shell structure.

The first step towards achieving this goal would be to develop an understanding of the basic wind pressure characteristics and their spatial variation. For this purpose, wind tunnel experiments in a turbulent boundary layer flow are used to define the relevant statistical properties of the wind pressure. The shell response theory is then formulated on a statistical basis.

Once it is possible to predict the shell response theoretically (more correctly, semi-empirically), it becomes essential to verify its adequacy to real situations. Wind tunnel measurements of shell response can be

very helpful in this regard, although full scale conditions are difficult to reproduce correctly in the laboratory.

A secondary objective of this work is to study the dependence of shell response on various structural and wind pressure parameters in order to assess the range in which different full scale towers behave and their relationship to wind tunnel models.

CHAPTER 2

STATIC WIND STRESSES

2.1 Introduction

The wind induced stresses in hyperbolic cooling towers can be regarded as the sum of a static (time-average) component and a dynamic (time-dependent) component. This chapter will be devoted entirely to the study of the static component of shell response.

The fundamental equations governing the state of stress in shells of double curvature subject to general cases of loading are highly complex. Under certain assumptions (1), the governing equations could be represented by a set of partial differential equations of the eighth order. The derivation of these equations is treated rigorously in books by Novozhilov (1), Flügge (2), Kraus (3) and many others.

In general, the resistance of shells of double curvature to deformation originates from two sources; membrane and bending actions. Under certain conditions (1), the membrane action is predominant and the bending stresses, therefore, becomes comparatively small. If these bending stresses could be neglected, the governing

shell equations could be reduced to a set of second order partial differential equations (1,4).

Initially, the membrane theory was used for cooling tower analysis. In 1961, the membrane equations as derived by Timoshenko (5) were solved by Martin and Scriven (4). Later, using numerical integration along the straight line generators, Martin, Maddock, and Scriven (6) described a similar solution to the theory of membrane displacements. Other membrane solutions were also given in Refs. (7,8).

The inadequacies of the membrane solutions are:

1. Bending stresses tend to increase if base is not tangentially restrained. Practical base conditions may permit tangential displacements to take place.
2. Normal displacements are generally subject to some restraint at base giving rise to bending moments.
3. Hyperbolic cooling towers have a negative Gaussian curvature. This means that disturbances at boundaries propagate to the shell interior along the straight line generators.
4. The theory is not adequate for studies such as the influence of flexibility of supports, stiffening ring beam and variable wall thickness.

With the advent of capable computing facilities and the development of efficient numerical techniques, the

solution of the general bending equations of thin shells became possible. The first bending solution was given by Albasiny and Martin (9) in 1967. Their finite difference solution of Novozhilov's shell equations required 162 unequal intervals. In 1969, Abu-Sitta (10) solved Novozhilov's general equations using a modified finite difference technique based on a physical analogue model by Schnobrick and Melin (11). In contrasting the accuracy of the modified finite difference solution against the conventional difference solution, it was found (12,13,14) that the former requires a much smaller number of grid intervals for the same accuracy. Solutions based on the finite element method were also given by Chan and Firmin (15), Gould (16) and others.

The analysis of wind stresses in cooling towers supported on columns was described by Abu-Sitta (17) and Gould (18). Wind stresses in ring stiffened towers with variable or constant thickness and supported on columns were investigated by Hashish and Abu-Sitta (19).

Reliable assessment of the static wind stresses in hyperbolic cooling towers obviously depends on a proper estimate of the wind pressure distribution on the tower. This problem has received considerable attention. In spite of the numerous investigations (20 to 27) of the static wind loads reported in recent years, the nature of these loads is still not well understood. In fact,

the results from different sources were often inconsistent.

Results obtained from wind tunnel tests (20 to 24) and from full scale measurements (25,26) have shown a strong dependence of the wind pressure distribution on Reynolds number. Model tests also indicate that the shell surface roughness has a strong influence on wind pressure at Reynolds number in the range 10^4 to 10^6 . Its influence on full scale structures at high Reynolds number ($\approx 10^8$) is not known due to the lack of experimental measurements.

Comparisons of results from different sources indicate also that the peak suction, angle of flow separation and base pressure coefficient are the most sensitive to changes in flow conditions, especially at low Reynolds number. The wind pressure in the windward face of the tower, however, is insensitive to these changes.

The purpose of this chapter is to investigate the stresses induced in the shell due to static wind loading. The analysis is based on the general Novozhilov's equations for thin elastic shells (1). Numerical solutions to the shell equations were obtained by means of the modified finite difference method. A brief review of the state of knowledge regarding the time-average wind loads on cooling towers is also given.

2.2 Analytical Procedure

2.2.1 Notation

The geometry of a hyperbolic cooling tower is given in Fig. 2.1. The notations and the positive directions of the three displacement components and the internal stress resultants are also shown.

2.2.2 Shell Equations

Hyperbolic cooling towers are very thin. Most of the towers in practice have a thickness to radius ratio in the order of 1:200. The use of a two-dimensional theory over a more rigorous three-dimensional elasticity theory is therefore justified. Also, a linear (geometric) analysis is favoured against a non-linear one due to the resistance of these towers to excessive deformation. A non-linear analysis that takes into account the finite behaviour of shell displacements was given by Chan and Firmin (28). They found that the difference between a linear and a non-linear analysis, within the range of practical wind loads, is insignificant, especially for the membrane stresses.

The general theory of thin elastic shells was first formulated by A. E. H. Love (29) in his famous treatise on the theory of elasticity. Several attempts have been made since, to improve and extend the theory. A survey

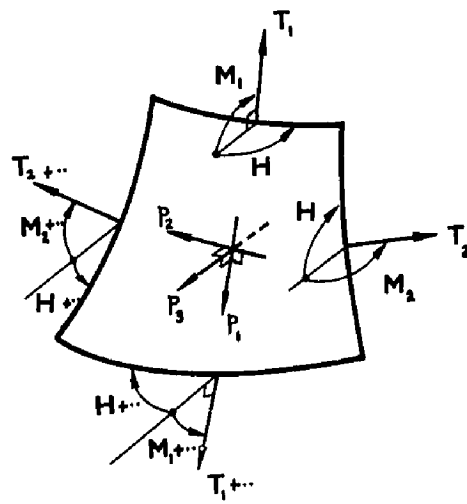
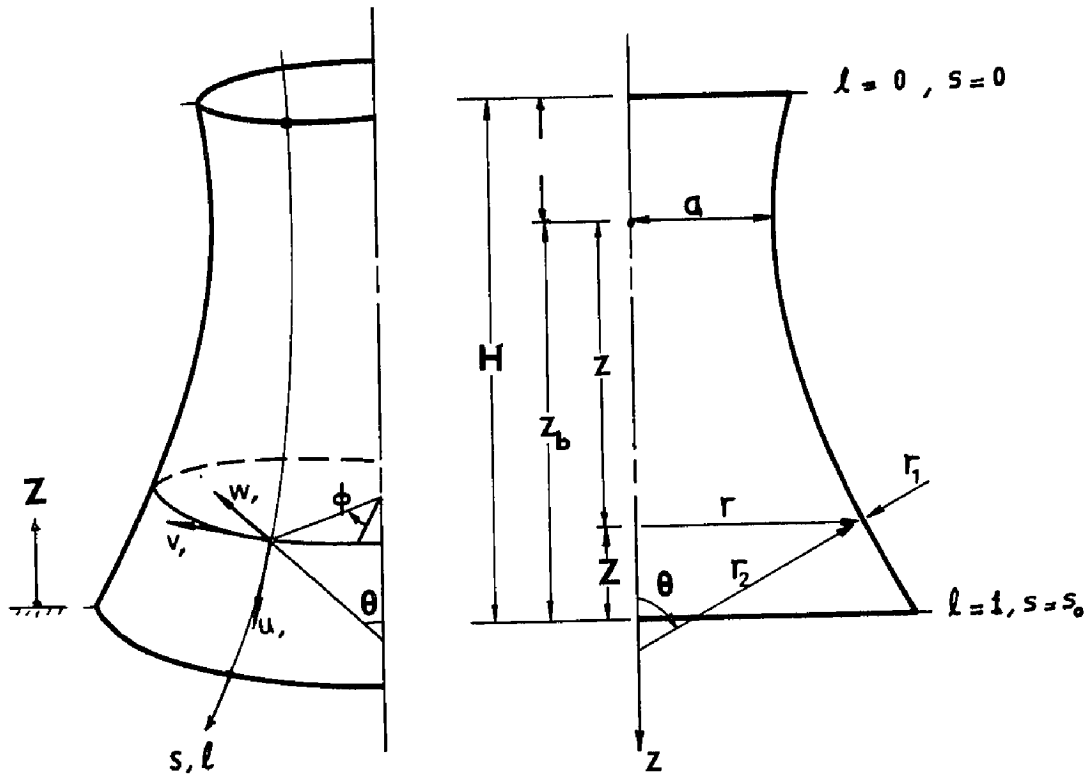


FIG.2.1 GEOMETRY&NOTATIONS

of recent progress in shell theory is given in Refs. (30 to 32).

The general theory of thin, elastic, homogeneous and isotropic shells can be represented by a set of partial differential equations of the eighth order. These could be represented in several forms. The most commonly used are:

1. Three differential equations in terms of shell displacements (10,12).
2. Four second order differential equations (3) in terms of shell displacements and meridional moment.
3. Eight first order differential equations in terms of the fundamental variables that appear in the natural boundary conditions. These are:
displacement components u , v and w , rotation β , axial force and moment T_1 and M_1 , and the effective in-plane and out-of-plane shear forces (3,13).

None of the above forms lends itself to a closed form solution and can only be solved numerically.

In the present analysis, both the displacement and the mixed eight first order differential equations schemes are used. The relevant equations for both schemes are presented in Appendix I. Therein, the shell partial differential equations are reduced to an ordinary differential form by separation of variables.

Each scheme obviously has its own advantages and disadvantages. The displacement scheme is more compact and, therefore, the number of equations to be solved is relatively small. However, the derivation of stresses from the computed displacements introduces errors due to differentiation. Difficulties also arise when stress boundary conditions, if they exist, have to be expressed in terms of displacements. These problems are partially eliminated when the mixed scheme is used. The absence of the derivatives of shell thickness, shell stiffnesses and the thermomechanical properties make this scheme more attractive. Its main drawback, however, is the large number of equations to be solved and the fact that the resulting matrix of coefficients is not positive definite. A thorough discussion of both schemes is given in Refs. (13,33).

Numerical solutions for both schemes were obtained by means of the modified finite difference method.

2.2.3 The Modified Finite Difference Method

In the conventional finite difference method, the shell differential equations are replaced by a set of simultaneous algebraic equations. In the transformation process, the continuous shell variables are replaced by their discrete values at selected points along the shell meridian (nodal points).

In first order finite difference approximations, the discretization errors for all derivatives are proportional to Δs^2 ($\Delta s = \text{grid interval}$). Errors inherent in the odd derivative expressions, however, are larger than those for the even derivatives since the former are based on double the mesh size.

Careful examination of the two forms of shell equations (Appendix I), shows that in any one equation, even derivatives of some variables are, in general, associated with the odd derivatives of the other variables. This situation suits the application of the modified finite difference method.

The modified finite difference method is based on shifting the grid lines for each shell variable such that odd and even derivatives could be computed with the same accuracy (11,34). Locating the meridional force T_1 , meridional moment M_1 , circumferential displacement v and normal displacement w at the node points of one mesh and the meridional displacement u , rotation β , effective in-plane shear force \bar{S} and effective out-of-plane shear force \bar{N}_1 at the node points of the other mesh, odd and even derivatives could be computed with the same accuracy. For example, the expression,

$$\frac{d^2 u}{ds^2} + k \frac{dv}{ds} \quad (2.1)$$

can be written at station i as,

$$\frac{1}{(\Delta s)^2} \{u_{i+1} - 2u_i + u_{i-1}\} + \frac{k_i}{\Delta s} \{v_{i+1/2} - v_{i-1/2}\} \quad (2.2)$$

This technique, which is adopted from an analogue treatment of cylindrical shells by Schnobrich and Melin (11) and similar to the principle of interlacing grids advanced by Gilles (34), has been used for a variety of static (10,12,19) and dynamic problems (12) and the agreement with other solutions was excellent.

The study of the convergence of the modified finite difference solutions together with comparisons with other solutions obtained using the conventional finite difference method, numerical integration techniques and the finite element method are given in Appendix II.

The solution of the banded difference equations was obtained by means of a routine developed by Martin and Wilkinson (35). The solution procedure is outlined in Ref. (12).

The present solutions could be used for the analysis of shells of revolution bounded by two parallel circles regardless of the meridional shape. They allow for any variation in shell thickness and stiffnesses. They could readily handle several boundary conditions at both edges of the shell.

2.3 Static Wind Pressure

2.3.1 General

Wind pressures on hyperbolic cooling towers in natural wind consist of two parts. First, the wind pressures exerted on the exterior surface of the shell. Second, the internal pressures on the interior surface of the shell.

The internal wind pressures experienced by cooling towers are negative (suction) and essentially static in character (36). Their average magnitude, relative to the local dynamic head ($1/2 \rho \bar{U}^2$), varies from -0.47 for towers with closed base to -0.2 for towers with open base (36,22). Bending moments and axial forces generated in the shell due to internal wind pressures are very small. Their only significance is on the axisymmetric component of the circumferential force. Their impact on the overall state of stress in the shell is negligible.

The external wind pressure exerted on the exterior surface of the shell consists of a static component and a fluctuating component. The distribution of the static component on the shell surface depends on many factors, the most important of which are:

1. Reynolds number, $R_e = \frac{\bar{U}d}{\nu}$
2. Intensity of turbulence.
3. Shell surface roughness.

4. Variation of mean wind speed with height.
5. Obstruction to the flow regime by nearby structures in the upstream or the sides of the tower.
6. Shell geometry:
 - a/ Height/radius ratio.
 - b/ Meridional curvature.
7. Degree of base venting.

2.3.2 Wind Pressure on Circular Cylinders in Uniform Flow

Some insight into the flow around cooling towers and its dependence on various parameters may be gained by considering the character of the flow around long circular cylinders in uniform flow. This problem has been covered extensively in the literature (37 to 41). Herein, a brief review of the development of flow around circular cylinders, as related to the present study, will be given.

In an ideal fluid (i.e. a fluid free of viscous forces), the pressure distribution on the surface of the cylinder can be determined by Bernoulli's equation,

$$p + 1/2 \rho U^2 = p_o + 1/2 \rho U_o^2 \quad (2.3)$$

where p_o and U_o are the pressure and velocity of the undisturbed flow, and U is the velocity of the fluid along the surface of the cylinder ($U=2U_o \sin\phi$; ϕ =circumferential angle).

The pressure coefficient C_p is defined by,

$$C_p = \frac{p - p_0}{1/2 \rho U_0^2} \quad (2.4)$$

For a cylinder in an ideal fluid,

$$C_p = 2\cos 2\phi - 1$$

The flow of natural wind past a circular cylinder is strongly dependent on Reynolds number. The flow gradually changes from a steady state at very low R_e , Fig. 2.2, to an unsteady state with increasing R_e , Fig. 2.3. This transition from steady to unsteady state is associated with considerable changes in the rear of the cylinder while the front region remains relatively unaffected. The two regions are separated by a layer of intense shear and vorticity (46).

The position of flow separation ϕ_s moves at different ranges of Reynolds number as follows:

1. At low R_e the separation takes place in the rear of the cylinder. With increasing R_e , the points of separation moves progressively forward till $\phi_s = 70-80^\circ$ at $R_e \approx 2 \times 10^5$ (38). This is accompanied by a progressive widening of the wake region.
2. For $R_e > 2 \times 10^5$, ϕ_s starts moving back to the rear of the cylinder till it reaches a value of $\phi_s = 120-140^\circ$

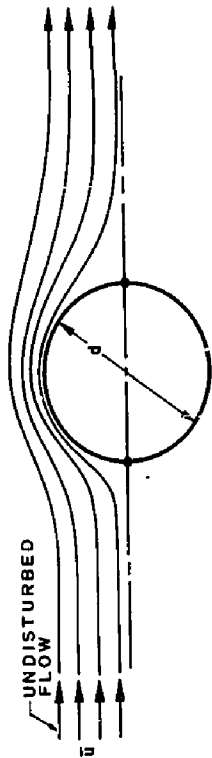
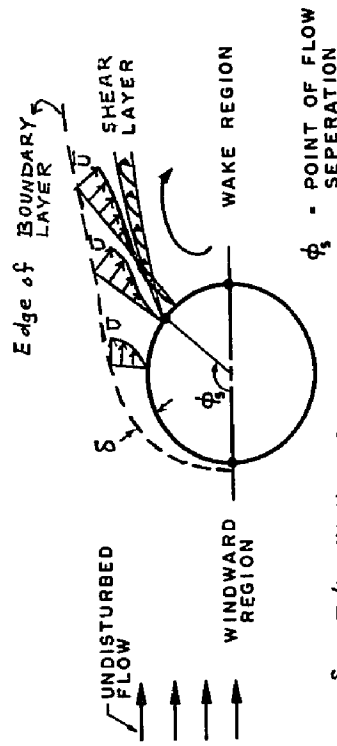


FIG. 2.2 FLOW AROUND CYLINDERS AT LOW Re
($Re \leq 5$)



$\delta = \beta/L$ THICKNESS

ϕ_s - POINT OF FLOW SEPERATION

FIG. 2.3 FLOW AROUND CYLINDERS AT HIGH Re

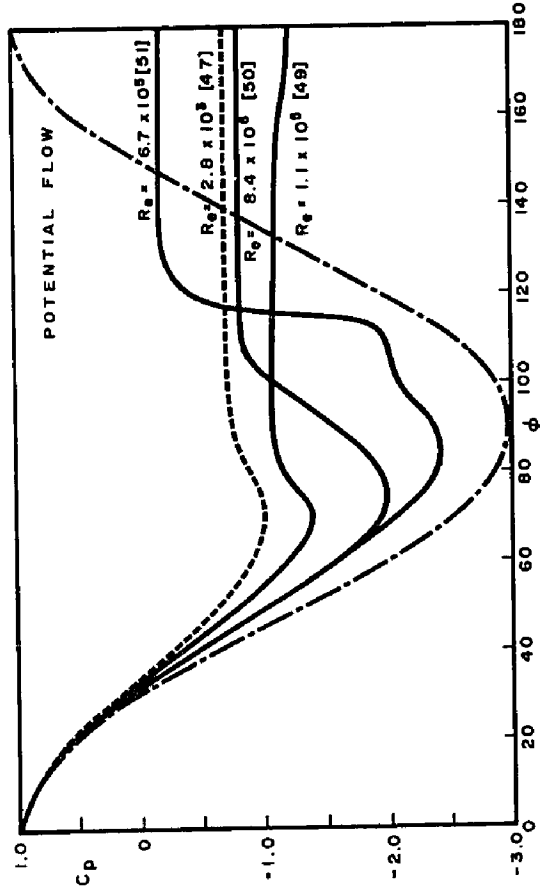


FIG. 2.4 PRESSURE CIRCUMFERENTIAL DISTRIBUTION AROUND LONG CYLINDERS — AFTER ROSKHO [50] WITH ADDITIONS

at $R_e = 3 \times 10^6$ (38).

3. A second forward movement of the points of flow separation starts again for $R_e > 3 \times 10^6$.

These continual changes in the state of flow are reflected in the pressure characteristics around the shell circumference. Fig. 2.4 shows the distribution of wind pressure coefficient at different Reynolds numbers. For all measurements, there is an obvious distinction between the front region and the wake region. The front is characterized by a strong pressure gradient while the pressure in the wake region is more or less uniform. This basic difference is due to the action of viscous forces. The energy dissipation due to these forces is very significant in the wake region. Note also that the variations in the position of flow separation due to increasing R_e is associated with considerable variations in the peak suction and wake pressure.

The previous discussion has so far been limited to cylinders with a smooth surface in a flow stream free of turbulence. The influence of shell surface roughness and the intensity of turbulence in the incoming flow, however, is very important.

From previous investigations (38,43) it was found that for $R_e < 10^4$, the flow around the cylinder is virtually unaffected by surface roughness or the intensity of

turbulence and almost entirely dependent on R_e . However, in the range of Reynolds numbers greater than $R_e \approx 10^4$, both parameters exert a strong influence on the flow and the pressure characteristics. In this range, an increase in shell surface roughness and/or intensity of turbulence, at a given R_e , is equivalent to an increase in Reynolds number. This is clearly evident from Fig. 2.5 showing the variation of the drag coefficient C_d , ($C_d = \int_0^{2\pi} C_p \cos\phi d\phi$) with R_e , surface roughness and intensity of turbulence. Their influence on the pressure distribution has also been investigated. The results from Ref. (44) are depicted in Fig. 2.6. The angle of flow separation and the peak suction appear to be the most sensitive to variation in flow conditions.

While most of the previous studies on the flow past circular cylinders were based on experimental measurements, few attempts have been made to predict the pressure distribution theoretically; e.g. Ref. (45). These require the prior knowledge of certain flow characteristics. For example, the approach described by Parkinson and Jandali (45) requires a prior knowledge of the position of flow separation ϕ_s and the magnitude of the base pressure coefficient C_{pb} (C_p at $\phi = 180^\circ$).

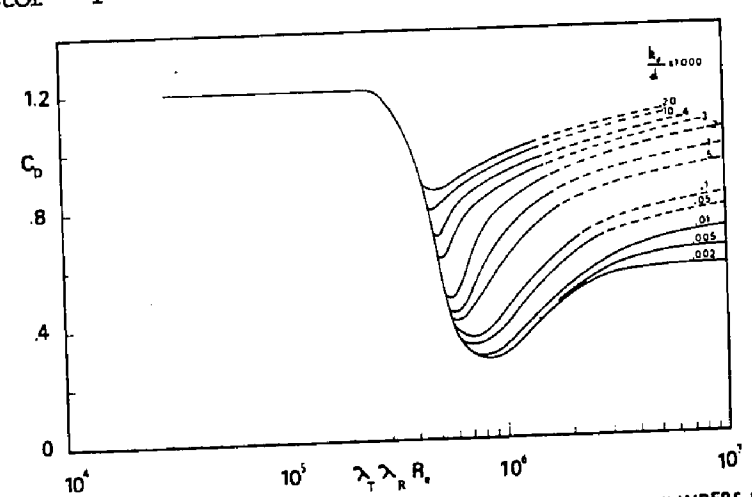
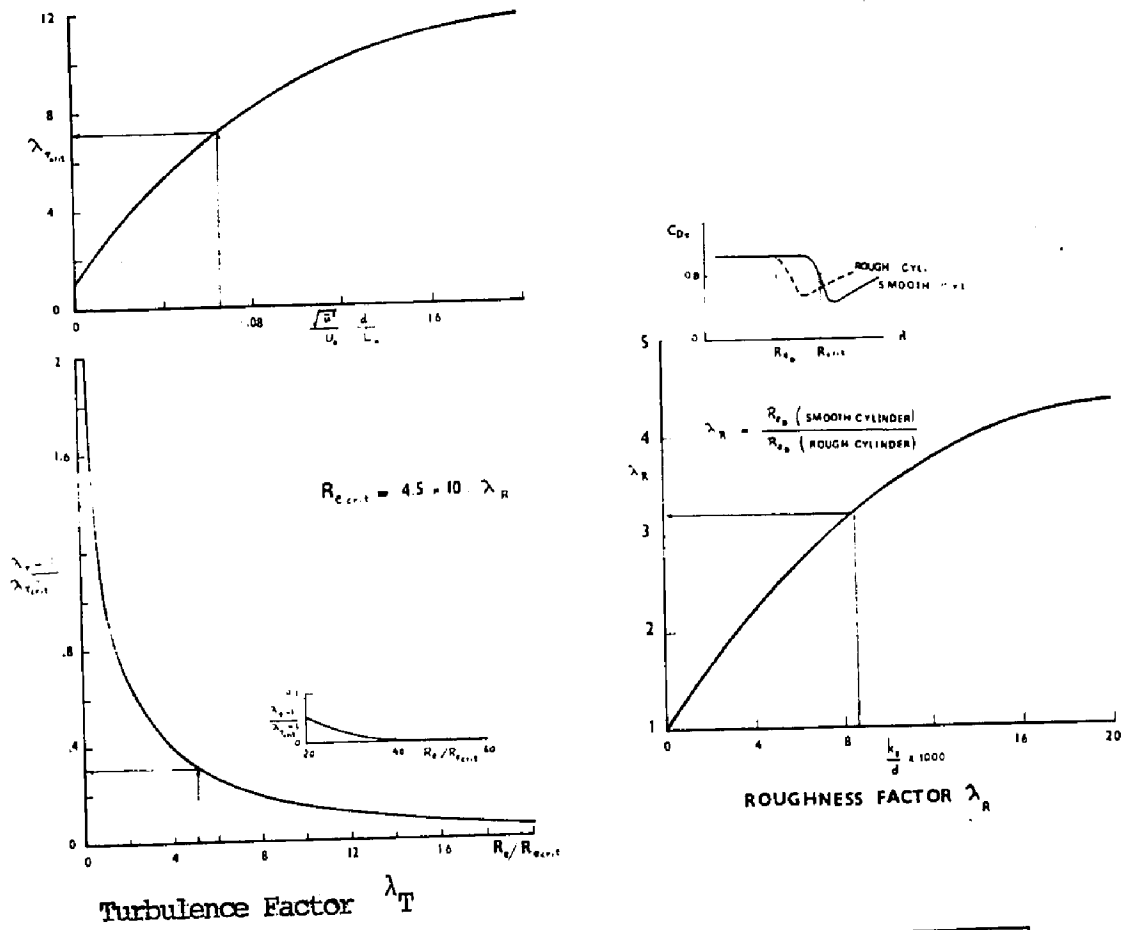


FIG.25 VARIATION OF DRAG COEFFICIENT FOR LONG CIRCULAR CYLINDERS WITH Re , SURFACE ROUGHNESS AND TURBULENCE INTENSITY

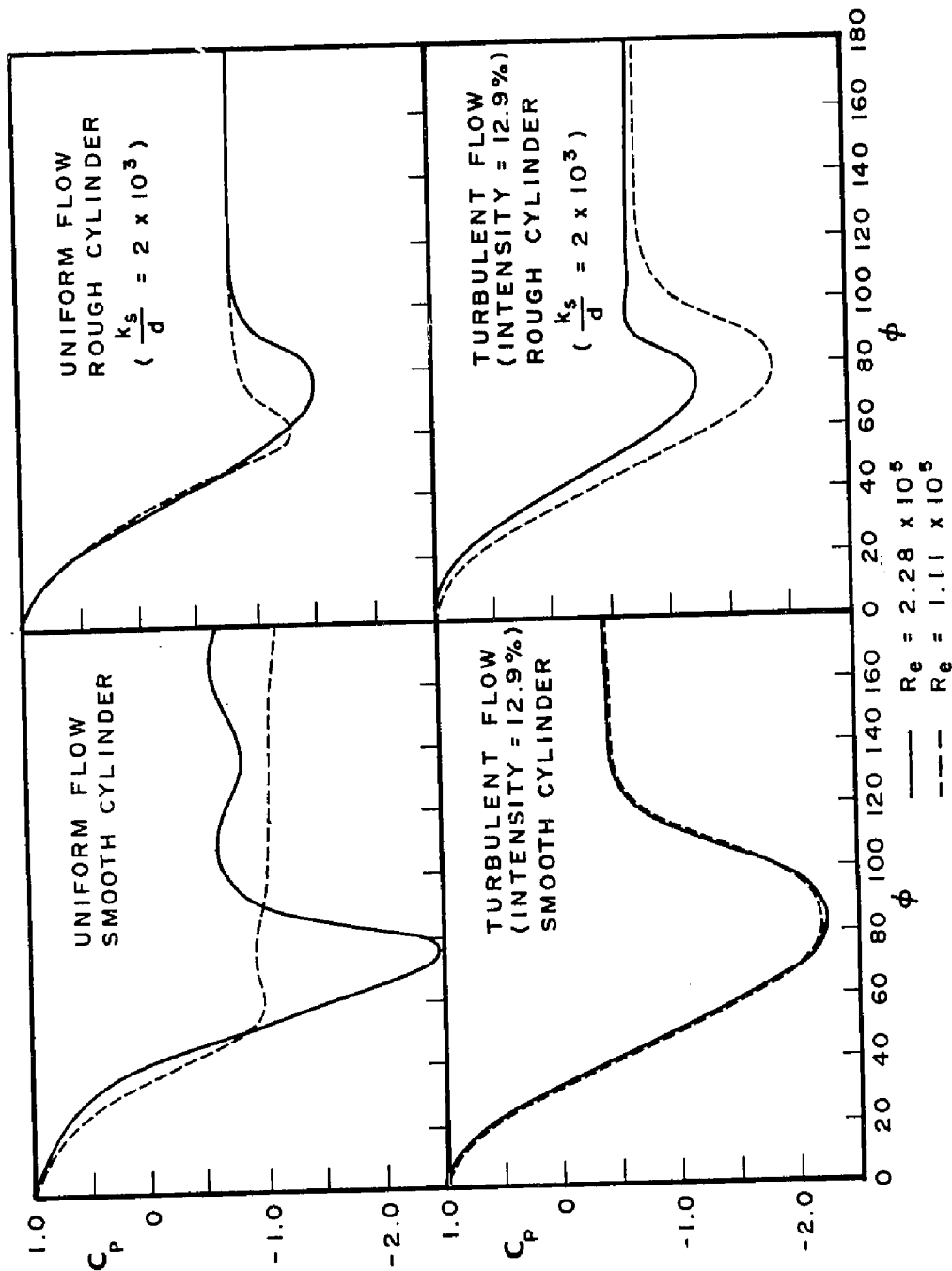


FIG. 2.6 PRESSURE DISTRIBUTION AROUND CIRCULAR CYLINDERS (AFTER BATHAM [54])

2.3.3 Static Wind Pressure on Cooling Towers

There are some basic differences between the wind pressure distribution on cooling towers in natural wind and that on circular cylinders in uniform flow. The flow around the cylinder is essentially two-dimensional, while the flow around a cooling tower is characterized by the development of a three-dimensional boundary layer including the flow over the top of the structure and the end effects on the flow near the base. Also, in natural wind, the local pressure head ($1/2 \rho U^2$) varies with height due to the effects of surface ground roughness. Other factors arise from the differences in geometry, base venting and obstruction to the flow by nearby structures. Nevertheless, the flow of wind around cooling towers exhibits some similar characteristics to the flow around cylinders in two-dimensional flow as will be shown later.

Most of the reported results on the static wind pressure distribution around cooling towers were obtained from wind tunnel measurements (20 to 24) and very limited data from full scale tests are available at present (26). Limited by size restrictions, the simulation of flow in the wind tunnel is only possible at Reynolds numbers two to three orders of magnitude less than full scale R_e , in strong wind conditions. Owing to the strong dependence of wind pressures on R_e , it is not surprising, therefore,

that the reported measurements were often inconsistent.

Measurements of the distribution of mean wind pressure coefficient obtained from model tests (20 to 23) at different Reynolds numbers are depicted in Fig. 2.7 and compared with full scale measurements by Niemann (26). The apparent diversity of the results could be explained in the light of the development of the flow around circular cylinders with varying flow conditions discussed in the previous section.

As in circular cylinders, the position of flow separation ϕ_s is strongly dependent on Reynolds number. Variations in ϕ_s are also associated with significant changes in the peak suction and its location. On the other hand, the base pressure does not appear to be sensitive to changes in R_e in the range of R_e covered in Fig. 2.7 and the results for this from model tests seem to be comparable with full scale measurements.

A parametric study of the important parameters of the wind pressure have been carried out by Niemann (25). Some useful results have emerged from his study and are reproduced in Figs. 2.8 and 2.9. Fig. 2.8 indicate that there exists a simple relationship between the peak suction and its position. A forward movement of the position of flow separation is associated with a reduction in peak suction. It was also found (Fig. 2.9) that the pressure difference between the peak suction and the base

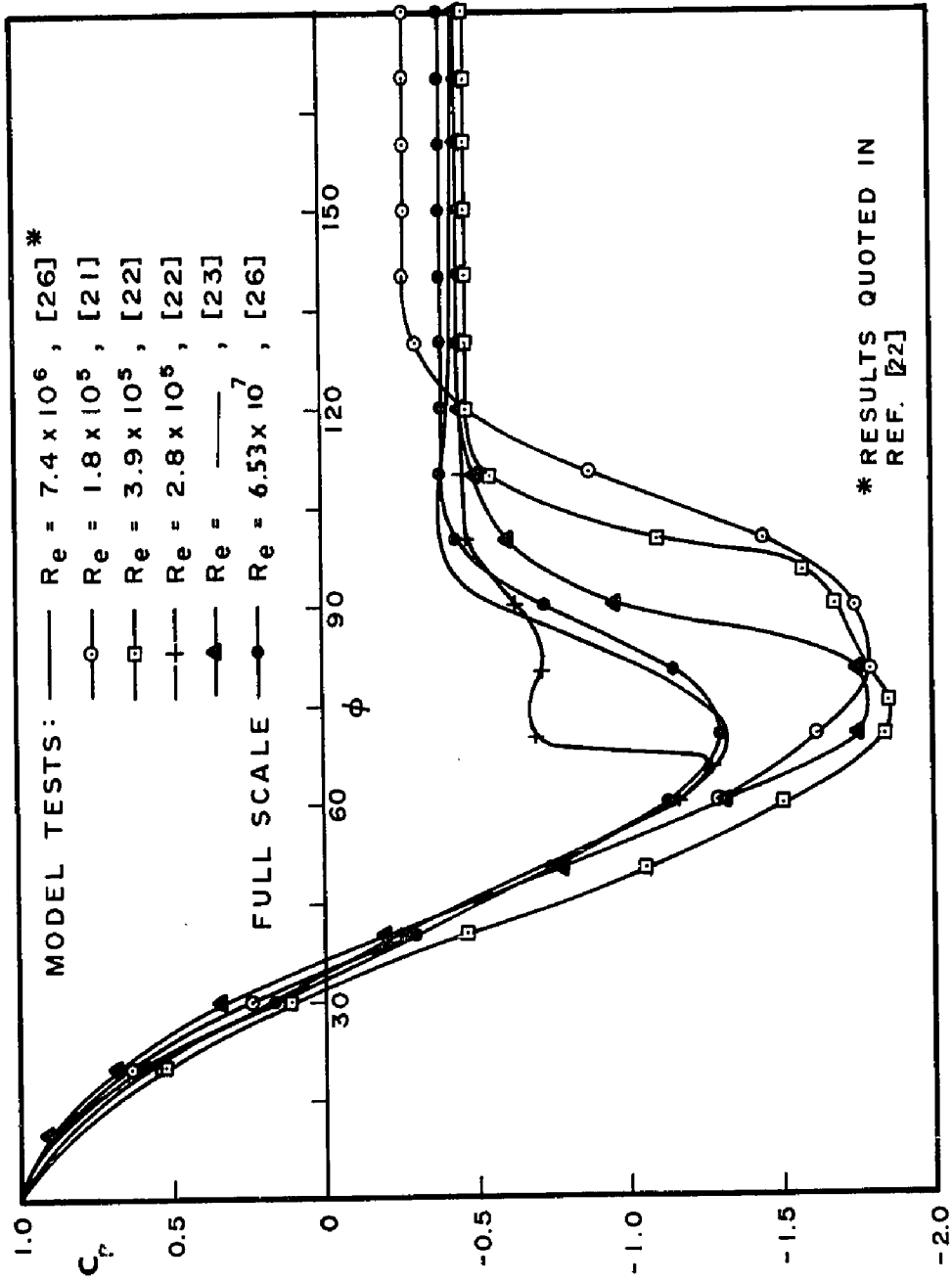


FIG. 2.7

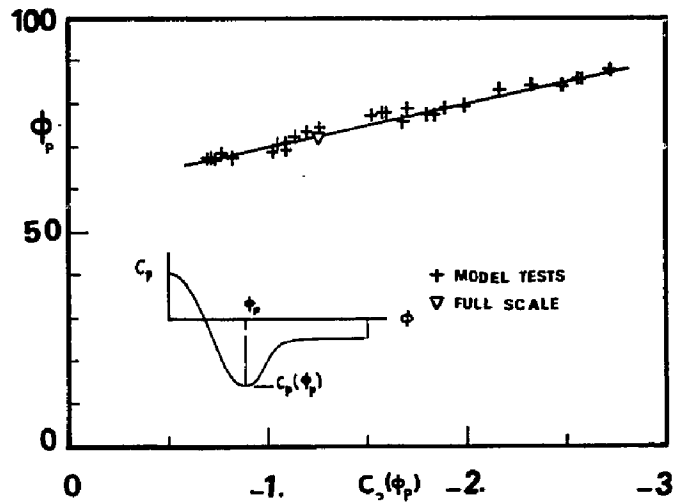


FIG. 2.8 RELATION BETWEEN PEAK SUCTION AND ITS POSITION (AFTER NIEMANN)

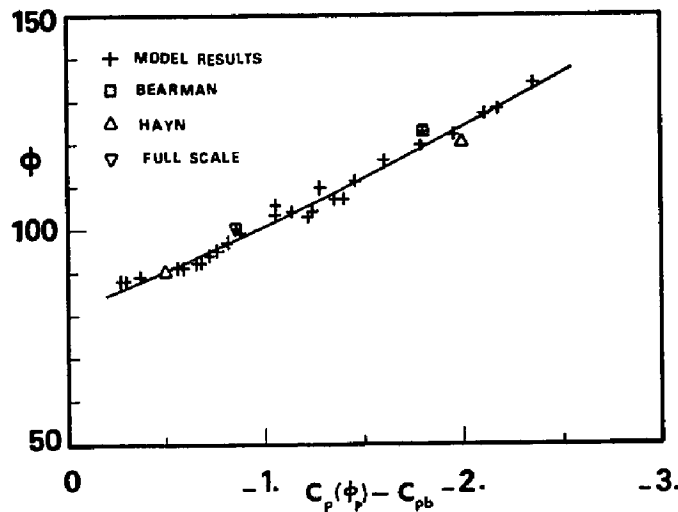


FIG. 2.9 RELATIONSHIP BETWEEN THE DIFFERENCE BETWEEN PEAK SUCTION AND BASE PRESSURE AND THE ANGLE OF FLOW SEPARATION (AFTER NIEMANN)

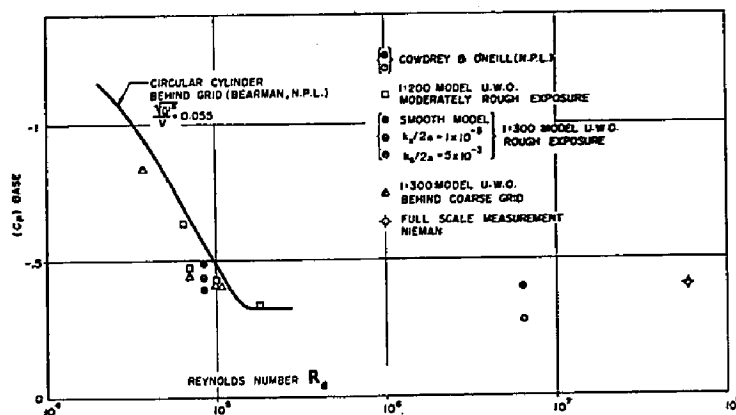


FIG. 2.10 VARIATION OF BASE PRESSURE COEFFICIENT WITH R_a (FROM REF. (36))

pressure could be approximately related to the angle of flow separation ϕ_s . That is, if ϕ_s and base pressure coefficient are known the peak suction and its location could be estimated. This is consistent with the theory of flow around bluff bodies in two-dimensional flow developed by Parkinson and Jandali (45).

The dependence of base pressure coefficient C_{pb} on R_e is depicted in Fig. 2.10 for both model and full scale measurements. For $R_e < 10^5$, C_{pb} is strongly dependent on R_e . At $R_e = 10^5$ it reaches an asymptotic value which is fairly comparable to full scale measurements.

With the apparent difficulties encountered in producing full scale wind conditions in the laboratory, some attempts have been made to utilize the shell surface roughness as a means of simulating high Reynolds number effects. The results obtained by Davenport and Isyumov (21) and by Armit (22) are shown in Figs. 2.11 and 2.12 respectively. The increase in surface roughness causes progressive widening of the wake region. The dependence of peak suction on both Reynolds number and shell surface roughness k_s is shown in Fig. 2.13 from results given in Refs. (20,21,22,25). In this figure, the peak suction is plotted vs. a surface roughness Reynolds number defined by,

$$R_k = \frac{k_s d}{\nu}$$

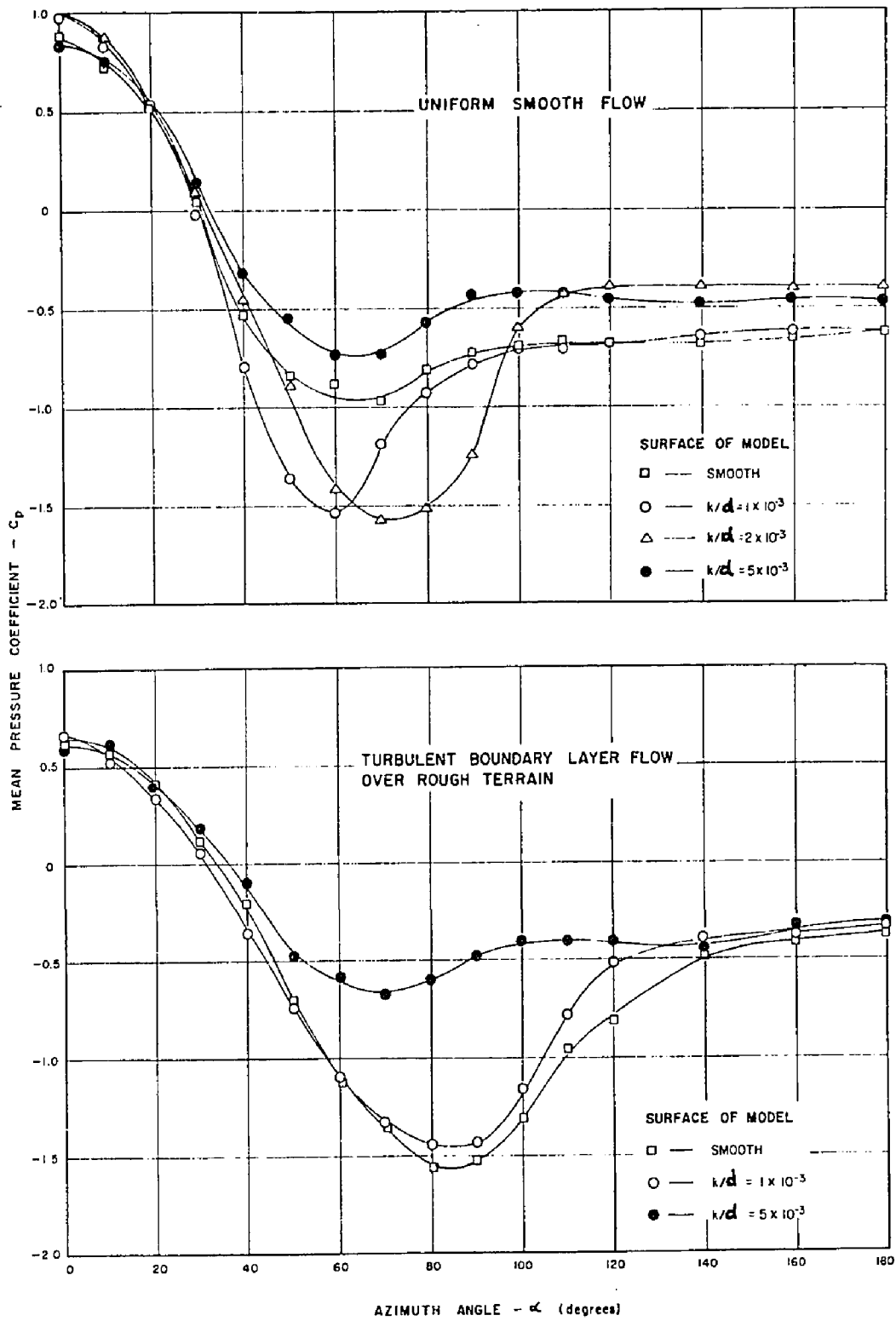
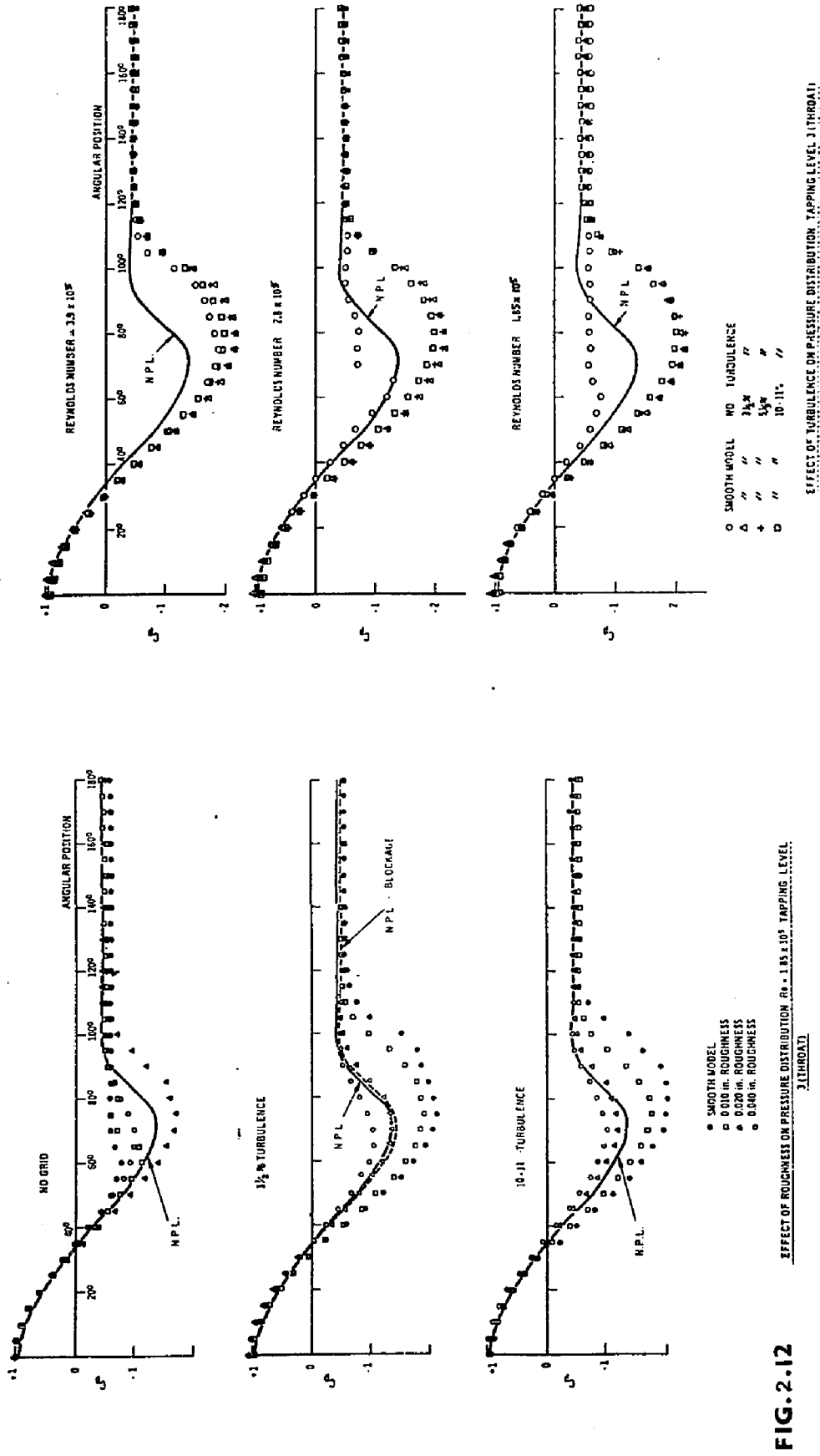


FIG.2.II EFFECT OF MODEL SURFACE ROUGHNESS ON THROAT PRESSURE OF 1:300 SCALE HYPERBOLIC COOLING TOWER MODEL (AFTER DAVENPORT AND ISYUMOV)



(AFTER ARMITT)

FIG. 2.12

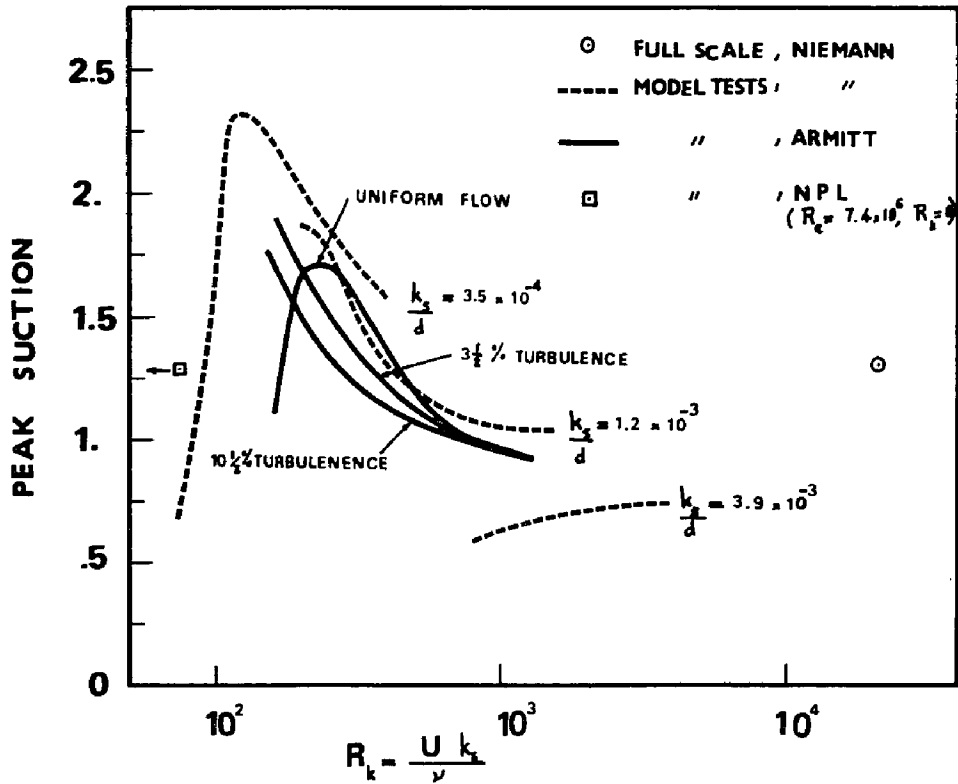


FIG. 2.13 VARIATION OF PEAK SUCTION WITH SURFACE ROUGHNESS REYNOLDS NUMBER

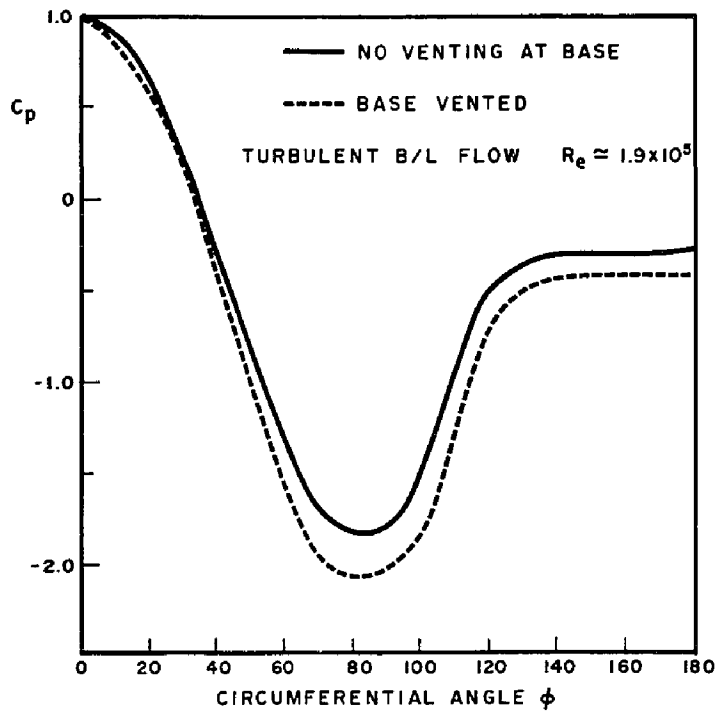


FIG. 2.14 INFLUENCE OF BASE VENTING ON THE PRESSURE DISTRIBUTION (AFTER DAVENPORT & ISYUMOV)

In Fig. 2.13, it is seen that while Armitt's results seem to be dependent only on R_k for a given intensity of turbulence, Niemann's results remain dependent on both k_s and R_k . It is further observed that the asymptotic state reached in Armitt's results does not seem to correspond to either full scale or NPL measurements at high R_e . The asymptotic value reached is some 30 to 40% lower than full scale results.

This discrepancy in the results adds to the uncertainty of the problem. The dependence of wind pressures on flow conditions still needs some more evidence especially from full scale measurements.

Nevertheless, the results of Figs. 2.11 and 2.12 show that the surface roughness may be utilized to produce flow conditions in the laboratory representative of those for cooling towers in strong wind conditions. Attempts toward this goal have to consider the following observations.

1. Wind pressures obtained with a progressive increase in model surface roughness do not seem to be converging to full scale values. Instead, these could be achieved at an intermediate value of k_s .
2. The required surface roughness could only be defined from comparisons with reliable full scale results.
3. As shown in Figs. 2.13, the appropriate value of k_s may fall in a range where the flow is still strongly dependent on k_s . Poor estimates of k_s , therefore,

may lead to unreliable results.

4. Roughness disrupts the true full scale turbulence, i.e. $\sigma_p(s, \phi)$ is not true.

So far, we have been mainly concerned with the influence of Reynolds number and shell surface roughness. However, there are many other factors that influence the pressure characteristics on cooling towers. Most important are:

1. Mean wind profile
2. Tower geometry
3. Base venting
4. Obstruction to the flow by nearby structures.

Some brief comments on these follow.

In natural wind conditions, the variation of mean wind speed $\bar{U}(Z)$ with height above the ground, Z , can be adequately described by a simple power law of the form,

$$\frac{\bar{U}(Z)}{\bar{U}(Z_G)} = \left(\frac{Z}{Z_G}\right)^\alpha \quad (2.6)$$

in which $\bar{U}(Z_G)$ is the wind speed at the gradient height Z_G . The values of α and Z_G for some typical terrains as suggested by Davenport (46) are given in Table 2.1.

Except for the boundary regions, where the flow is influenced by end effects, the wind pressures along the upstream stagnation line follow closely the variation of the dynamic head $(1/2 \rho \bar{U}^2)$ with height (26,47).

TABLE 2.1 (after Davenport (46))

TERRAIN	POWER LAW EXPONENT α	GRADIENT HEIGHT Z_G - ft.
Rough sea	.12	-
Open grassland	.16	900
Forest & Suburban areas	.28	1300
City Centres	.40	1700

The flow around cooling towers could be somewhat influenced by the shape of its meridional profile. This influence is not yet clear, but is thought to be insignificant as can be seen from comparisons of the wind pressure distributions with circular cylinders of finite length.

The influence of base venting on the wind pressure distributions has been reported in Ref. (36) and is depicted in Fig. 2.14. The magnitude of peak suction increases with increasing base venting. The increase, however, is very small and is likely to be insignificant for real base conditions.

The proximity of nearby structures in the upstream or on the sides of the cooling tower could strongly affect the development of flow around the tower. The Ferrybridge failure is a case in point (48). A reliable evaluation of their influence on the wind pressure for a specific project could be assessed from wind tunnel studies.

2.4 Static Wind Stresses

2.4.1 Description of Sample Problem

The analysis of the static wind stresses in hyperbolic cooling towers is investigated, herein, by considering a sample problem. The tower selected is 451 ft. high and its thickness is variable with height as shown in Fig. 2.15. The other geometric and material properties of the tower are: Height above throat = 104 ft.; Throat radius $a = 94.55$ ft.; Meridional Curvature parameter $b = 260.053$ ft.; Young's modulus $E = 4 \times 10^6$ psi; Poisson's ratio = 0.15; Material density $\gamma = 150$ lb./ft.³.

In this study, four different combinations of boundary conditions are considered. These are:

<u>Base</u>	<u>Top</u>
1. Fixed	Free
2. Column-supported	Free
3. Fixed	Ring-stiffened
4. Column-supported	Ring-stiffened

The treatment of the above boundary conditions and their incorporation into the shell equations is described in Appendix I.

The static wind pressure distribution considered is that obtained by Niemann (26) from his full scale measurements and is shown in Fig. 2.7. The Fourier

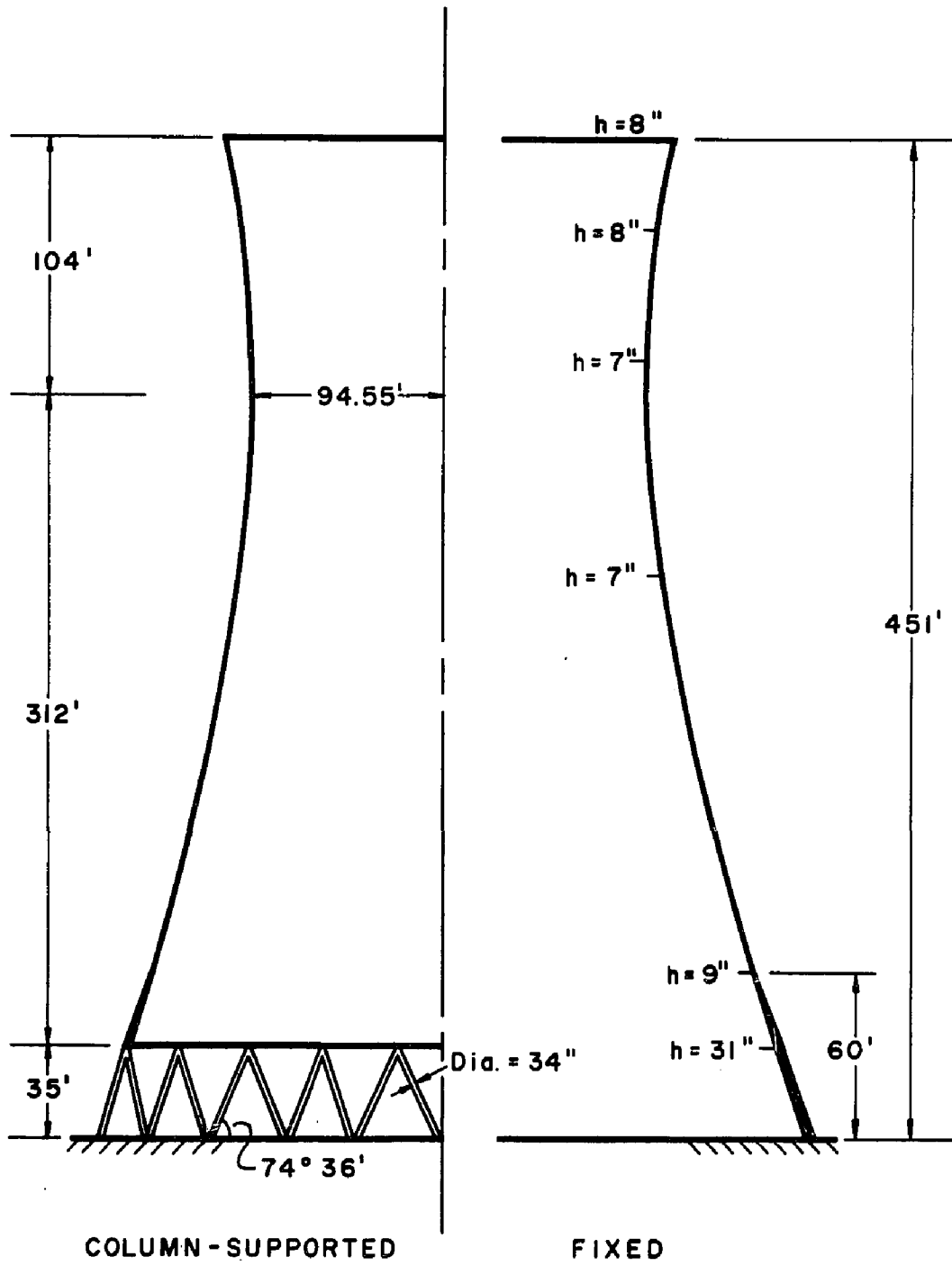


FIG. 2.15

decomposition of this distribution is given in Table 2.2. The variation of wind pressure with height is taken to correspond approximately to exposure A of the NBC 1970 (49). That is,

$$\frac{p(Z)}{p(H)} = \left(\frac{Z}{H}\right)^{0.28} \quad (2.7)$$

in which Z is height above ground. For convenience, the dynamic head at the tower top is set to unity. (1 psf).

2.4.2 Numerical Results

The variation of the meridional force T_1 , the circumferential force T_2 , the meridional moment M_1 and the circumferential moment M_2 along the upwind stagnation line are shown in Figs. 2.16 to 2.19 respectively.

For all combinations of boundary conditions, the most important forces acting on the shell are the meridional force T_1 and the circumferential moment M_2 . T_1 attains its largest values in the lower part of the shell while M_2 is largest in the top part, above the throat.

In order to explore the significance of M_2 on the proportioning of shell reinforcement, the distribution of meridional and circumferential stresses for the fixed-free tower was examined. It was found that, for a unit velocity head at the top edge, the maximum circumferential tensile stress is about 4 psi. (± 5 psi bending stress and

Table 2.2 Harmonic Coefficients for Various Pressure Distributions

Ref. m	0	1	2	3	4	5
CEGB #III	-0.5650	0.0877	0.7423	0.5612	0.1271	0.0235
Marley	-0.5411	0.2268	1.0130	0.4916	-0.1358	-0.0464
Hammon	-0.2338	0.3401	0.5409	0.3871	0.0515	-0.0782
Batch & Hopley	-0.2951	0.2778	0.5982	0.4701	0.0627	-0.1201
NPL	-0.3652	0.2881	0.5211	0.4766	0.1350	-0.1137
Niemann		0.2744	0.5725	0.4909	0.1221	-0.0971

Ref. m	6	7	8	9	10
CEGB #III	0.0400	0.0196	0.0093	0.0027	0.0001
Marley	-0.0231	-0.0168	-0.0056	0.0072	0.0105
Hammon	-0.0068	0.0271	-0.0096	-0.0153	0.0053
Batch & Hopley	-0.0268	0.0444	0.0018	-0.0198	-0.0009
NPL	-0.0772	0.0580	0.0635	-0.0049	-0.0309
Niemann	-0.0436	0.0481	0.0313	-0.0162	

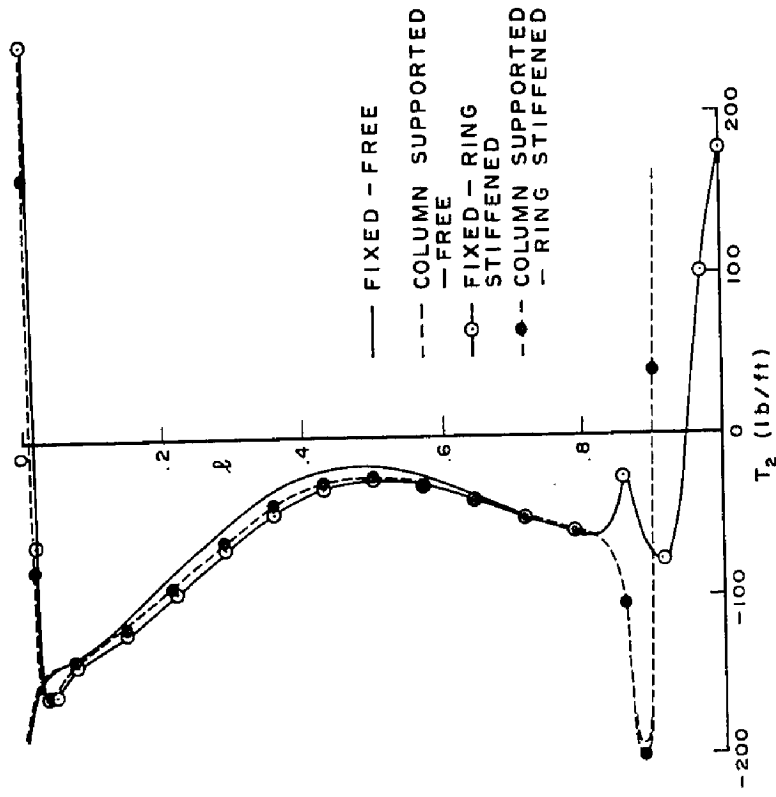


FIG. 2.17

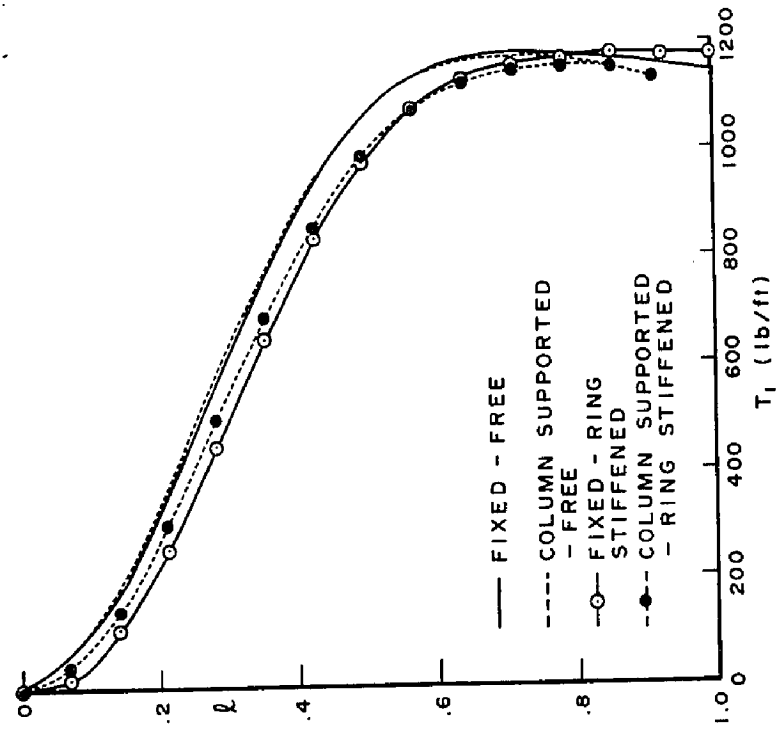


FIG. 2.16

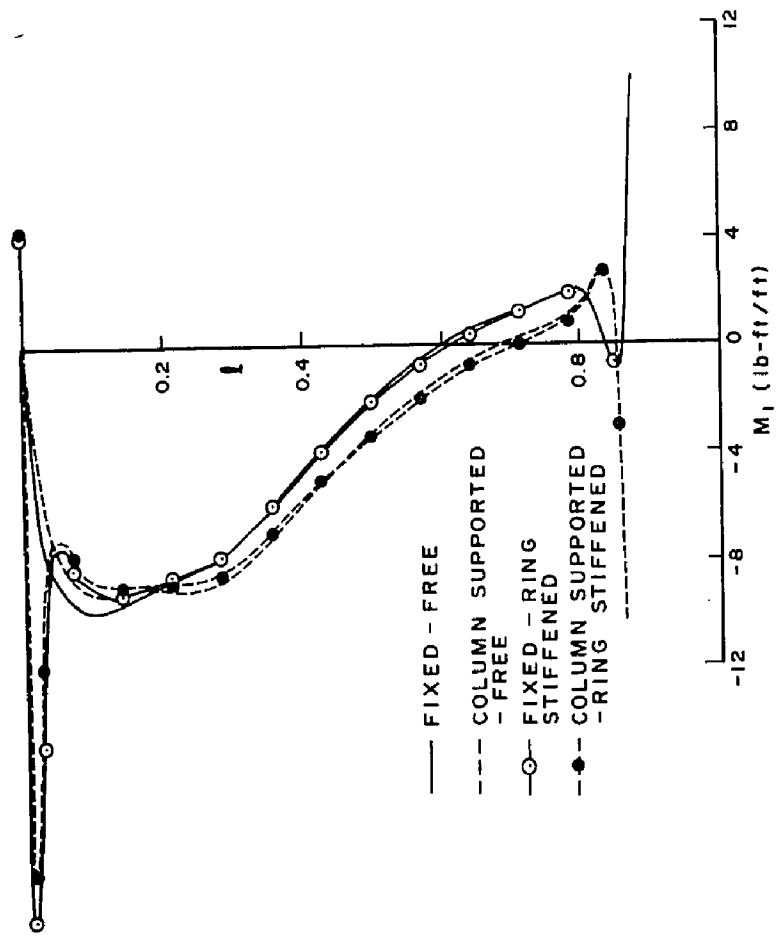


FIG. 2.18

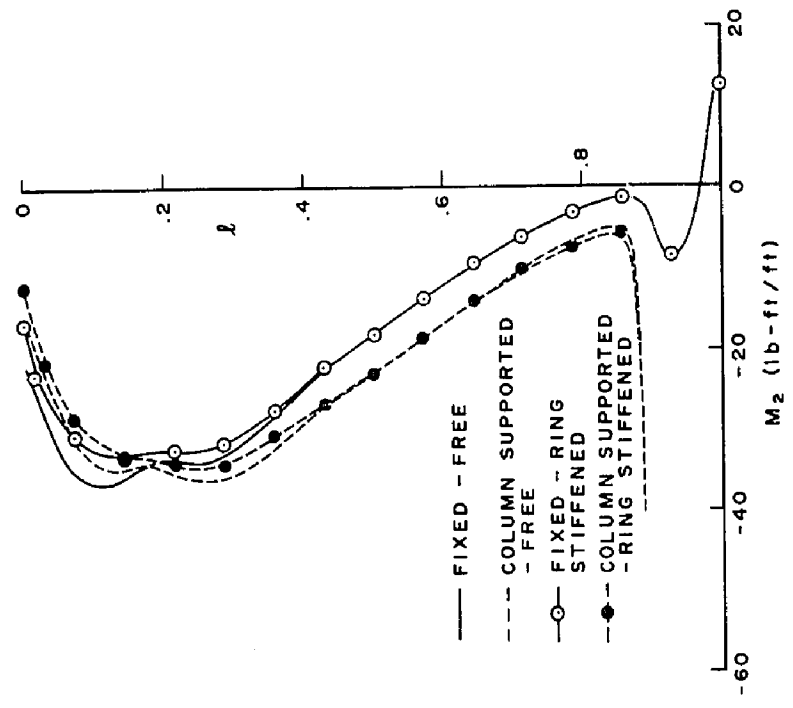


FIG. 2.19

-1 psi membrane stress). The maximum tensile stress in the meridional direction above the base ring is about 13 psi; caused mainly by the membrane force. A significant portion of the meridional tensile stress is counterbalanced by the compressive stresses due to self weight of the shell. The remaining net tensile stresses in the meridional direction will therefore be of the same order as the tensile stresses in the circumferential direction. T_1 and M_2 are therefore equally important in shell design.

Figs. 2.18 and 2.19 indicate that except for the boundary regions, the meridional moment M_1 varies with height in a manner similar to that of the circumferential moment M_2 . Noting that,

$$M_1 = \mu M_2 + (1-\mu^2)D_o\kappa_1 \quad (2.8)$$

in which D_o = shell bending stiffness and κ_1 = change in meridional curvature.

Since κ_1 is very small (50), expression (2.8) approximately reduces to,

$$M_1 \approx \mu M_2 \quad (2.9)$$

Of course, this is a rough approximation. Nevertheless, it shows the strong dependence of M_1 on Poisson's ratio μ . The influence of μ on M_2 is hardly significant; of the order of μ^2 . Therefore,

$$M_2 \approx D_o \kappa_2 \quad (2.10)$$

$$\approx \frac{D_o}{r^2} \sum_m b_m (m^2 w_m + m v_m) \quad (2.11)$$

in which κ_2 = change of curvature in the circumferential direction, m = harmonic wave number, b_m = pressure coefficient of the m th harmonic, and r = radius of a parallel circle. But since (12),

$$v_m \approx -\frac{w_m}{m} \quad \text{for } m > 0 \quad (2.12)$$

then,

$$M_2 \approx \frac{D_o}{r^2} \sum_m b_m (m^2 - 1) w_m \quad (2.13)$$

The above relation provides a reasonable approximation for M_2 , provided w_m is known. In fact, near the throat where M_2 reaches its largest value, the errors in equation (2.13) are very small (roughly of the order 3%) and could be neglected.

Equation (2.13) shows that, M_2 and M_1 practically vanish for $m=1$. The harmonic component of M_2 increases rapidly with increasing wave number m ; roughly as $m^2 w_m$ for $m > 3$. The variation of M_2 , and therefore M_1 , with height follows variations of shell displacement except at the edge zones.

As to the influence of boundary conditions, Figs. 2.17

to 2.19 indicate that for the circumferential force T_2 and moments M_1 and M_2 , the influence of the top ring beam and column supports is localized in the top and lower portions of the shell respectively. Their effect on the state of stress in the rest of the shell is only marginal.

Unlike their influence on all other forces and moments, the effects of ring beam and column supports on the meridional force T_1 , Fig. 2.16, propagate throughout the shell. Nevertheless, their effects are very small everywhere including the boundary regions.

The existence of a top ring beam causes in general a reversal of stress in the uppermost portions of the shell. At the top, T_2 changes from -186 lb./ft. for a fixed-free tower to +245 lb./ft. if the top edge is ring stiffened. This reversal of stress could produce significant tensile stresses in strong wind conditions at the beam junction with the shell. Combined with shrinkage stresses, they could lead to meridional cracks at the junction extending downwards; a phenomena commonly observed in cooling towers (51,52).

The variations of forces and moments in the ring beam along its circumferential axis are shown in Figs. (2.21 and 2.22). By far the largest quantity is the moment in the horizontal plane M_y . If the shell base is fixed, the stresses due to M_y for a typical wind pressure of 33 lb./ft.² is about 170 psi. Other

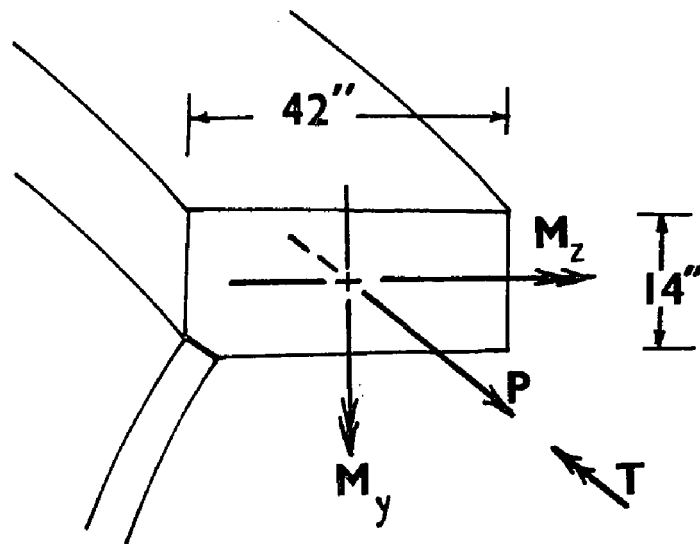


FIG. 2.20

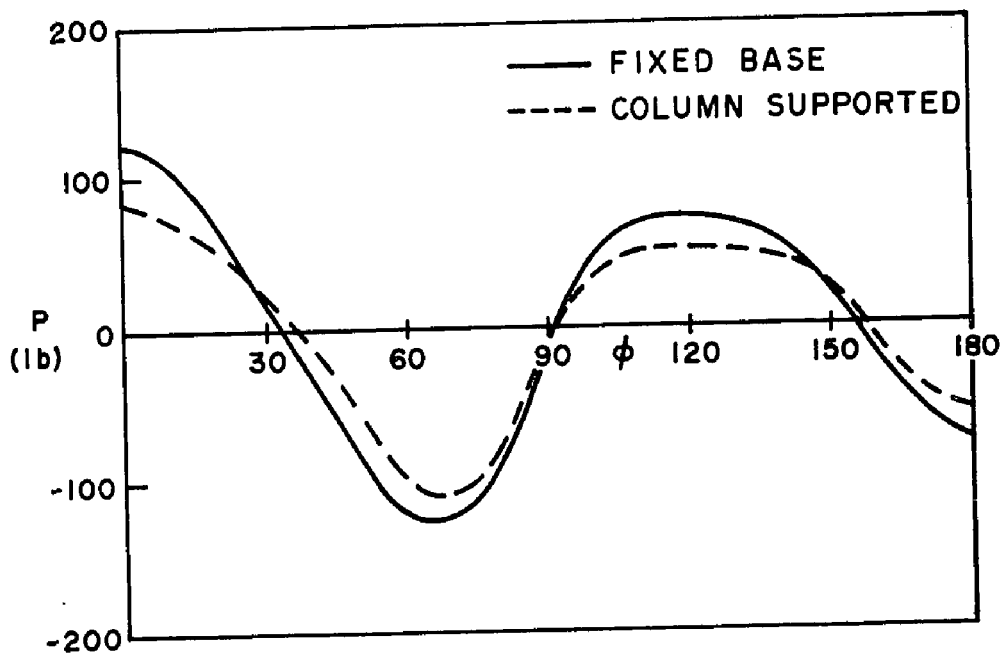


FIG. 2.21 DISTRIBUTION OF AXIAL FORCE IN THE RING BEAM

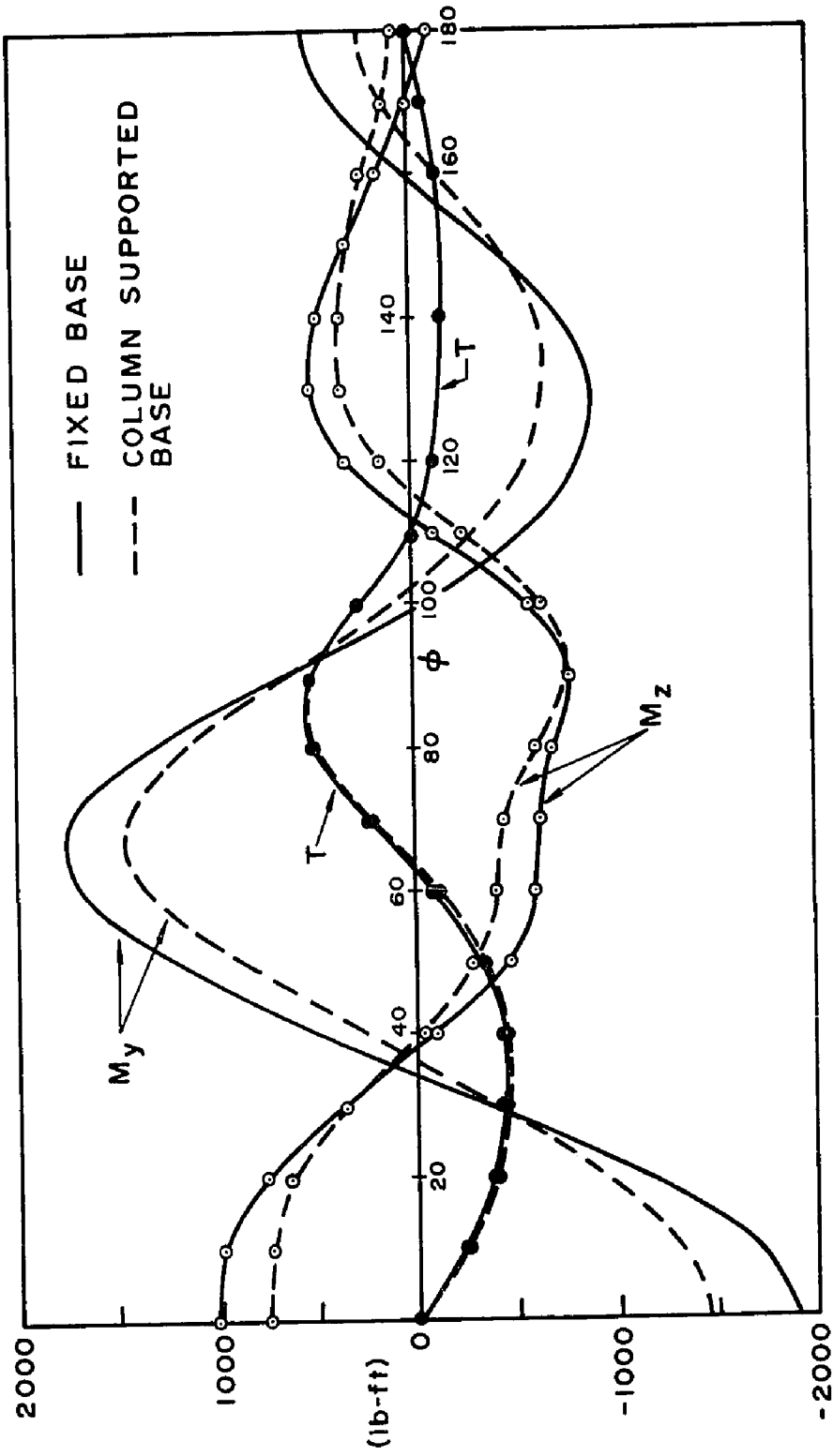


FIG. 2.22 DISTRIBUTION OF INTERNAL MOMENTS IN THE RING BEAM

quantities (P , M_2 and T) are small. The influence of base flexibility on the stresses in the beam are also shown in Figs. (2.21 and 2.22). It is apparent that the beam forces and moments are somewhat reduced if the base becomes flexible.

2.5 Dependence of Static Wind Stresses on Various Parameters

The static wind stresses in hyperbolic cooling towers depend on many factors, amongst which the most important are:

1. Variation of mean wind pressure around shell circumference.
2. Variation of wind pressure with height.
3. Geometrical profile; most important is the meridional curvature.
4. Boundary conditions.

The influence of boundary conditions has already been investigated in the previous section for four different combinations of edge restraints. The dependence of wind stresses on the other three parameters will be examined here. In all cases, the meridional force T_1 and the circumferential moment M_2 only are shown because of their special significance (Section 2.4).

The geometry and material properties of the sample problem considered are the same as in Section 2.4. Fixed-

free boundary conditions are assumed.

2.5.1 Mean Wind Pressure Distribution

As pointed out earlier, the reported measurements of the mean wind pressure distributions differ considerably due to their strong dependence on flow conditions. As a result, it is not possible to suggest a reliable distribution for the design. At present, designers use a variety of wind pressure distributions.

Some selected distributions of the wind pressure adopted in the design are depicted in Fig. 2.23. The large differences between these and the available full scale and model tests are evident from comparisons with results given in Fig. 2.7. It is, therefore, useful to study the sensitivity of the shell response to the different pressure distributions. The Fourier coefficients of the selected distributions considered in the sensitivity analysis are given in Table 2.2. The large variation of the harmonic coefficient for $m=2$ observed in Table 2.2, is directly related to the variations in the peak suction and its location for different distributions as shown in Figs. 2.7 and 2.23.

The pressure coefficients of harmonics $m=0$ to 3 are found to be the only significant ones for all distributions. In the analysis, however, summation over modes is taken up to $m=9$ due to the rapid increase of bending

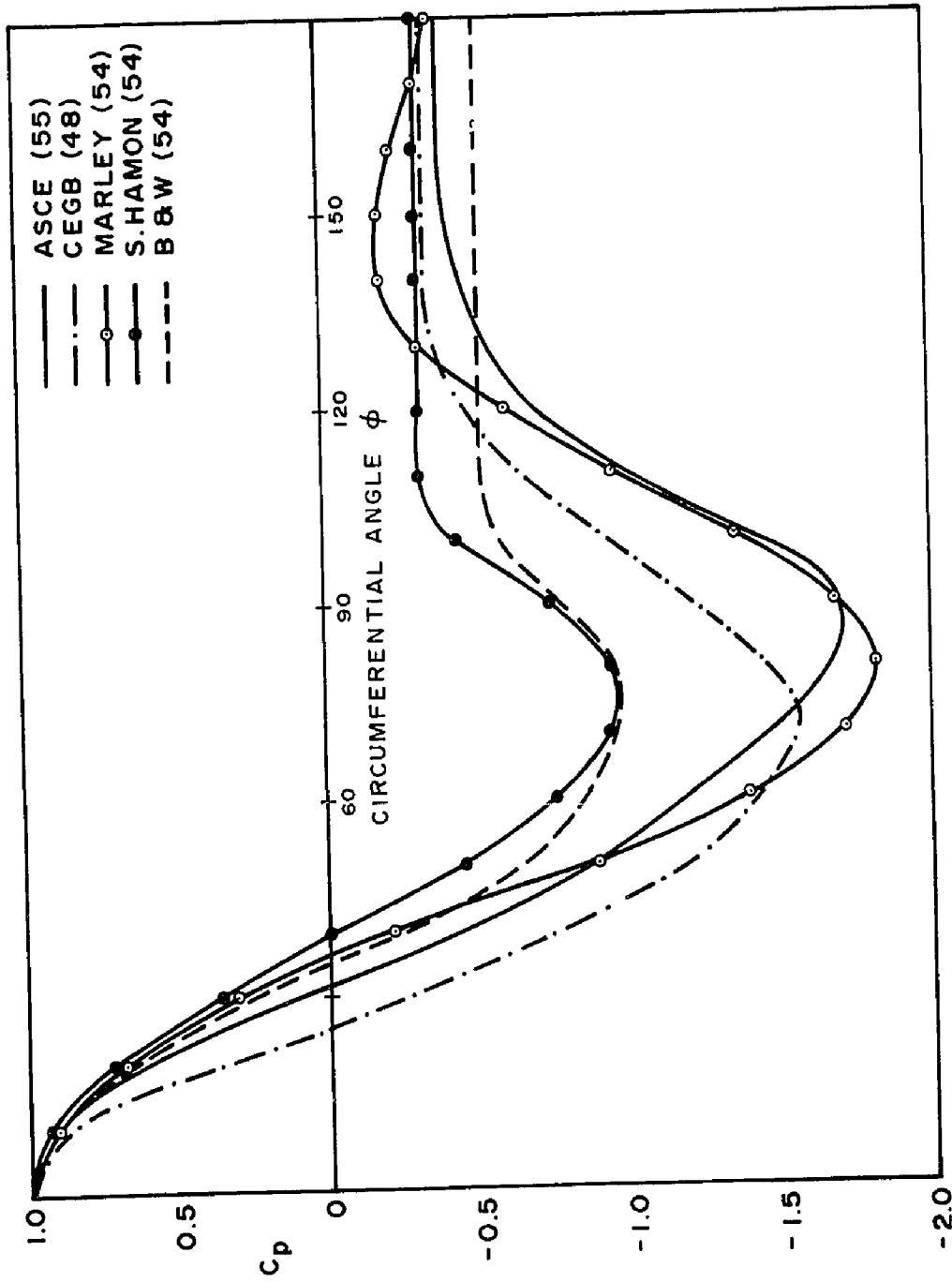


FIG. 2.23 WIND PRESSURE DISTRIBUTION

moments with circumferential wave number m , equation (2.13).

The variation of T_1 and M_2 with height along the upstream stagnation line ($\phi=0$) is shown in Figs. 2.24 and 2.25 respectively.

The CEGB distribution produces the largest stresses in both the meridional and circumferential directions, almost everywhere. It is further observed that while the meridional force produced by the Marley distribution is close to that of CEGB, its circumferential moment is the lowest generated by any other distribution. This is attributed to the fact that the meridional force T_1 is made up mainly from contributions of lower harmonics ($m=1, 2, \text{ and } 3$), while the bending moments are mainly produced from harmonics $m \geq 4$. Therefore, it would be expected that changes in T_1 would be somewhat independent of changes in M_2 for different pressure distributions.

If the full scale measurements by Niemann (26) are taken as a reference, then it could be shown that the largest meridional force varies between +27% and -16% for different distributions. In the upper portion of the shell where the circumferential stresses are the most important, M_2 varies between +60% and -35%. It is thus evident that M_2 is much more sensitive than T_1 to variations in the pressure distribution. This is because the pressure coefficients for high harmonics are more sensitive, than those for low harmonics, to differences in the pressure distribution. Since,

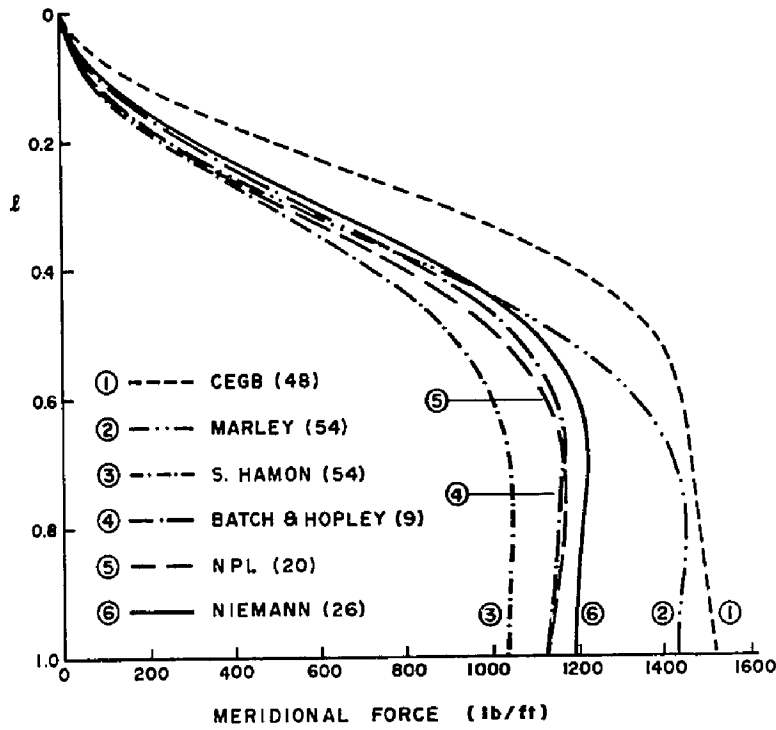


FIG. 2.24 DEPENDENCE OF T_1 ON THE WIND PRESSURE DISTRIBUTION

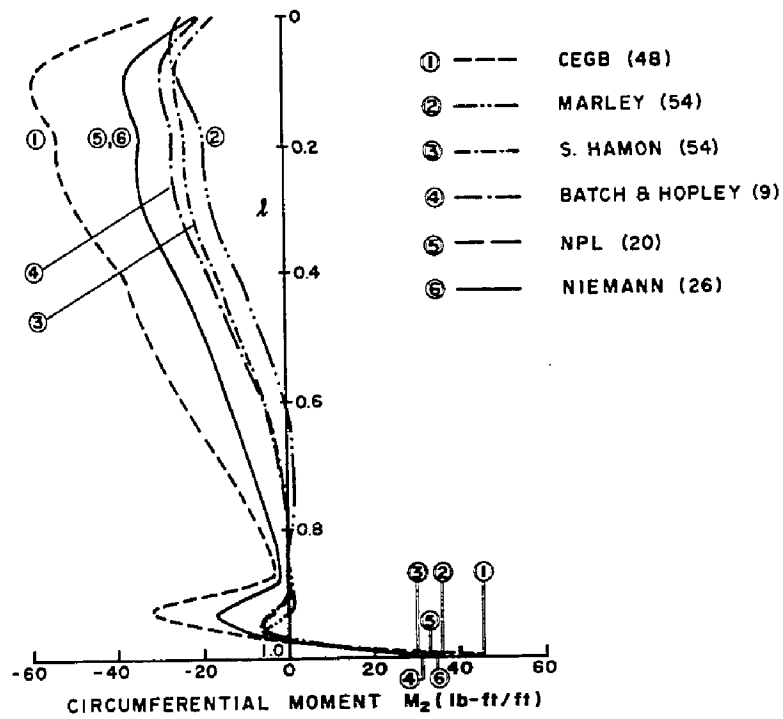


FIG. 2.25 DEPENDENCE OF M_2 ON THE WIND PRESSURE DISTRIBUTION

$$T_1 \propto \sum_m b_m \left(\frac{\partial u_m}{\partial s} + \frac{w_m}{r_1} \right)$$

and from equation (2.13),

$$M_2 \propto \sum_m b_m (m^2 - 1) w_m$$

it becomes evident that variation of modal components of M_2 , unlike T_1 , are magnified by a factor of $(m^2 - 1)$.

Now let us investigate the impact of variations in T_1 and M_2 on the net tensile stresses. The net circumferential stresses are almost directly related to M_2 in regions of largest stresses due to the small contribution of T_2 . Therefore, the range of variation of the circumferential net tensile stress is nearly the same as for M_2 . However, the net tensile stresses in the meridional direction are the differences between the compressive stresses due to self weight and the tensile wind stresses which are both significant. Therefore, the range of the net meridional tensile stresses could be considerably wider than that of T_1 , depending on the design wind velocity and the pressure distribution. This fact is of prime significance in the design since an improper evaluation of wind stresses could lead to either a serious underestimation of shell reinforcement or an unnecessary overestimation. Therefore, safe and economic design can only be insured if reliable estimates of the pressure distribution and the design wind

speed can be made.

2.5.2 Variation of Wind Pressure With Height

The variation of mean wind pressure with height along the upstream stagnation line can be represented by,

$$\frac{\bar{p}(Z)}{\bar{p}(H)} = \left(\frac{Z}{H}\right)^{2\alpha}$$

The values of α for some typical terrain exposures, as suggested by Davenport, are given in Table 2.1.

The type of exposure that has to be considered in design will depend largely on the direction of the prevailing winds and an attempt will have to be made to predict the worst conditions to which the cooling tower could be exposed. For the latter part, it is generally beneficial to conduct wind tunnel studies to define the appropriate value of α for a given terrain. For a typical cooling tower, the value of α is likely to lie somewhere between that for exposures A and B of the NBC (49).

In the present analysis, the values of α considered are:

- a/ $\alpha = 0$; constant pressure distribution.
- b/ $\alpha = 0.14$; exposure A, open terrain.
- c/ $\alpha = 0.25$; exposure B, suburban and urban areas.

The variation of T_1 and M_2 with height along the

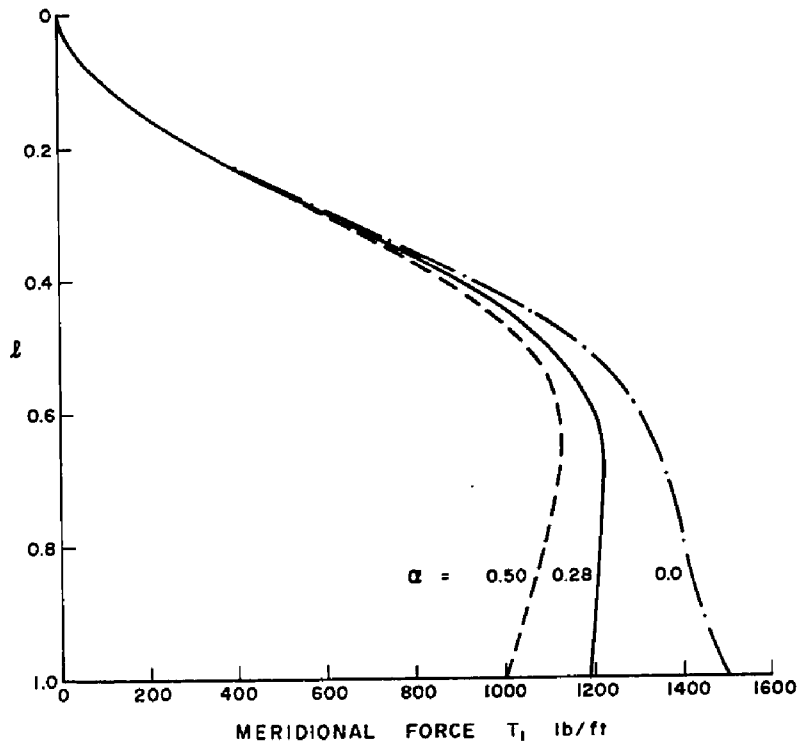


FIG. 2.26 INFLUENCE OF WIND SHEAR ON T_1

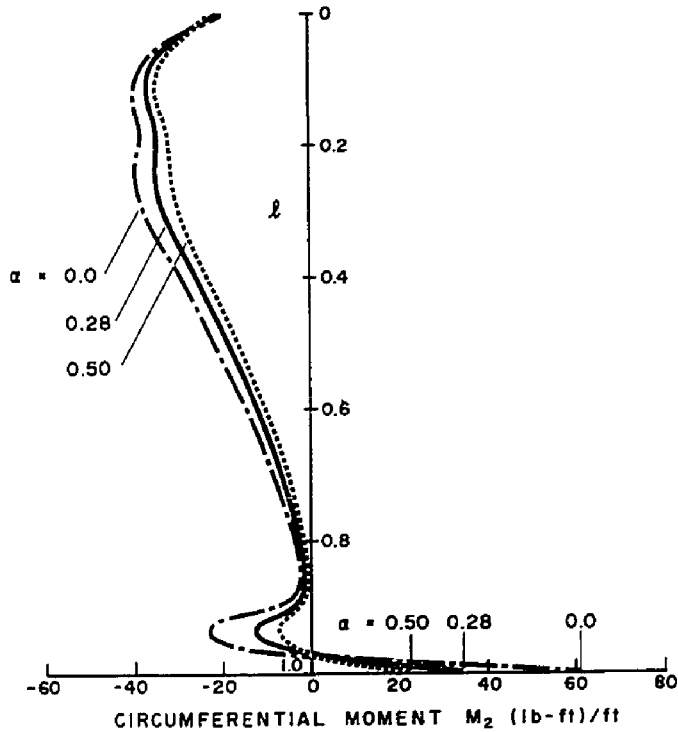


FIG. 2.27 INFLUENCE OF WIND SHEAR ON M_2

upstream stagnation line, for the three values of α is shown in Figs. 2.26 and 2.27 respectively. The strong influence of ground roughness on the meridional stresses in the lower part of the shell is evident from Fig. 2.26. Taking $\alpha = 0$ as a reference, then ground roughness of types A and B will reduce the base stresses by 20% and 35% respectively. Their influence on M_2 in the upper part of the shell where the circumferential stresses are the most important is very small.

The differences between results for T_1 and to some degree M_2 , for the three different values of α , decrease gradually with height above ground. This is consistent with the variation of the corresponding wind pressure with height.

2.5.3 Meridional Curvature

The resistance of cooling towers to wind action arises from two different sources; membrane and bending action. For fixed base conditions, the membrane energy is generally predominant and provides the main source for the overall shell stiffness.

In previous investigations (12,50,53), the dependence of both the membrane and bending action on various parameters was examined. It was found that the membrane energy is particularly sensitive to changes in the meridional curvature. The bending energy, on the other

hand, is almost invariant with changes in meridional curvature (12). Therefore, a study of the dependence of wind stresses on the meridional curvature is essential for an optimum design of the cooling tower.

In the analysis, the following geometric properties were kept constant: a - height, b - throat radius, and c - height above throat. The following values of the ratio k_o describing the meridional curvature were considered;

$$k_o = a/b = 0, 0.3, 0.365, 0.4 \text{ and } 0.5$$

$k_o = 0$ corresponds to a circular cylinder. $k_o \approx 0.4$ is the most common value for hyperbolic cooling towers in the U.S.A.

The variation of T_1 and M_2 with height for different values of k_o are shown in Figs. 2.28 and 2.29, respectively. Both T_1 and M_2 are found to decrease rapidly with increasing meridional curvature. This is a direct result of a consistent rise of the membrane action as k_o increases (12).

The value of k_o lies somewhere between 0.35 and 0.45 for most towers built in U.S.A. (see Chapter 1). Wind stresses generated in towers with meridional curvature in this range expressed as a proportion of the stresses in a corresponding cylinder are found to be some 16 to 23% for the meridional force T_1 in the lower portion of the shell;

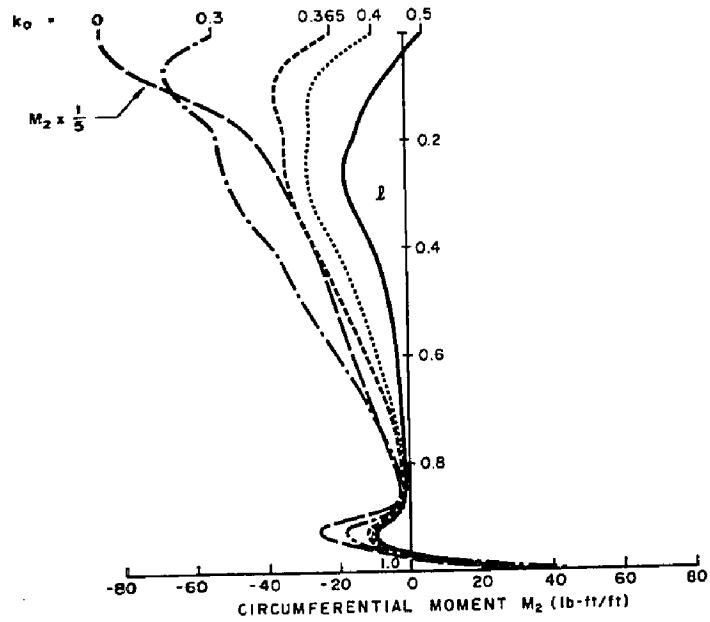


FIG. 2.29 INFLUENCE OF MERIDIONAL CURVATURE; M_2

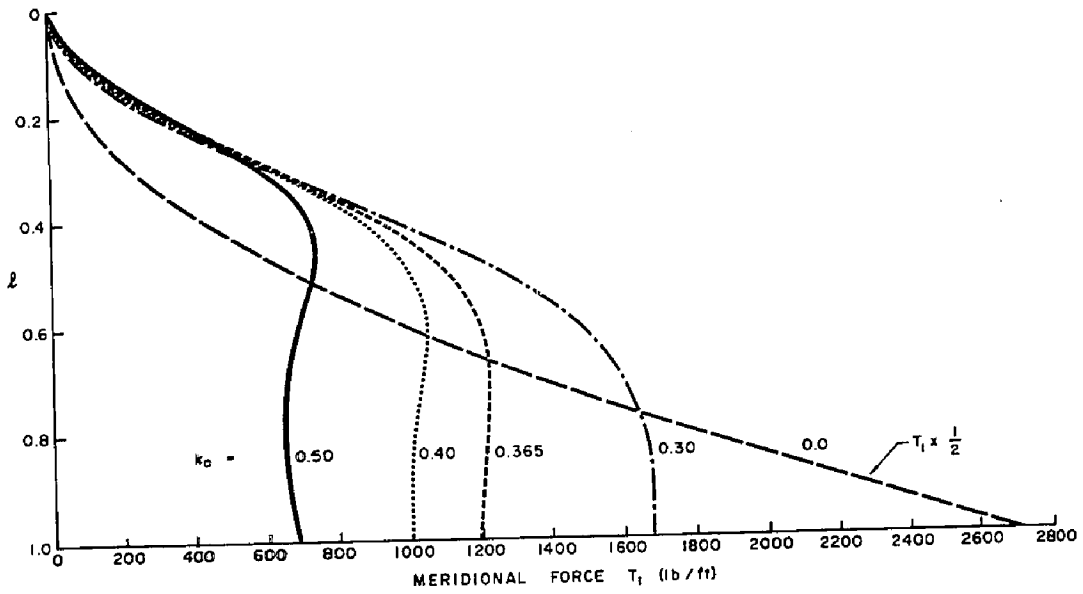


FIG. 2.28 INFLUENCE OF MERIDIONAL CURVATURE ON T_1

and only 5 to 10% for the circumferential moment M_2 in the upper portion of the shell. This again emphasizes the marked superiority of the hyperbolic profile over the cylindrical shape.

CHAPTER 3

THEORY OF COOLING TOWERS RESPONSE

3.1 Introduction

The wind loads on structures are in part random in nature. Owing to their random fluctuations in both magnitude and direction, the analysis of the wind response of a spatially extended structure is rather complex. This is because (a) a great deal of information is required to describe the character of the wind forces over the surface of the structure, and (b) the response of the structure has to include the interaction of the wind and the structure, and the vibration characteristics of the structure itself.

Recently, however, significant advances have been made towards a realistic evaluation of the wind response taking into account the random nature of the wind and the dynamic characteristics of the structure, by a number of authors (1 to 7); notably Davenport (1,2,3). These were inspired in part by the failure of some major structures, the increasing flexibility of some important civil engineering structures and the recent advances in random vibration analysis (8,9,10).

Most of the work in civil engineering, however, has

been mainly concerned with structures whose behaviour is governed by one major dimension, such as masts and high rise buildings. The response of cooling towers and similar shells of revolution to wind, however, is basically different from line-like structures. The variation of wind pressure characteristics in the horizontal direction is as important as their variation in the vertical direction. Both directions, plus the interaction between them, have to be taken into account. To the author's knowledge, no comprehensive treatment of cooling tower response to wind is published.

The purpose of this chapter is to develop the theory of response of shells of revolution to turbulent wind loads. The theory takes account of the random nature of wind, structural and vibration properties of the shell, and the wind/shell interaction.

In the formulation of the theory, the wind loads are regarded as composed of a mean component and a fluctuating component, superimposed linearly. The treatment of the static component has been dealt with in Chapter 2.

3.2 Assumptions

The assumptions concerning the shell material and the state of deformation of the shell are the usual ones for linear shell theory (11) and are outlined in Appendix I. The following assumptions are considered acceptable in the

shell wind response:

1. The wind pressures could be regarded as a stationary random process.
2. The shell response could be adequately described by a linear analysis.
3. The critical damping ratio is very small.

3.3 Modal Representation

The instantaneous patterns of the wind pressure fluctuations continually change with time. Hence, the wind response of each mode could be conveniently resolved into a symmetric and an anti-symmetric component about the prevailing wind direction. Expressions for shell displacements can then be written in terms of the natural modes of vibration in the following manner:

$$u(s, \phi, t) = \sum_m \sum_i \{q_{m,i}(t) \cos m\phi + q'_{m,i}(t) \sin m\phi\} u_{m,i}(s) \quad (3.1)$$

$$w(s, \phi, t) = \sum_m \sum_i \{q_{m,i}(t) \cos m\phi + q'_{m,i}(t) \sin m\phi\} w_{m,i}(s) \quad (3.2)$$

$$v(s, \phi, t) = \sum_m \sum_i \{q_{m,i}(t) \sin m\phi - q'_{m,i}(t) \cos m\phi\} v_{m,i}(s) \quad (3.3)$$

in which s, ϕ = meridional and circumferential coordinates, Fig. 2.1, t = time, u, v and w = displacement components in the meridional, circumferential and normal directions, $q_{m,i}(t), q'_{m,i}(t)$ = symmetric and anti-symmetric time dependent generalized coordinates of the i th mode associated with a circumferential harmonic wave number m respectively, $u_{m,i}, v_{m,i}$ and $w_{m,i}$ = mode shapes of displacement components in the meridional direction.

Expressions for the meridional force T_1 and moment M_1 and the circumferential force T_2 and moment M_2 are similar to those of u or w ; equations (3.1 and 3.2). Those for the effective-in-plane shear force \tilde{S} and twist H are similar to that of v ; equation (3.3).

3.4 Equations of Motion

The shell equations of motion under time dependent loads can be deduced from the equilibrium equations of the shell presented in Appendix I by the proper addition of the inertia and damping forces. The resulting equations can then be written in terms of the generalized coordinates, $q_{m,i}(t)$ and $q'_{m,i}(t)$, by substituting for shell displacements from equations (3.1 to 3.3). They are:

$$\sum_i \{ \rho h \ddot{q}_{m,i}(t) + c \dot{q}_{m,i}(t) + \rho h \omega_{m,i}^2 q_{m,i}(t) \} u_{m,i}(s) \cos m \phi +$$

$$\sum_{m,i} \{ \rho h \ddot{q}'_{m,i}(t) + c \dot{q}'_{m,i}(t) + \rho h \omega_{m,i}^2 q'_{m,i}(t) \} u_{m,i}(s) \sin m\phi =$$

$$p_1(s, \phi, t) \quad (3.4)$$

$$\sum_{m,i} \{ \rho h \ddot{q}'_{m,i}(t) + c \dot{q}'_{m,i}(t) + \rho h \omega_{m,i}^2 q'_{m,i}(t) \} v_{m,i}(s) \sin m\phi -$$

$$\sum_{m,i} \{ \rho h \ddot{q}'_{m,i}(t) + c \dot{q}'_{m,i}(t) + \rho h \omega_{m,i}^2 q'_{m,i}(t) \} v_{m,i}(s) \cos m\phi =$$

$$p_2(s, \phi, t) \quad (3.5)$$

$$\sum_{m,i} \{ \rho h \ddot{q}'_{m,i}(t) + c \dot{q}'_{m,i}(t) + \rho h \omega_{m,i}^2 q'_{m,i}(t) \} w_{m,i}(s) \cos m\phi +$$

$$\sum_{m,i} \{ \rho h \ddot{q}'_{m,i}(t) + c \dot{q}'_{m,i}(t) + \rho h \omega_{m,i}^2 q'_{m,i}(t) \} w_{m,i}(s) \sin m\phi =$$

$$p_3(s, \phi, t) \quad (3.6)$$

in which ρ = mass density, h = shell thickness, $\omega_{m,i}$ = natural frequency of the i th mode of the m th harmonic, c = combined structural and aerodynamic damping, p_1 , p_2 , and p_3 = meridional, circumferential, and normal components of the wind pressure respectively, and dots refer to derivatives w.r.t. time.

Now, multiplying equation (3.4) by $u_{n,j} \cos n\phi$, equation (3.5) by $v_{n,j} \sin n\phi$ and equation (3.6) by $w_{n,j} \cos n\phi$ and integrating over the shell surface while observing the orthogonality conditions between natural modes of vibration,

stating that for all values of m, n, i and j except those for $m = n$ or $i = j$, the integrals,

$$\int_0^{s_0} \int_0^{2\pi} u_{m,i}(s) u_{n,j}(s) \cos m\phi \cos n\phi \rho h r(s) d\phi ds = 0 \quad (3.7)$$

$$\int_0^{s_0} \int_0^{2\pi} v_{m,i}(s) v_{n,j}(s) \sin m\phi \sin n\phi \rho h r(s) d\phi ds = 0 \quad (3.8)$$

$$\int_0^{s_0} \int_0^{2\pi} w_{m,i}(s) w_{n,j}(s) \cos m\phi \cos n\phi \rho h r(s) d\phi ds = 0 \quad (3.9)$$

and that for all values of m and n ,

$$\int_0^{2\pi} \cos m\phi \sin n\phi = 0$$

then, it could be shown that,

$$\begin{aligned} & \{\ddot{q}_{n,j}(t) + \omega_{n,j}^2 q_{n,j}(t)\} \int_0^{s_0} \pi \rho h u_{n,j}^2(s) r(s) ds + \sum_{m \neq i} \{\dot{q}_{m,i}(t) \\ & \int_0^{s_0} \int_0^{2\pi} c u_{m,i}(s) u_{n,i}(s) \cos m\phi \cos n\phi r(s) d\phi ds + \dot{q}'_{m,i}(t) \int_0^{s_0} \int_0^{2\pi} \\ & c u_{m,i}(s) u_{n,j}(s) \sin m\phi \cos n\phi r(s) d\phi ds\} = \\ & \int_0^{s_0} \int_0^{2\pi} p_1(s, \phi, t) u_{n,j}(s) \cos n\phi r(s) d\phi ds \quad (3.10) \end{aligned}$$

$$\begin{aligned} & \{\ddot{q}_{n,j}(t) + \omega_{n,j}^2 q_{n,j}(t)\} \int_0^{s_0} \pi \rho h v_{n,j}^2(s) r(s) ds + \sum_{m \neq i} \{\dot{q}_{m,i}(t) \\ & \int_0^{s_0} \int_0^{2\pi} c v_{m,i}(s) v_{n,j}(s) \sin m\phi \sin n\phi r(s) d\phi ds - \dot{q}'_{m,i}(t) \end{aligned}$$

$$\int_0^{s_0} \int_0^{2\pi} c v_{m,i}(s) v_{n,j}(s) \cos m\phi \sin n\phi r(s) d\phi ds =$$

$$\int_0^{s_0} \int_0^{2\pi} p_2(s, \phi, t) u_{n,j}(s) \sin n\phi r(s) d\phi ds \quad (3.11)$$

$$\{\ddot{q}_{n,j}(t) + \omega_{n,j}^2 q_{n,j}(t)\} \int_0^{s_0} \pi \rho h \omega_{n,j}^2(s) r(s) ds + \sum_{m,i} \ddot{q}_{m,i}(t)$$

$$\int_0^{s_0} \int_0^{2\pi} c w_{m,i}(s) w_{n,j}(s) \cos m\phi \cos n\phi r(s) d\phi ds + \dot{q}'_{m,i}(t)$$

$$\int_0^{s_0} \int_0^{2\pi} c w_{m,i}(s) w_{n,j}(s) \sin m\phi \cos n\phi r(s) d\phi ds = \int_0^{s_0} \int_0^{2\pi}$$

$$p_3(s, \phi, t) w_{n,j}(s) \cos m\phi r(s) d\phi ds \quad (3.12)$$

It is readily observed that each of the above three equations of motion are coupled due to the presence of damping. They could be decoupled if:

1. The following term of equation (3.10) satisfies the following condition:

$$\sum_{m,i} \dot{q}_{m,i}(t) \int_0^{s_0} \int_0^{2\pi} c u_{m,i}(s) u_{n,j}(s) \cos m\phi \cos n\phi r(s) d\phi ds$$

$$= \dot{q}_{n,i}(t) \int_0^{s_0} \pi c u_{n,j}^2(s) r(s) ds$$

for $m = n, i = j$

$$= 0 \text{ for all other values of } m \text{ and } i$$

$$(3.13)$$

and

$$2. \sum_{mi} \dot{q}'_{m,i}(t) \int_0^{s_0} \int_0^{2\pi} c u_{m,i}(s) u_{n,j}(s) \sin m\phi \cos n\phi r(s) d\phi ds$$

$$= 0 \text{ for all values of } m, i \quad (3.14)$$

and that the corresponding terms in equations (3.11 and 3.12) satisfy similar conditions to (3.13) and (3.14).

Conditions (3.13) and (3.14) imply that the total damping c (mechanical and aerodynamic) is proportional to the mass (ρh) everywhere throughout the shell. In general, the orthogonality and the uncoupling conditions can be invoked on the assumption* that:

- a - The damping is proportional to the mass, the stiffness or a linear combination of both. In practice, this is not exactly the case but nearly so, since the damping elements tend to be distributed in a manner similar to the mass and stiffness.
- b - The mass, stiffness and boundary conditions are not frequency dependent.

*If this assumption is not applicable, the uncoupling of the equations of motion can still be achieved through a new system of coordinates (13).

Summation of equations (3.10 to 3.12), while neglecting the cross coupling terms due to damping, yields:

$$\ddot{q}_{m,i}(t) + \xi_{m,i} \dot{q}_{m,i}(t) + \omega_{m,i}^2 q_{m,i}(t) = \frac{1}{M_{m,i}} \left\{ \int_0^s \int_0^{2\pi} (p_1 u_{m,i}(s) \cos m\phi + p_2 v_{m,i}(s) \sin m\phi + p_3 w_{m,i}(s) \cos m\phi) r(s) d\phi ds \right\} \quad (3.15)$$

in which $M_{m,i}$ = the generalized mass of the i th mode of the m th harmonic

$$= \pi \int_0^s \rho h \{ u_{m,i}^2(s) + v_{m,i}^2(s) + w_{m,i}^2(s) \} r(s) ds \quad (3.16)$$

and $\xi_{m,i}$ = damping parameter for mode (m, i) .

$$= \frac{\pi}{M_{m,i}} \int_0^s c \{ u_{m,i}^2(s) + v_{m,i}^2(s) + w_{m,i}^2(s) \} r(s) ds \quad (3.17)$$

Equation (3.15) describes the symmetric component of motion of mode (m, i) . The equivalent equation for the anti-symmetric component could be obtained by multiplying equation (3.4) by $u_{n,j}(s) \sin n\phi$, equation (3.5) by $-v_{n,j}(s) \cos n\phi$ and equation (3.6) by $w_{n,j}(s) \sin n\phi$ and performing the same operation as above. It is,

$$\ddot{q}'_{m,i}(t) + \xi_{m,i} \dot{q}'_{m,i}(t) + \omega_{m,i}^2 q'_{m,i}(t) = \frac{1}{M_{m,i}} \left\{ \int_0^s \int_0^{2\pi} (p_1 u_{m,i}(s) \sin m\phi - p_2 v_{m,i}(s) \cos m\phi + p_3 w_{m,i}(s) \sin m\phi) r(s) d\phi ds \right\} \quad (3.18)$$

Now, introducing the notations $p_{m,i}(t)$ and $p'_{m,i}(t)$ for the symmetric and anti-symmetric components of the generalized force for the i th mode of the m th harmonic, where:

$$p_{m,i}(t) = \int_0^s \int_0^{2\pi} \{p_1 u_{m,i}(s) \cos m\phi + p_2 v_{m,i}(s) \sin m\phi + p_3 w_{m,i}(s) \cos m\phi\} r(s) d\phi ds \quad (3.19)$$

$$p'_{m,i}(t) = \int_0^s \int_0^{2\pi} \{p_1 u_{m,i}(s) \sin m\phi - p_2 v_{m,i}(s) \cos m\phi + p_3 w_{m,i}(s) \sin m\phi\} r(s) d\phi ds \quad (3.20)$$

Then, equations (3.15 and 3.18) reduces to:

$$\ddot{q}_{m,i}(t) + \xi_{m,i} \dot{q}_{m,i}(t) + \omega_{m,i}^2 q_{m,i}(t) = p_{m,i}(t) / M_{m,i} \quad (3.21)$$

$$\ddot{q}'_{m,i}(t) + \xi_{m,i} \dot{q}'_{m,i}(t) + \omega_{m,i}^2 q'_{m,i}(t) = p'_{m,i}(t) / M_{m,i} \quad (3.22)$$

So far, the problem has been reduced to the solution of two sets of uncoupled equations of motion; each of which is similar to the equation of motion of a single degree of freedom system. Their solution is readily available in the literature. It could be shown that (9):

$$q_{m,i}(t) = \frac{1}{M_{m,i0}} \int_0^\infty W_{m,i}(\tau) p_{m,i}(t-\tau) d\tau \quad (3.23)$$

$$q'_{m,i}(t) = \frac{1}{M_{m,i_0}} \int_0^{\infty} W_{m,i}(\tau) p'_{m,i}(t-\tau) d\tau \quad (3.24)$$

where,

$$W_{m,i}(\tau) = \frac{1}{\bar{\omega}_{m,i}} e^{-\frac{1}{2}\xi_{m,i}\tau} \sin \bar{\omega}_{m,i}\tau \quad (3.25)$$

$$\bar{\omega}_{m,i}^2 = \omega_{m,i}^2 - \left(\frac{\xi_{m,i}}{2}\right)^2 \quad (3.26)$$

The critical damping ratio for mode (m,i) is:

$$\eta_{cr} = \frac{\xi_{m,i}}{2\omega_{m,i}} \quad (3.27)$$

hence,

$$\bar{\omega}_{m,i}^2 = \omega_{m,i}^2 (1 - \eta_{cr}^2) \quad (3.28)$$

η_{cr} is generally of the order of 1%, therefore,

$$\bar{\omega}_{m,i} \approx \omega_{m,i} \quad (3.29)$$

3.5 Statistical Properties of Generalized Forces

For our purpose, the relevant statistical properties of the two components of the generalized forces are:

1. Variance and Co-variance functions; $\tilde{C}_{p_{m,i} p_{n,j}'}$
 $\tilde{C}_{p_{m,i}' p_{n,j}'}$ and $\tilde{C}_{p_{m,i} p_{n,j}'}$.

2. Correlation and Cross-correlation functions;

$$R_{p_{m,i}p_{n,j}}(\tau), R_{p'_{m,i}p'_{n,j}}(\tau), R_{p_{m,i}p'_{n,j}}(\tau) \text{ and}$$

$$R_{p'_{m,i}p_{n,j}}(\tau).$$

3. Spectral and Cross-spectral density functions;

$$S_{p_{m,i}p_{n,j}}(f), S_{p'_{m,i}p'_{n,j}}(f), S_{p_{m,i}p'_{n,j}}(f) \text{ and}$$

$$S_{p'_{m,i}p_{n,j}}(f).$$

Expressions for the instantaneous values of the generalized forces, $p_{m,i}(t)$ and $p'_{m,i}(t)$, were given in the previous section in terms of the three-components of the wind pressure, p_1 , p_2 and p_3 . The tangential components of pressure p_1 and p_2 are much smaller compared to the normal component p_3 . Therefore p_1 and p_2 will be dropped in the following analysis. If necessary, they could be treated in the same manner as p_3 .

Since, the static component of the load could be treated separately, then for simplicity it will be assumed that p_3 has a zero mean and will be denoted, in subsequent analysis, by $p(s, \phi, t)$. Therefore, expressions (3.19 and 3.20) reduce to:

$$p_{m,i}(t) = \int_0^s \int_0^{2\pi} p(s, \phi, t) w_{m,i}(s) \cos m\phi r(s) d\phi ds \quad (3.30)$$

$$p'_{m,i}(t) = \int_0^s \int_0^{2\pi} p(s, \phi, t) w_{m,i}(s) \sin m\phi r(s) d\phi ds \quad (3.31)$$

The covariance functions are obtained from equations (3.30 and 3.31) as follows:

$$\begin{aligned} \tilde{C}_{p_{m,i} p_{n,j}} &= \overline{p_{m,i}(t) p_{n,j}(t)} \\ &= \int_0^s \int_0^{2\pi} \int_0^s \int_0^{2\pi} p(s, \phi, t) p(s', \phi', t) w_{m,i}(s) w_{n,j}(s) \cos m\phi \cos n\phi' \\ &\quad r(s) r(s') d\phi d\phi' ds ds' \end{aligned} \quad (3.32)$$

in which, $\overline{p(s, \phi, t) p(s', \phi', t)}$ is the covariance of pressures at points (s, ϕ) and (s', ϕ') .

$\tilde{C}_{p_{m,i} p_{n,j}}$ could be represented in a non-dimensional form by a correlation coefficient $C_{p_{m,i} p_{n,j}}$ where

$$C_{p_{m,i} p_{n,j}} = \tilde{C}_{p_{m,i} p_{n,j}} / s_0^4 \sigma_p^2(s_1, \phi_1) \quad (3.33)$$

and $\sigma_p(s_1, \phi_1)$ = Standard deviation of wind pressure at a reference point (s_1, ϕ_1)

Equation (3.32) could now be put in a non-dimensional form as follows:

$$C_{p_{m,i} p_{n,j}} = \int_0^1 \int_0^1 \int_0^{2\pi} \int_0^{2\pi} C(l, \phi, l', \phi') f_p(l, \phi) f_p(l', \phi') \\ w_{m,i}(l) w_{n,j}(l') \cos m\phi \cos n\phi' \gamma_2(l) \gamma_2(l') d\phi d\phi' dl dl' \quad (3.34)$$

in which, $l = s/s_0$; $\gamma_2 = r(s)/s_0$; and $C(l, \phi, l', \phi') =$
correlation coefficient of wind pressure.

$$= \frac{\overline{p(l, \phi, t) p(l', \phi', t)}}{\sigma_p(l, \phi) \sigma_p(l', \phi')} \quad (3.35)$$

$\sigma_p(l, \phi) =$ standard deviation of wind pressure.
and $f_p(l, \phi) = \frac{\sigma_p(l, \phi)}{\sigma_p(l_1, \phi_1)} =$ shape function (3.36)

Similarly,

$$C_{p'_{m,i} p'_{n,j}} = \int_0^1 \int_0^1 \int_0^{2\pi} \int_0^{2\pi} C(l, \phi, l', \phi') f_p(l, \phi) f_p(l', \phi') \\ w_{m,i}(l) w_{n,j}(l') \sin m\phi \sin n\phi' \gamma_2(l) \gamma_2(l') d\phi d\phi' dl dl' \quad (3.37)$$

$$C_{p_{m,i} p'_{n,j}} = \int_0^1 \int_0^1 \int_0^{2\pi} \int_0^{2\pi} C(l, \phi, l', \phi') f_p(l, \phi) f_p(l', \phi') \\ w_{m,i}(l) w_{n,j}(l') \cos m\phi \sin n\phi' \gamma_2(l) \gamma_2(l') d\phi d\phi' dl dl' \quad (3.38)$$

Equations (3.34, 3.37 or 3.38) describe the expressions
for the variance and covariance of the generalized forces.

Their evaluation requires a prior knowledge of the distribution of the standard deviation and the correlation coefficient of the wind pressures acting on the surface of the shell.

The components of the auto-correlation and cross-correlation functions of the generalized forces could be written in terms of the cross-correlation functions of the wind pressures using equations (3.30) and (3.31) as follows:

$$\overline{p_{m,i}(t)p_{n,j}(t+\tau)} = \int_0^{s_0} \int_0^{s_0} \int_0^{2\pi} \int_0^{2\pi} \overline{p(s,\phi,t)p(s',\phi',t+\tau)} \\ w_{m,i}(s)w_{n,j}(s')\cos m\phi\cos n\phi'r(s)r(s')d\phi d\phi'ds ds' \quad (3.39)$$

Non-dimensionalizing, we get,

$$R_{p_{m,i}p_{n,j}}(\tau) = \int_0^1 \int_0^1 \int_0^{2\pi} \int_0^{2\pi} R_p(l,\phi,l',\phi',\tau)f_p(l,\phi)f_p(l',\phi') \\ w_{m,i}(l)w_{n,j}(l')\cos m\phi\cos n\phi'\gamma_2(l)\gamma_2(l')d\phi d\phi'dl dl' \quad (3.40)$$

in which, τ = time-delay; and

$$R_{p_{m,i}p_{n,j}}(t) = \frac{\overline{p_{m,i}(t)p_{n,j}(t+\tau)}}{s_0^2 \sigma_p^2(l_1,\phi_1)} \quad (3.41)$$

$$R_p(l, \phi, l', \phi', \tau) = \frac{p(l, \phi, t)p(l', \phi', t+\tau)}{\sigma_p(l, \phi)\sigma_p(l', \phi')} \quad (3.42)$$

$$R_{p'_m, i p'_n, j}(\tau) = \int_0^1 \int_0^1 \int_0^{2\pi} \int_0^{2\pi} R_p(l, \phi, l', \phi', \tau) f_p(l, \phi) f_p(l', \phi')$$

$$w_{m, i}(l) w_{n, j}(l') \sin m \phi \sin n \phi' \gamma_2(l) \gamma_2(l') d\phi d\phi' dl dl' \quad (3.43)$$

$$R_{p'_m, i p'_n, j}(\tau) = \int_0^1 \int_0^1 \int_0^{2\pi} \int_0^{2\pi} R_p(l, \phi, l', \phi', \tau) f_p(l, \phi) f_p(l', \phi')$$

$$w_{m, i}(l) w_{n, j}(l') \cos m \phi \sin n \phi' \gamma_2(l) \gamma_2(l') d\phi d\phi' dl dl' \quad (3.44)$$

$$R_{p'_m, i p'_n, j}(\tau) = \int_0^1 \int_0^1 \int_0^{2\pi} \int_0^{2\pi} R_p(l', \phi', l, \phi, \tau) f_p(l', \phi')$$

$$f_p(l, \phi) w_{m, i}(l') w_{n, j}(l) \sin m \phi' \cos n \phi \gamma_2(l') \gamma_2(l) d\phi' d\phi dl' dl \quad (3.45)$$

Prior knowledge of the variation of the standard deviation and cross-correlation functions of the wind pressures throughout the shell surface are essential for the evaluations of expressions (3.40, 3.43 to 3.45)

Since the spectral density function is related to the auto-correlation function by,

$$S(f) = 4 \int_0^{\infty} R(\tau) \cos(2\pi f\tau) d\tau \quad (3.46)$$

where f is frequency in cps.

Then, the spectral and cross-spectral density of the generalized forces could be derived from expressions (3.40, 3.43, 3.44, 3.45). They are,

$$\frac{S_{p_{m,i} p_{n,j}}(f)}{s_o^4 \sigma_p^2(l_1, \phi_1)} = \int_0^1 \int_0^1 \int_0^{2\pi} \int_0^{2\pi} \frac{S_p(l, \phi, l', \phi', f)}{\sigma_p(l, \phi) \sigma_p(l', \phi')} f_p(l, \phi) f_p(l', \phi') w_{m,i}(l) w_{n,j}(l') \cos m\phi \cos n\phi' \gamma_2(l) \gamma_2(l') d\phi d\phi' dl dl' \quad (3.47)$$

$$\frac{S_{p_{m,i} p_{n,j}}(f)}{s_o^4 \sigma_p^2(l_1, \phi_1)} = \int_0^1 \int_0^1 \int_0^{2\pi} \int_0^{2\pi} \frac{S_p(l, \phi, l', \phi', f)}{\sigma_p(l, \phi) \sigma_p(l', \phi')} f_p(l, \phi) f_p(l', \phi') w_{m,i}(l) w_{n,j}(l') \sin m\phi \sin n\phi' \gamma_2(l) \gamma_2(l') d\phi d\phi' dl dl' \quad (3.48)$$

$$\frac{S_{p_{m,i} p_{n,j}}(f)}{s_o^4 \sigma_p^2(l_1, \phi_1)} = \int_0^1 \int_0^1 \int_0^{2\pi} \int_0^{2\pi} \frac{S_p(l, \phi, l', \phi', f)}{\sigma_p(l, \phi) \sigma_p(l', \phi')} f_p(l, \phi) f_p(l', \phi') w_{m,i}(l) w_{n,j}(l') \cos m\phi \sin n\phi' \gamma_2(l) \gamma_2(l') d\phi d\phi' dl dl' \quad (3.49)$$

$$\frac{S_{p_m, i p_n, j}^{(f)}}{s_o^4 \sigma_p^2(l_1, \phi_1)} = \int_0^1 \int_0^1 \int_0^{2\pi} \int_0^{2\pi} \frac{S_p(l', \phi', l, \phi, f)}{\sigma_p(l', \phi') \sigma_p(l, \phi)} f_p(l', \phi')$$

$$f_p(l, \phi) w_{m, i}(l') w_{n, j}(l) \sin m \phi' \cos n \phi \gamma_2(l') \gamma_2(l) d\phi' d\phi dl' dl$$

(3.50)

in which $S_p(l, \phi, l', \phi', f)$ is the cross spectral density function of the wind pressure. It is a complex quantity.

That is,

$$S_p(l, \phi, l', \phi', f) = G(l, \phi, l', \phi', f) + i Q(l, \phi, l', \phi', f)$$

(3.51)

where, $i = \sqrt{-1}$.

The co-spectra $G(l, \phi, l', \phi', f)$ and the quadrature spectra $Q(l, \phi, l', \phi', f)$ have the following properties,

$$G(l, \phi, l', \phi', f) = G(l', \phi', l, \phi, f) \quad (3.52)$$

$$Q(l, \phi, l', \phi', f) \equiv -Q(l', \phi', l, \phi, f) \quad (3.53)$$

3.6 Statistical Properties of the Generalized Coordinates

The instantaneous values of the generalized coordinates $q_{m, i}(t)$ and $q'_{m, i}(t)$ are related to the generalized forces by equations (3.23 and 3.24). Noting that,

$$R_{q_{m, i} q_{n, j}}(\tau) = \overline{q_{m, i}(t) q_{n, j}(t+\tau)} \quad (3.54)$$

and

$$S_{q_{m,i}q_{n,j}}(\tau) = 4 \int_0^{\infty} R_{q_{m,i}q_{n,j}}(\tau) \cos(2\pi f\tau) d\tau \quad (3.55)$$

then by substituting from equations (3.23 and 3.24) to equations (3.54 and 3.55) the spectra and cross-spectra of the generalized coordinates could be obtained. It could be shown that (9),

$$S_{q_{m,i}q_{n,j}} = \frac{1}{16\pi^4 f_{m,i}^2 f_{n,j}^2 M_{m,i} M_{n,j}} \chi_{m,i}^*(if) \chi_{n,j}(if) S_{p_{m,i}p_{n,j}}(f) \quad (3.56)$$

in which the mechanical admittance function is defined by,

$$\chi_{m,i}(if) = \left\{ \left(1 - \frac{f^2}{f_{m,i}^2} \right) + 2i \eta_{cr} \left(\frac{f}{f_{m,i}} \right) \right\}^{-1} \quad (3.57)$$

Similar expressions for $S_{q'_{m,i}q'_{n,j}}$, $S_{q_{m,i}q'_{n,j}}$ and

$S_{q'_{m,i}q_{n,j}}$ could be obtained by replacing $S_{p_{m,i}p_{n,j}}(f)$ in

equation (3.56) by $S_{p'_{m,i}p'_{n,j}}(f)$, $S_{p_{m,i}p'_{n,j}}(f)$ and $S_{p'_{m,i}p_{n,j}}(f)$

respectively.

The variance and co-variance function of the generalized coordinates could be directly obtained from the spectra and cross-spectra functions. For example,

$$\overline{q_{m,i}(t)q_{n,j}(t)} = \int_0^{\infty} S_{q_{m,i}q_{n,j}}(f) df \quad (3.58)$$

3.7 Statistical Description of Total Response

The statistical properties of the total shell response could now be obtained in terms of those of the generalized coordinates. For our purpose, the following statistical properties are particularly important:

1. Standard deviation
2. Power spectral density function
3. Peak response

Expressions for these will be given in the following sections. For brevity, the normal displacement w , only, will be considered. Other response parameters, whether displacements, stresses, ..etc., could be treated in exactly the same manner.

3.7.1 Standard Deviation

Based on equation (3.2), it could be shown that the standard deviation of the normal displacement $\sigma_w(s, \phi)$ at position (s, ϕ) is given by,

$$\sigma_w^2(s, \phi) = \sum_{m=0}^{\infty} \sum_{i=1}^{\infty} \sum_{n=0}^{\infty} \sum_{j=1}^{\infty} \{ \overline{q_{m,i}(t) q_{n,j}(t)} w_{m,i}(s) w_{n,j}(s) \cos m\phi \cos n\phi + \overline{q'_{m,i}(t) q'_{n,j}(t)} w_{m,i}(s) w_{n,j}(s) \sin m\phi \sin n\phi + 2 \overline{q_{m,i}(t) q'_{n,j}(t)} w_{m,i}(s) w_{n,j}(s) \cos m\phi \sin n\phi \} \quad (3.59)$$

in which, the first term in the RHS represents the symmetric component of the response, the second represents the anti-symmetric component, while the last term accounts for the coupling between the symmetric and anti-symmetric components.

3.7.2 Power Spectral Density Function

Following equation (3.2), the power spectral density function of the normal displacement $S_w(s, \phi, f)$ is found to be,

$$\begin{aligned}
 S_w(s, \phi, f) = & \sum_{m=0}^{\infty} \sum_{i=1}^{\infty} \sum_{n=0}^{\infty} \sum_{j=1}^{\infty} \{ S_{q_{m,i} q_{n,j}}(f) w_{m,i}(s) w_{n,j}(s) \\
 & \cos m\phi \cos n\phi + S_{q'_{m,i} q'_{n,j}}(f) w_{m,i}(s) w_{n,j}(s) \sin m\phi \sin n\phi + \\
 & S_{q_{m,i} q'_{n,j}}(f) w_{m,i}(s) w_{n,j}(s) \cos m\phi \sin n\phi + \\
 & S_{q'_{m,i} q_{n,j}}(f) w_{m,i}(s) w_{n,j}(s) \sin m\phi \cos n\phi \} \quad (3.60)
 \end{aligned}$$

Usually, most of the response resides in a limited number of modes and for practical purposes, the summation could be terminated at reasonably low values of m , n , i and j .

3.7.3 Peak Response

The prediction of the extreme values of the response of structures to random excitation is treated in detail in many references. Here, the procedure suggested by Davenport (12) will be briefly described.

Considering, the normal displacement $w(s, \phi, t)$ then for any mode of vibration (m, i) , the maximum value of $w_{m,i}$ expected during a period of time T , $\hat{w}_{m,i}$, can be represented by,

$$\hat{w}_{m,i}(s, \phi) = \bar{w}_{m,i}(s, \phi) + g_{m,i} \sigma_{w_{m,i}}(s, \phi) \quad (3.61)$$

in which, $\bar{w}_{m,i}(s, \phi)$ and $\sigma_{w_{m,i}}(s, \phi)$ are the mean and standard deviation of $w_{m,i}$ during the same period of time T and $g_{m,i}$ is a peak factor.

Davenport has shown that the mean value of the peak factor can be expressed by,

$$g_{m,i} = \sqrt{2 \log_e \bar{v}_{m,i} T} + \frac{0.577}{\sqrt{2 \log_e \bar{v}_{m,i} T}} \quad (3.62)$$

in which \bar{v} is the rate of zero crossing with positive slope of the fluctuating component of the response and is given by,

$$\bar{v}_{m,i} = \left\{ \frac{\int_0^{\infty} f^2 S_{w_{m,i}}(f) df}{\int_0^{\infty} S_{w_{m,i}}(f) df} \right\}^{1/2} \quad (3.63)$$

The total peak response expected during a period of time T , could then be obtained from the summation of the various modal contributions.

CHAPTER 4

VIBRATION CHARACTERISTICS

4.1 Introduction

The study of the dynamic action of wind on hyperbolic cooling towers using a modal analysis approach requires a comprehensive knowledge of their vibration characteristics; namely, the natural frequencies, mode shapes, and the generalized mass, stiffness, and also damping (both mechanical and aerodynamic) for various modes.

Several numerical procedures to determine the natural frequencies and mode shapes of hyperbolic shells of revolution have been developed in recent years (1,2,3,4). Experimental results are also reported in Refs. (4,5,6).

The strong dependence of the shell vibration characteristics on various parameters is investigated in Refs. (2,6). Some selected results are shown in Figs. 4.1 and 4.2. For fixed base conditions, the frequency increases rapidly with increasing curvature in the meridional direction. If constraints on axial displacements are removed, the natural frequency is sharply reduced. In general, these changes in frequency were found to be a

$E = 3 \times 10^6 \text{ psi}$
 $\mu = 0.150$
 $\gamma = 150.111 \text{ lb/ft.}^3 \quad (\rho = 0.225 \times 10^{-3} \text{ lb. sec.}^2/\text{in.}^4)$

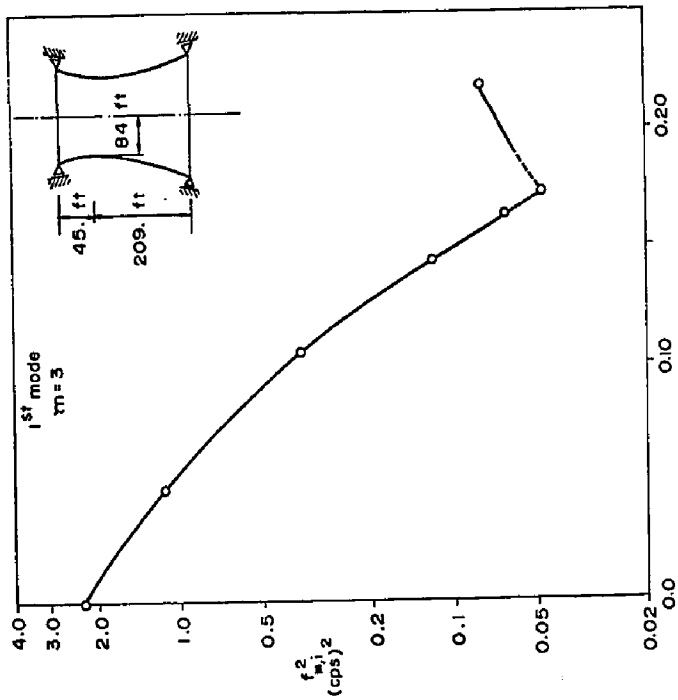


FIG. 4.1

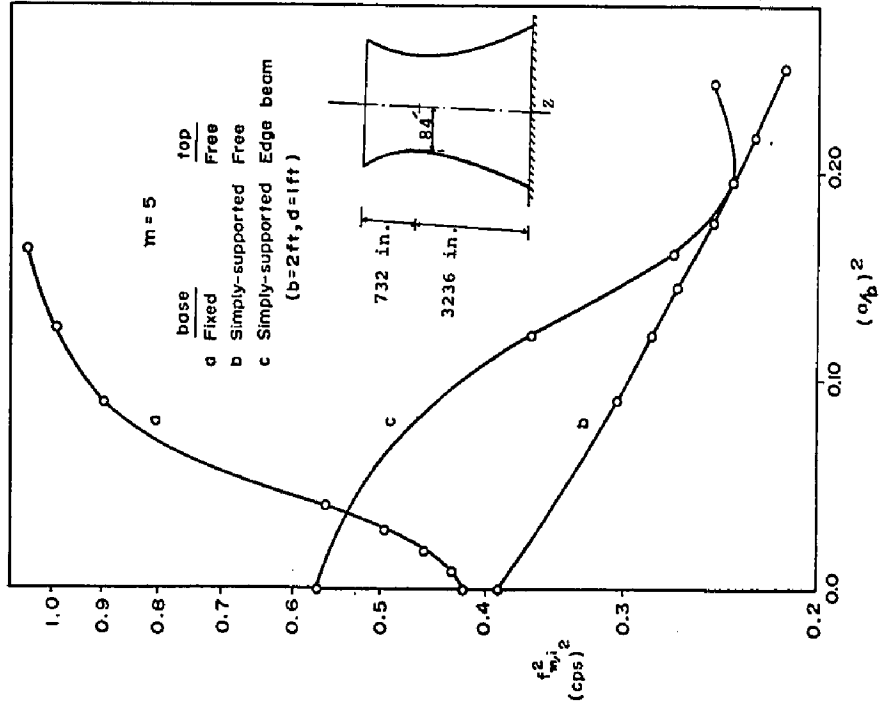


FIG. 4.2

direct result of similar changes in the membrane energy. For shells simply supported at both edges, there exists a meridional curvature at which the membrane energy practically vanishes and the natural frequency reaches a minimum.

In this chapter some features of the vibration characteristics of hyperbolic cooling towers are described. Special attention is given to column-supported towers with or without a top ring beam. The dependence of the shell vibration characteristics on various geometric parameters is examined in detail for ranges of practical interest. Universal curves showing the variation of the shell frequencies with the fundamental geometric ratios are given for fixed-free shells.

4.2 Natural Frequencies and Mode Shapes of a Typical Tower

The basic characteristics of the natural frequencies and mode shapes of cooling towers are investigated by considering a typical tower. The geometry of the sample tower is given in Chapter 2, with some material properties. In the analysis, four different combinations of boundary conditions are considered.

They are:

	<u>TOP</u>	<u>BASE</u>
1.	Free	Fixed
2.	Ring-stiffened	Fixed
3.	Free	Column-supported
4.	Ring-stiffened	Column-supported

The dimensions of the top ring beam and column supports are illustrated in Fig. 2.15.

The natural frequencies and mode shapes of the tower were computed using the modified finite difference method described in Section 2.3. Results are given for the fundamental modes of harmonics $m = 1$ to 9 .

4.2.1 Natural Frequencies

Fig. 4.3, shows the variation of natural frequencies with harmonic wave number m . For all combinations of boundary conditions, the natural frequency decreases with increasing m till a minimum is reached after which it starts to rise again. This behaviour was examined in Refs. (2,6,7). It was found that it results from the interchange of the relative contribution of the membrane and bending energies to the total strain energy for different harmonics. The membrane energy decreases rapidly with increasing m , while the bending energy increases gradually with increasing m . For fixed base, the membrane energy is predominant at low harmonics, $m \leq 3$

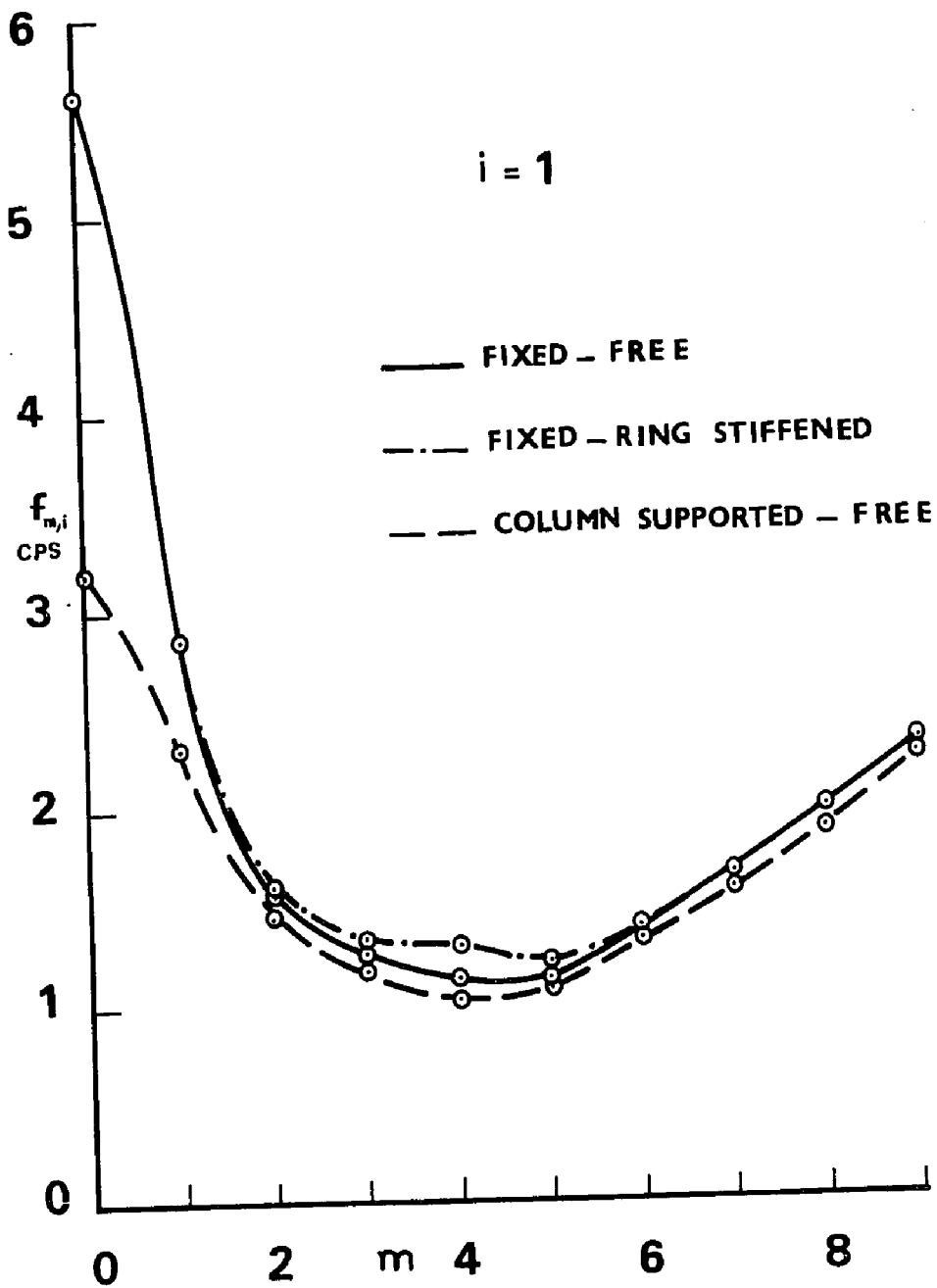


FIG. 4.3 NATURAL FREQUENCIES FOR HARMONICS $m = 0$ TO 9

where the bending contribution is negligible. The bending energy, however, becomes predominant at high values of m .

Fig. 4.3 further indicates that the flexibility of base supports results in a considerable reduction in the natural frequencies at low values of m . This was found to be the direct result of a significant drop in the membrane energy at these harmonics, thus supporting earlier findings, regarding the sensitivity of the shell membrane action to base flexibility, reported in Refs. (2,6). It is interesting to note that while the lack of the meridional constraints causes the release of the membrane energy of the shell, the bending energy, however, remains almost invariant from fixed base conditions for all values of m . Therefore, it would be expected that the natural frequencies at high harmonics will almost be insensitive to changes in the stiffness of the supporting structure. The opposite should be expected at low harmonics. This fact is of importance since the response of cooling towers to the horizontal component of earthquake loading is confined to the swaying motion, $m=1$ (8) and their response to the vertical component is confined to $m = 0$. Their response due to wind, as will be shown in the following chapters, resides in modes associated with low harmonic wave number. Therefore, an underestimation of the columns stiffness could be detrimental to their resistance to both earthquake and wind action.

The influence of a stiffening ring beam at the top edge on the natural frequencies is shown also in Fig. 4.1. The maximum increase in the natural frequencies of about 17% occurs for the fundamental mode of harmonic $m = 4$. For all other harmonics, especially those associated with a low wave number, the increase in frequency due to the presence of the ring beam is not significant. The ring beam appears, therefore, to be of no apparent advantage in improving the resistance of cooling towers to common design loads; namely wind and earthquake. Furthermore, the ring beam causes a reversal of stresses from compression to tension in the uppermost portion of the shell, due to static wind (Fig. 2.17). This might lead to meridional cracks extending downwards, in strong wind action, thus offsetting any advantage the beam might have in improving the overall shell resistance.

4.2.2 Mode Shapes

Fig. 4.4 shows the mode shapes of the normal displacement w for harmonics $m = 1$ to 3. Comparisons are made between four different combinations of boundary conditions.

For a fixed-free tower, the mode shape of the swaying motion ($m=1$) in the meridional direction is similar to that of a cantilever cylinder. For this mode, the circumferential displacement w is of the same

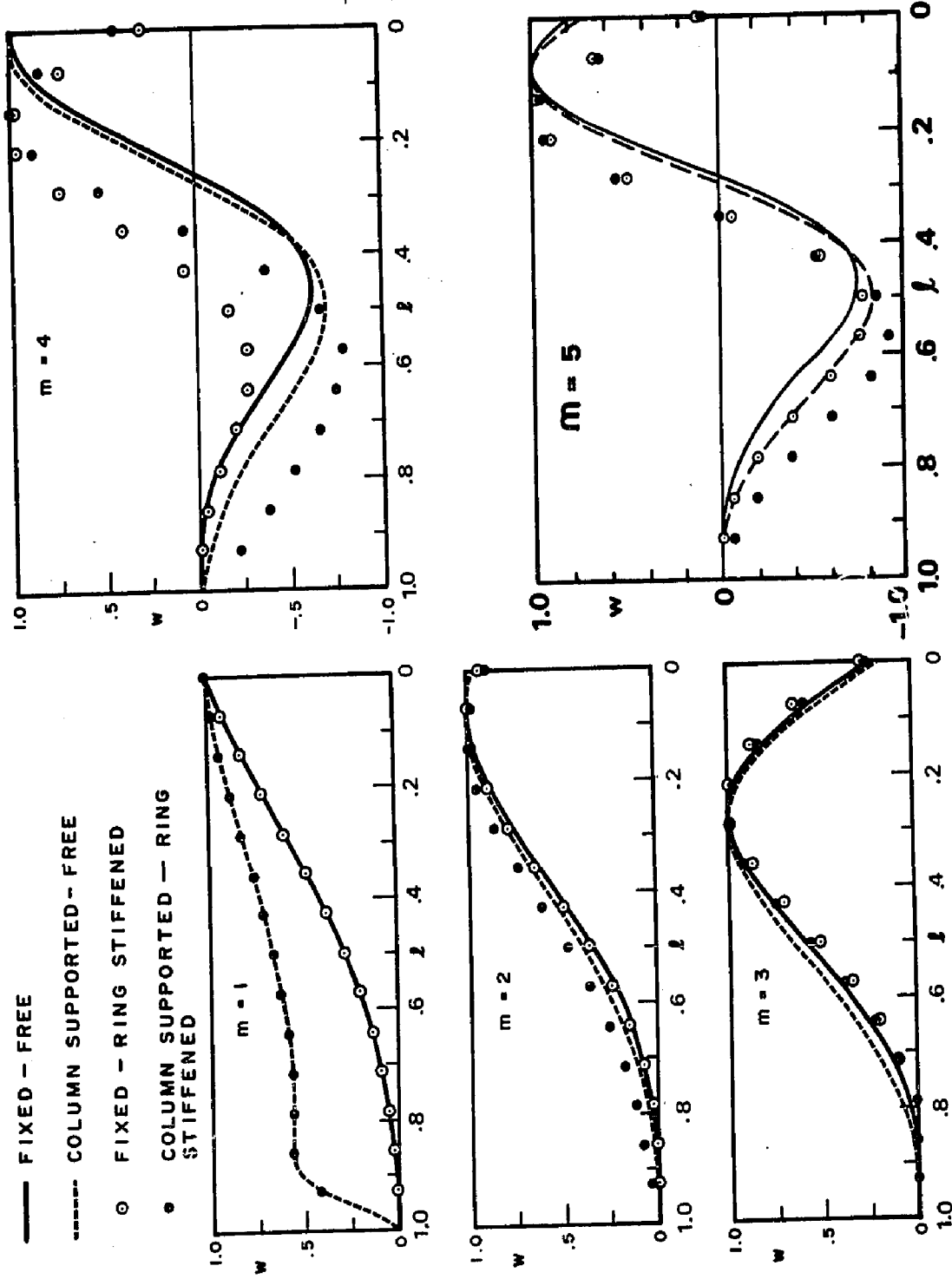


FIG. 4.4A

FUNDAMENTAL MODE SHAPES FOR NORMAL DISPLACEMENT w

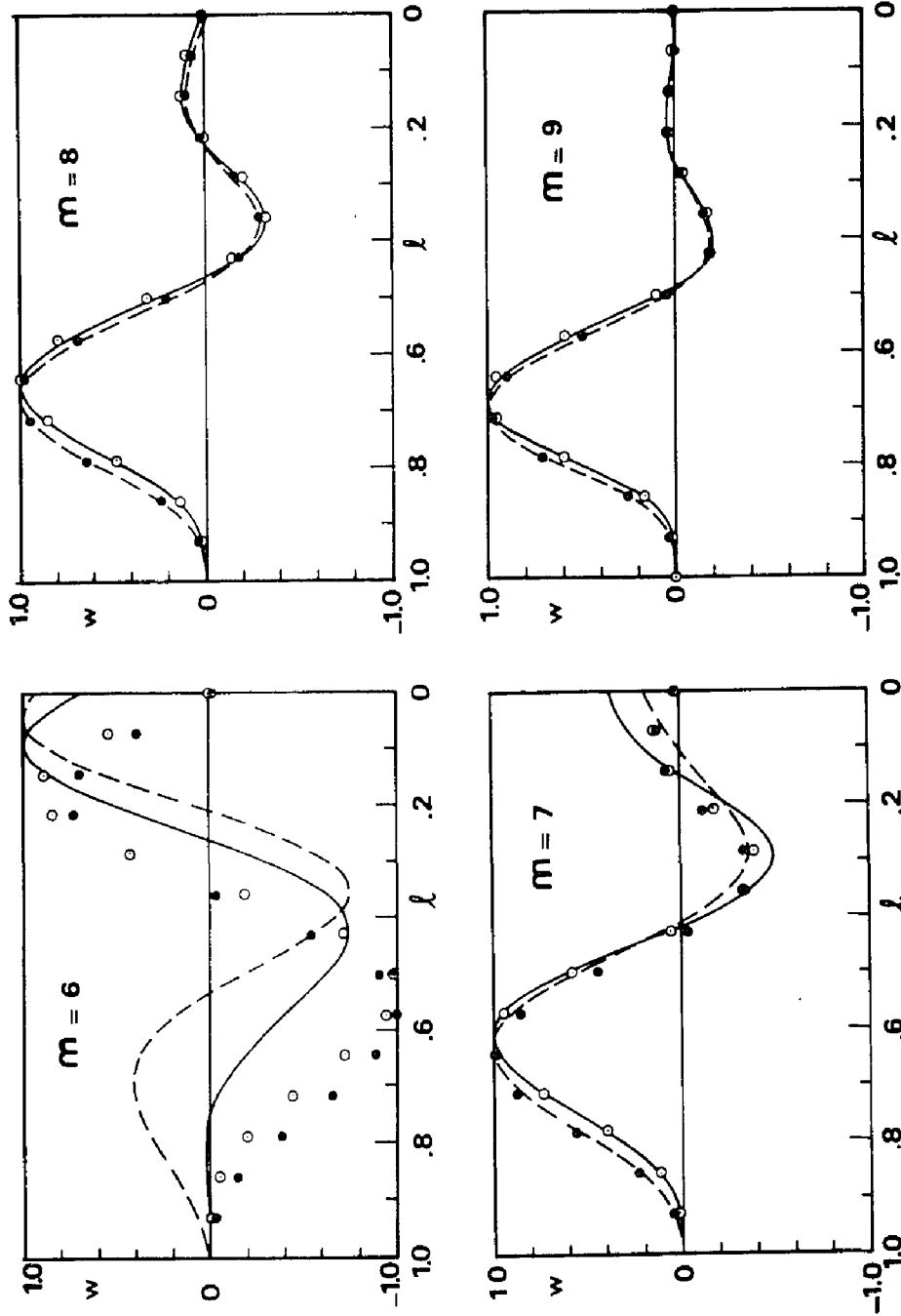


FIG. 4.4 B

magnitude and opposite sign as the normal displacement except for a small deviation at the base boundary ($v \approx -w$). The ring beam has little or no influence on the swaying motion because it may add mass but not stiffness.

The ring beam seems to be effective in restraining the top movement of the tower for harmonics $m = 4, 5$ and 6 only. For lower harmonics, the effect is very small and is hardly significant. For higher harmonics ($m > 6$), the top edge, with or without a stiffening beam, does not undergo any significant movement and the beam becomes ineffective in this respect.

On the other hand, the sway motion is very sensitive to variations in the flexibility of the supporting structure. Comparison with other harmonics indicate that column supports are much more vulnerable to motion in this mode. That is, their resistance to deformation in this mode is by far the lowest. If the design load component in this mode is significant, such as in earthquake (8), ways of stiffening the supporting structure might be necessary. An X shaped column system could prove to be stronger than the V shaped system.

For the swaying mode, the horizontal movement of the tip of the column supports are carried up to the top edge almost constantly. This might not be apparent from Fig. 4.4 due to the normalization adopted for the mode shape.

Mode shapes for harmonic wave numbers greater than $m = 1$, become progressively more complex with increasing m . For all harmonics $m \geq 1$, it was found that the circumferential displacement v could be related to the normal displacement w by:

$$v = -\frac{w}{m}$$

Thus indicating that for high harmonics, the circumferential motion becomes gradually small. For all harmonics $m > 1$, the axial displacement u is very small compared to w and v . Therefore, for high harmonics the motion becomes predominant in the transverse direction.

4.3 Dependence of Vibration Characteristics on Various Parameters

Introducing a non-dimensional frequency parameter Ω defined by,

$$\Omega = \frac{4\pi^2 f^2 \rho_s H^2}{E} \quad (4.2)$$

in which ρ_s = shell mass density, H = shell height and E = Young's modulus of elasticity, Ω and the mode shapes depend on:

1. Boundary Conditions.
2. Poisson's ratio.

3. External loads and gravitational effects.
4. Various geometric ratios.

The strong dependence of the vibration characteristics on the boundary conditions is examined in detail in Ref. (2) and referred to in Section 4.1.

The influence of Poisson's ratio μ on the modal displacements and strains is likely to be very small (2). Modal stresses, for a given μ , could be adequately obtained from modal strains for $\mu=0$ using the actual value of μ . For example, T_1 could be obtained as follows:

$$T_1(\mu \geq 0) = \frac{Eh}{1-\mu^2} \{ \epsilon_{1\mu=0} + \mu \epsilon_{2\mu=0} \} \quad (4.3)$$

The variation of Ω with μ could be approximately accounted for as follows:

$$\Omega(\mu \geq 0) = \frac{\Omega(\mu=0)}{(1-\mu^2)} \quad (4.4)$$

According to Ref. (4), the influence of the external lateral loads on the vibration characteristics is very small in the practical range of design wind speeds. The effects of gravitational forces are also expected to be small for towers up to 500 to 600 ft. high. A recent study (9) of their effects, have shown that beyond that range the gravitational effects start to be significant and could result in a reduction in the lowest frequency

of the shell in the order of 20% for towers 1000 ft. high. The reduction in frequency increases with circumferential wave number.

The geometry of a hyperbolic cooling tower with constant wall thickness could be completely described by a length scale, e.g. height H , and the following geometric ratios:

- a. Curvature parameter; $k_0 = a/b$
- b. Throat radius to height ratio; $k_1 = a/H$
- c. Height above throat to total height ratio;
 $k_2 = -z_t / H$
- d. Shell thickness to height ratio, $k_3 = h/H$

All other geometrical quantities could be obtained from those ratios as outlined in Appendix I.

Consideration is given to the variation of k_0 to k_3 for the towers now in practice. Histograms describing the variation of these ratios for cooling towers built in U.S.A. are shown in Figs. (1.6 to 1.9). Except for k_3 , there is a wide spread in the variation of the other three ratios. In accordance with these histograms, the values of k_0 to k_3 selected for the parametric study are:

$$k_0 = 0, 0.1, 0.2, 0.3, 0.4, 0.5.$$

$$k_1 = \frac{1}{6}, \frac{1}{5}, \frac{1}{4}$$

$$k_2 = 0, \frac{1}{6}, \frac{1}{4}$$

$$k_3 = \frac{1}{600}$$

Figs. 4.5 to 4.13 show the variation of Ω^2 with the curvature parameter k_0 for different values of k_1 and k_2 . The results shown for harmonics $m=1$ to 3 are typical for all other harmonics. Selected results showing the basic features of the variation of mode shapes for the normal displacement w , with k_0 , k_1 and k_2 are given in Figs. 4.14 to 4.16.

The natural frequencies are found to be particularly sensitive to changes in curvature parameter k_0 . For all harmonics, the frequency increases rapidly with increasing curvature in the meridional direction. This change in frequency results from the progressive rise of the membrane energy with increasing curvature. The bending energy and the kinetic energy on the other hand remain almost unchanged with variations in k_0 (2).

The natural frequency for harmonic $m = 2$ seems to be insensitive to changes in the ratio of height above throat to total shell height, k_2 . This is not the case, however, for harmonics $m = 1$ and 3. For $m=3$, the frequency increases as k_2 increases for k_0 less than about 0.4. The opposite happens for $m=1$ at all values of k_0 . This may be significant in earthquake analysis.

The frequency varies significantly with throat radius to shell height ratio k_1 . The trend of variation, however, is rather complex. The frequency of almost cylindrical shells increases with increasing k_1 . For

high values of k_0 , however, no general trend is observed as the type of change in frequency due to k_1 becomes dependent on m , k_0 and k_2 .

For the swaying motion, the mode shape for the normal displacement w is not too sensitive to changes in k_0 , k_1 and k_2 . For other harmonics, however, the mode shapes become strongly dependent on these ratios. Again, the changes in curvature parameter k_0 are particularly important.

Finally, approximate expressions for Ω^2 in terms of k_0 , k_1 and k_2 for the fundamental modes of harmonics $m=1$ to 3 were obtained. These are only applicable in the ranges of k_0 to k_3 tested in the analysis and are given by:

$$\overset{m=1}{\Omega^2} = (k_1 - 0.04) + \frac{1}{4k_1} \left(2.8 - \frac{2.25 k_2}{\sqrt{k_1}} \right) k_0^2$$

$$\overset{m=2}{\Omega^2} = (0.4 k_1^2 + 0.03 k_1) + \frac{0.38 k_0^2}{\sqrt{k_1}}$$

$$\overset{m=3}{\Omega^2} = 0.01 + \frac{1}{2\sqrt{k_1}} \left\{ (0.44 - 0.58\sqrt{k_2}) k_0^2 + 2k_0^3 \sqrt{k_2} \right\}$$

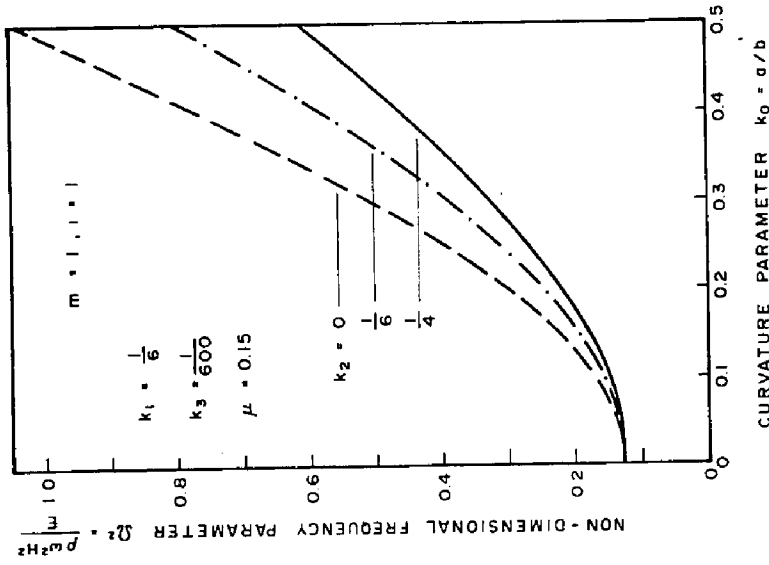


FIG. 4.7 INFLUENCE OF GEOMETRIC RATIOS ON FUNDAMENTAL FREQUENCY OF $m = 1$; $k_1 = 1/6$

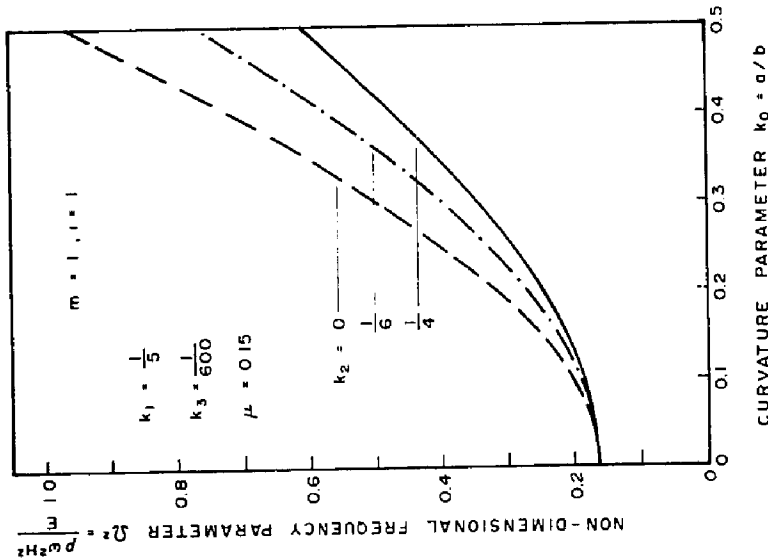


FIG. 4.6 INFLUENCE OF GEOMETRIC RATIOS ON FUNDAMENTAL FREQUENCY OF $m = 1$; $k_1 = 1/5$

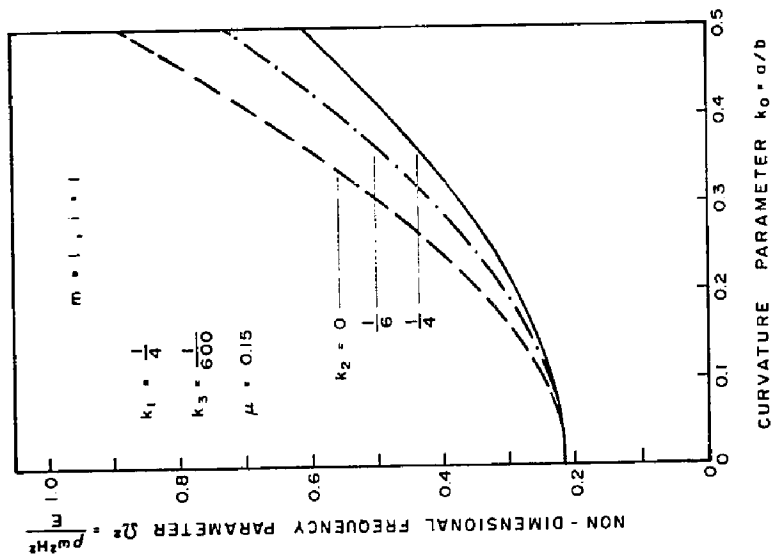


FIG. 4.5 INFLUENCE OF GEOMETRIC RATIOS ON FUNDAMENTAL FREQUENCY OF $m = 1$; $k_1 = 1/4$

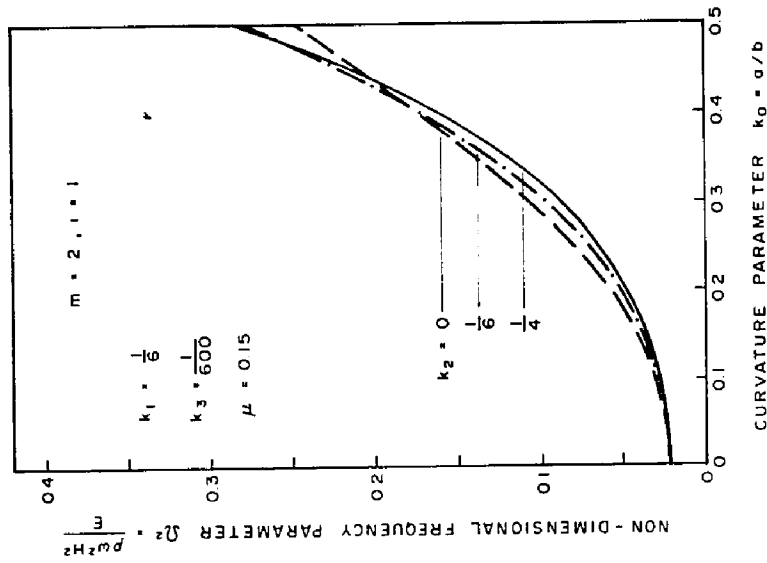


FIG. 4.10 INFLUENCE OF GEOMETRIC RATIOS ON FUNDAMENTAL FREQUENCY OF $m = 2; k_1 = 1/6$

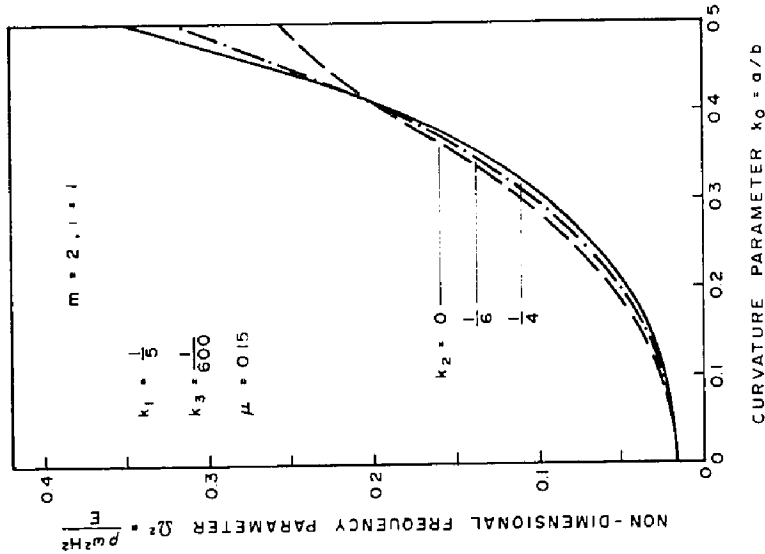


FIG. 4.9 INFLUENCE OF GEOMETRIC RATIOS ON FUNDAMENTAL FREQUENCY OF $m = 2; k_1 = 1/5$

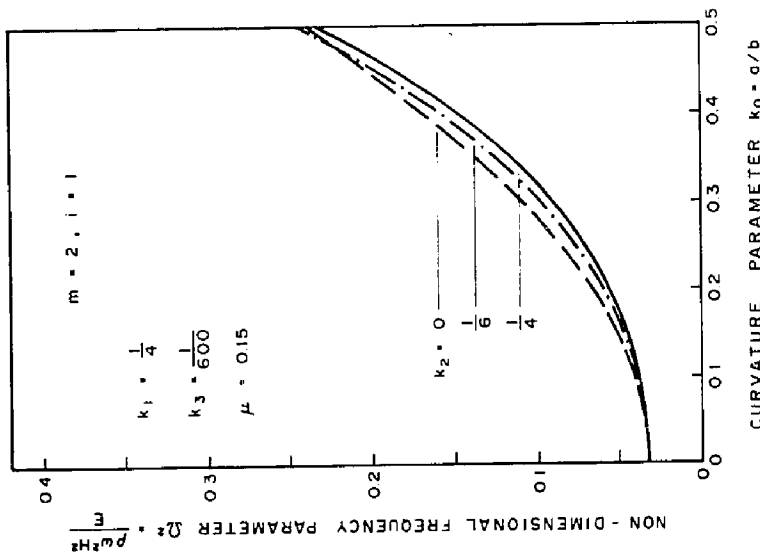


FIG. 4.8 INFLUENCE OF GEOMETRIC RATIOS ON FUNDAMENTAL FREQUENCY OF $m = 2; k_1 = 1/4$

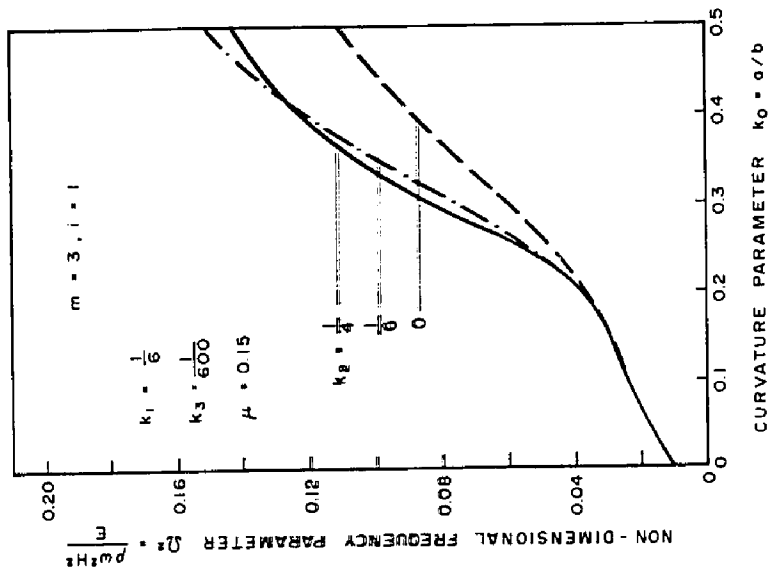


FIG. 4.13 INFLUENCE OF GEOMETRIC RATIOS ON FUNDAMENTAL FREQUENCY OF $m = 3 ; k_1 = 1/6$

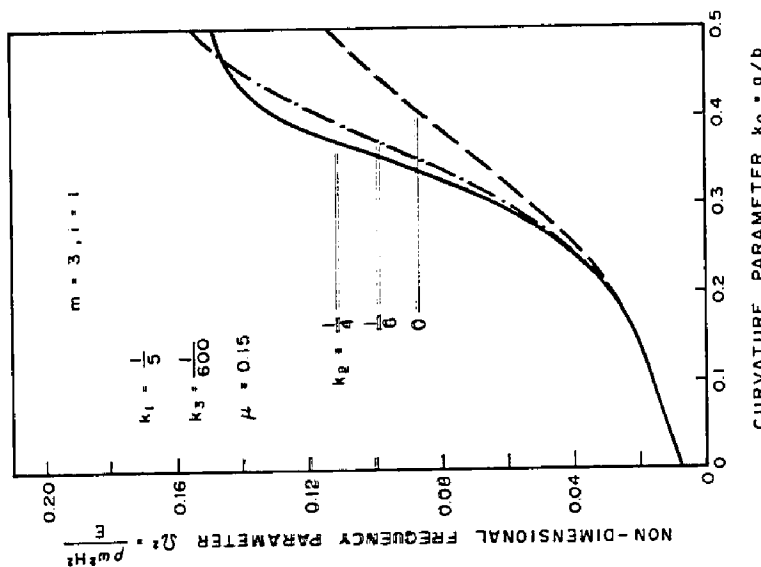


FIG. 4.12 INFLUENCE OF GEOMETRIC RATIOS ON FUNDAMENTAL FREQUENCY OF $m = 3 ; k_1 = 1/5$

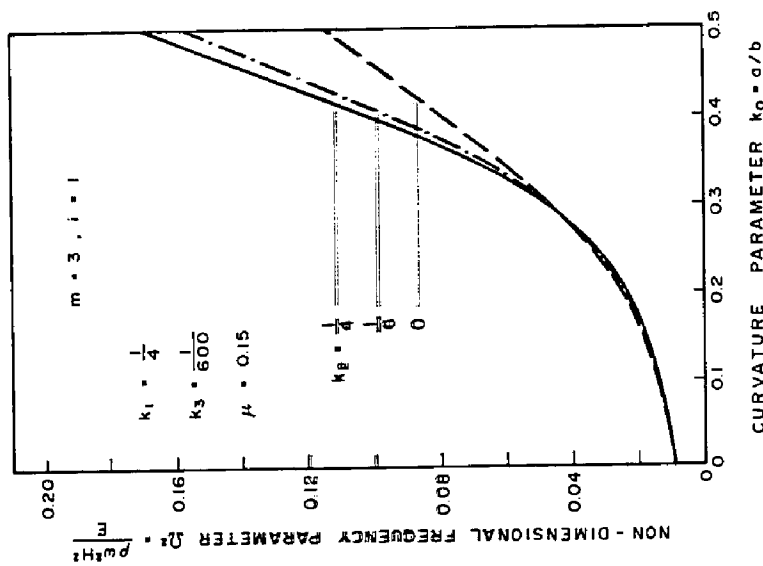


FIG. 4.11 INFLUENCE OF GEOMETRIC RATIOS ON FUNDAMENTAL FREQUENCY OF $m = 3 ; k_1 = 1/4$

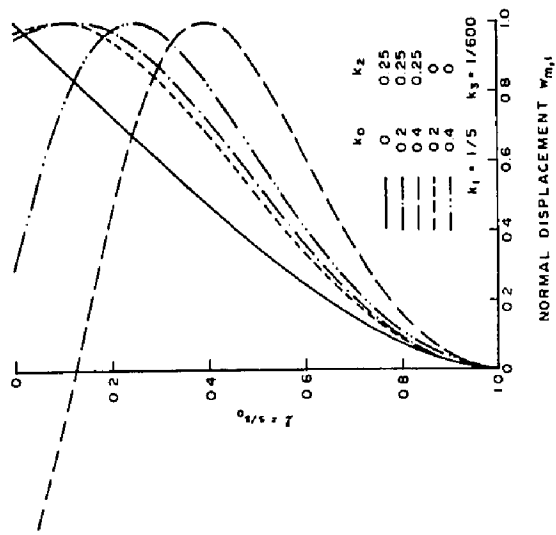


FIG. 4.16 DEPENDENCE OF MODE SHAPE ON GEOMETRIC RATIOS ($m=3, i=1$)

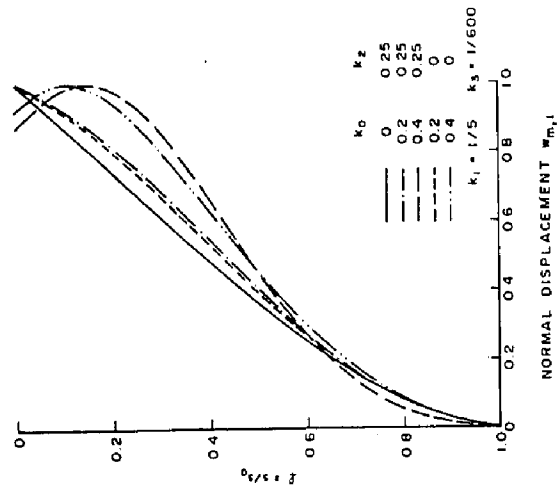


FIG. 4.15 DEPENDENCE OF MODE SHAPE ON GEOMETRIC RATIOS ($m=2, i=1$)

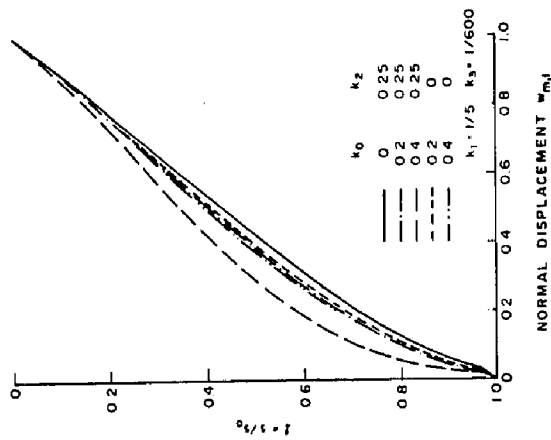


FIG. 4.14 DEPENDENCE OF MODE SHAPE ON GEOMETRIC RATIOS ($m=1, i=1$)

CHAPTER 5

EXPERIMENTAL INVESTIGATION OF WIND PRESSURE

5.1 Introduction

The purpose of this chapter is twofold; first, to provide an understanding of the nature of wind loading on hyperbolic cooling towers, and second, to determine the relevant characteristics of the wind pressure input required for an analytical prediction of the shell response as described in Chapter 3.

The wind pressure on cooling towers could be conveniently divided into two parts; a mean and a fluctuating component. The mean component, usually related to the dynamic head ($\frac{1}{2}\rho\bar{v}^2$), could be directly measured. The random nature of the fluctuating component makes its description meaningful only in statistical terms. This requires a knowledge of the following functions:

1. Standard deviation
2. Correlation coefficient
3. Power spectral density
4. Cross-spectral density

The study of the mean wind pressure around cooling towers has received increasing attention in recent years especially after the collapse of the Ferrybridge towers. A brief review of the current state of knowledge in this respect is given in Chapter 2. On the other hand, the pressure fluctuations has received very little attention (1). In terms of stresses, pressure fluctuations are very significant. It has been shown (2,3) that the dynamic wind stresses are as important as the static wind stresses.

The wind pressure fluctuations on cooling towers are dependent on many factors related to the characteristics of the incoming flow as well as the shell geometry. Of these, the most important are:

1. Reynolds number
2. Turbulence characteristics
3. Shell surface roughness

In a wind tunnel study of the static and dynamic behaviour of cooling towers, Davenport and Isyumov (1) have measured the standard deviation of wind pressure fluctuations in turbulent and in smooth uniform flow at $R_e = 1.8 \times 10^5$. The influence of varying shell surface roughness was also investigated. Their findings are summarized in Figs. (5.1 and 5.2). The strong influence of the shell surface roughness and the intensity of turbulence of the incoming flow is clearly evident. In

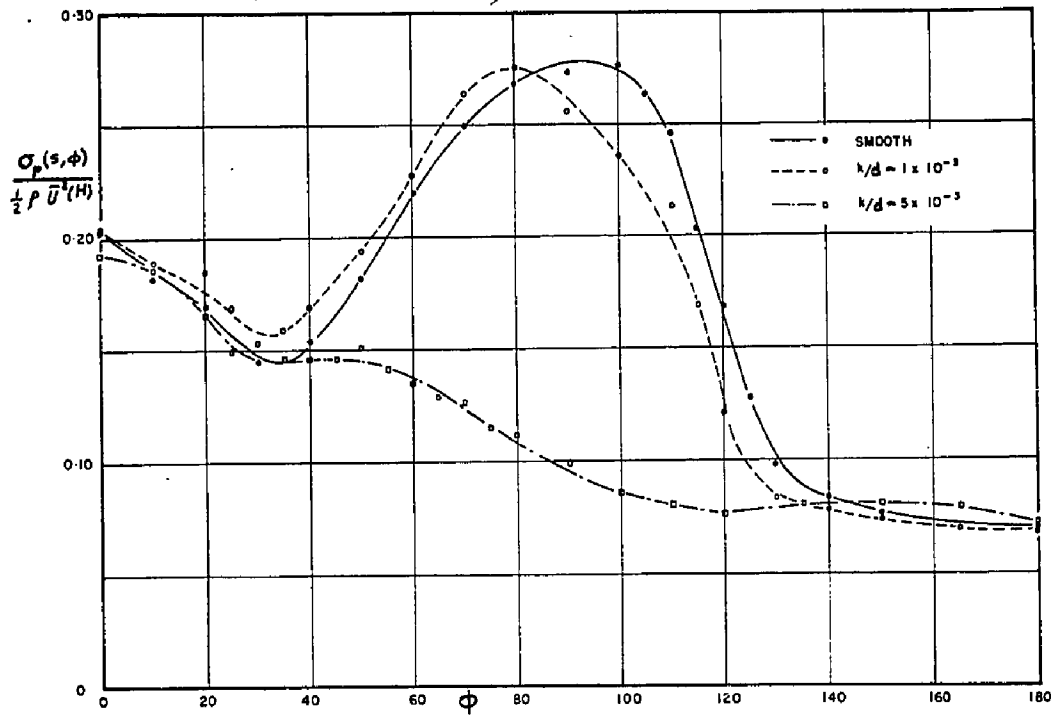


FIG.5.1 RMS PRESSURES AT THROAT OF 1:300 SCALE HYPERBOLIC COOLING TOWER MODEL IN TURBULENT BOUNDARY LAYER FLOW

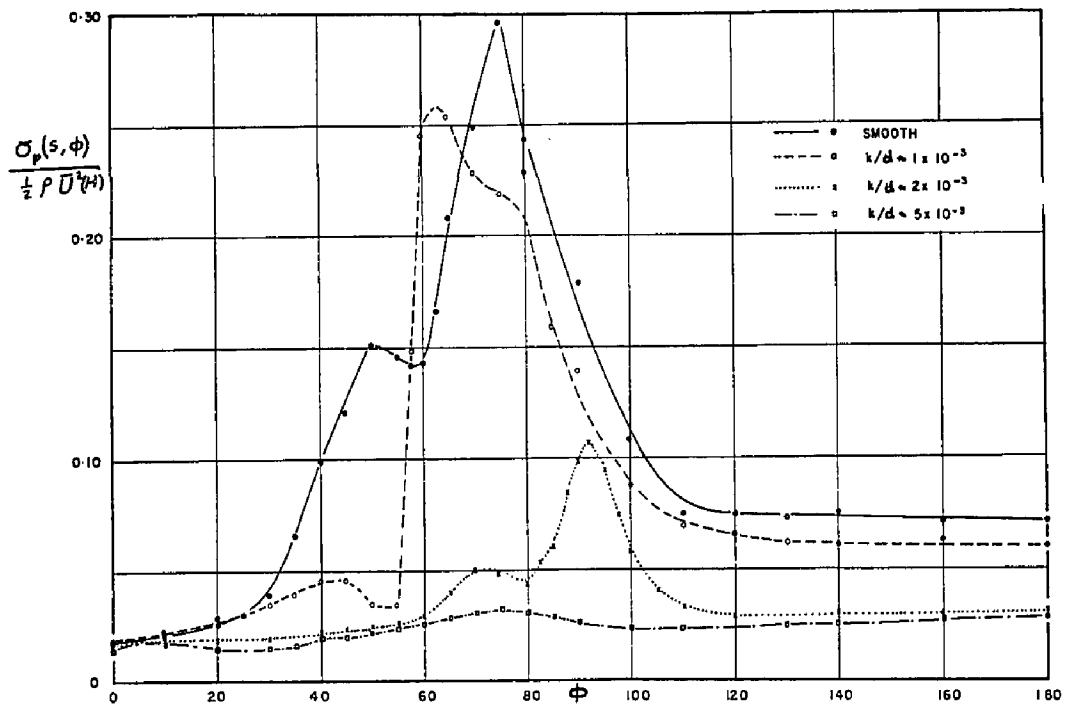


FIG.5.2 RMS PRESSURES AT THROAT OF 1:300 SCALE HYPERBOLIC COOLING TOWER MODEL IN SMOOTH UNIFORM FLOW

(AFTER DAVENPORT AND ISYUMOV)

particular, the pressure fluctuations on the upstream face of the model are very sensitive to changes in the intensity of turbulence. The intensity of the pressure fluctuations on the leading stagnation line is about twice the intensity of turbulence. On the other hand, the influence of the shell surface roughness is largely felt in the side regions, where the mean suction reaches its peak. For a surface roughness of about $\frac{k_s}{d} = 5 \times 10^{-3}$ the pressure fluctuations on the sides were effectively suppressed.

Other than the standard deviation, there has been no information concerning the other statistical parameters required for a complete description of the wind pressure fluctuations on cooling towers.

In view of the present limited knowledge of the pressure fluctuations on cooling towers, an experimental program aimed at a complete description of their statistical properties was carried out. The maximum Reynolds number attained in the experiments was about 1.8×10^5 ; which is about three orders of magnitude less than that for full scale towers in severe wind conditions. These results cannot, therefore, be directly extended to full scale towers, but they may be used to examine the nature of flow around cooling towers and the type of functions used to describe it.

5.2 Experimental Set-up

The experiments were conducted in the Boundary Layer Wind Tunnel Laboratory of The University of Western Ontario. The tunnel has a working section of 80 ft. long, 8 ft. width, and 5 to 7 ft. high. A detailed description of the tunnel is given elsewhere (4).

A vertical cross section of the rigid pressure model used in the tests is shown in Fig. 5.3. The model is made from a metalized plastic epoxy called Devcon A and has a relatively smooth surface. The model was used in an earlier study by Davenport and Isyumov (1). Its geometry is defined by the following parameters:

- a) Curvature parameter: $k_o = a/b = 0.42$.
- b) Throat radius to total height ratio = 0.254.
- c) Height above throat to total height ratio = 0.216.

The above ratios are close to the average ratios of the geometric parameters of hyperbolic cooling towers built in U.S.A. (See Figs. 1.6 to 1.9).

The tests were carried out in a turbulent flow to simulate wind flow regimes over moderately rough terrain. The velocity profile has a power law exponent of about 0.32. Measurements of wind velocity were recorded using a hot-wire anemometer.

The model was fitted with 36 pressure taps arranged at ten different levels, Fig. (5.3). The various pressure

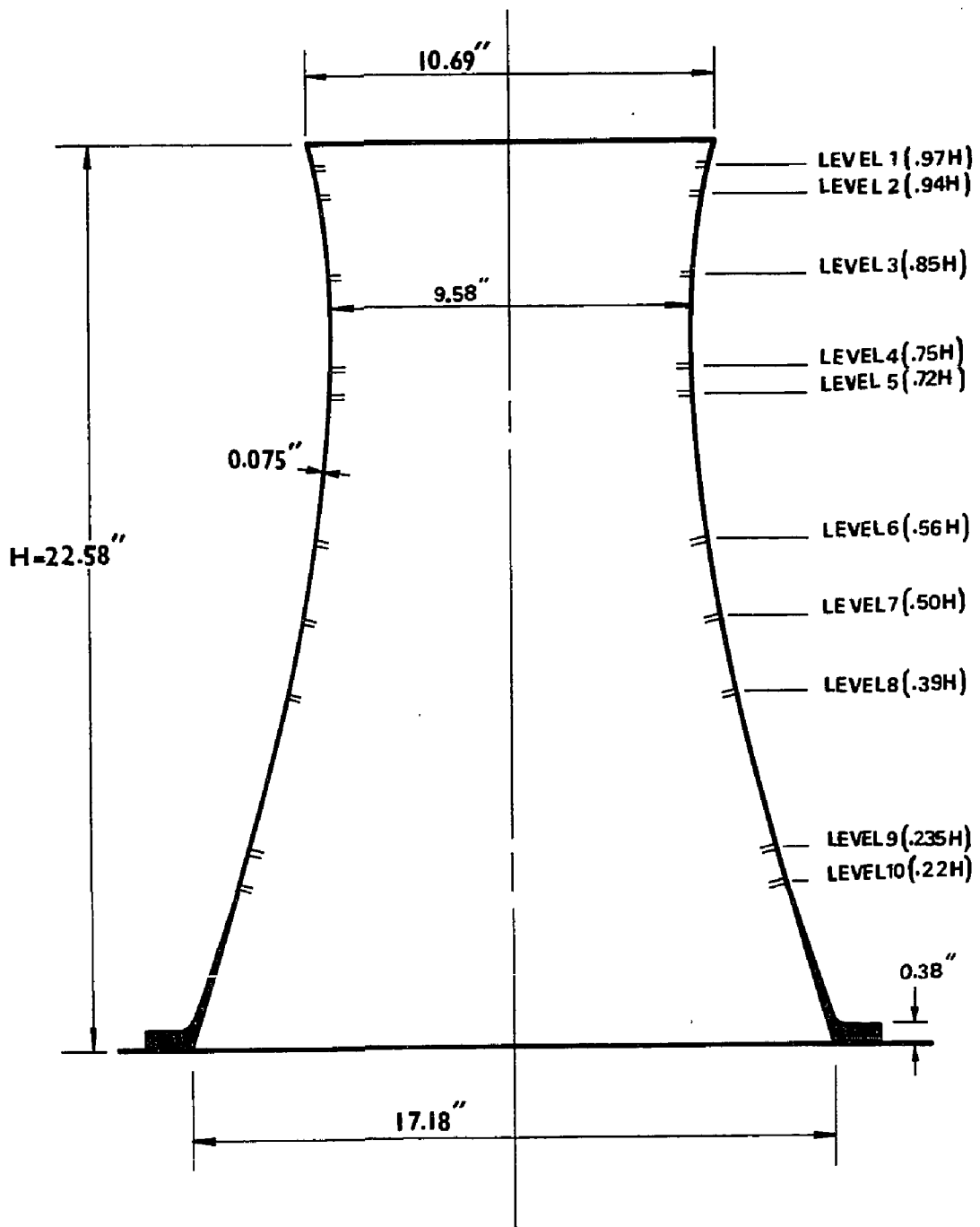


FIG. 5.3 PRESSURE MODEL

tappings were connected to a central pressure transducer through a scanning device. When measuring pressure cross-correlation functions, two central transducers were used. The output of the pressure transducer was then fed into a digital data acquisition system to determine the mean and the standard deviation of the fluctuating component. In the meantime, the pressure signals were stored on magnetic tapes for subsequent analysis of the correlation functions. The correlator employed for the measurements of the auto- and cross-correlation function is the CAT Model 1000 computer. The arrangement of the testing instruments is shown in Fig. 5.4.

Mean and standard deviation of the wind pressures were obtained using a time-averaging period of 60 seconds. Pressure cross-correlations were obtained with time averaging periods of 250 seconds, lag-time increments of 4 or 8 milliseconds and the number of lag points sampled was either 128 or 256 points. Measurements of the wind pressure characteristics on the cooling tower model were obtained for the model with and without vents at the base. From repeated measurements, it was found that errors in the results range between $\pm 5\%$.

5.3 Flow Properties

Fig. 5.5 shows the variation of mean wind speed with height $\bar{U}(z)$ at the test section. These results could be fitted adequately by a power law of the form,

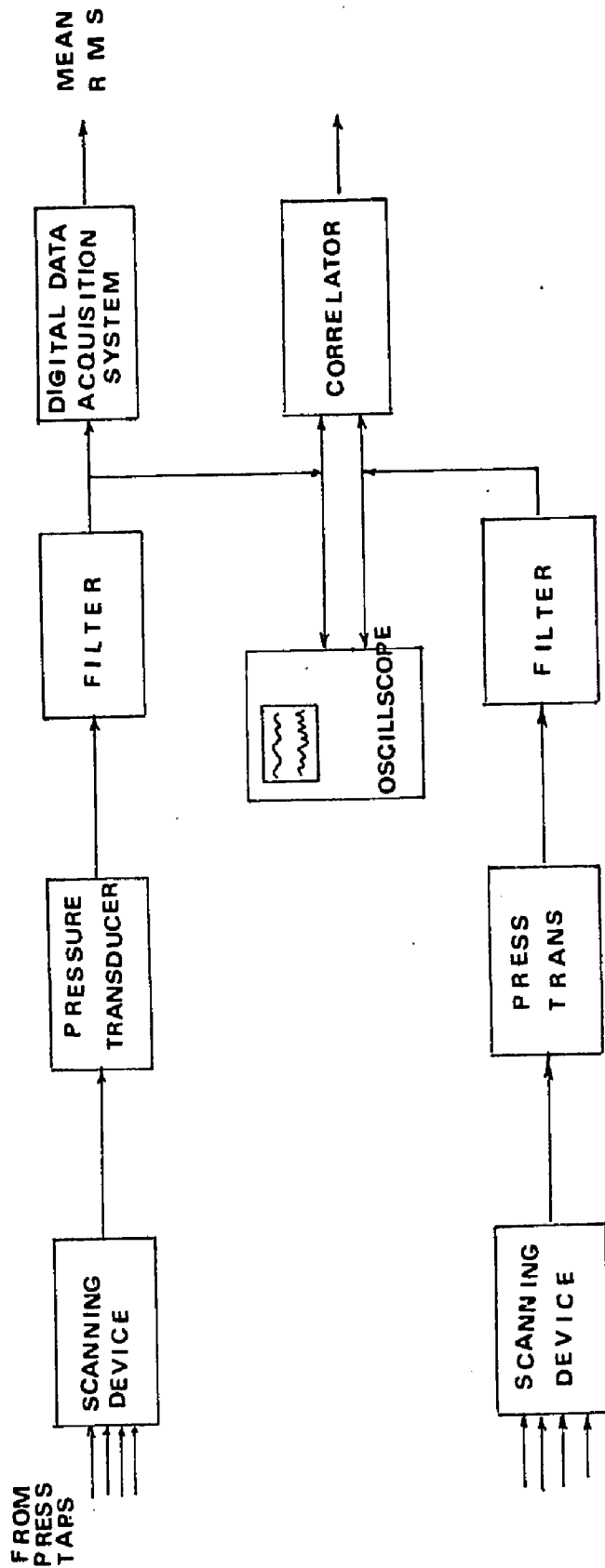


FIG. 5.4 EXPERIMENTAL SET-UP

$$\frac{\bar{U}(Z)}{\bar{U}(H)} = \left(\frac{Z}{H}\right)^{0.32} \quad (5.1)$$

in which, H = model height.

This velocity profile simulates flow over moderately rough terrain (see Table 2.1).

The variation of the standard deviation of the velocity fluctuations with height, $\sigma_u(Z)$, is shown in Fig. 5.6. For values of Z up to 20 inches above the tunnel floor, the value of $\sigma_u(Z)$ could be approximately related to the gradient wind speed by,

$$\sigma_u(Z) = 0.11\bar{U}(Z_G) \quad (5.2)$$

in which Z_G = gradient height. This is consistent with results given by Davenport (5). For higher values of Z , $\sigma_u(Z)$ diminishes till it reaches zero at gradient height.

The power spectral density of the wind pressure fluctuations at three different levels are shown in Figs. (5.7 to 5.9). The variation of the wind spectra with frequency is almost invariant with height. The results are in good agreement with Davenport's strong wind spectrum given by,

$$S(f) \propto \frac{\tilde{f}}{\{1+f^2\}^{4/3}} \quad (5.3)$$

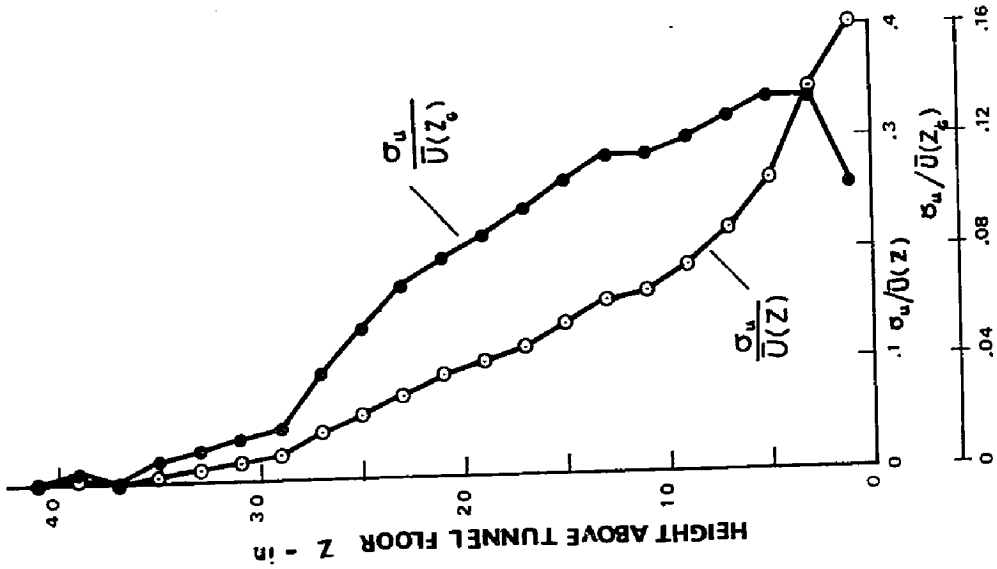


FIG. 5.6 VARIATION OF TURBULENCE INTENSITIES WITH HEIGHT

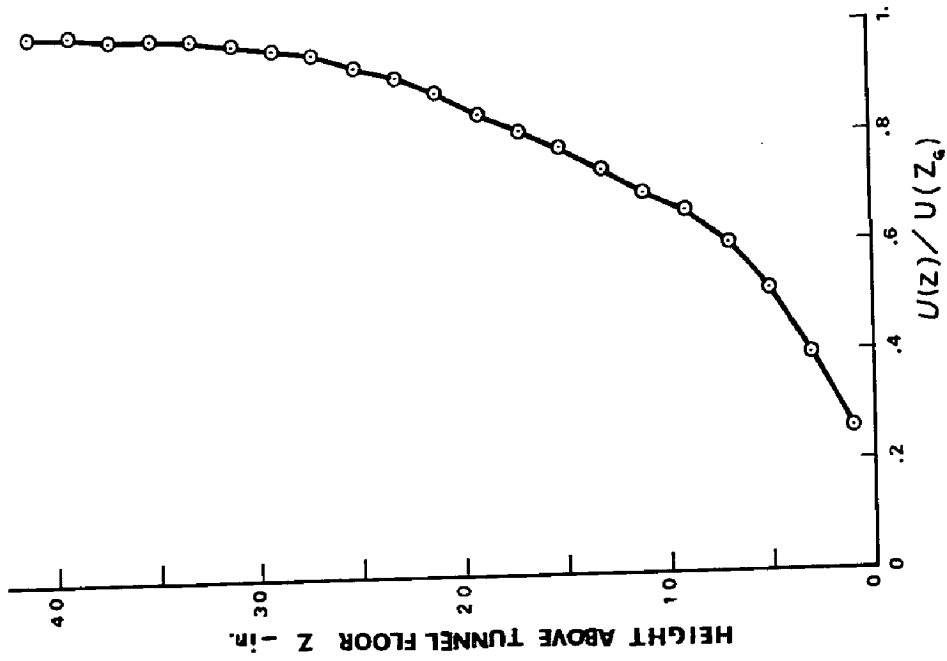


FIG. 5.5 VARIATION OF MEAN WIND SPEED WITH HEIGHT

where $\tilde{f} = \frac{fL_u(Z)}{\bar{U}(Z)}$, and $L_u(Z)$ = a scale length.

For full scale conditions, Davenport (5) suggests a value for L_u of 4000 ft. while Harris (6) suggests a value of 5900 ft. Model values for $L_u(Z)$ are 14.51, 16.65, and 17.51 ft. at heights 11.5, 16.5, and 22.5 in. above tunnel floor, respectively.

5.4 Mean Wind Pressure

Measurements of the mean wind pressure distribution around the cooling tower model were obtained at the ten levels marked in Fig. 5.3. Results were obtained for the model with and without vents at base. Reynolds number based on throat diameter is 1.8×10^5 .

In terms of the local velocity head, the mean wind pressure on the exterior surface of the shell could be described by,

$$\bar{p}(s, \phi) = \frac{1}{2} \bar{U}^2(Z) C_p(s, \phi) \quad (5.4)$$

in which Z = height above tunnel floor, s and ϕ = meridional and circumferential coordinates (Fig. 2.1) and C_p = mean pressure coefficient.

Comparisons of pressure distributions for model with and without base venting are shown in Figs. (5.10 to 5.15) at some selected levels. Excepting the uppermost and lowermost portions of the model where the flow is influenced

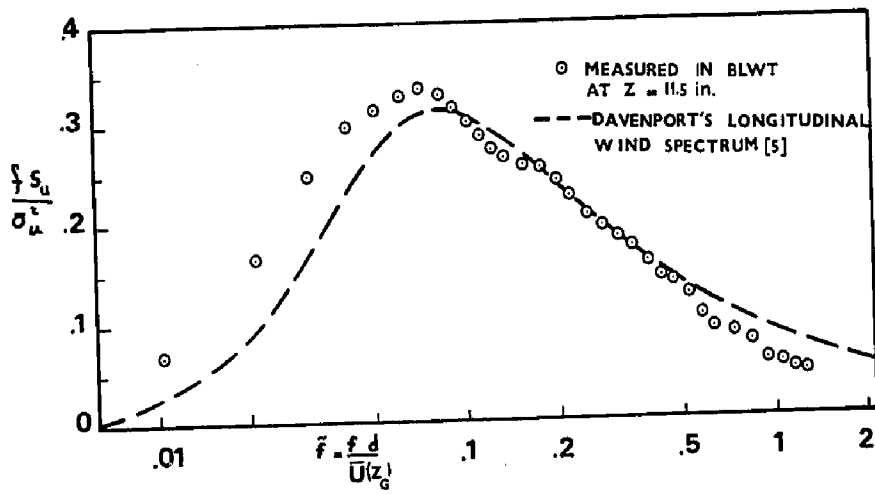


FIG. 57 SPECTRA OF VELOCITY FLUCTUATIONS IN BLWT AND IN NATURAL WIND

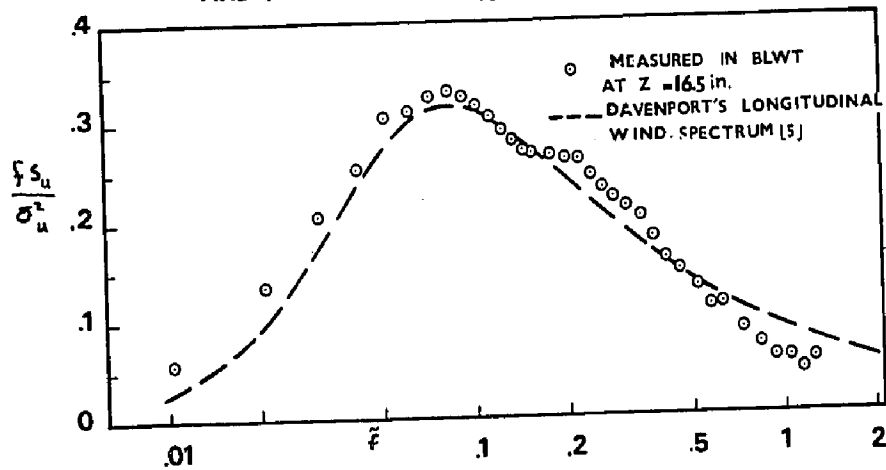


FIG. 58 SPECTRA OF VELOCITY FLUCTUATIONS IN BLWT AND IN NATURAL WIND

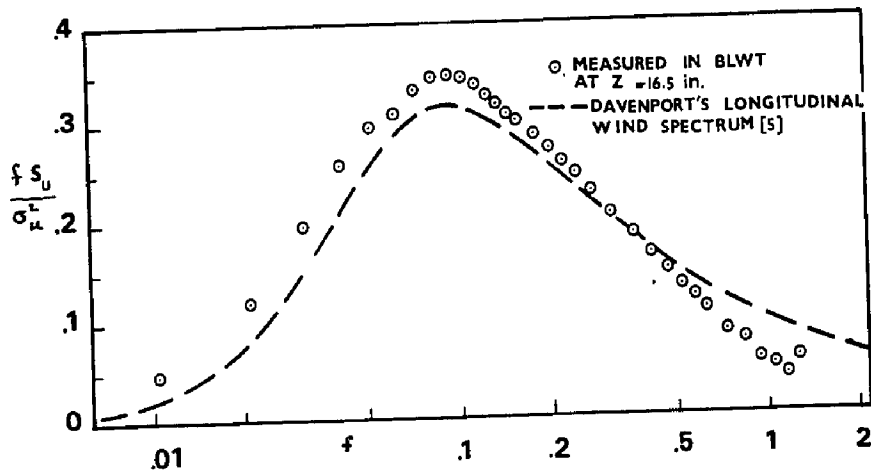


FIG. 59 SPECTRA OF VELOCITY FLUCTUATIONS IN BLWT AND IN NATURAL WIND

by end effects, the wind pressure increases gradually with height and is almost proportional to the local pressure head ($\frac{1}{2}\rho\bar{U}^2$). The variation of wind pressure around the circumference in the upwind face of the model is similar to that of circular cylinders in two-dimensional flow (see Section 2.3.2).

The flow separation takes place at a circumferential position of approximately $\phi_s = \pm 120^\circ$. The wake region at all levels is characterized by the lack of any significant pressure gradient and the pressure coefficient is almost invariant with ϕ .

The peak suction is in the order of $-1.8(\frac{1}{2}\rho\bar{U}^2)$, and occurs at approximately $\phi = \pm 80^\circ$ for model without base venting. If complete base venting is allowed for, the peak suction increases by about 10% but its location remains almost the same. At the top and base regions, the peak suction is markedly reduced.

The wind pressures in the wake region are strongly influenced by base venting, especially in the edge regions. In general, the negative pressures in the wake region increases with base venting.

The present results and conclusions confirm earlier results described in Ref. (1,2) for same model.

In the present approach to the analysis of wind stresses in cooling towers outlined in Chapter 2 the wind

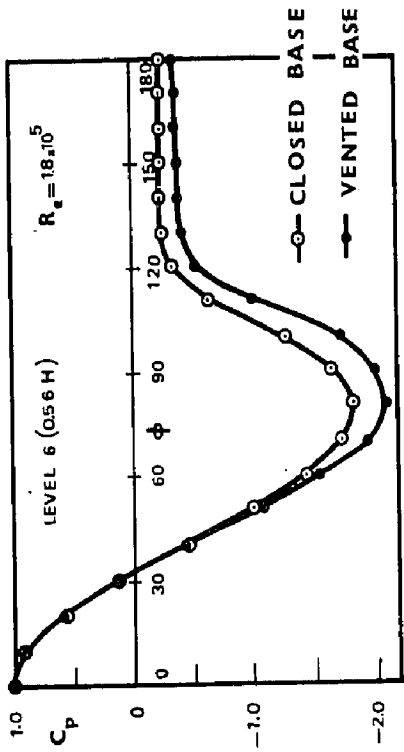


FIG. 5.12 MEAN PRESSURE DISTRIBUTION AT LEVEL 6

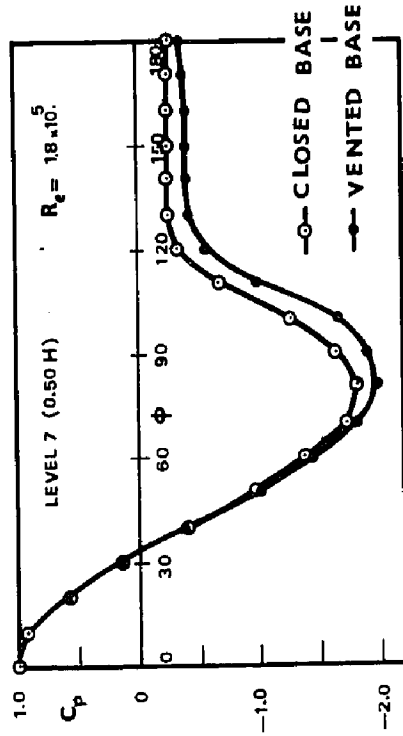


FIG. 5.13 MEAN PRESSURE DISTRIBUTION AT LEVEL 7

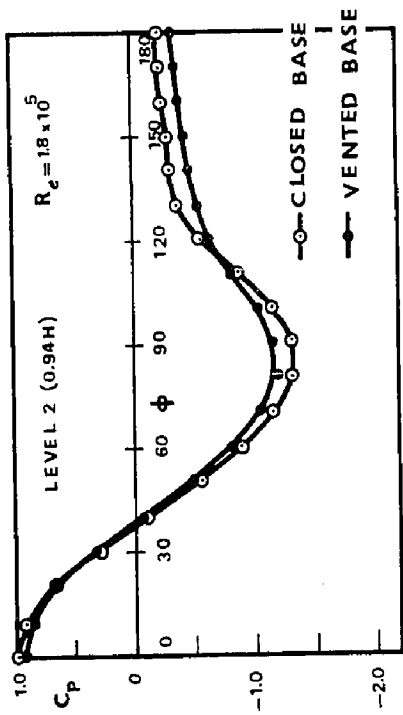


FIG. 5.10 MEAN PRESSURE DISTRIBUTION AT LEVEL 2

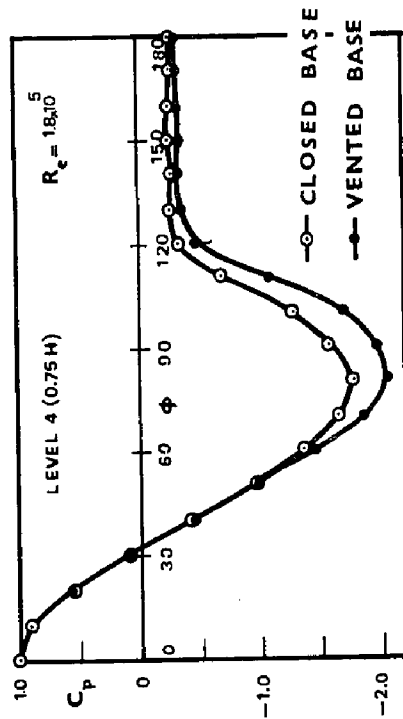


FIG. 5.11 MEAN PRESSURE DISTRIBUTION AT LEVEL 4

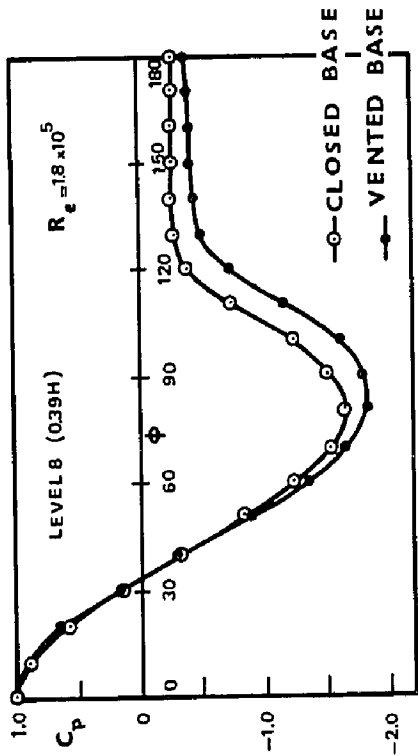


FIG. 5.14 MEAN PRESSURE DISTRIBUTION AT LEVEL 8

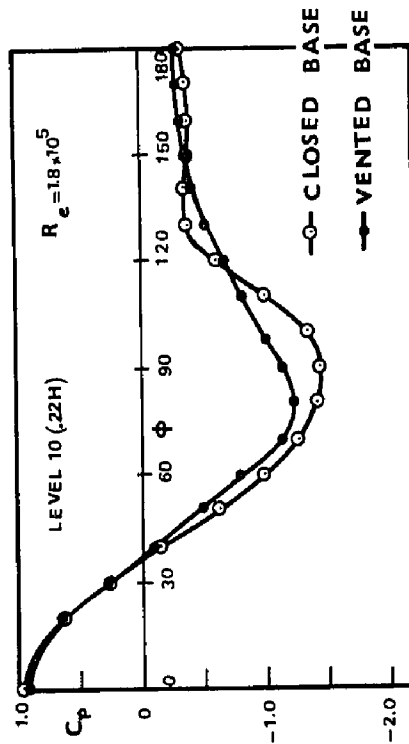


FIG. 5.15 MEAN PRESSURE DISTRIBUTION AT LEVEL 10

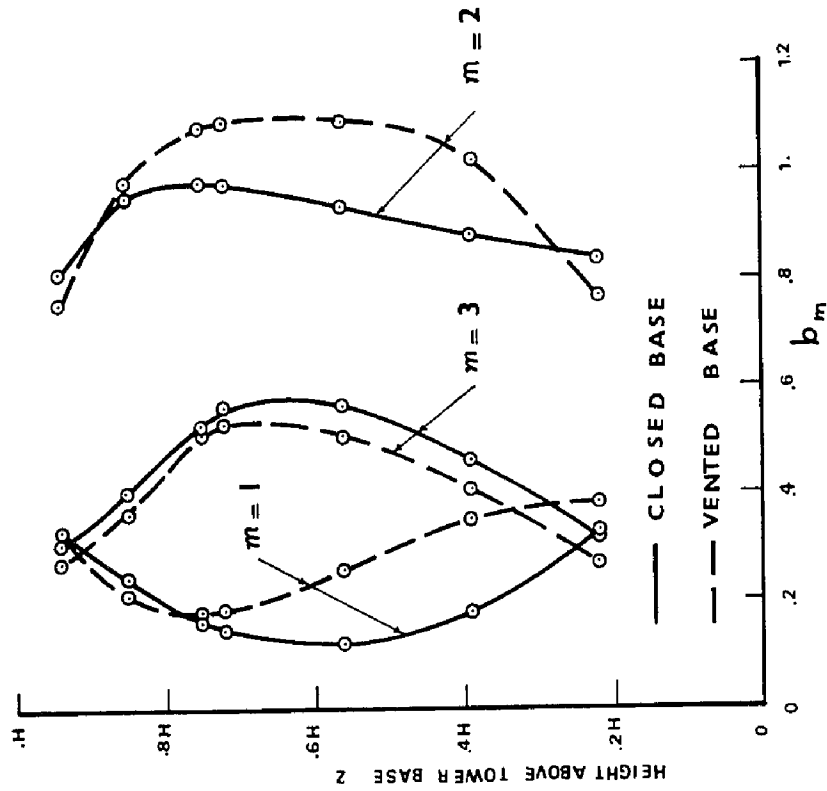


FIG. 5.16 VARIATION OF PRESSURE COEFFICIENTS b_m WITH HEIGHT

loading is conveniently represented in a Fourier series form. Accordingly, the pressure coefficients can be represented by,

$$C_p(s, \phi) = \sum_m b_m(s) \cos m\phi \quad (5.5)$$

It has been a common practice, in the analysis of cooling tower response to wind loading, to assume that the wind pressure distribution is invariant with height and likewise the Fourier coefficient b_m . As shown earlier, this is not generally the case and b_m , in fact, is dependent on height. It is, therefore, necessary to examine the variation of b_m with height for various harmonics.

Fig. 5.16 shows the variation of b_m with height for model with and without vents. Harmonics $m=1, 2$ and 3 are considered only since they are the only significant ones in regard to the wind induced stresses in the meridional direction. It is apparent that b_1 and b_2 are strongly dependent on height. On the other hand, b_3 shows little variation with height except at the edge zones. b_1 is greatly affected by base venting especially in the lower half of the shell. Similarly, b_2 increases with base venting. For b_3 , the influence is small.

Variations of b_m with height could be easily incorporated in the present numerical approach (Chapter 2).

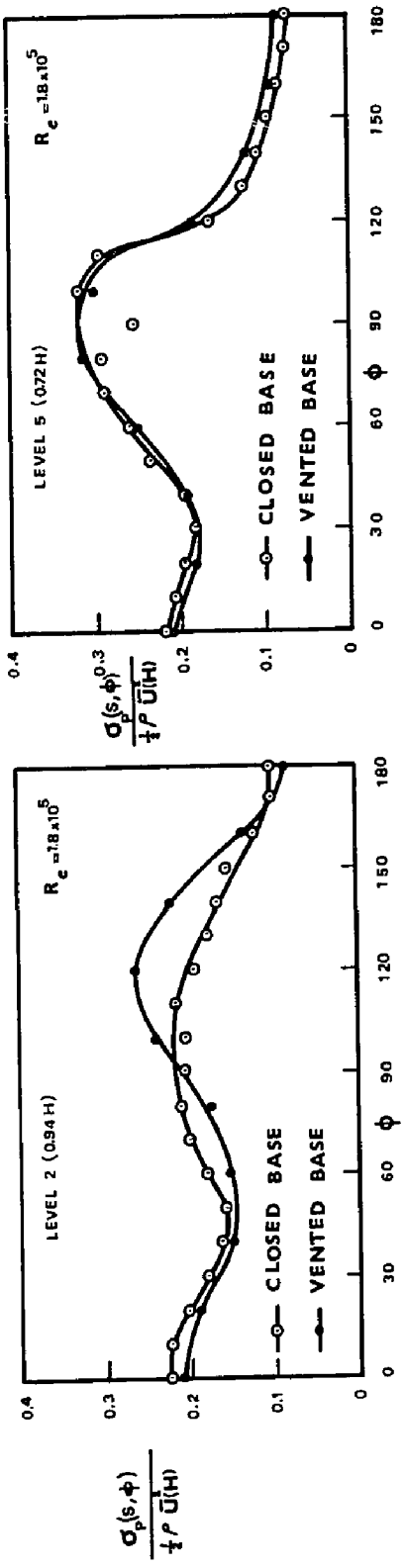


FIG. 5.17 DISTRIBUTION OF THE STANDARD DEVIATION OF PRESSURE FLUCTUATIONS AT LEVEL 2

FIG. 5.19 DISTRIBUTION OF THE STANDARD DEVIATION OF PRESSURE FLUCTUATIONS AT LEVEL 5

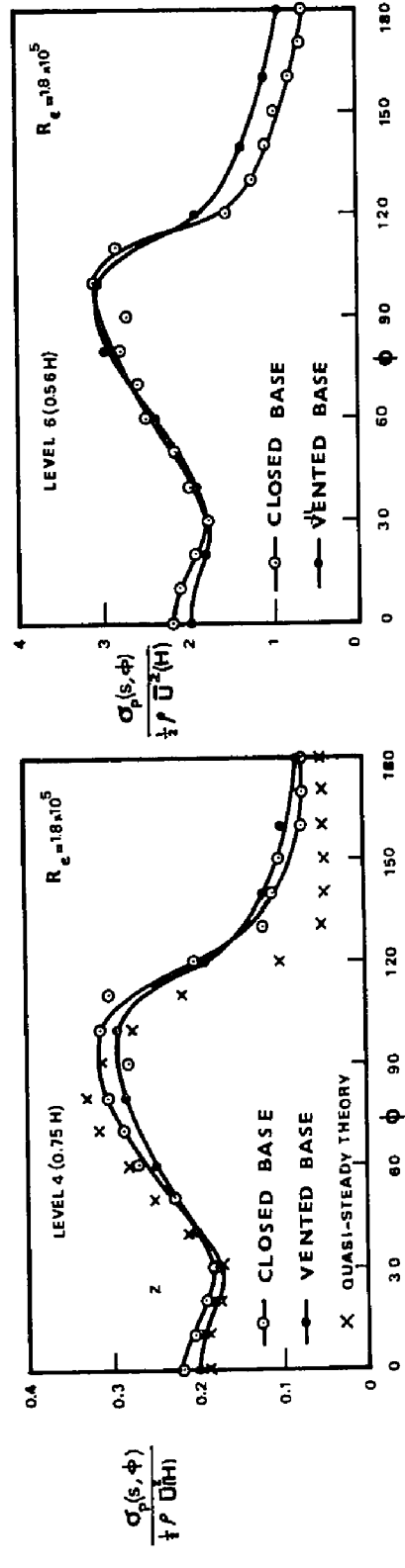


FIG. 5.18 DISTRIBUTION OF THE STANDARD DEVIATION OF PRESSURE FLUCTUATIONS AT LEVEL 4

FIG. 5.20 DISTRIBUTION OF THE STANDARD DEVIATION OF PRESSURE FLUCTUATIONS AT LEVEL 6

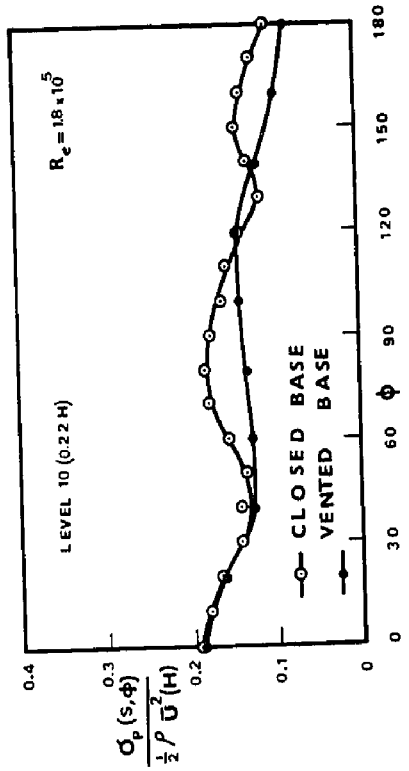


FIG. 5.23 DISTRIBUTION OF THE STANDARD DEVIATION OF PRESSURE FLUCTUATIONS AT LEVEL 10

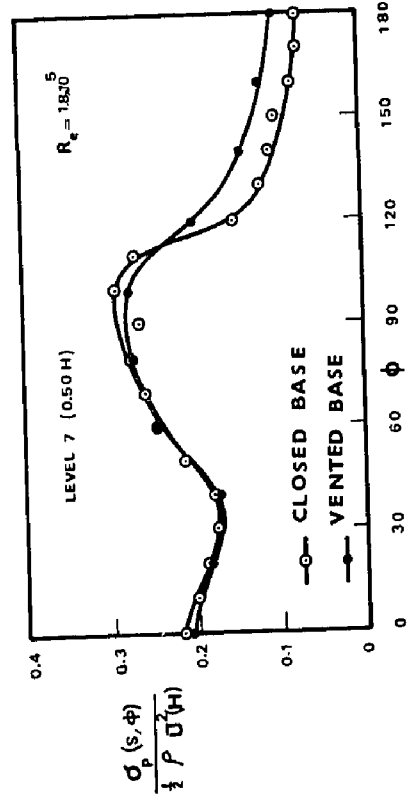


FIG. 5.21 DISTRIBUTION OF THE STANDARD DEVIATION OF PRESSURE FLUCTUATIONS AT LEVEL 7

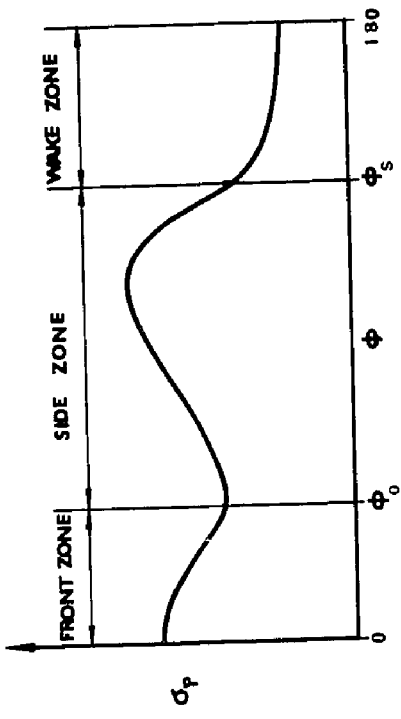


FIG. 5.24

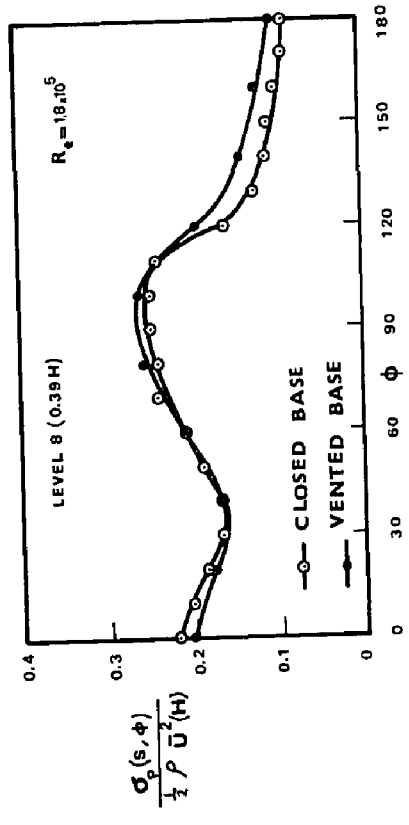


FIG. 5.22 DISTRIBUTION OF THE STANDARD DEVIATION OF PRESSURE FLUCTUATIONS AT LEVEL 8

5.5 Statistical Properties of Pressure Fluctuations

The wind pressure fluctuations acting on the exterior surface of the shell could be conveniently described in statistical terms. An overall understanding of the nature of the pressure fluctuations requires the definition of the statistical properties of pressure fluctuations at individual points as well as the joint statistical properties between pressure fluctuations acting at different points across the shell surface. These were obtained experimentally from wind tunnel measurements and are described herein.

5.5.1 Standard Deviation

By definition, the standard deviation of the wind pressure fluctuations is given by,

$$\sigma_p(s, \phi) = \sqrt{p^2(s, \phi, t)} \quad (5.6)$$

$\sigma_p(s, \phi)$ provides a measure of the spread of the pressure fluctuations around the mean value.

Wind tunnel measurements of the distribution of $\sigma_p(s, \phi)$ around the shell circumference at various levels are given in Figs. 5.17 to 5.23. Comparisons are made between model with and without base venting. Except for the uppermost and lowermost portions of the model, the

distribution of $\sigma_p(s, \phi)$ around the shell circumference could be divided into three distinct zones as shown in Fig. (5.24). These are:

- a) Frontal zone, extending from the upstream stagnation line, $\phi = 0$ to $\phi = 35^\circ$. In this zone, $\sigma_p(s, \phi)$ decreases slowly with ϕ , until a minimum is reached at $\phi = 35^\circ$. The intensity of the pressure fluctuations along the upstream stagnation line is twice as much as the intensity of turbulence in the incoming flow. Venting at base is of little significance in the frontal zone and has the effect of reducing the value of $\sigma_p(s, \phi)$ slightly.
- b) Side zone, covering approximately the area between $\phi = 35^\circ$ and the points of flow separation ϕ_s . In this zone, $\sigma_p(s, \phi)$ increases gradually from a minimum value at $\phi = 35^\circ$ to a maximum at $\phi = 100^\circ$, then it decreases rapidly as it approaches the points of flow separation. Here also, the influence of base venting is very small.
- c) Wake region, covering the area between the separation points, on the leeward side of the shell. In this region, $\sigma_p(s, \phi)$ decreases slowly as ϕ increases until a minimum value is attained at $\phi = 180^\circ$. The intensity of pressure fluctuations increases if the base is vented. The increase is in the order of 25%.

In the top and lower portions of the model, the pressure fluctuations in the side zone are reduced markedly than everywhere else in the shell. There are no distinguished boundaries between the side and wake regions. The influence of base venting is very pronounced and causes a significant increase in the intensity of the pressure fluctuations in the wake region. In the frontal region, the distribution and intensity of $\sigma_p(s, \phi)$ are not significantly influenced by end effects and are similar to those everywhere else in the shell.

The variation of $\sigma_p(s, \phi)$ in the central portion of the shell, away from edge effects could be examined in terms of a two-dimensional quasi-steady theory (at the top and base, variations with height cannot be ignored). Based on this theory, Tunstall (7) has shown that,

$$\sigma_p(s, \phi) = \frac{1}{2} \rho \bar{U}^2 (Z) \left\{ 4 \left(\frac{\sigma_u}{U} C_p(s, \phi) \right)^2 + \left(\frac{\sigma_v}{U} \frac{dC_p(s, \phi)}{d\phi} \right)^2 \right\}^{1/2} \quad (5.7)$$

in which, σ_u and σ_v are the standard deviations of the longitudinal and lateral components of velocity fluctuations.

The distribution of $\sigma_p(s, \phi)$ at the throat, computed using equation 5.7, is compared with the experimental results in Fig. 5.18. In the computation, σ_v is assumed to be approximately equal to 80% of σ_u (8). In general,

there is good agreement between the quasi-steady results and the experimental measurements especially in the windward face of the model, ahead of the separation points. The large discrepancy between both results in the wake region is not very significant as the intensity of the pressure fluctuations is very small.

Equation (5.7) was also used to predict the variation of the standard deviation of the pressure fluctuations along the upstream stagnation line. Here, equation (5.7) reduces to,

$$\sigma_p(s, \phi) = \rho \sigma_u \bar{U}(z) \quad (5.8)$$

since, $\frac{dC_p(s, \phi)}{d\phi} = 0$ and $C_p(s, \phi) \approx 1.0$ along the stagnation line. Fig. (5.25) shows a comparison between quasi-steady theory and experiments. Except for the edge zone, both results appear to be in good agreement.

Similar results have also been observed by Tunstall (7) when comparing the quasi-steady predictions around the circumference with full scale measurements on a reinforced concrete chimney at $R_e = 2.3$ to 2.8×10^7 . It is, therefore, concluded that the intensity of the wind pressure fluctuations on the cooling tower surface could be predicted with reasonable accuracy (except at top and base) using a two-dimensional quasi-steady theory.

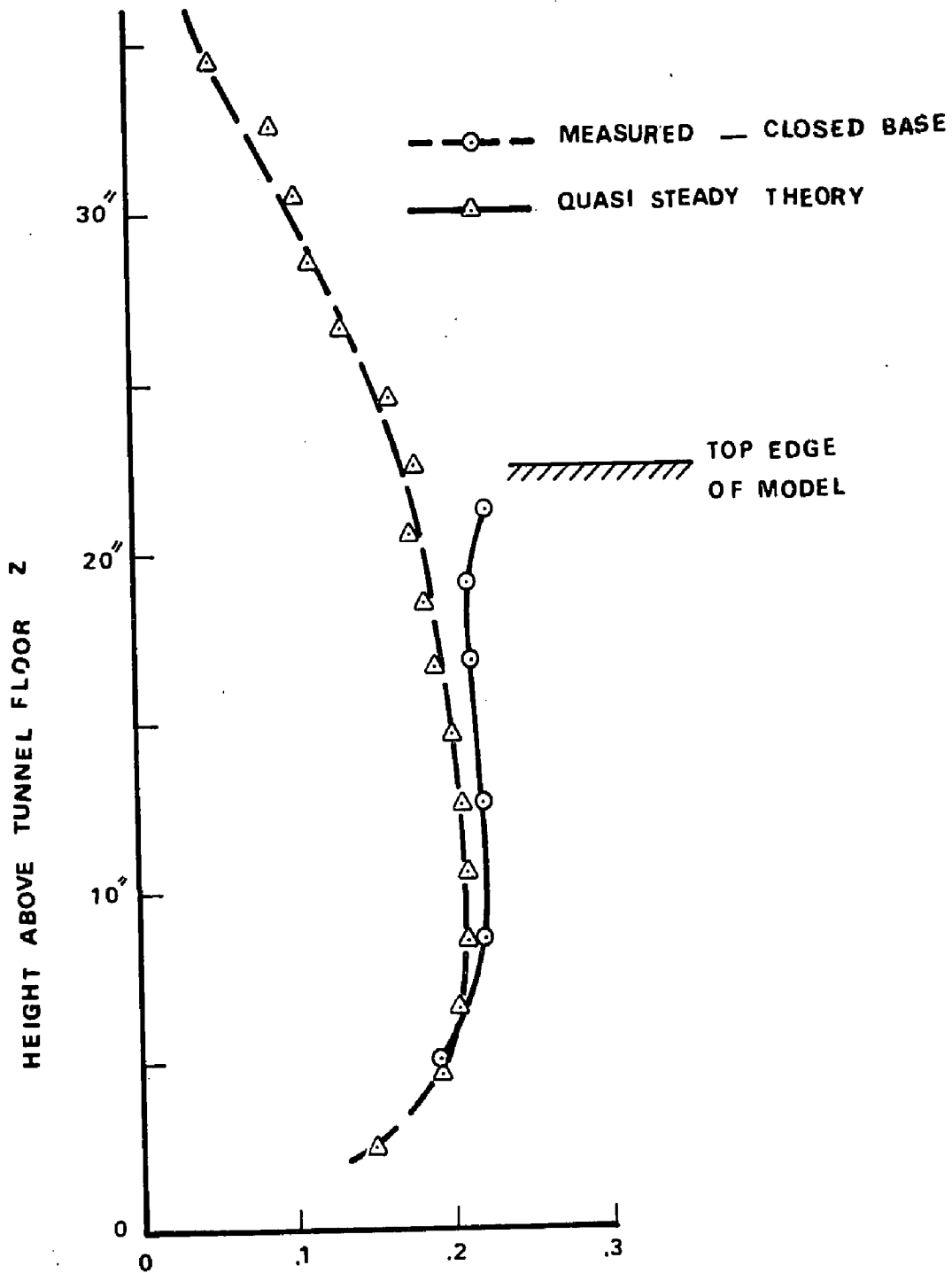


FIG. 5.25 VARIATION OF THE STANDARD DEVIATION OF PRESSURE FLUCTUATIONS WITH HEIGHT AT $\phi = 0$

5.5.2 Covariance

For spatially extended structures like cooling tower shells, the wind pressure fluctuations across the surface are not full correlated. The loss of correlation will reduce the effectiveness of the dynamic wind loads experienced by the structure. Knowledge of the pressure correlations across the shell surface is, therefore, necessary for the prediction of the dynamic wind stresses induced in the structure.

The covariance function provides a quantitative measure of the loss of correlation across the shell surface. The magnitude of this function, between any two points on the shell surface, depends not only on the separation between them but also on the location of the two points.

By definition, the pressure covariance at points (s, ϕ) and (s', ϕ') is given by,

$$\bar{C}(s, \phi, s', \phi') = \overline{p(s, \phi, t)p(s', \phi', t)} \quad (5.9)$$

where the bar indicates time average.

For convenience, the covariance function is put in a normalized form as follows:

$$C(s, \phi, s', \phi') = \frac{\tilde{C}(s, \phi, s', \phi')}{\sigma_p(s, \phi)\sigma_p(s', \phi')} \quad (5.10)$$

The normalized function is commonly referred to as the correlation coefficient and its magnitude lies between +1 and -1.

It is possible to regard the correlation coefficient as the product of two functions, one of which reflects the correlation in the meridional direction and the other in the circumferential direction, as follows:

$$C(s, \phi, s', \phi') = C_y(s, s') C_h(\phi, \phi') \quad (5.11)$$

Experimental evidence justifies the above decomposition and will be described later in this section.

Measurements of $C_y(s, s')$ were carried out along three representative meridians,

- a) frontal stagnation line ($\phi=0$), representative of the front region,
- b) leeward stagnation line ($\phi=180^\circ$), representative of the wake region, and
- c) side meridian at $\phi=90^\circ$, in the vicinity of which the pressure fluctuations have their maximum intensity.

Some selected results along the three meridians are shown in Figs. 5.26 to 5.28. For all locations, the loss of correlation increases slowly with increase in the meridional separation Δs , until Δs reaches about 10%

CORRELATION COEFFICIENTS FOR VERTICAL SEPARATIONS

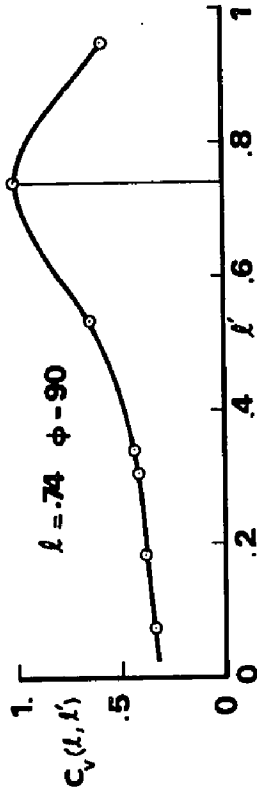
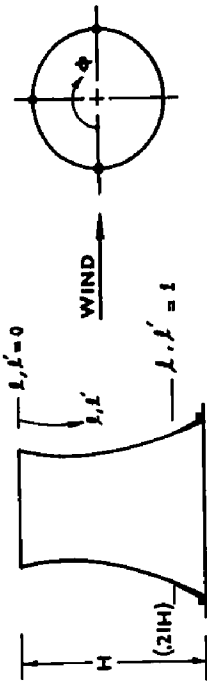


FIG. 5.27

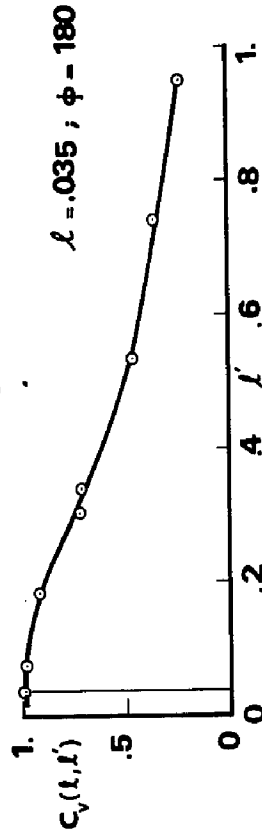


FIG. 5.28A

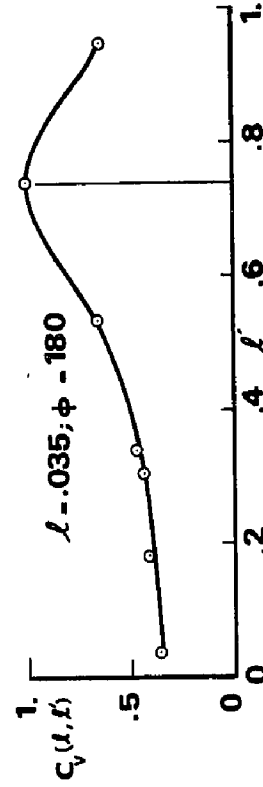


FIG. 5.28B

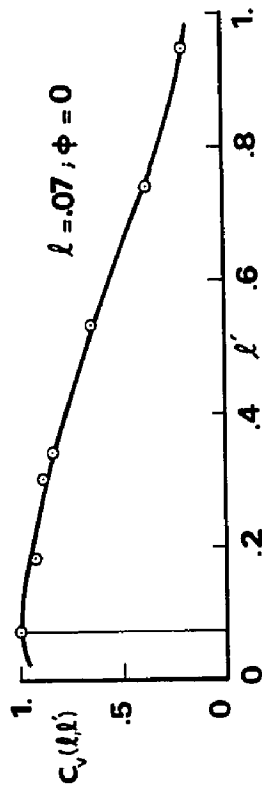


FIG. 5.26A

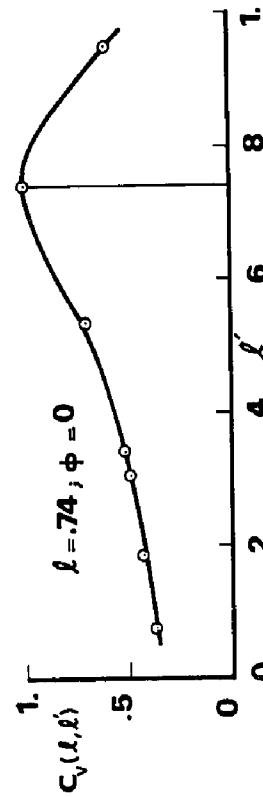


FIG. 5.26B

of the total meridional length, s_0 , after which it increases rapidly. While the loss of correlation is strongly dependent on the separation, its dependence on the actual position of the two points, while existing, does not seem to be significant.

Correlation between the pressure fluctuations along the frontal meridian seems to be stronger than the other two meridians. The difference, however, does not seem to be significant.

In view of the above remarks and for the benefit of an analytical treatment of wind action on cooling towers, $C_v(s, s')$ could be adequately considered as invariant with the circumferential coordinate ϕ , independent of the position of the two points (s, s') and dependent only on the separation Δs . According to these simplifications, the present measurements of $C_v(s, s')$, Figs. 5.26 to 5.28, could be adequately fitted with a simple exponential function of the form,

$$C_v(s, s') = e^{-\beta \Delta z^2} \quad (5.12)$$

in which $\beta = 1.85$ and $\Delta z = \Delta s / s_0$.

Turning now to the horizontal component of the correlation coefficient, $C_h(\phi, \phi')$, measurements were obtained at three different levels (Fig. 5.3),

a) Level 1 (0.97H) near the top edge to represent

- the uppermost portion of the model,
- b) Level 10(0.22 H) near the base to represent the lowermost portion of the model, and
 - c) Level 4 (0.75H) at throat which reflects the general behaviour of the function at all levels away from the edge regions.

Of these three levels, extensive measurements were made only at Level 4 to determine the basic characteristics of $C_h(\phi, \phi')$. Measurements at Levels 1 and 9 were limited, however, since their primary purpose was to examine the variation of $C_h(\phi, \phi')$ near the shell boundaries.

Figs. (5.29 and 5.30) show the shape of $C_h(\phi, \phi')$ vs. ϕ' at seven different stations ($\phi = 0, 30, \dots, 180^\circ$) at Level 4. The variations of $C_h(0, \phi')$ and $C_h(180^\circ, \phi')$ with ϕ' at Levels 1 and 9 are given in Figs. (5.31 and 5.32) respectively. The results indicate that there is no significant correlation between the pressure fluctuations in the windward region and those in the wake region. Moreover, the general behaviour of $C_h(\phi, \phi')$ exhibits two different characteristics, in the windward region and in the wake region. It is possible, therefore, to split $C_h(\phi, \phi')$ into $C_f(\phi, \phi')$ and $C_r(\phi, \phi')$ for the windward and wake regions respectively.

While $C_r(\phi, \phi')$ seems to be strongly dependent on the separation angle $\Delta\phi = (\phi - \phi')$, its dependence on position

CORRELATION COEFFICIENTS FOR CIRCUMFERENTIAL SEPARATIONS AT THROAT
IN WINDWARD REGION

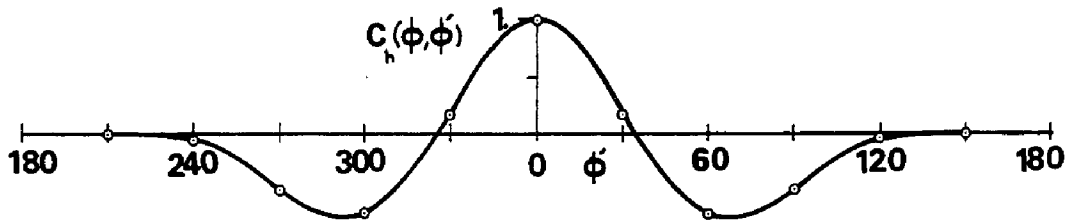


FIG. 5.29A $\phi = 0$

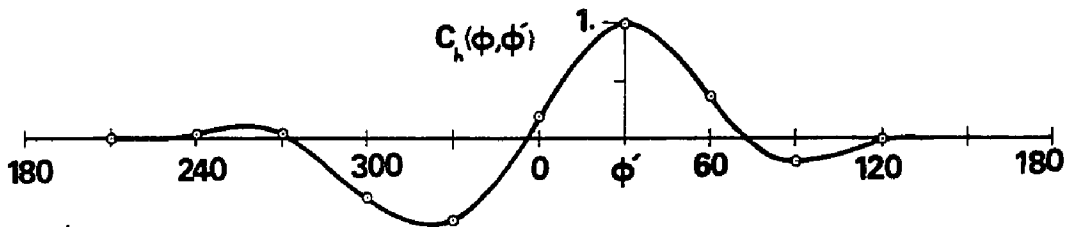


FIG. 5.29B $\phi = 30$

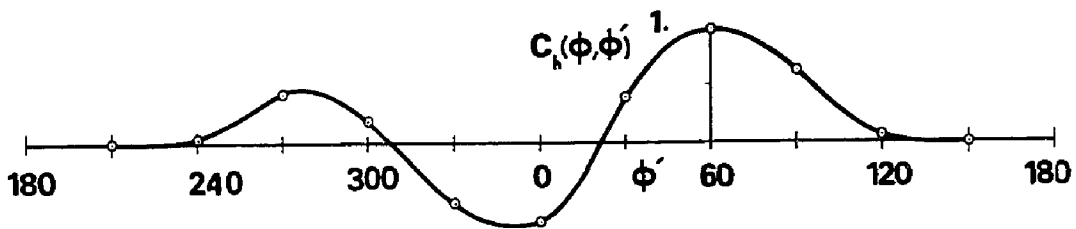


FIG. 5.29C $\phi = 60$

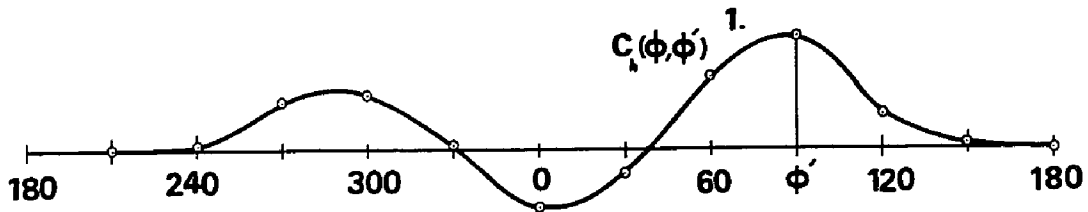


FIG. 5.29D $\phi = 90$

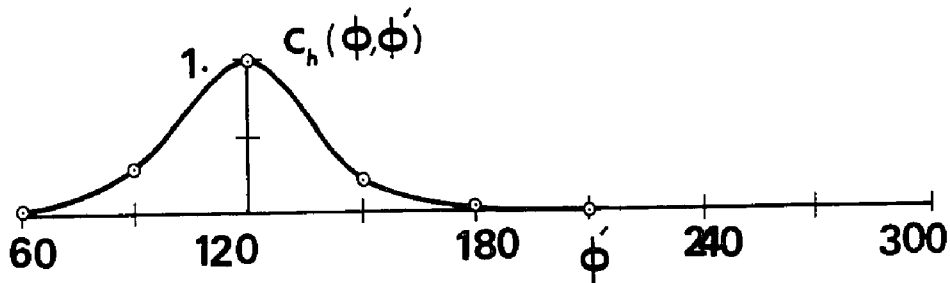
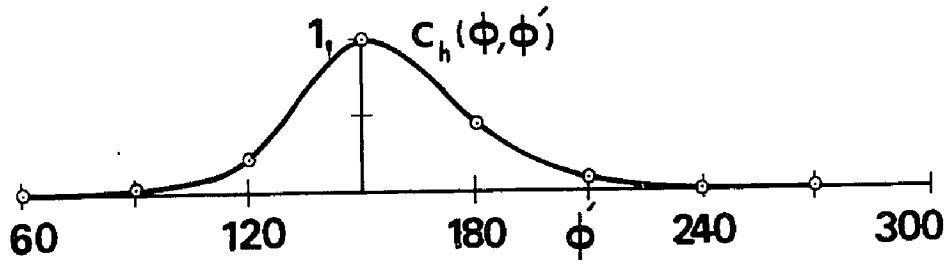
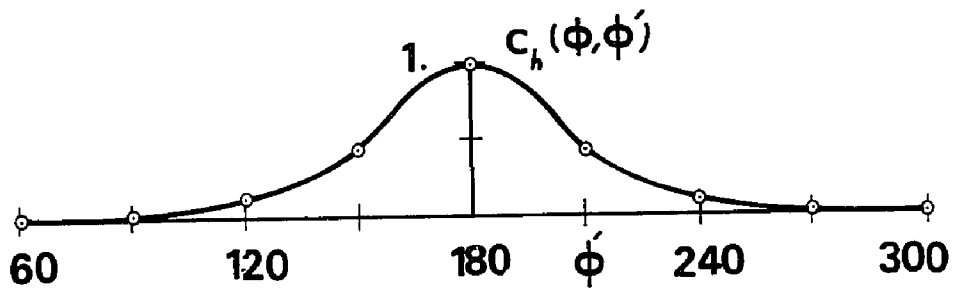
FIG. 5.30A $\phi = 120$ FIG. 5.30B $\phi = 150$ FIG. 5.30c $\phi = 180$

FIG. 5.30 CORRELATION COEFFICIENTS FOR CIRCUMFERENTIAL SEPARATIONS AT THROAT IN WAKE REGION

does not seem to be of practical significance. For simplicity in the analytic treatment of the response, $C_p(\phi, \phi')$ could justifiably be represented by a function that depends solely on the separation $\Delta\phi$. Such a function could also be considered invariant with height (see Figs. 5.30 and 5.32).

Unlike the wake region, the correlation of pressure fluctuations in the windward region is strongly dependent on the position of the points ϕ and ϕ' . This is clearly evident from a direct comparison of, say $C_f(\theta, \phi')$ and $C_f(90^\circ, \phi')$. Some general characteristics of $C_f(\phi, \phi')$ can be outlined as follows:

1. Correlation between pressure fluctuations in the front region and those in the side region, and vice versa, are generally negative.
2. There is strong positive correlation between pressure fluctuations at the two side regions, e.g. $C_f(90^\circ, -90^\circ) = +0.45$.
3. Since the function $C_f(\phi, \phi')$ satisfies the following conditions,

$$C_f(\phi, \phi') \equiv C_f(\phi', \phi)$$

$$C_f(\phi, \phi') \equiv C_f(-\phi, -\phi')$$

for all values of ϕ and ϕ' , then by introducing the following new coordinates,

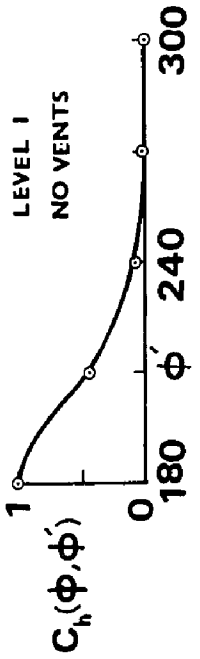


FIG. 5.32A $\phi = 180$

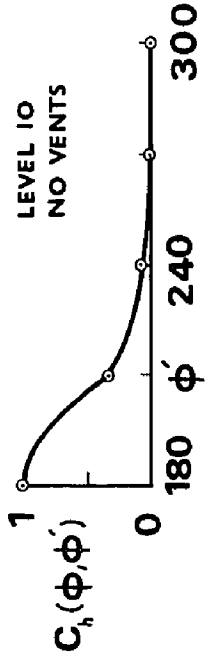


FIG. 5.32B $\phi = 180$

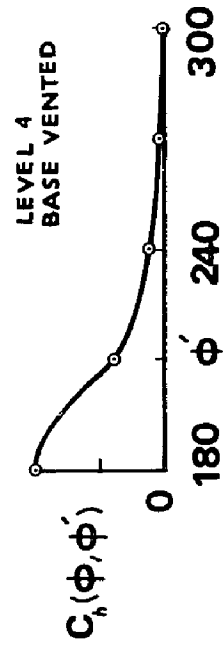


FIG. 5.34 $\phi = 180$

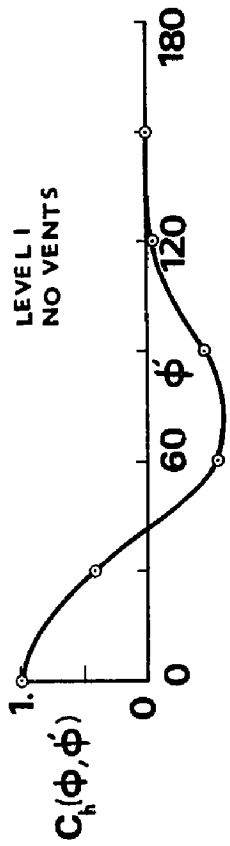


FIG. 5.31A $\phi = 0$

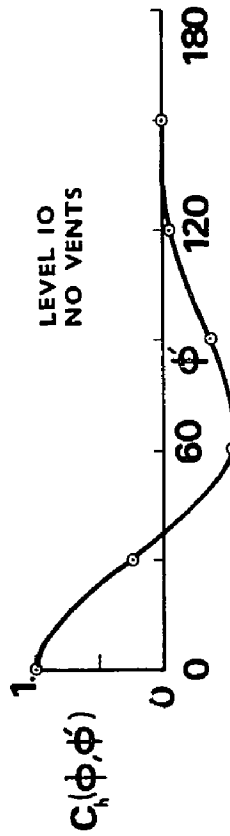


FIG. 5.31B $\phi = 0$

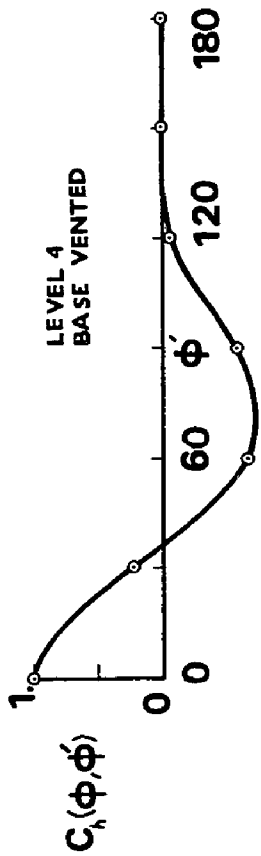


FIG. 5.33 $\phi = 0$

TABLE 5.1

pt. A		pt. B		$C_v(s, s')$	$C_h(\phi, \phi')$	$C_v(s, s') \times C(\phi, \phi')$	$C(s, \phi, s', \phi')$
Z	ϕ	Z	ϕ				
0.94H	0	0.75H	30	0.880	0.175	0.154	0.160
0.94H	0	0.75H	60	0.880	-0.705	-0.620	-0.632
0.94H	0	0.75H	90	0.880	-0.48	-0.422	-0.420
0.94H	0	0.75H	120	0.880	-0.04	-0.035	-0.04
0.94H	0	0.75H	150	0.880	-0.02	-0.018	-0.03
0.94H	0	0.75H	180	0.880	-0.02	-0.018	0.006
0.39H	0	0.75H	30	0.482	0.175	0.085	0.093
0.39H	0	0.75H	60	0.482	-0.705	-0.340	-0.361
0.39H	0	0.75H	90	0.482	-0.48	-0.232	-0.239
0.39H	0	0.75H	120	0.482	-0.04	-0.019	-0.006
0.39H	0	0.75H	150	0.482	-0.02	-0.010	0.006
0.39H	0	0.75H	180	0.482	-0.02	-0.010	-0.007

$$x = \phi + \phi'$$

$$y = \phi - \phi'$$

it becomes evident that $C_f(\phi, \phi')$ will be completely symmetric about the x and y axes. This transformation of coordinates reduces the complexity of $C_f(\phi, \phi')$ considerably.

4. The characteristics of $C_f(\phi, \phi')$ are almost invariant with height, Figs. (5.29 and 5.31).
5. Figs. (5.29, 5.30, 5.33, and 5.34) indicate that the influence of base venting on $C_f(\phi, \phi')$ and $C_r(\phi, \phi')$ is very small and lies within the possible range of experimental errors.

It was pointed out earlier, that the correlation coefficient $C(s, \phi, s', \phi')$ could be regarded as the product of $C_v(s, s')$ and $C_h(\phi, \phi')$. Measurements of the correlation coefficient at various points were obtained and compared with values calculated according to the above decomposition. Both results are shown in Table 5.1. In general, the differences are small and insignificant. It is, therefore, concluded that this decomposition of $C(s, \phi, s', \phi')$ is well justified.

5.5.3 Power Spectral Density

Comprehensive knowledge of the spectra of wind pressure fluctuations is essential for a complete statistical description of the wind pressure characteristics

on hyperbolic cooling towers.

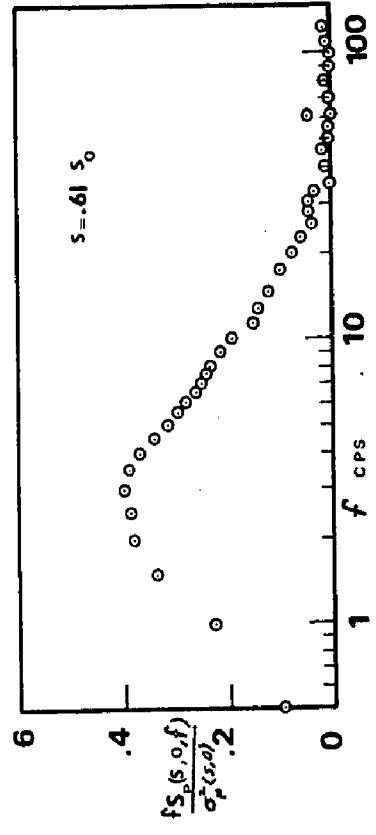
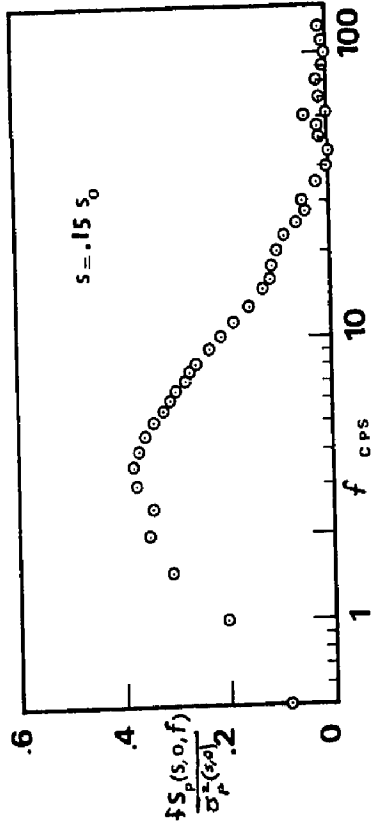
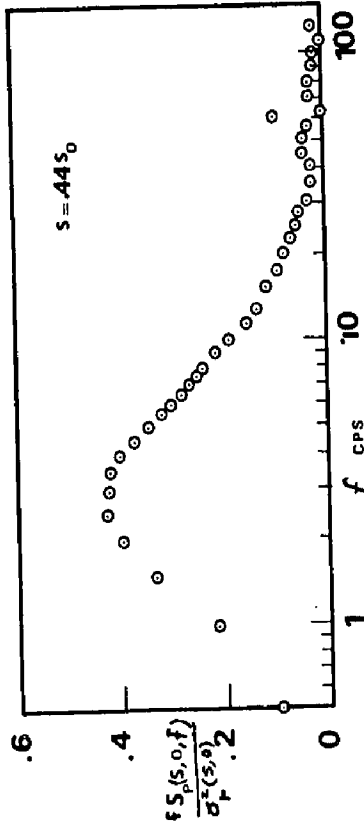
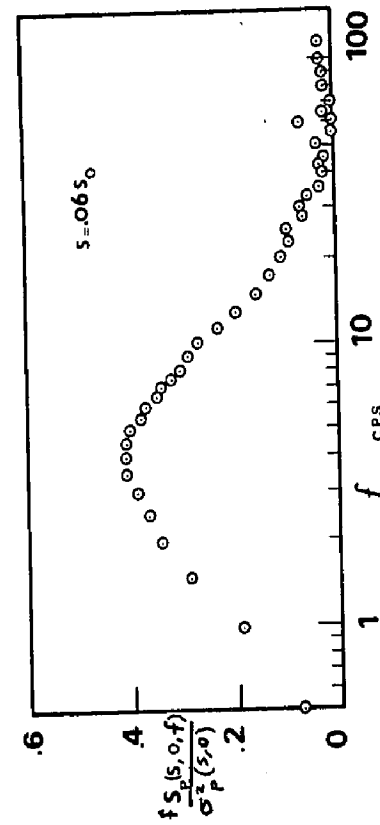
The pressure spectral density function $S_p(s, \phi, f)$ describes the manner in which the energy of the wind pressure fluctuations is distributed in the frequency domain at a point (s, ϕ) . $S_p(s, \phi, f) \Delta f$, gives the contribution to the variance $\sigma_p^2(s, \phi)$ in the frequency range f to $f + \Delta f$. It follows that,

$$\sigma_p^2(s, \phi) = \int_0^{\infty} S_p(s, \phi, f) df \quad (5.13)$$

For hyperbolic cooling towers, the character of $S_p(s, \phi, f)$ varies considerably across the shell surface. This could be attributed to the fact that the pressure fluctuations are produced by many sources other than the turbulence in the unobstructed flow. These sources arise from the complex interaction of the tower and the approaching wind flow regime. Therefore, extensive measurements of the pressure spectra, at various points on the shell surface, were carried out. Measurements were restricted to the model without vents at base at a Reynolds number of 1.8×10^5 . Some selected results showing the basic features of the variation of $S_p(s, \phi, f)$ are given herein.

The pressure spectra at different points along the frontal stagnation line are shown in Figs. (5.35 to 5.38). Measurements around the shell circumference at points

POWER SPECTRA OF PRESSURES ALONG THE UPSTREAM STAGNATION LINE



POWER SPECTRA OF PRESSURES AROUND SHELL CIRCUMFERENCE AT THROAT

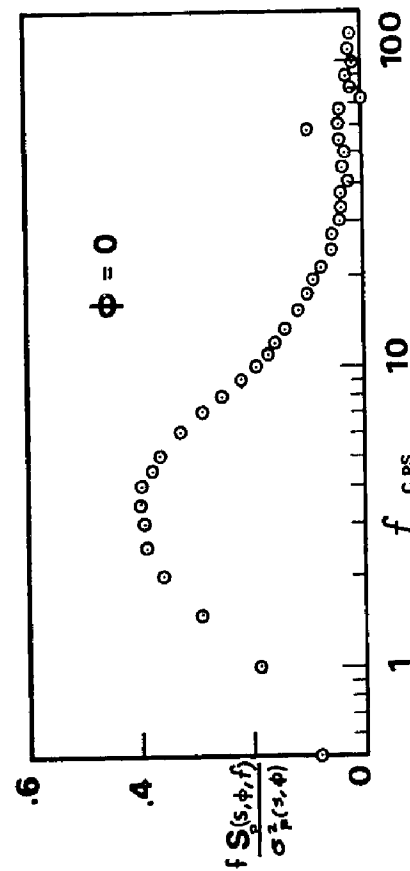


FIG. 5.39

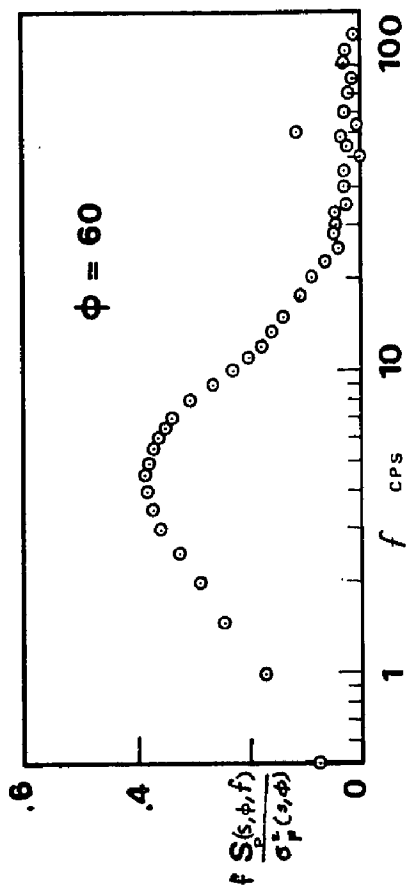


FIG. 5.41

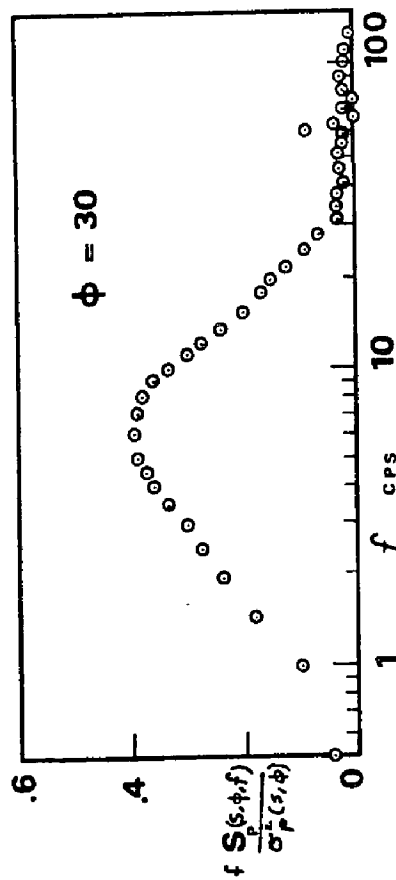


FIG. 5.40

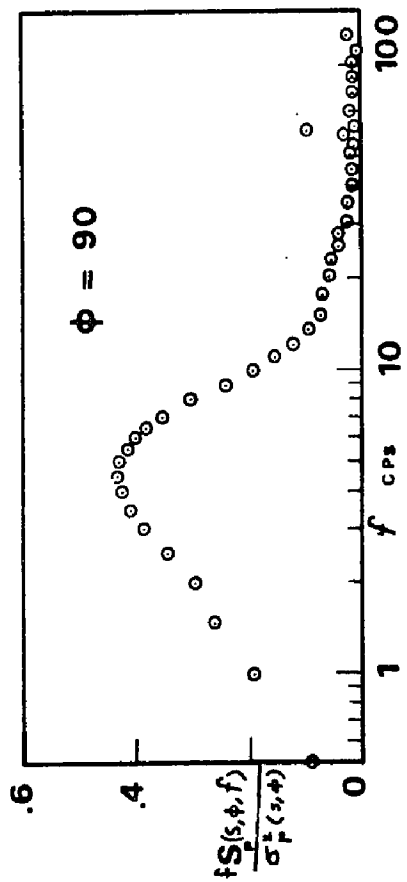


FIG. 5.42

POWER SPECTRA OF PRESSURES AROUND SHELL CIRCUMFERENCE
AT THROAT

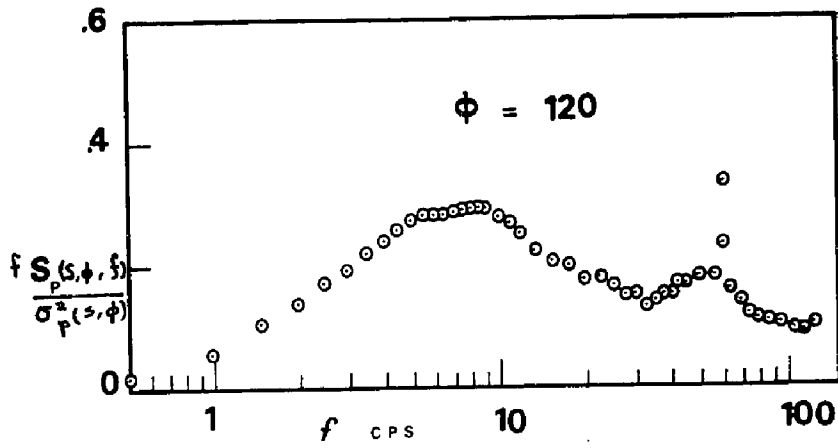


FIG. 5.43

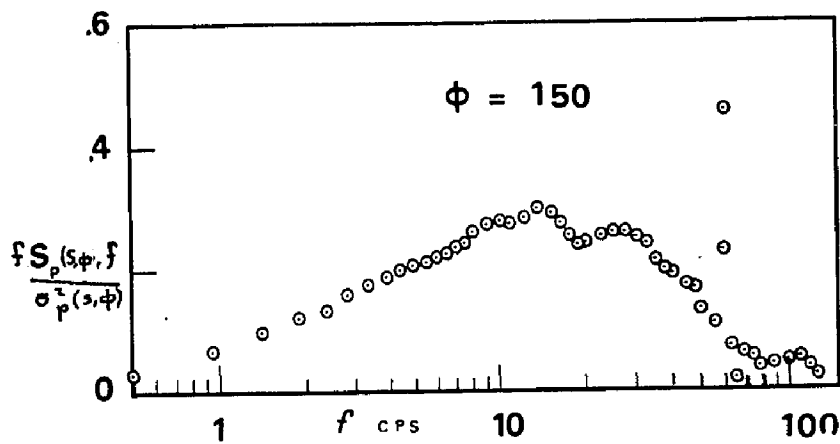


FIG. 5.44

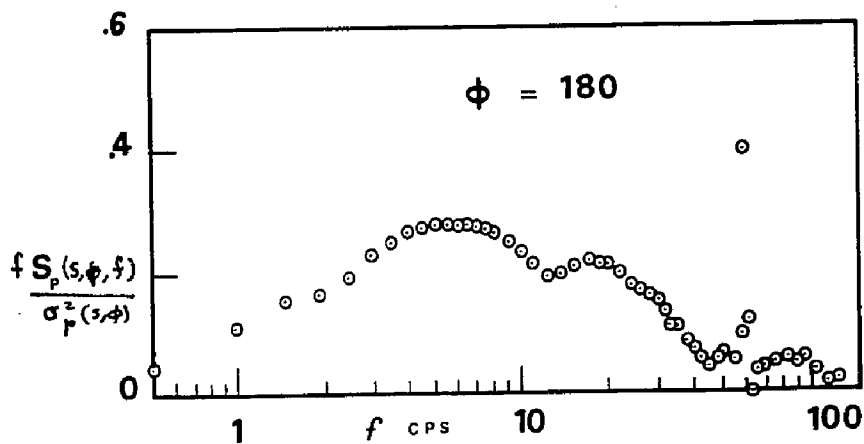


FIG. 5.45

spaced by 30° are plotted in Figs. (5.39 to 5.45) at the throat. The results are presented in a normalized form such that the area under each curve is unity.

By examining the results in Figs. (5.35 to 5.45), it is observed that $S_p(s, \phi, f)$ could be classified according to two distinct regions; a) windward region, and b) wake region. The boundaries between the two regions are defined by the separation point. Because of the unsteadiness of the wind pressure, this point exhibits some random variations and is somewhat ill-defined. However, for our purpose, it can be defined by its average value which is about $\pm 120^\circ$. The variation in this position is in the order of $\sigma_v/\bar{U} \approx 7^\circ$ (9).

The pressure spectra in the windward direction, especially along the frontal stagnation line, are somewhat similar to those of the turbulence spectra shown in Figs. (5.7 to 5.9). Most of the energy is contained in the same low frequency range. This range extends from $f = 0.5$ to 20 cps. For both the pressure and velocity, the contribution of the high frequency components is small and decreases as the frequency increases. Nevertheless, there are some noted differences. The intensities of the pressure fluctuations at moderate frequencies are higher than those of the velocity fluctuations. The opposite occurs at high frequencies. These differences become larger as the point of flow

separation is approached.

In order to explain these strong variations of the pressure spectra at different points across the shell surface, one has to examine the main sources of the wind pressure fluctuations.

For hyperbolic cooling towers in natural wind, the pressure fluctuations exerted on the shell are caused mainly by:

1. The turbulence in the incoming flow.
2. The distortion of the wind flow regime as it approaches the structure.
3. The unsteadiness of the flow in the wake region of the structure.

Another factor that could influence the nature of the pressure fluctuations arises from the movement of the tower in response to the wind action. However, this is found to be of minor significance owing to the great resistance of hyperbolic cooling towers to deformation.

The pressure fluctuations in the front face of the structure, especially in the vicinity of the frontal stagnation line, will be expected to derive most of their energy from the turbulence in the incoming flow. As such, they would be expected to display the basic characteristic features of the power spectra of the wind velocity. This becomes evident when comparing the

spectra of the pressure fluctuations at different points along the frontal stagnation line shown in Figs. (5.35 to 5.38) and the velocity spectra shown in Figs. (5.7 to 5.9). Therefore, it is possible to introduce a transfer function that would relate the spectra of the pressure fluctuations on the front face region of the structure to the wind velocity spectra. This transfer function, denoted by $X(s, \phi, f)$, is defined as follows:

$$X(s, \phi, f) = \frac{\sigma_u^2(Z)}{\sigma_p^2(s, \phi)} \frac{S_p(s, \phi, f)}{S_u(Z, f)} \quad (5.14)$$

Results for $X(s, \phi, f)$, computed at various points along the frontal stagnation line are shown in Fig. 5.46. At low frequencies ($f \leq 1.5$ cps), there exists a direct linear relationship between the pressure fluctuations and the turbulence in the incoming flow. The pressure spectra in this frequency range could be predicted on the basis of quasi-steady theory, i.e.:

$$\frac{S_p(s, \phi, f)}{\sigma_p^2(s, \phi)} = \frac{S_u(Z, f)}{\sigma_u^2(Z)} \quad (5.15)$$

Measurements of the pressure fluctuations on a long prism of rectangular cross-section (2 in. \times $\frac{7}{8}$ in.) in uniform turbulent flow, by Kao (10), have shown similar characteristics. His results for the cross-spectra of turbulence in the incoming flow and the pressure fluctuations, shown in Fig. 5.47, clearly indicate the linear relationship

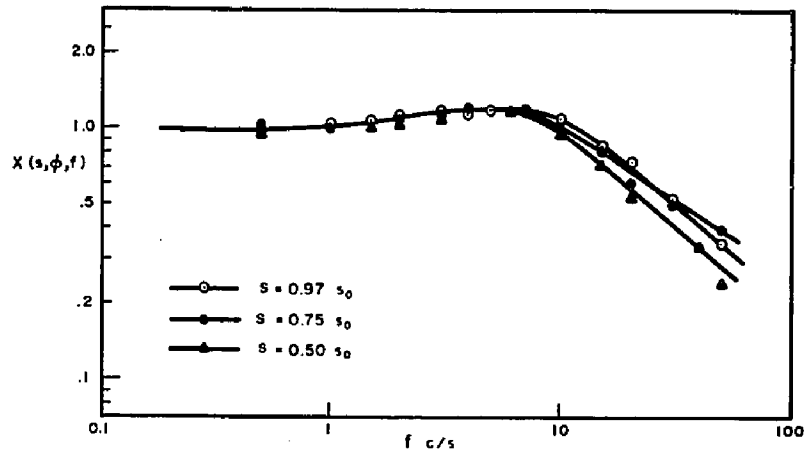


FIG. 5.46 VALUES OF THE TRANSFER FUNCTION $X(s, \phi, f)$ AT DIFFERENT POINTS ALONG THE UPSTREAM STAGNATION LINE

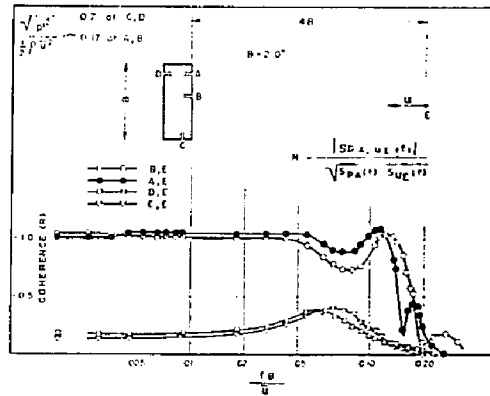


FIG. 5.47 PRESSURE / VELOCITY COHERENCE (AFTER KAO)

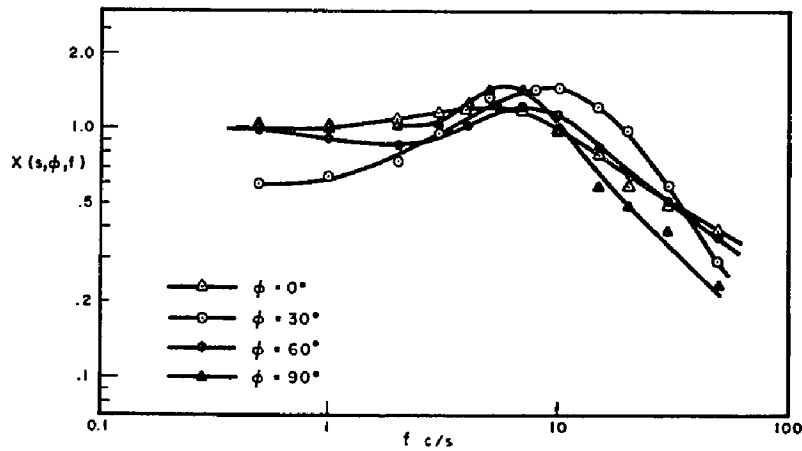


FIG. 5.48 VALUES OF THE TRANSFER FUNCTION $X(s, \phi, f)$ AT DIFFERENT POINTS AROUND THE SHELL CIRCUMFERENCE AT THROAT

between the velocity and pressure fluctuations at low frequencies.

At higher frequencies, in the range $f \approx 1.5$ to 10 cps, the intensities of the frequency components of pressure fluctuations are somewhat larger than those for the velocity fluctuations. This difference arises from the interaction between the tower and the incoming flow. In this frequency range, the following sources, in addition to the turbulence in the unobstructed flow, could possibly contribute to the pressure fluctuations,

1. distortion of turbulence characteristics as the streamlines diverge past the tower (11,12),
2. accelerative forces in the flow (13,14), and,
3. vortex shedding in the wake of the tower (14).

In the present measurements, however, the vortices shed in the wake of the cooling tower were found to be spread out over a broad range* of frequencies, weak and disorganized, as shown in Figs. 5.43 to 5.45. Therefore, it is unlikely that they could influence the pressure fluctuations on the windward face of the structure significantly.

At higher frequencies, the correlation between the pressure fluctuations and turbulence in the incoming flow drops rapidly (see Fig. 5.47). The pressure fluctuations become strongly dependent on the local conditions at the shell surface. In this frequency range, the pressure

*The peaks shown in Figs. 5.43 to 5.45 at $f = 60$ cps are due to the frequency of the power supply.

fluctuations on the cooling tower model attenuate more rapidly than the velocity fluctuations. It is found that,

$$S_u \propto f^{-5/3} \quad (5.16)$$

$$S_p \propto f^{-2} \quad (5.17)$$

for $f \geq 15$ cps.

The transfer function $X(s, \phi, f)$ was also obtained at different locations around the shell circumference in the windward region. The computed results for $\phi = 30, 60,$ and 90° at the throat are depicted in Fig. 5.48. They appear to display the basic characteristics described above for $X(s, \phi, f)$ along the frontal stagnation line.

5.5.4 Cross-Correlations and Cross-Spectra

It is necessary to define the cross-correlations and cross-spectra of the pressure fluctuations in order to determine the dynamic response of cooling towers to wind. This is so, because the wind pressure fluctuations are both space and time-dependent. The pressure fluctuations acting at two different points on the shell surface will experience some loss of correlation dependent on the actual position of the two points and the separation between them.

The cross-spectral density $S_p(s, \phi, s', \phi', f)$ is, in general, a complex quantity. That is,

$$S_p(s, \phi, s', \phi', f) = G(s, \phi, s', \phi', f) + iQ(s, \phi, s', \phi', f) \quad (5.18)$$

in which $i = \sqrt{-1}$.

The real part, $G(s, \phi, s', \phi', f)$ is generally referred to as the co-spectrum, while the imaginary part, $Q(s, \phi, s', \phi', f)$, is referred to as the quadrature spectrum. It should be noted that,

$$G(s, \phi, s', \phi', f) = G(s', \phi', s, \phi, f) \quad (5.19)$$

$$Q(s, \phi, s', \phi', f) = -Q(s', \phi', s, \phi, f) \quad (5.20)$$

Both components are related to the cross-correlation functions by,

$$G(s, \phi, s', \phi', f) = 2 \int_0^{\infty} \{R_p(s, \phi, s', \phi', \tau) + R_p(s', \phi', s, \phi, \tau)\} \cos 2\pi f \tau d\tau \quad (5.21)$$

$$Q(s, \phi, s', \phi', f) = 2 \int_0^{\infty} \{R_p(s, \phi, s', \phi', \tau) - R_p(s', \phi', s, \phi, \tau)\} \sin 2\pi f \tau d\tau \quad (5.22)$$

in which the cross-correlation functions are defined by,

$$R_p(s, \phi, s', \phi', \tau) = \overline{p(s, \phi, t)p(s', \phi', t+\tau)} \quad (5.23)$$

$$R_p(s', \phi', s, \phi, \tau) = \overline{p(s', \phi', t)p(s, \phi, t+\tau)} \quad (5.24)$$

Direct measurements of the cross-correlation functions were made from the model tests. The two components of the cross-spectra were then obtained using equations (5.21 and 5.22).

Results for the cross-correlations and cross-spectral density functions are presented herein for a model without vents at base in a turbulent boundary layer flow. For brevity, no attempt has been made to reproduce all the results obtained. Selected results displaying the basic characteristics of these functions are shown. Results for model with vents at base are not shown here since they did not show any marked differences from those for model without vents.

Figs. (5.49 to 5.58) show the cross-correlation functions of the pressure fluctuations at various points along the frontal stagnation line and around the shell circumference at the throat. The ordinates of these functions at zero time-delay ($\tau=0$), give the values of the correlation coefficients described in Section 5.5.2. For separations along the frontal stagnation line, the loss of correlation increases as the separation and/or time-delay increases. The maximum correlation is attained

CROSS-CORRELATIONS OF PRESSURES ALONG THE UPSTREAM STAGNATION LINE

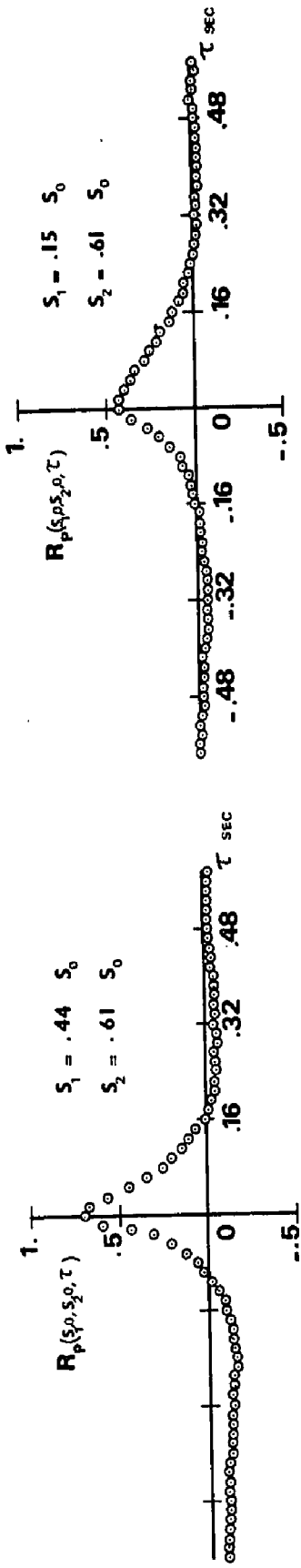


FIG. 549

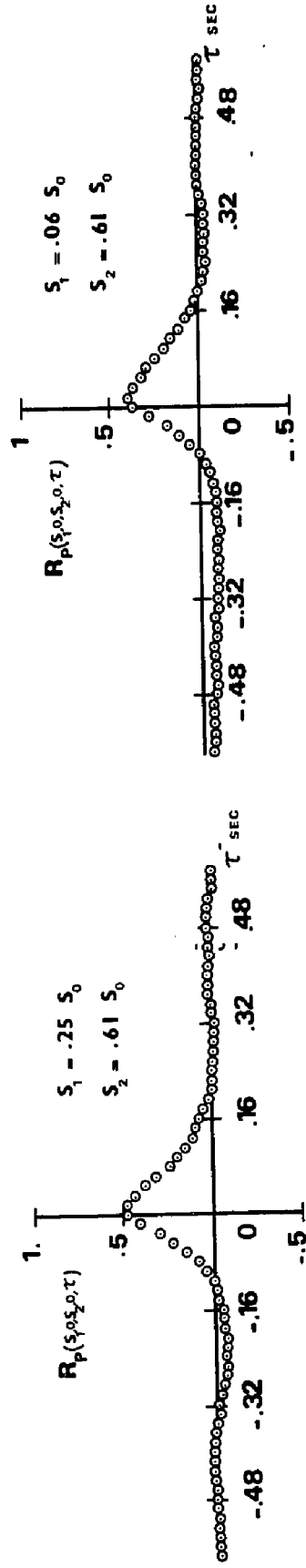


FIG. 550

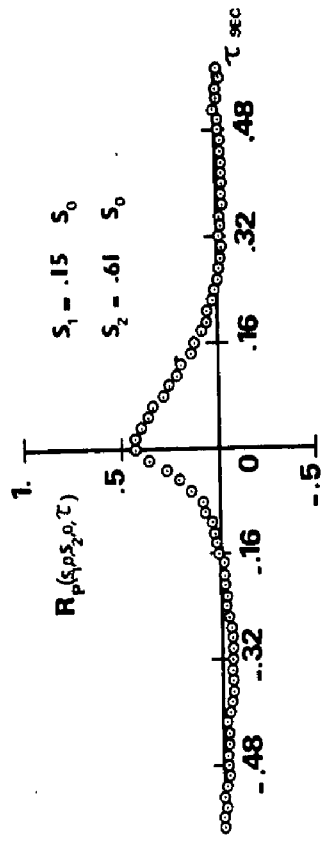


FIG. 551

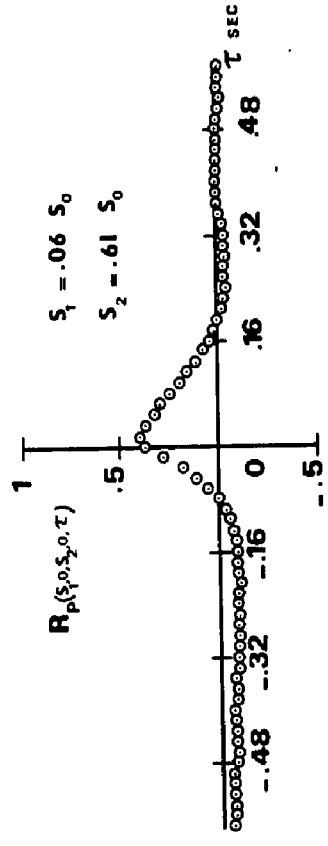


FIG. 552

CROSS CORRELATIONS OF PRESSURES AROUND THE SHELL CIRCUMFERENCE AT THROAT

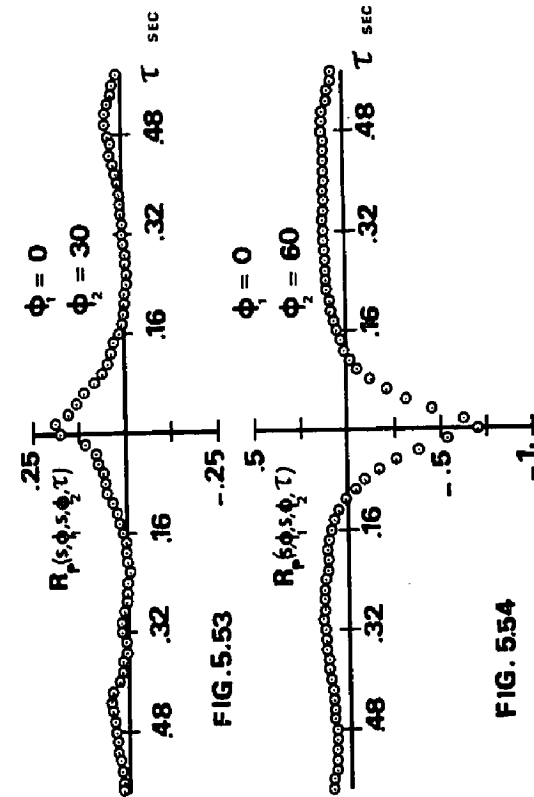


FIG. 5.54

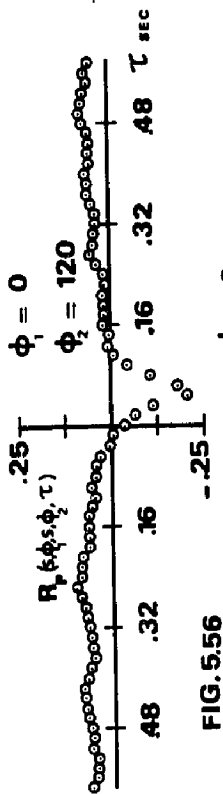
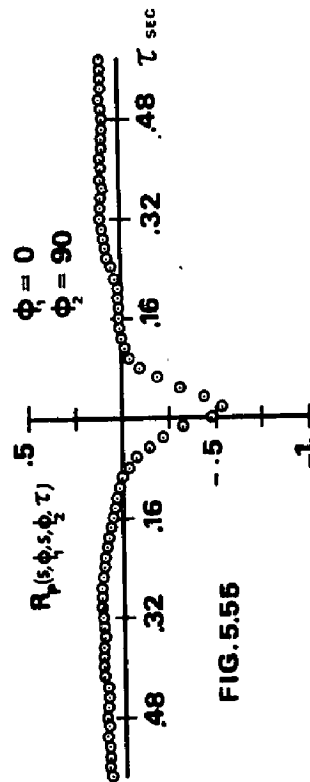


FIG. 5.57

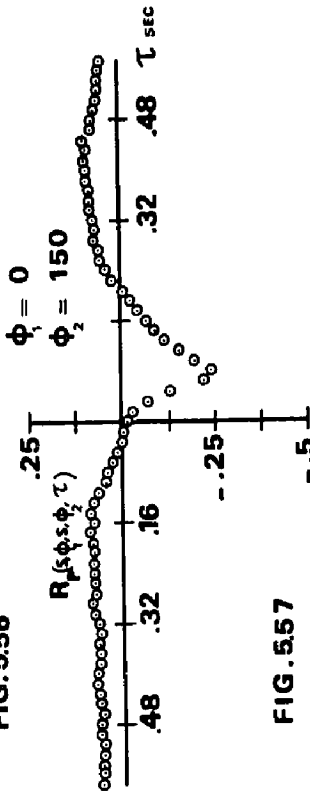


FIG. 5.58

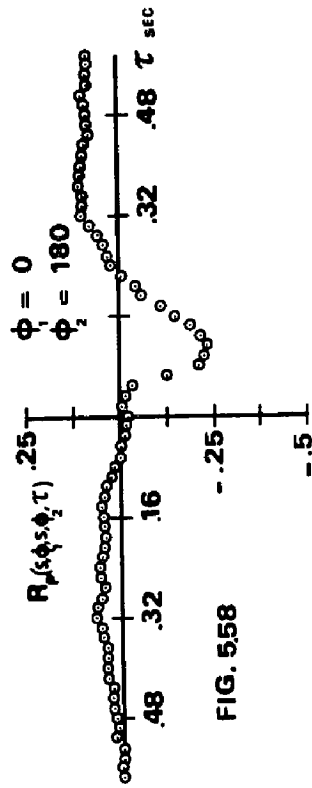
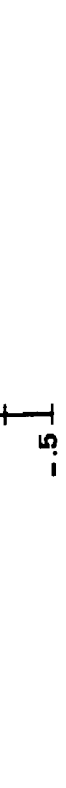


FIG. 5.55



after some time-delay which increases as separation increases.

The results emphasize the conclusions made earlier regarding the lack of any effective correlation between the pressure fluctuations acting on the windward face of the model and those in the wake region.

Both components of the cross-spectra, $G(s, \phi, s', \phi', f)$ and $Q(s, \phi, s', \phi', f)$ obtained for different separations along the frontal stagnation line are shown in Figs. (5.59 to 5.62). The insignificance of the quadrature spectra, $Q(s, \phi, s', \phi', f)$ could be observed even for large separations. This suggests that the pressure fluctuations along the upstream stagnation line are acting largely in-phase. Therefore, it seems justifiable to disregard the quadrature part of the cross-spectra in the analytical prediction of the shell response. On the other hand, the pressure fluctuations acting in-phase are strongly correlated for small separations. The co-spectral densities seem to be fairly comparable to the pressure spectra at low frequencies and display, more or less, the same basic features. However, they attenuate more rapidly at high frequencies. The loss of correlation increases as either the frequency or separation increases. While the dependence of co-spectra on separation is very important, its dependence on the actual location of the two points, while existing, is fairly small.

CROSS SPECTRA OF PRESSURES ALONG THE UPSTREAM STAGNATION LINE $S_p(\xi_1, \xi_2, \rho, f)$

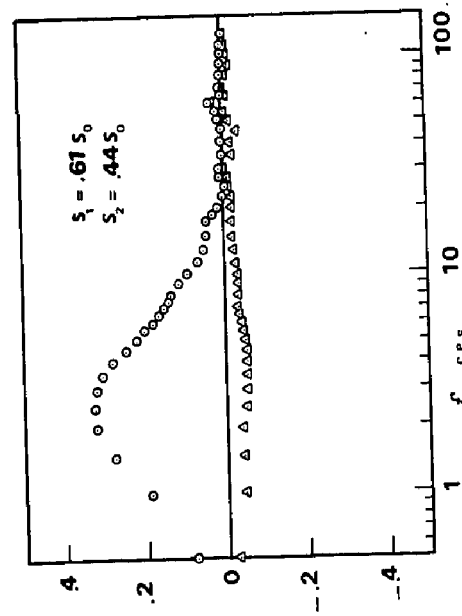


FIG. 5.59

○ CO-SPECTRUM
 ▲ QUADRATURE SPECTRUM

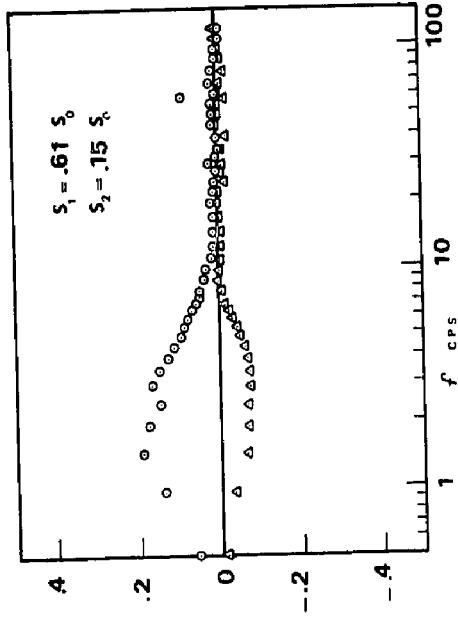


FIG. 5.61

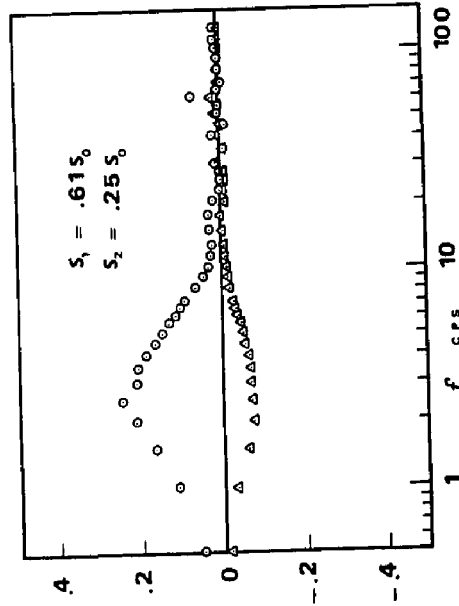


FIG. 5.60

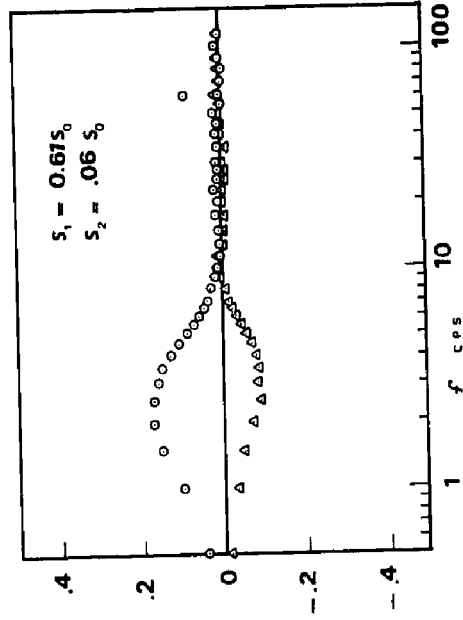


FIG. 5.62

Results for the cross-spectra obtained for various separations around the shell circumference at the throat are shown in Figs. (5.63 to 5.68). Separations were measured from the frontal stagnation point. For separations within the frontal zone (Fig. 5.63), the quadrature spectra are very small in the low frequency range. At high frequencies, they become slightly important. Their effect on the response, however, will be largely offset by the concentration of the energy of the pressure fluctuations in the low frequency range. In this zone, the correlation between the pressure fluctuations, acting in-phase, decreases as separation and/or frequency increases. For separations extending to the side zone, the quadrature spectrum, while increasing in intensity at high frequencies as the separation increases remains comparatively small. The co-spectral densities, however, are by far more important and indicate strong negative correlation between the pressure fluctuations in the front and side zones over a broad range of frequencies. That is, when the pressure fluctuations in the front zone are acting inward, those in the side zone will be acting outwards and vice versa.

For separations extending to the wake region, both components of the cross-spectra become of the same order, but with fairly small intensities. The refinement that could be gained from their inclusion in the prediction of the shell response, while desirable, will be largely outweighed by the

CROSS SPECTRA OF PRESSURES AROUND SHELL CIRCUMFERENCE AT THROAT $S_p(s, \phi_1, s, \phi_2, f)$

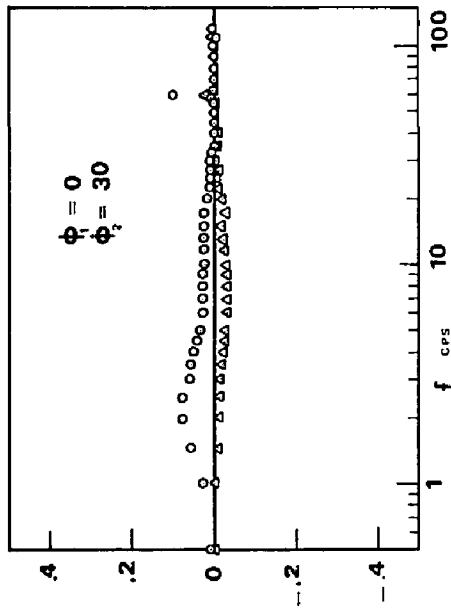


FIG. 5.63

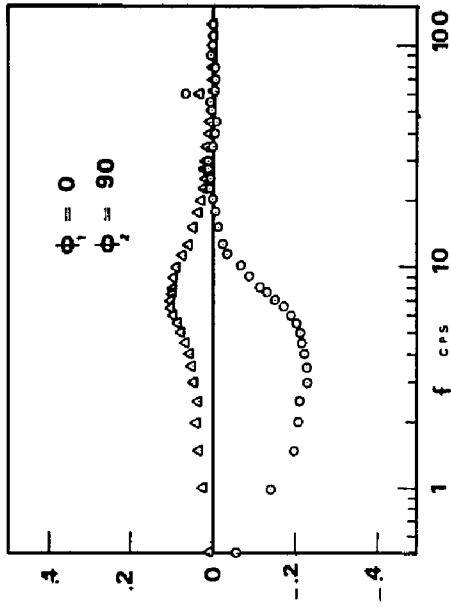


FIG. 5.65

o CO-SPECTRA
Δ QUADRATURE SPECTRA

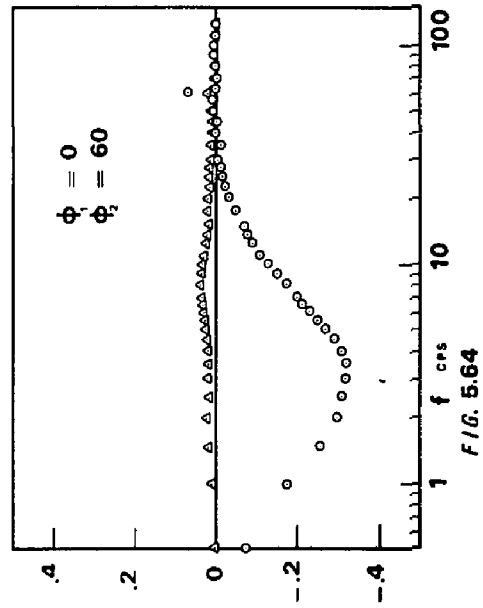


FIG. 5.64

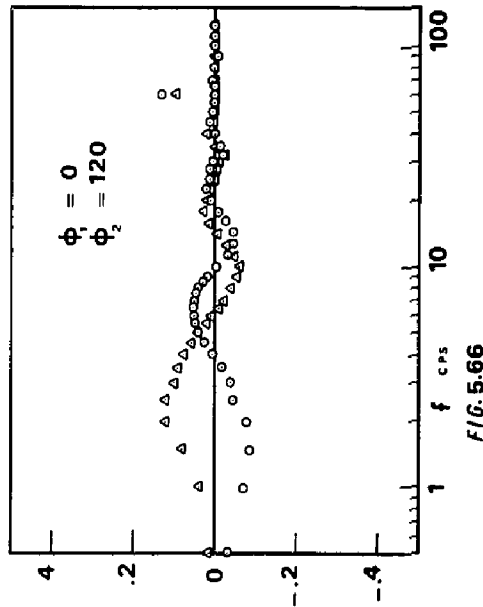


FIG. 5.66

CROSS SPECTRA OF PRESSURES AROUND SHELL CIRCUMFERENCE AT THROAT $S_p(s, \phi_1, s, \phi_2, f)$

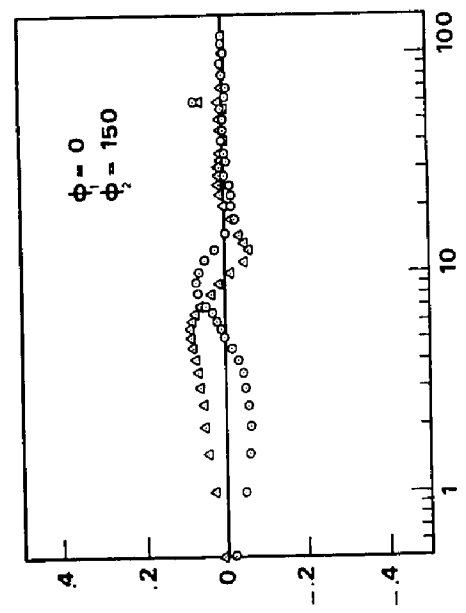


FIG. 5.67

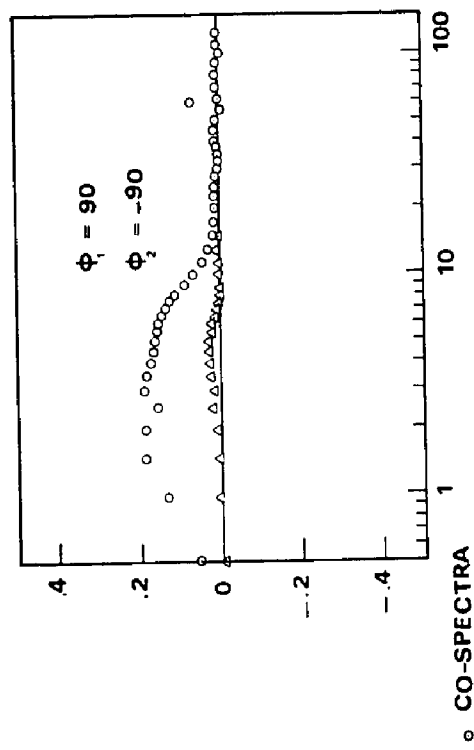


FIG. 5.69

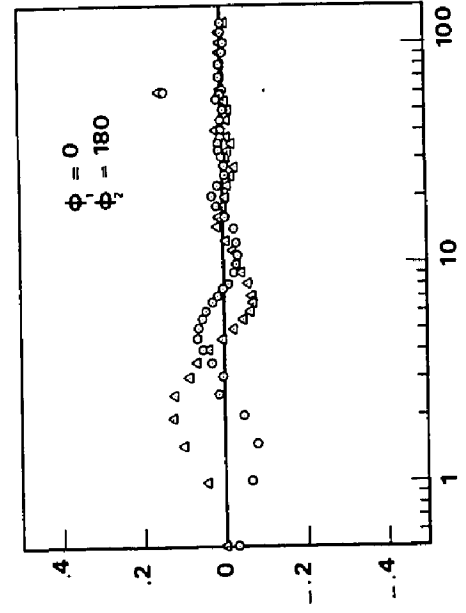


FIG. 5.68

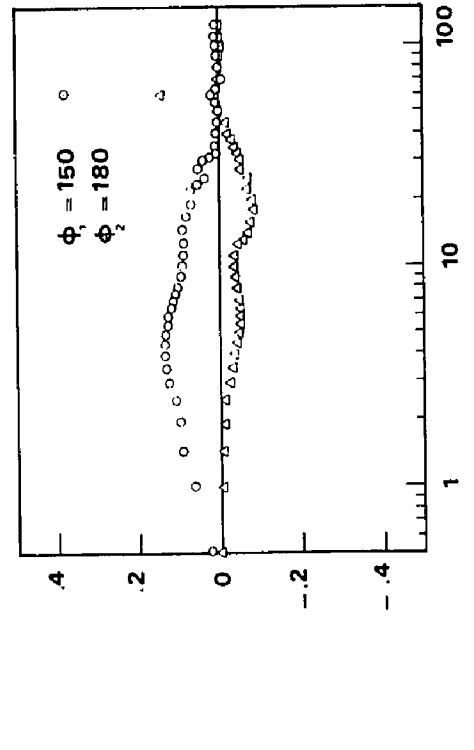


FIG. 5.70

○ CO-SPECTRA
 △ QUADRATURE SPECTRA

added complexity of analysis and the errors in the experimental measurements.

The preceding discussion has so far indicated the strong dependence of the cross-spectra between two different points around the shell on the angular separation. Also, the real and imaginary parts of the cross-spectra are strongly dependent on the actual location of the two points around the shell circumference. Fig. (5.69) shows the co-spectrum between pressures at $\phi = +90^\circ$ and $\phi' = -90^\circ$. If these results are compared with the cross-spectrum at $\phi = 0$ and $\phi' = 180^\circ$, which are separated by the same angle, it becomes clearly evident that the actual location of the two points around the shell is as important as the separation between them. This is also the case even for small separations, and can easily be detected by comparing results in Figs. (5.63 and 5.70).

The components of the cross-spectrum of the pressure between the two opposite sides of the shell ($\phi = 90^\circ$ and $\phi = -90^\circ$) shown in Fig. 5.69, show some interesting results. Although the two points are separated by half the circumference, the quadrature spectrum is almost zero at all frequencies. Thus indicating that, by and large, the pressure fluctuations at the two points are acting in-phase.

An attempt was made to represent the present results for the co-spectra in a compact and simple form that could

be easily incorporated in the theoretical analysis, with a minimum loss of accuracy. In doing this, the following assumptions were introduced.

1. For vertical separations along the shell, the co-spectrum is primarily dependent on separation and frequency only. Dependence on the actual location of points could be neglected. The same can be assumed for horizontal separations in the wake region.
2. The correlation between the pressure fluctuations in the windward and wake zones could be ignored at all frequencies.
3. The co-spectrum for vertical separation is independent of circumferential location.
4. The co-spectrum for circumferential separation is invariant with height above ground.

Therefore, it is possible to represent the co-spectra of the pressure fluctuations in the windward and wake regions by:

1. Windward region

$$G(s, \phi, s', \phi', f) = R_v(s, s', f) R_f(\phi, \phi', f) \sqrt{S_p(s, \phi, f) S_p(s', \phi', f)}$$

(5.25)

2. Wake region

$$G(s, \phi, s', \phi', f) = R_y(s, s', f) R_p(\phi, \phi', f) \sqrt{S_p(s, \phi, f) S_p(s', \phi', f)} \quad (5.26)$$

in which $R_y(s, s', f)$ and $R_p(\phi, \phi', f)$ are independent of the actual position of the points considered.

Some selected results for $R_y(s, s', f)$ are shown in Fig. 5.71. It is seen that its general characteristics are similar to those of the equivalent function for line-like structures (chimneys, tall buildings, etc.) described by Davenport (5), Vickery and Kao (14), and Harris (6). The given results for $R_y(s, s', f)$ could be adequately represented by,

$$R_y(s, s', f) = e^{-\beta_1 \tilde{f}_1} \quad (5.27)$$

in which $\tilde{f}_1 = \frac{f \Delta s}{U}$ and $\Delta s = |s - s'|$.

A similar expression was also derived to fit the results for $R_p(\phi, \phi', f)$ given in Fig. 5.72. It is:

$$R_p(\phi, \phi', f) = e^{-\beta_2 \tilde{f}_2} \quad (5.28)$$

in which $\tilde{f}_2 = \frac{f r \Delta \phi}{U}$ and $\Delta \phi = |\phi - \phi'|$.

The expression for $R_f(\phi, \phi', f)$ was not as straightforward owing to its dependence on the actual position of ϕ and ϕ' as well as $\Delta\phi$ and f . It was possible, however, to isolate the dependence of $R_f(\phi, \phi', f)$ on position by introducing the following relation:

$$R_f(\phi, \phi', f) = C_f(\phi, \phi') \tilde{R}_f(\Delta\phi, f) \quad (5.29)$$

in which, $C_f(\phi, \phi')$ is the correlation coefficient of the pressure fluctuations described in Section 5.5.2, and $\tilde{R}_f(\Delta\phi, f)$ is a shape function independent of the position of ϕ and ϕ' .

Some representative results of $\tilde{R}_f(\Delta\phi, f)$ are given in Fig. 5.73. They could be adequately represented by,

$$\tilde{R}_f(\phi, \phi', f) = e^{-\beta_3 \tilde{f}_2^2} \quad (5.30)$$

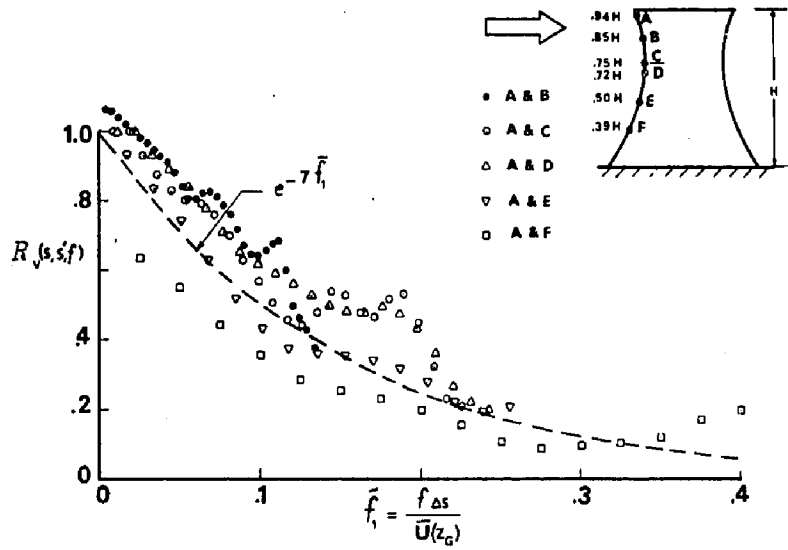


FIG. 5.71 NORMALIZED CO-SPECTRUM $R_v(s,s,f)$ AT $\phi = 0$

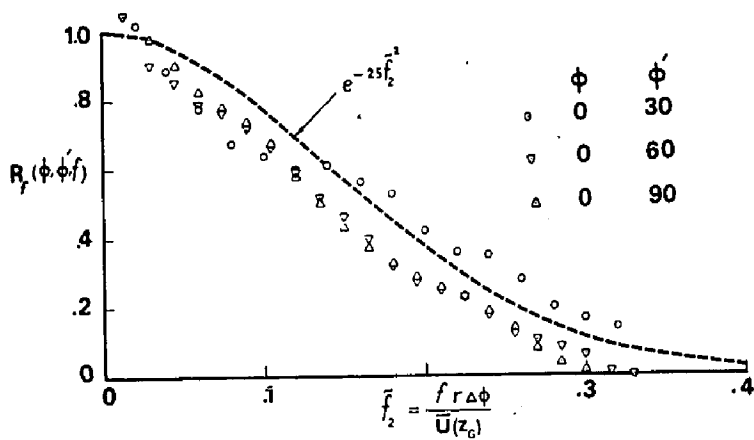


FIG. 5.72 NORMALIZED CO SPECTRUM $R_f(\phi, \phi', f)$ AT THROAT

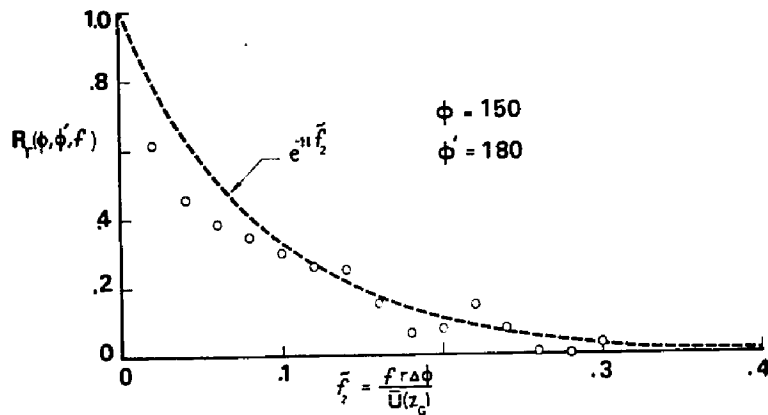


FIG. 5.73 NORMALIZED CO-SPECTRUM $R_f(\phi, \phi', f)$ AT THROAT

CHAPTER 6

EXPERIMENTAL INVESTIGATION OF RESPONSE

6.1 Introduction

The aim of these experiments is to define the basic characteristics of the response of cooling towers to turbulent wind flow. They could also provide a useful tool to assess, wherever possible, the reliability of the basic assumptions in the analytical approach to the prediction of the shell response to wind.

Earlier experiments on the dynamic response of a cooling tower model in a turbulent flow regime has been reported by Davenport and Isyumov (1). Their measurements show that the peak dynamic response, at positions where meridional stresses are maximum, is about 80% of the mean response. It was also found (2) that the resonant response is very small compared to the quasi-static response and makes for about 5% only of the total dynamic response in the front face of the model.

Wind tunnel tests on the dynamic response of a Ferrybridge cooling tower model were reported recently by Armitt (3). His measurements indicate that the

resonant response of the Ferrybridge towers is of the same order as the quasi-static and becomes predominant at high wind speeds. In contrasting this result with those of Refs. (1,2), it should be noted that the Ferrybridge towers has a cone-toroid profile while the model employed in the experiments of Refs. (1,2) has a hyperbolic profile. This difference in profile has a considerable impact on the shell stiffness (4,5). The lowest natural frequency of the Ferrybridge towers is about half of that of the corresponding hyperboloid (4). This makes them more susceptible to dynamic excitation. The two case studies further underline the need for a comprehensive study of the dynamic response of cooling towers to wind.

The present experiments were carried out in the Boundary Layer Wind Tunnel Laboratory of The University of Western Ontario. The model used in the tests is geometrically similar to that used in Ref. (1), but with a reduced scale of 1/400; in accordance with the scales of the simulated flow (6).

The turbulence in the boundary layer flow was generated naturally by roughening the tunnel floor with randomly placed blocks of heights ranging from 1 in. to 4 in. The generated flow simulates an atmospheric boundary layer flow over a moderately rough terrain.

The response of the model could be conveniently separated into a mean and a fluctuating component.

Measurements of the mean component and the standard deviation and power spectra of the fluctuating component were carried out at various locations on the shell surface.

As already noted, the instantaneous response of the shell $y(s, \phi, t)$ at position (s, ϕ) could be conveniently represented in terms of the natural modes of vibration $y_{m,i}(s)$ as follows:

$$y(s, \phi, t) = \sum_m \sum_i \{q_{m,i}(t) \cos m\phi + q'_{m,i}(t) \sin m\phi\} y_{m,i}(s) \quad (6.1)$$

in which, $q_{m,i}(t)$ and $q'_{m,i}(t)$ are the generalized time dependent coordinates of the i th mode of harmonic m . This representation requires the definition of the vibration characteristics of the shell. These were obtained experimentally and theoretically. The results are presented in Section 6.4. Decomposition of the total response into its modal components was then achieved experimentally by utilizing the special properties of mode shapes of cooling towers as described in Section 6.3. Time records of the generalized coordinates, $q_{m,i}(t)$ and $q'_{m,i}(t)$ were thus obtained and analysed to determine their mean component and the statistical properties of their fluctuating component.

The symmetric and anti-symmetric components of the generalized forces, $p_{m,i}(t)$ and $p'_{m,i}(t)$, experienced by

each mode were then obtained from the experimental results of $q_{m,i}(t)$ and $q'_{m,i}(t)$. This helps in,

1. establishing a qualitative understanding of the wind loads experienced by different modes of vibration, and
2. investigating the influence of various shell properties on the response due to wind.

The experiments were carried out at a Reynolds number of about 10^5 which is about three orders of magnitude less than that for full scale towers at design wind speeds. Therefore, interpretation of the results given herein to full scale behaviour should be approached with caution.

6.2 Aeroelastic Model

6.2.1 Principles of Aeroelastic Modelling

The general principles of aeroelastic modelling for structures in natural wind have been discussed by Whitebread (7), Scruton (8), and many others (9,10). The basic requirement that has to be considered in the design of cooling tower models have been outlined by Davenport and Isyumov (1).

The laws of similitude require that the model be geometrically similar to the prototype structure and that the wind flow properties be representative of natural

wind conditions (11). Other similarity requirements could be derived from the equations of motion or simply from dimensional analysis. Using the latter approach, Whitbread (7) has shown that for correct aeroelastic scaling, the following non-dimensional parameters have to be the same for both model and prototype structures:

1. Inertia forces of air/viscous forces of air;
Reynolds number $R_e = \frac{Ud}{\nu}$.
2. Elastic forces of the structure/inertia forces of air; $\frac{\rho U^2}{E}$.
3. Inertia forces of the structure/inertia forces of air; ρ_s/ρ .
4. Critical damping ratio; η_{cr} .
5. Gravitational forces on the structure/inertia forces of air; $\frac{gd}{U^2}$.

where, ρ_s = density of structural material, ρ = air density, E = Young's modulus, d = typical tower dimension taken as throat diameter, and g = gravitational acceleration.

For cooling towers, the influence of gravitational forces on wind stresses is insignificant (1). Results of Ref. (12) indicate that gravitational effects on the natural frequencies of towers up to 500 to 600 ft. high could be neglected. Therefore, condition number 5 can

be relaxed. Conditions 2 to 4 could be adequately satisfied with a suitable choice of model material, such that its density and damping ratios are equivalent to those of reinforced concrete but with a considerably reduced Young's modulus ($E_m = E_p \times \frac{u_m^2}{u_p^2}$, subscripts m, p refer to model and prototype respectively).

Reynolds number has considerable influence on the wind induced stresses in cooling towers. However, the equivalence of Reynolds number cannot be easily achieved in reduced-scale model tests. The use of surface roughness at low R_e , to produce flow conditions similar to those at high R_e , is not yet conclusive, although some results indicate that this can be done (1,13). Even if mean pressure profile can be simulated by roughening the surface, the characteristics of the fluctuating component may be changed as a result.

6.2.2 Model Geometry and Material Properties

A 1:400 aeroelastic model of the 375 ft. high cooling tower built at the Muskingum River power station is used in the present experiments. The model geometric scale was selected in accordance with the available wind tunnel facility (6). A vertical cross section of the model is shown in Fig. 5.1. It has a constant wall thickness of 0.015 in. and its geometry is defined by:
 a - total height = 11.1 in., b - height above throat =

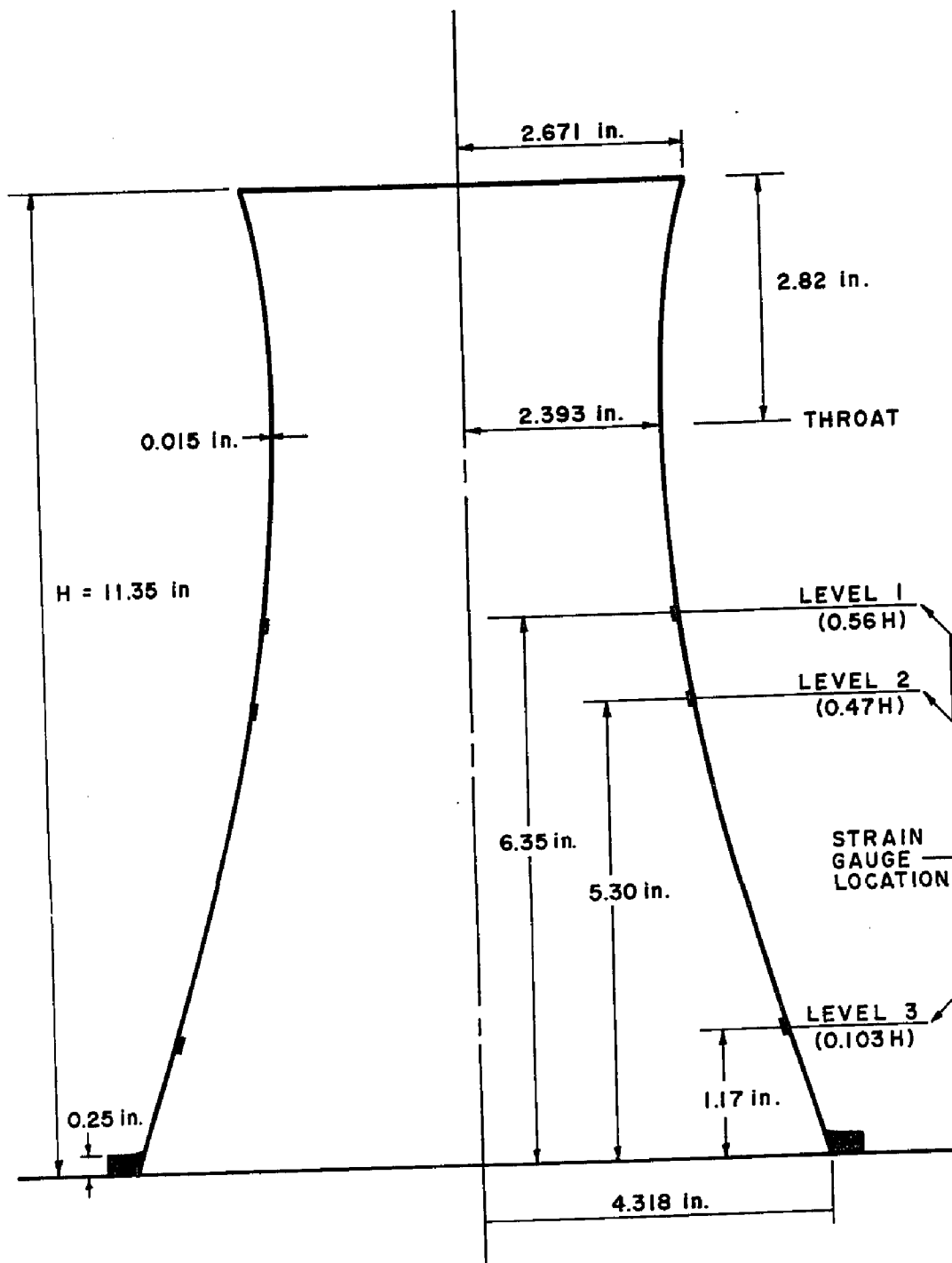


FIG. 6.1 1:400 COOLING TOWER MODEL

2.82 in., c - throat radius $a = 2.393$ in., and d - meridional curvature parameter, $k_o = a/b = 0.422$.

The model is made from Devcon A. A brief description of this material, model construction and the test specimens used to determine the material properties are given in Appendix III. The basic physical properties of the model material are: a - Young's modulus $E = 0.507 \times 10^6$ psi, material density = 127 lb./ft.^3 , and Poisson's ratio = 0.30. The total damping of the model (mechanical and aerodynamic) was found to be in the order of 1% (values given in Section 6.7.2).

6.3 Separation of Modes

The total response of cooling towers to random loads could be conveniently considered as the summation of the individual contributions of an infinite number of modes of vibration as described by equation (6.1). The following procedure for separation of modal components experimentally utilizes the special properties of the mode shapes of vibration.

Consider Fig. 6.2a in which points a and b lie on the diagonal along the mean wind direction and points c and d on the diagonal perpendicular to it. Then, from equation (6.1) it could be easily shown that at $\phi_o = 0$,

$$(y_a + y_b) = (y_c + y_d) = 4 \sum_{m=2,6,\dots} \sum_{i=1,2} q_{m,i}(t) y_{m,i}(s) \quad (6.2)$$

in which y_a , y_b , y_c and y_d represent the total response at points a , b , c , and d respectively.

It is readily seen that in performing the above operation, all the anti-symmetric components of the shell response have been completely eliminated. Also, out of all the symmetric components, modes with harmonic wave number $m = 2, 6, 10, \dots$ only, contribute to the summation while the rest have been eliminated.

If modes with harmonic wave number $m \geq 10$ are neglected, and considering only the fundamental modes, then equation (6.2) reduces to the following simple form,

$$(y_a + y_b) - (y_c + y_d) = 4q_{2,1}(t)y_{2,1}(s) + 4q_{6,1}(t)y_{6,1}(s) \quad (6.3)$$

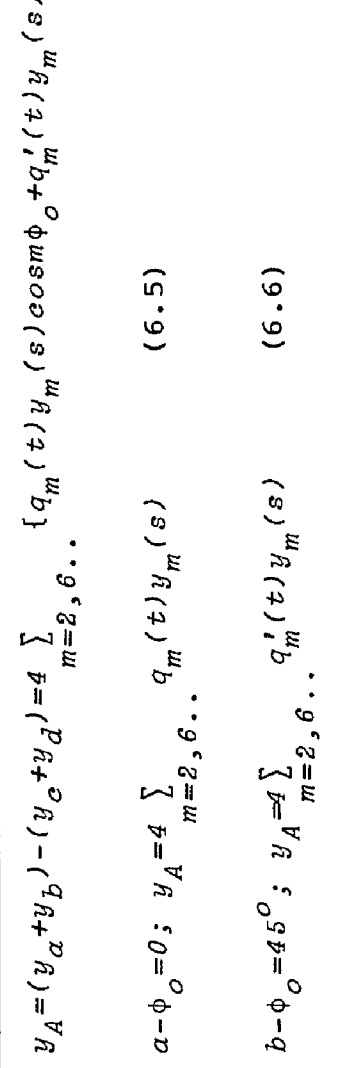
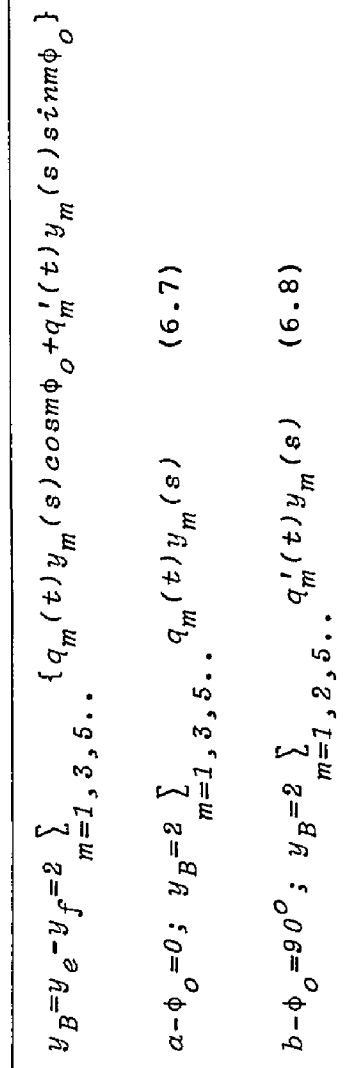
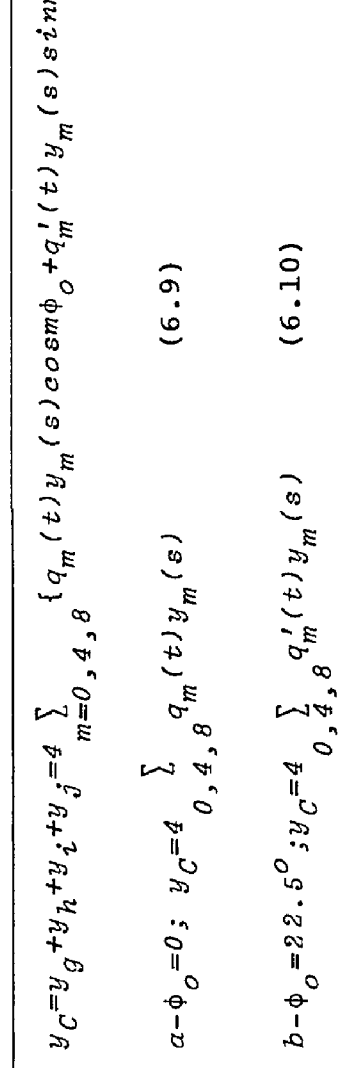
It could be further reduced to,

$$(y_a + y_b) - (y_c + y_d) = 4q_{2,1}(t)y_{2,1}(s) \quad (6.4)$$

if the response measurements are made at the level where the fundamental mode of $m = 6$ has a nodal circle, Fig. 6.4. Hence, the time record of $q_{2,1}(t)$ could be readily obtained.

Along these lines, similar expressions for single modes or for combinations of a limited number of modes could be obtained for other symmetric and anti-symmetric

TABLE 6.1

$y_A = (y_a + y_b) - (y_c + y_d) = 4 \sum_{m=2, 6, \dots} \{ q_m(t) y_m(s) \cos m \phi_0 + q'_m(t) y'_m(s) \sin m \phi_0 \}$ $a - \phi_0 = 0; y_A = 4 \sum_{m=2, 6, \dots} q_m(t) y_m(s) \quad (6.5)$ $b - \phi_0 = 45^\circ; y_A = 4 \sum_{m=2, 6, \dots} q'_m(t) y'_m(s) \quad (6.6)$	 <p style="text-align: center;">Fig. 6.2a Circuit A</p>
$y_B = y_e - y_f = 2 \sum_{m=1, 3, 5, \dots} \{ q_m(t) y_m(s) \cos m \phi_0 + q'_m(t) y'_m(s) \sin m \phi_0 \}$ $a - \phi_0 = 0; y_B = 2 \sum_{m=1, 3, 5, \dots} q_m(t) y_m(s) \quad (6.7)$ $b - \phi_0 = 90^\circ; y_B = 2 \sum_{m=1, 2, 5, \dots} q'_m(t) y'_m(s) \quad (6.8)$	 <p style="text-align: center;">Fig. 6.2b Circuit B</p>
$y_C = y_g + y_h + y_i + y_j = 4 \sum_{m=0, 4, 8} \{ q_m(t) y_m(s) \cos m \phi_0 + q'_m(t) y'_m(s) \sin m \phi_0 \}$ $a - \phi_0 = 0; y_C = 4 \sum_{m=0, 4, 8} q_m(t) y_m(s) \quad (6.9)$ $b - \phi_0 = 22.5^\circ; y_C = 4 \sum_{m=0, 4, 8} q'_m(t) y'_m(s) \quad (6.10)$	 <p style="text-align: center;">Fig. 6.2c Circuit C</p>

components. Arrangements of these and the relevant expressions are summarized in Table 6.1. On this basis, the stations for measuring the response were conveniently located at three different levels. The arrangements of the strain gauges at these levels are shown in Fig. 6.1.

6.4 Model Vibration Characteristics

The vibration characteristics of the cooling tower model could be obtained either theoretically or experimentally.

Using the modified finite difference method described in Chapter 2, the natural frequencies and mode shapes of the shell were obtained for various harmonics. In the analysis, the model was assumed to be fixed at base. This seemed reasonable, since the model was clamped firmly to a massive table during the experimental measurements. Deviations from absolute fixity were therefore minimized and are expected to be of minor significance.

Fig. 6.3 shows the mode shapes of the normal displacement w for harmonics $m = 0$ to 8 . Modal configurations for the strain components in the meridional and circumferential directions were obtained from the computed mode shapes of the displacement components (u , v and w) by means of the strain displacement relations given in Appendix I. Figs. (6.4 and 6.5) show the modal strains on the inside surface of the shell for harmonics $m = 0$ to 8 .

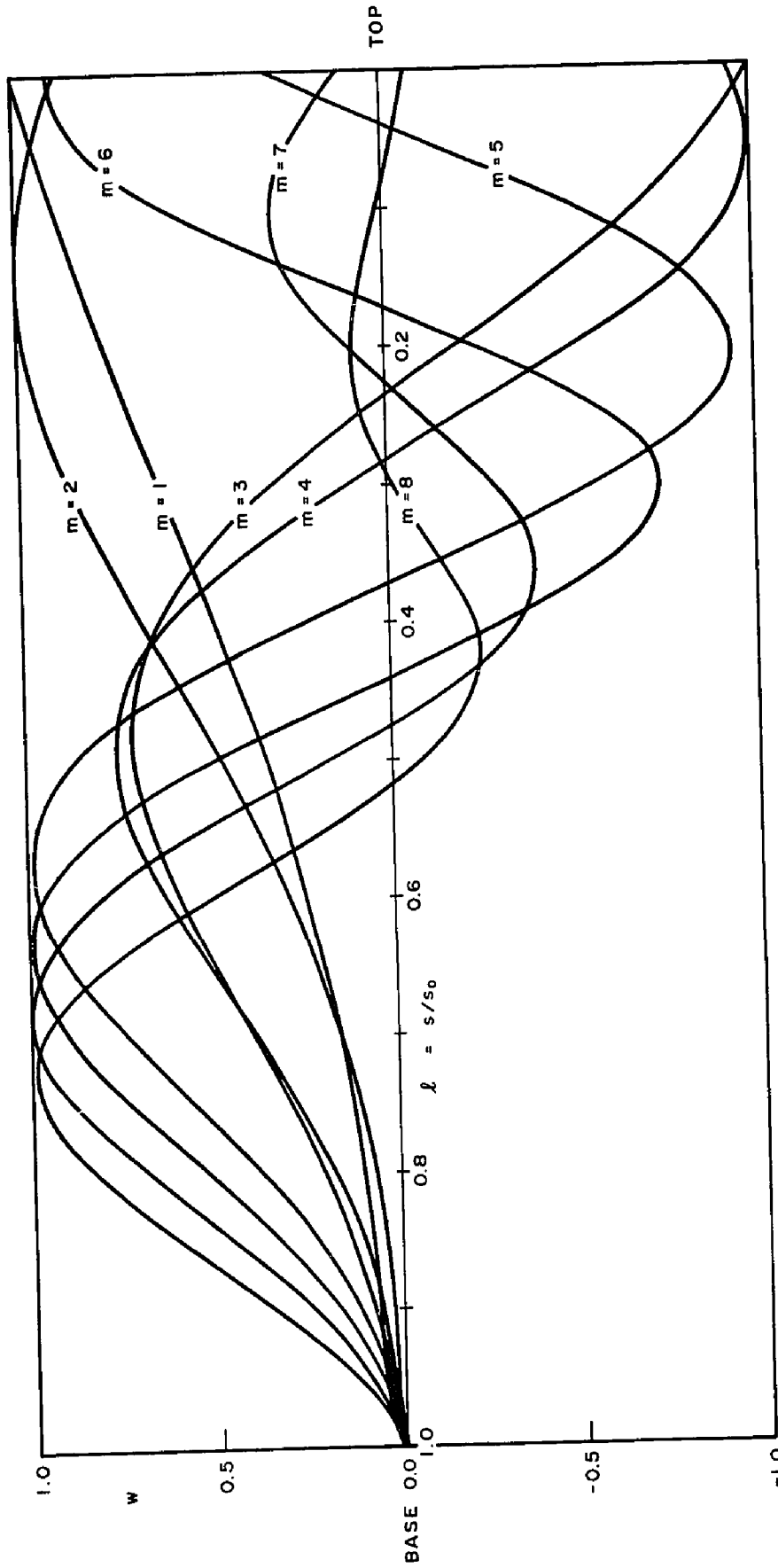


FIG. 6.3 MODE SHAPES FOR NORMAL DISPLACEMENT w

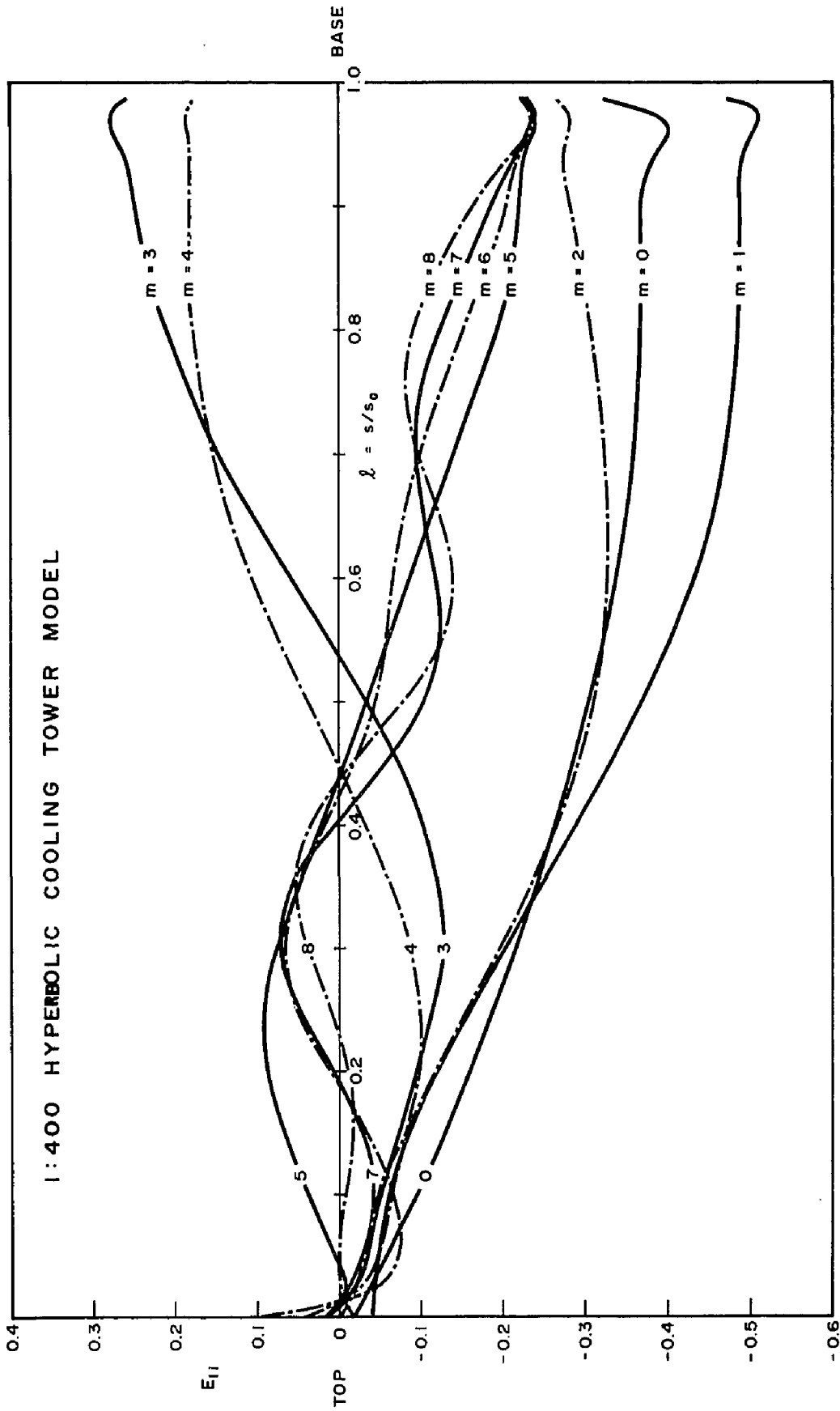


FIG. 6.4 MODE SHAPES FOR MERIDIONAL STRAIN ON INSIDE SURFACE OF MODEL (E_{II})

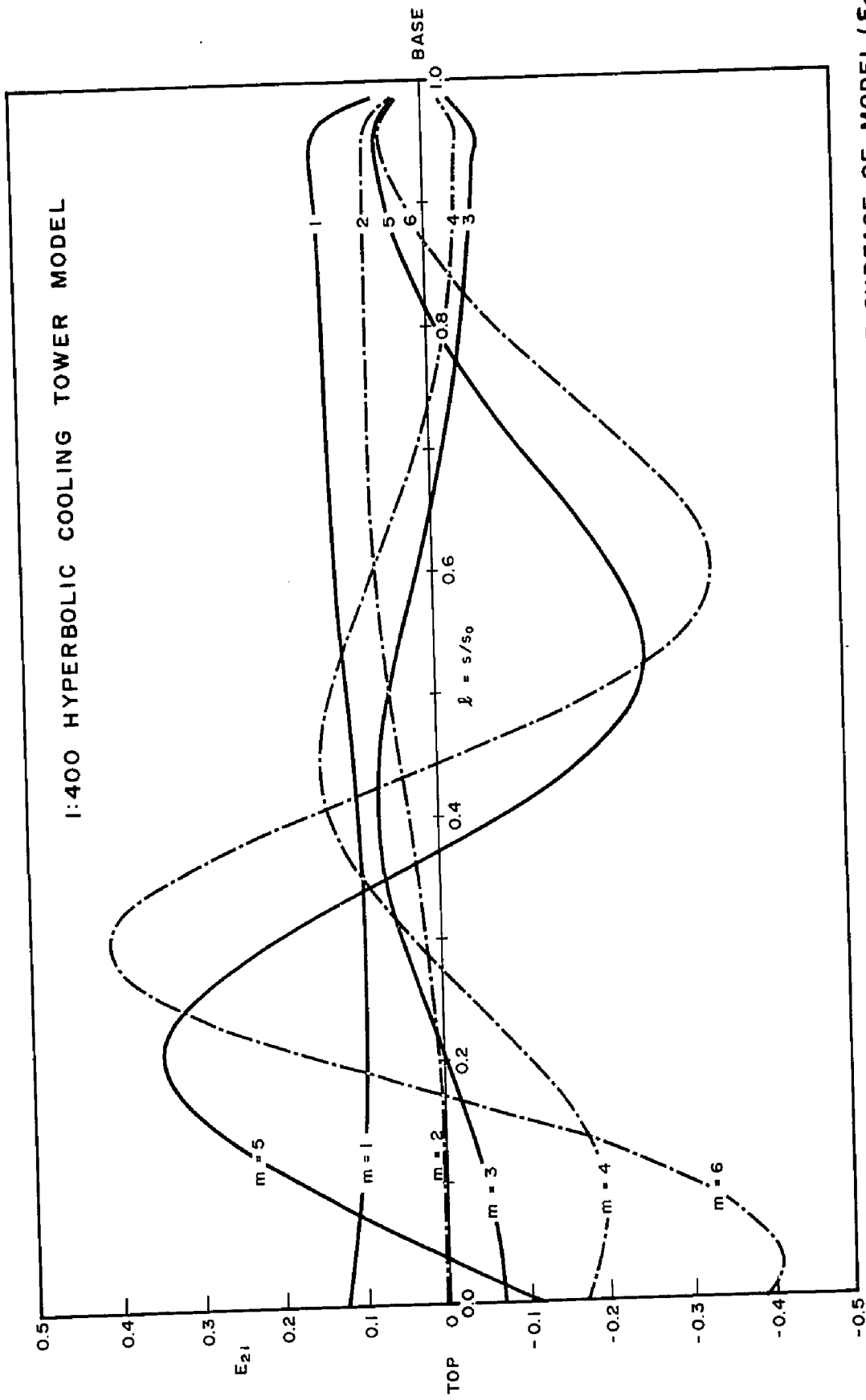


FIG. 6.5 MODE SHAPES FOR CIRCUMFERENTIAL STRAIN ON INSIDE SURFACE OF MODEL (E_{21})

In Fig. (6.4), it is observed that a group of modes for harmonics $m = 4, 5, 6$ and 8 have their modal points very close together at $Z \approx 0.56H$. Therefore, the first group of strain gauges were located at this level to allow for separation of other harmonics in the modal response measurements.

The computed natural frequencies are given in Table 6.2. The lowest natural frequency of 198 cps is associated with a circumferential wave number $m = 4$. For $m < 4$, most of the shell energy originates from membrane action and therefore the frequency decreases with increasing values of m (5,14). However, for $m \geq 4$ this trend is reversed as the relative contribution of bending energy starts to be increasingly important with increasing values of m and the membrane action becomes less significant.

TABLE 6.2 Natural Frequencies of Cooling Tower Model

m	Natural Frequency f (cps)	
	Finite Difference	Experiments
1	512	525
2	306	300
3	264	258
4	198	201
5	218	225
6	252	265
7	270	-
8	300	-
9	334	-

Experimental measurements were also carried out to determine the natural frequencies of the model. The objectives of the experiments were twofold. First, to provide a comparison with the theoretically obtained results. This was not intended as a check on the theoretical analysis itself since its accuracy is already well established (5,15), but rather to check the material properties and boundary conditions used in the computation. Since the former were obtained from beam and ring specimens, they might deviate from the actual properties of the shell model. Second, to test the procedure for the separation of modes outlined in Section 6.3.

Fig. 6.6 shows the arrangement of the testing instruments. The model was excited acoustically by means of a loudspeaker. Measurements of the total and modal response in terms of the meridional strain were detected at level 3, Fig. 6.1. Results were obtained for frequencies up to 600 cps.

Measurements of rms amplitude of the total response are given in Fig. 6.7. Modal measurements using circuit A for $m = 2, 6, \dots$, circuit B for $m = 1, 3, \dots$ and circuit C for $m = 0, 4, \dots$ are given in Figs. 6.8 to 6.10 respectively. From these results and from similar measurements at levels 1 and 2, it was found that the mode separation procedure was very efficient in isolating the different modes of interest. The natural frequencies obtained from these measurements are compared with those obtained using the

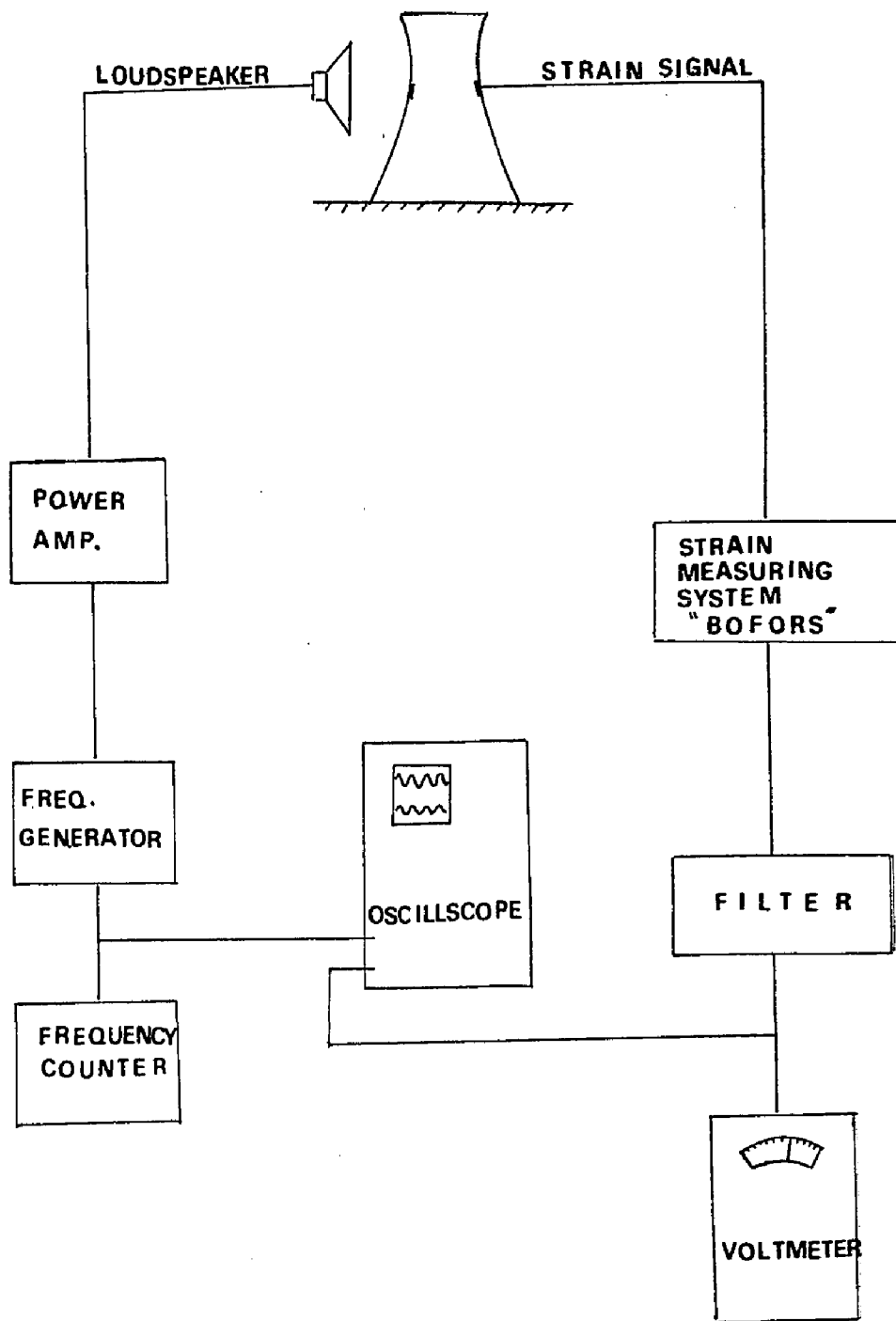


FIG. 6.6

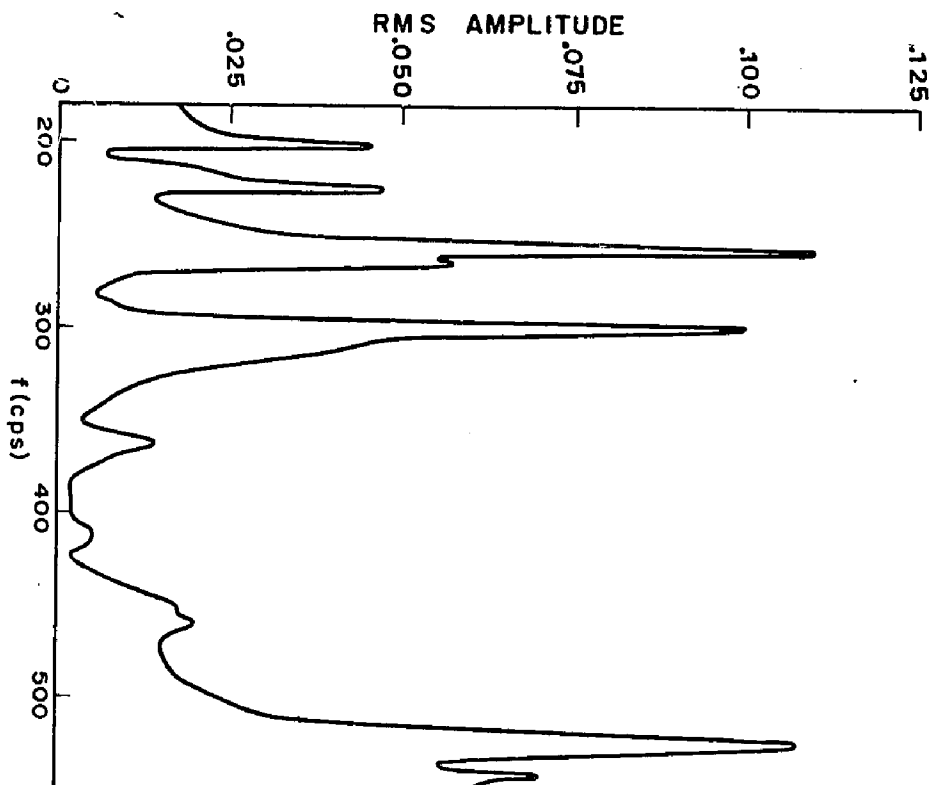


FIG. 6.7 RESPONSE OF COOLING TOWER MODEL TO ACOUSTIC EXCITATION (LEVEL 3; $\phi_0 = 0$)

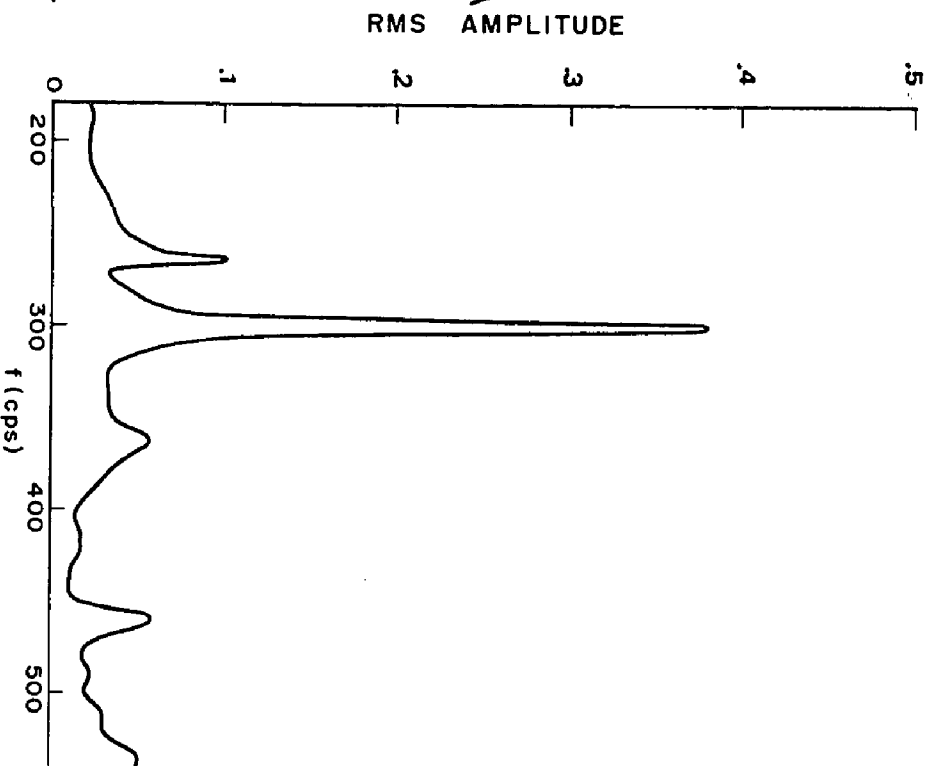


FIG. 6.8 OUTPUT OF CIRCUIT 'A' AT LEVEL 3, $\phi_0 = 0$

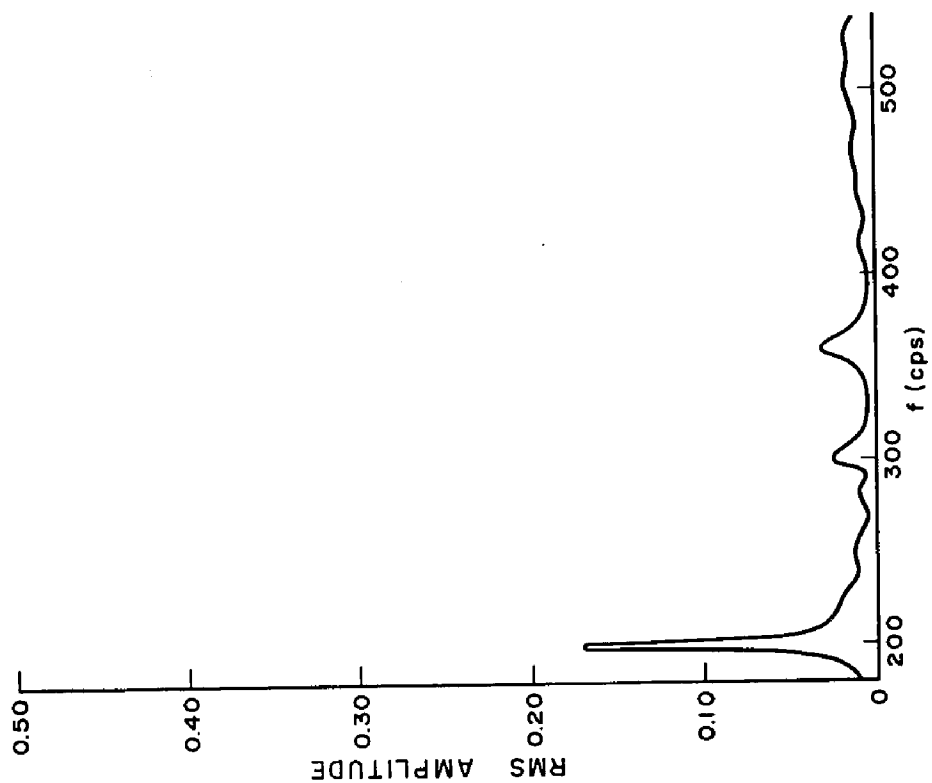


FIG. 6.10 OUTPUT OF CIRCUIT 'C'
AT LEVEL 3, $\phi_0 = 0$

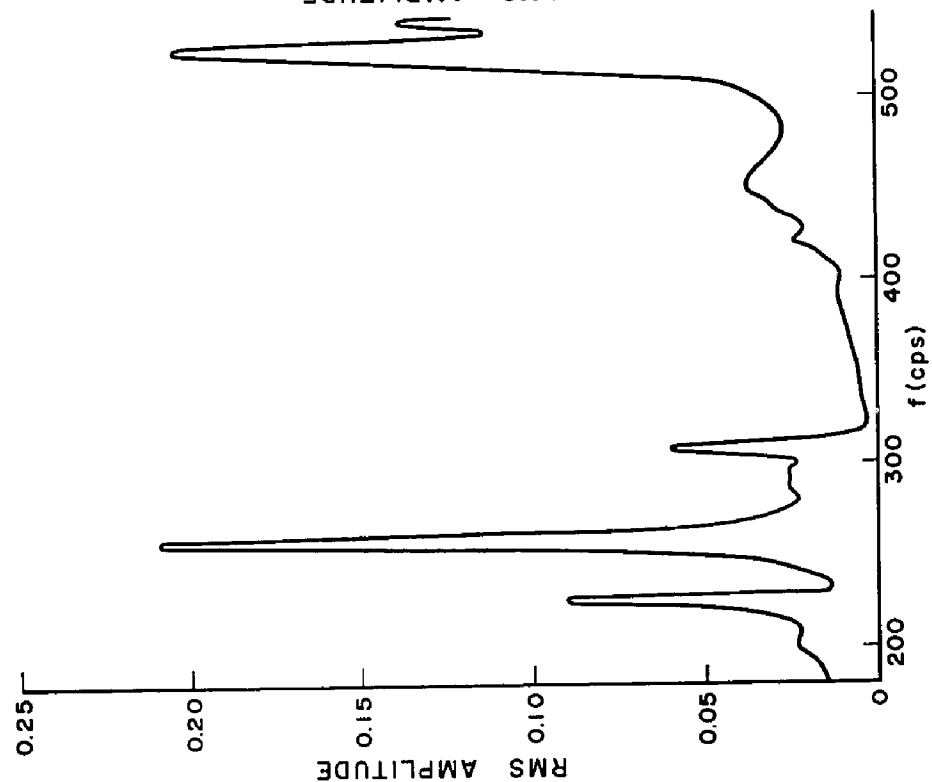


FIG. 6.9 OUTPUT OF CIRCUIT 'B'
AT LEVEL 3, $\phi_0 = 0$

finite difference method in Table 6.1. As shown, the theoretical results compare fairly well with the experiments.

From the response diagrams shown in Figs. 6.8 to 6.10, the critical damping ratio η_{cr} of the model for various harmonics could be easily obtained. Since the resonant peaks are well separated (Figs. 6.8 to 6.10), the response of each mode could be treated as an S.D.F. system; in which case η_{cr} is given by

$$\eta_{cr} = \frac{B}{2 \sqrt{3} f} \quad (6.11)$$

where, f = natural frequency and B = frequency bandwidth at half peak. Results for η_{cr} thus obtained are shown in Table 6.3.

TABLE 6.3 Critical Damping Ratio for Various Harmonics
(Mechanical Damping Only)

m	f_m	B	$\eta_{cr}\%$
1	525	20	1.10
2	300	9	0.87
3	258	10	0.96
4	201	6	0.87
5	225	8	1.02

6.5 Flow Properties and Experimental Set-Up

The experiments were conducted in the Boundary Layer Wind Tunnel Laboratory of The University of Western Ontario.

The tunnel floor was covered with randomly placed blocks of heights ranging from 1 to 4 in. approximately. The properties of the flow at the test section are given in Section 5.3. The mean velocity profile can be described by:

$$\frac{\bar{U}(Z)}{U(Z_G)} = \left(\frac{Z}{Z_G}\right)^{0.32} \quad (6.12)$$

This profile corresponds to boundary layer flow over a moderately rough terrain (see Table 2.1).

Measurements of the modal and total shell response were made at three different levels as shown in Fig. 6.1. The strain gauges used for measuring the meridional and circumferential strain were located on the inside surface of the shell. The strain gauge circuits suggested earlier for the separation of modes eliminate most of the temperature effects on the strain gauge measurements; especially for the dynamic response component.

The output from the strain gauge measuring system was then analysed to determine the mean and the standard deviation using a digital data acquisition system. Fig. 6.11 shows a diagrammatic sketch of the arrangement of the testing instruments.

The CAT Model 1000 computer was employed for the measurements of the auto correlation function. The number of correlation points sampled was either 128 or 256 points

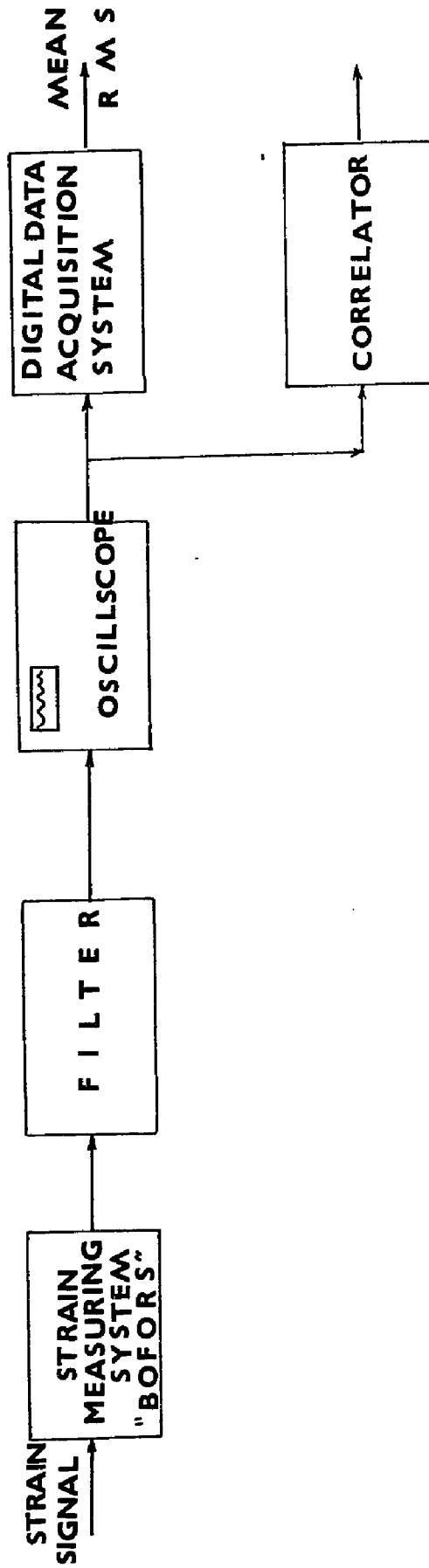


FIG. 6.II EXPERIMENTAL SET-UP

with a lag time interval of 0.8 and/or 0.4 milliseconds. The power spectra of the shell response were obtained from the auto correlation functions by direct Fourier transformation.

6.6 Mean Response

In terms of its modal components, the total mean response $\bar{y}(s, \phi)$ could be represented by the following relationship,

$$\bar{y}(s, \phi) = \sum_m \sum_i \bar{q}_{m,i} \cos m\phi y_{m,i}(s) \quad (6.13)$$

in which, $\bar{q}_{m,i}$ is the mean component of the generalized coordinate $q_{m,i}(t)$ for the i th mode associated with harmonic wave number m .

Following the mode separation procedure outlined in Section 6.3, contributions of the significant harmonics could be obtained directly from the experimental measurements. Measurements of the harmonic components of the meridional and circumferential strain on the inside surface of the shell were obtained at levels 1 and 3, Fig. 6.1. Strain gauge circuits A and B employed in the measurements are shown in Fig. 6.2.

Results for the meridional strain obtained from circuit A at levels 1 and 3 are shown in Figs. 6.12 and 6.13 respectively. The corresponding measurements for

the circumferential strain are shown in Figs. 6.14 and 6.15. The results clearly indicate the predominance of harmonic $m = 2$ at both levels for the meridional and circumferential strain. The contribution of higher harmonics $m = 6, 10, \dots$, if any, is within the range of experimental scatter. The ratio between the amplitudes of harmonic $m = 2$ at levels 1 and 3 indicate that the fundamental mode ($i = 1$) is predominant.

Measurements of the meridional strain at levels 1 and 3, obtained using circuit B, are shown in Figs. 6.16 and 6.17. Simple analysis of the results indicate that harmonics $m = 1$ and 3, only, have significant contributions. The participation of higher harmonics $m = 5, 7, \dots$ is found to be small and lies within the range of experimental scatter. Consequently, these measurements could be adequately summarized by the following two expressions:

$$\text{Level 1: } \frac{1}{4} \bar{y}_B = (95 \cos \phi + 450 \cos 3\phi) \frac{\frac{1}{2} \rho \bar{U}^2 (H)}{E} \quad (6.15)$$

$$\text{Level 3: } \frac{1}{4} \bar{y}_B = (160 \cos \phi + 490 \cos 3\phi) \frac{\frac{1}{2} \rho \bar{U}^2 (H)}{E} \quad (6.16)$$

in which $(\frac{1}{2} \rho \bar{U}^2 (H)) =$ pressure head at tower top. Although the contribution of harmonic $m=1$ is found to be significant, it is much smaller than the contribution of harmonics $m = 2$ and 3.

It is interesting to note that the amplitudes of

harmonic $m=1$ could be related fairly well to the fundamental mode shape of this harmonic shown in Fig. 6.4, thus indicating that higher modes may be insignificant. This is not the case, however, for harmonic $m=3$. It seems that the response in this harmonic is made up of several modes. The fundamental mode shape varies rapidly with height and changes sign near mid-height. Therefore, it is not sufficient to describe the total response of harmonic $m=3$ which was found to vary slowly with height and is almost constant in the lower half of the shell. More than one mode are thus necessary to describe its variation.

Similar results for the circumferential strain obtained using circuit B at levels 1 and 3 are given in Figs. 6.18 and 6.19. They basically show the same trends described earlier for the meridional strain. Note that the circumferential strain for each harmonic is much smaller than the meridional strain.

The output of circuit C, Fig. 6.2c, including the response of modes $m=0,4,8,..$ for the meridional and circumferential strain was found to be very small at both levels 1 and 3.

The total mean response could be obtained from the summation of the individual contributions of different harmonics. For example, the distribution of the total meridional strain around the shell circumference at level 3 was obtained and is shown in Fig. 6.20. The results

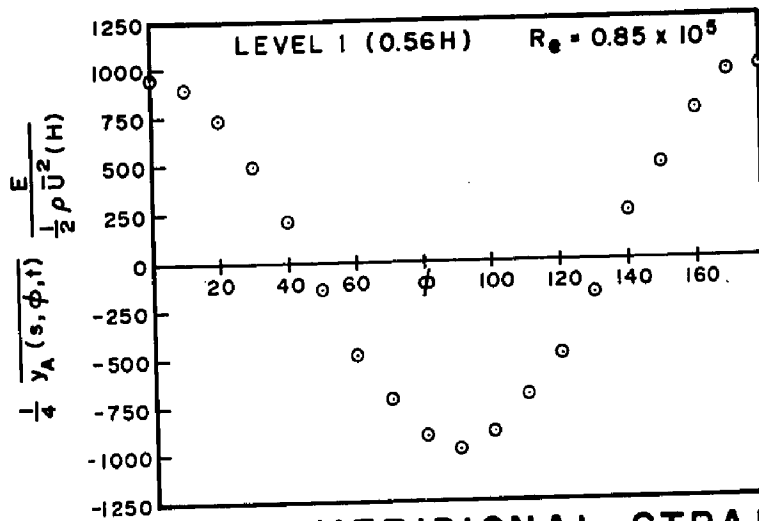


FIG. 6.12 MEAN MERIDIONAL STRAIN - CIRCUIT A

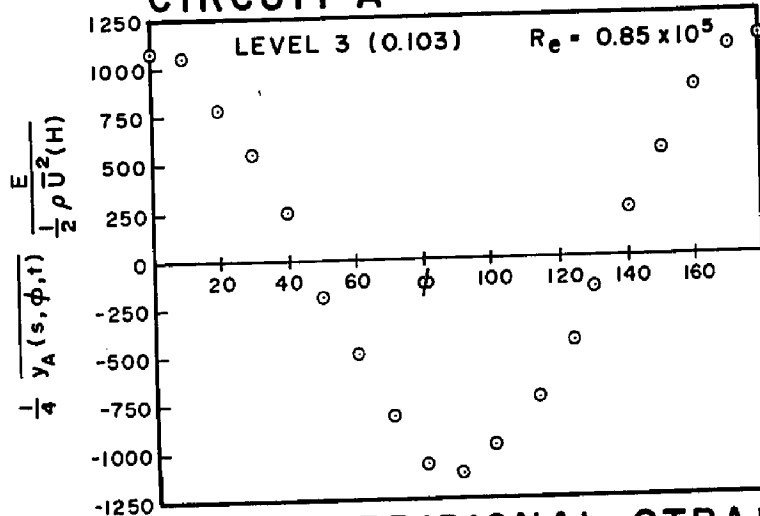


FIG. 6.13 MEAN MERIDIONAL STRAIN - CIRCUIT A

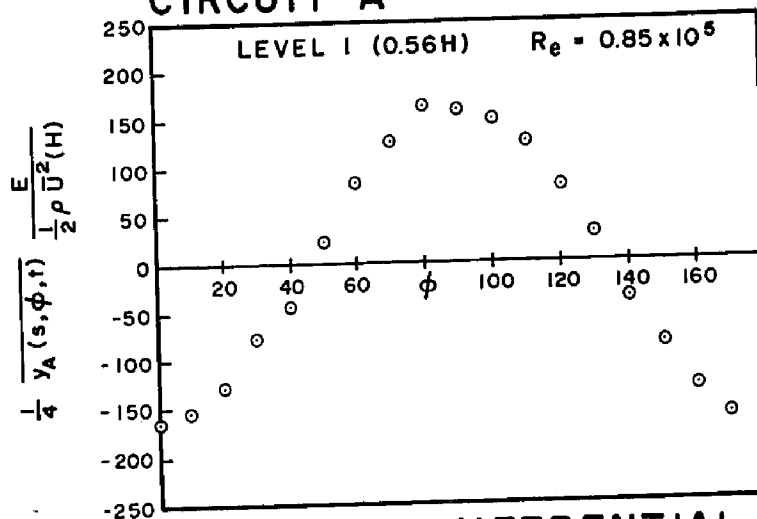


FIG. 6.14 MEAN CIRCUMFERENTIAL STRAIN - CIRCUIT A

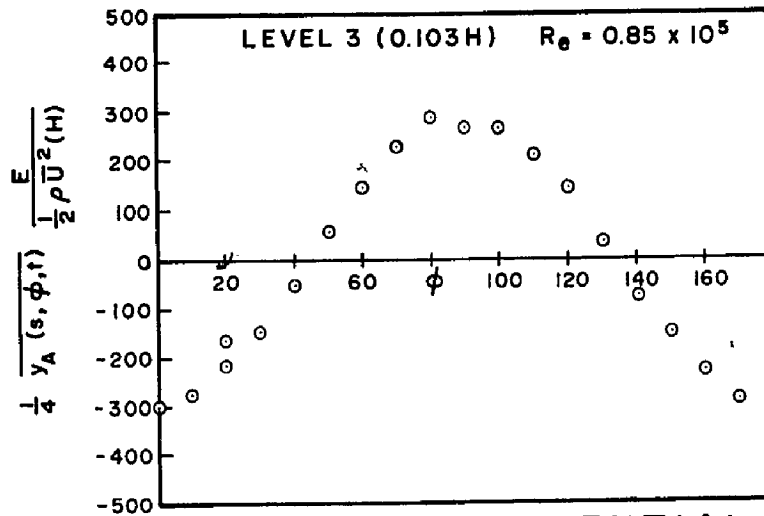


FIG. 6.15 MEAN CIRCUMFERENTIAL STRAIN - CIRCUIT A

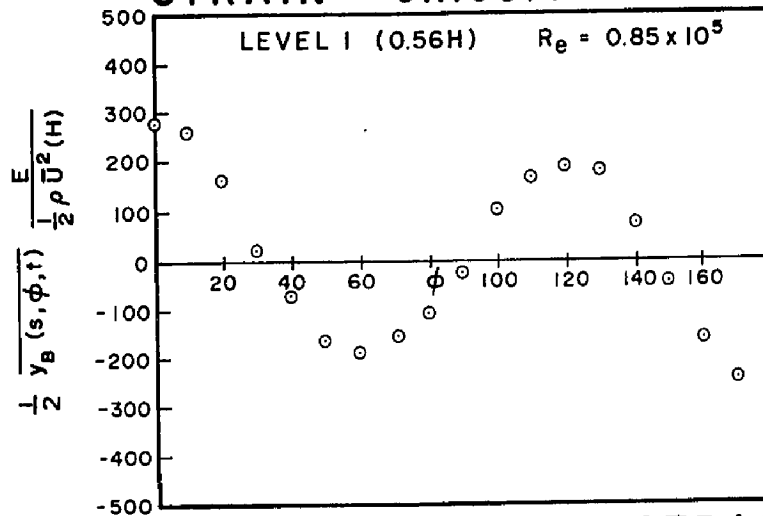


FIG. 6.16 MEAN MERIDIONAL STRAIN - CIRCUIT B

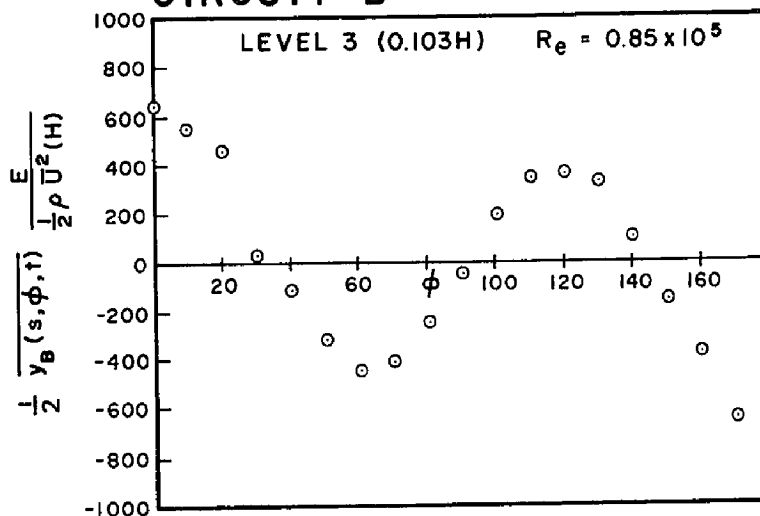


FIG. 6.17 MEAN MERIDIONAL STRAIN - CIRCUIT B

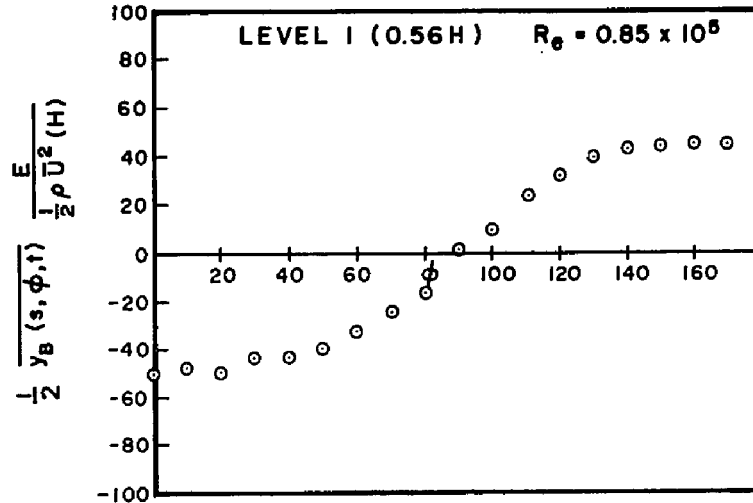


FIG. 6.18 MEAN CIRCUMFERENTIAL STRAIN - CIRCUIT B

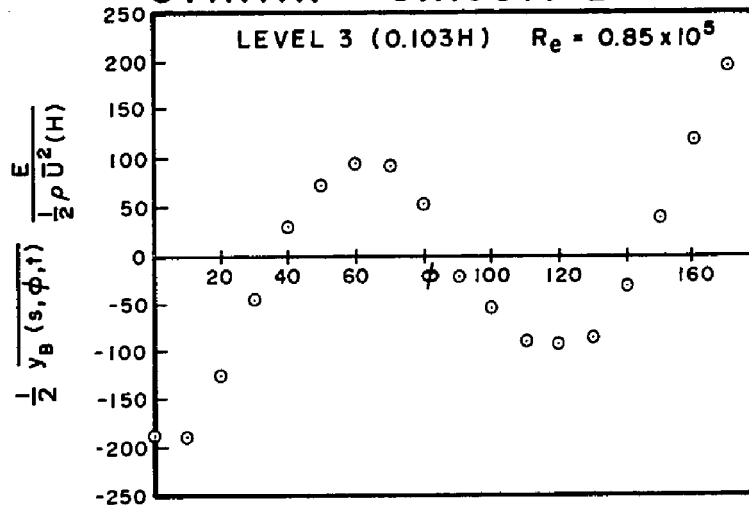


FIG. 6.19 MEAN CIRCUMFERENTIAL STRAIN - CIRCUIT B

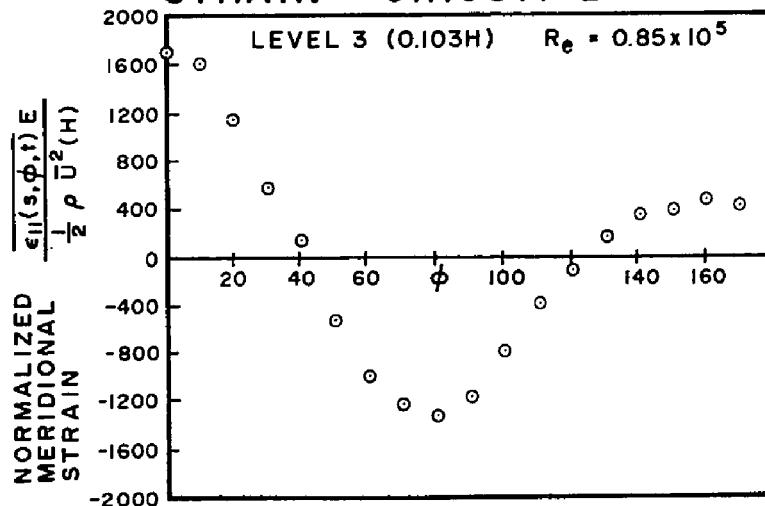


FIG. 6.20 TOTAL MEAN MERIDIONAL STRAIN ON INSIDE SURFACE OF MODEL

include the significant harmonics only, (i.e. $m = 1, 2,$ and 3) and could be described by:

$$\text{Level 3: } \bar{\epsilon}_{1_i}(\phi) = \frac{\frac{1}{2}\rho\bar{U}^2(H)}{E} \{160\cos\phi + 1100\cos 2\phi + 490\cos 3\phi\} \quad (6.17)$$

The above expression shows the predominance of the contribution of harmonic $m=2$ to the total shell response.

Values of mean wind stresses on the inside surface of the shell in the meridional and circumferential direction ($\bar{\sigma}_{1_i}$ and $\bar{\sigma}_{2_i}$) could be obtained from the strain measurements using the following stress-strain relations:

$$\bar{\sigma}_{1_i} = \frac{E}{1-\mu^2} \{ \bar{\epsilon}_{1_i} + \mu \bar{\epsilon}_{2_i} \} \quad (6.18)$$

$$\bar{\sigma}_{2_i} = \frac{E}{1-\mu^2} \{ \bar{\epsilon}_{2_i} + \mu \bar{\epsilon}_{1_i} \} \quad (6.19)$$

in which $\mu =$ Poisson's ratio. Since the influence of Poisson's ratio on strains could be neglected (5,16), the above relations could be employed to investigate the influence of Poisson's ratio on the mean wind stresses.

6.7 Dynamic Response

In the preceding section, the time average component of the response was considered. Herein, we will be mainly concerned with the fluctuating component.

The shell dynamic response is best described in statistical terms. Two quantities are of main interest; namely, the standard deviation and the power spectral density functions.

6.7.1 Standard Deviation

Unlike the time-average component of the shell response which follows symmetrical patterns around the mean wind direction, the corresponding patterns for the fluctuating component are not, and vary with time. This fact was considered in the representation of the shell response in terms of its modal components given by equation (6.1).

The variance of the shell response could be easily deduced from equation (6.1) and is given by:

$$\begin{aligned} \overline{y^2(s, \phi, t)} = & \sum_m \sum_i \sum_n \sum_j \{ \overline{q_{m,i}(t) q_{n,j}(t)} \cos m\phi \cos n\phi y_{m,i}(s) y_{n,j}(s) + \\ & \overline{q'_{m,i}(t) q'_{n,j}(t)} \sin m\phi \sin n\phi y_{m,i}(s) y_{n,j}(s) + \\ & 2 \overline{q_{m,i}(t) q'_{n,j}(t)} \cos m\phi \sin n\phi y_{m,i}(s) y_{n,j}(s) \} \end{aligned} \quad (6.20)$$

Assuming that $y(s, \phi, t)$ has a zero mean, then the standard deviation is simply given by:

$$\sigma_y(s, \phi) = \sqrt{y^2(s, \phi, t)} \quad (6.21)$$

In the experimental measurements, an attempt was made to measure the standard deviation of the contribution of each significant harmonic using the procedure of mode separation outlined earlier. This attempt while being very successful for harmonic $m=2$ was not entirely successful for other harmonics as will be shown later on.

Measurements of the standard deviation of the meridional strain on the inside surface of the shell at levels 1 and 3 using circuit A are shown in Figs. 6.21 and 6.22 respectively. The results include contributions of harmonics $m = 2, 6, 10, \dots$. However, no significant contribution from the high harmonics $m=6, 10, \dots$ could be detected from Figs. 6.21 and 6.22 as the response of harmonic $m=2$ is predominant. Based on these results, the variance of the output of circuit A, $y_A(s, \phi, t)$, could be adequately represented by:

$$\begin{aligned} \text{Level 1:} \\ y_A^2(s, \phi, t) = 16 \left(\frac{\frac{1}{2} \rho \bar{U}^2 (H)}{E} \right)^2 \{ 62600 \cos^2 2\phi + 26000 \sin^2 2\phi \} \end{aligned} \quad (6.22)$$

$$\begin{aligned} \text{Level 2:} \\ y_A^2(s, \phi, t) = 16 \left(\frac{\frac{1}{2} \rho \bar{U}^2 (H)}{E} \right)^2 \{ 81200 \cos^2 2\phi + 30500 \sin^2 2\phi \} \end{aligned} \quad (6.23)$$

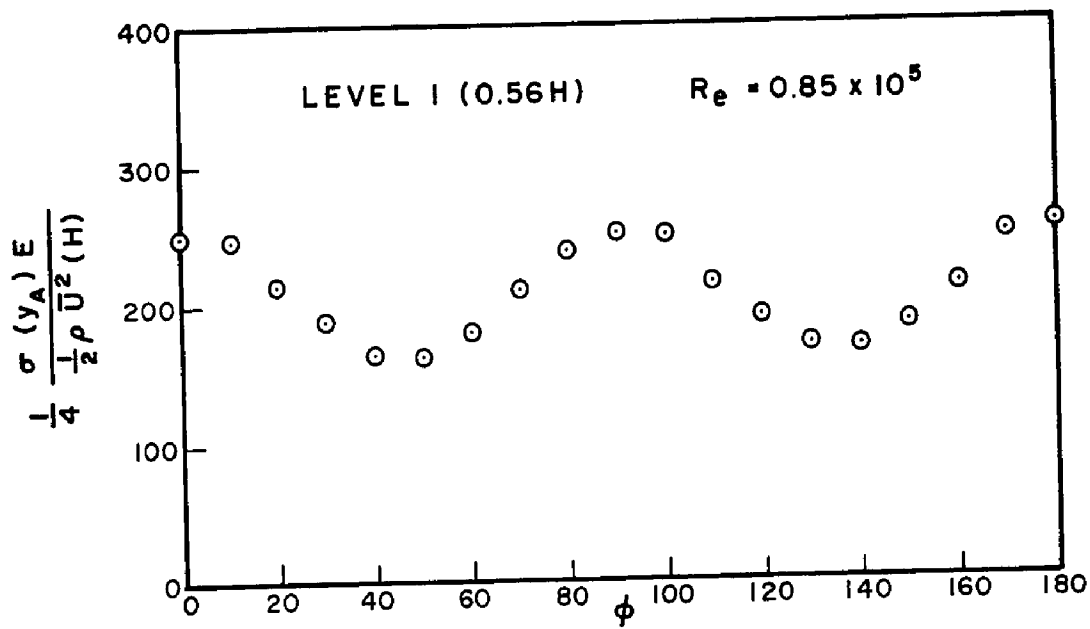


FIG. 6.21 RMS MERIDIONAL STRAIN -
CIRCUIT A

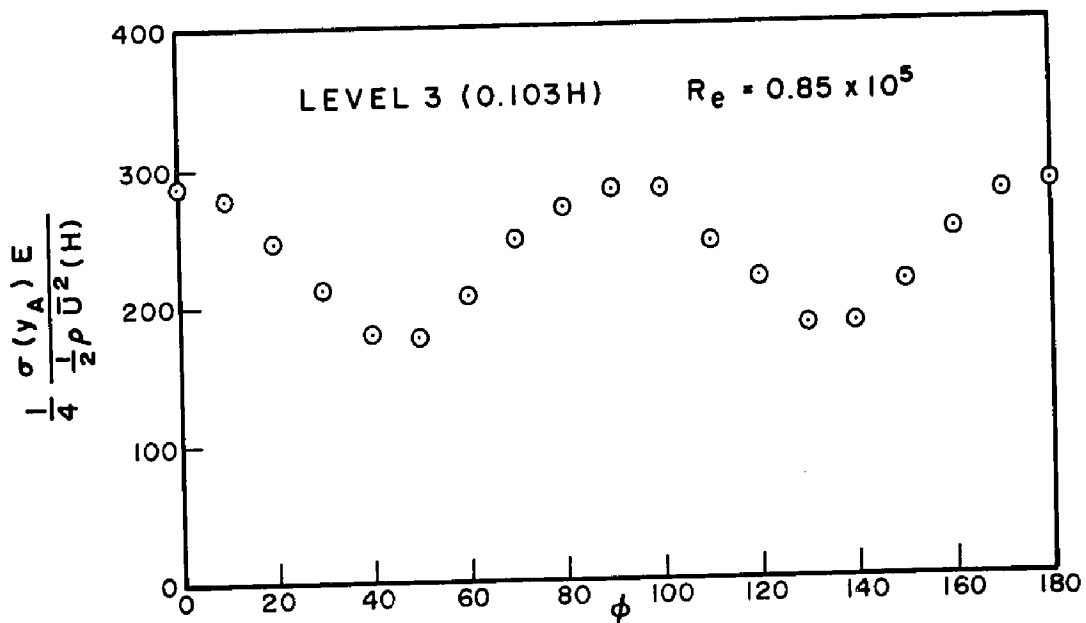


FIG. 6.22 RMS MERIDIONAL STRAIN -
CIRCUIT A

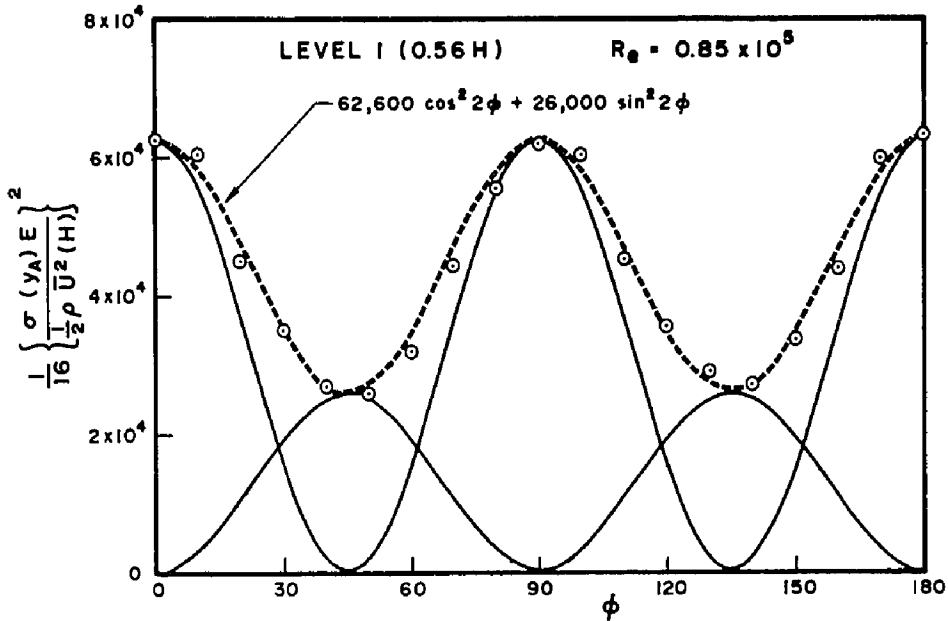


FIG. 6.23 VARIANCE OF MERIDIONAL STRAIN - CIRCUIT A

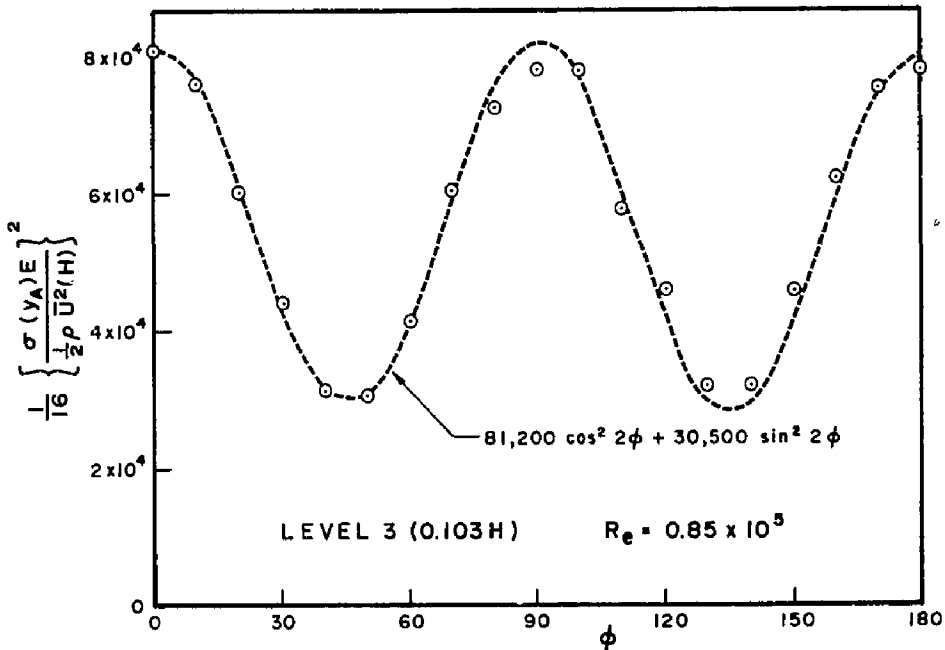


FIG. 6.24 VARIANCE OF MERIDIONAL STRAIN - CIRCUIT A

The above expressions are compared with the experimental measurements in Figs. 6.23 and 6.24.

Equations (6.22 and 6.23) readily show that the variance of $y_A(s, \phi, t)$ is made primarily from the variance of both the symmetric and anti-symmetric modes of harmonic $m=2$. The coupling between both modes of this harmonic and contributions of other harmonics, if any, are too small to be distinguished from the experimental scatter.

Equations (6.22 and 6.23) further indicates that the ratios between the coefficients of both the cosine and sine terms at levels 1 and 3 compare quite well with the fundamental mode shape of harmonic $m=2$; thus suggesting that higher modes ($i>1$) may be insignificant. The dominance of this mode has also been observed in the mean response measurements.

The contribution of harmonic $m=2$ to the total shell response has a strong anti-symmetric component. The variance of this component is about 40% of the symmetric component and its standard deviation is about 65%. Further elaboration on this is given in the discussion of the analytical prediction of the shell response given in Chapter 7.

The output of circuit B, $y_b(s, \phi, t)$ for the standard deviation of the meridional strain on the inside surface of the shell at levels 1, 2, and 3 is given in Figs. 6.25

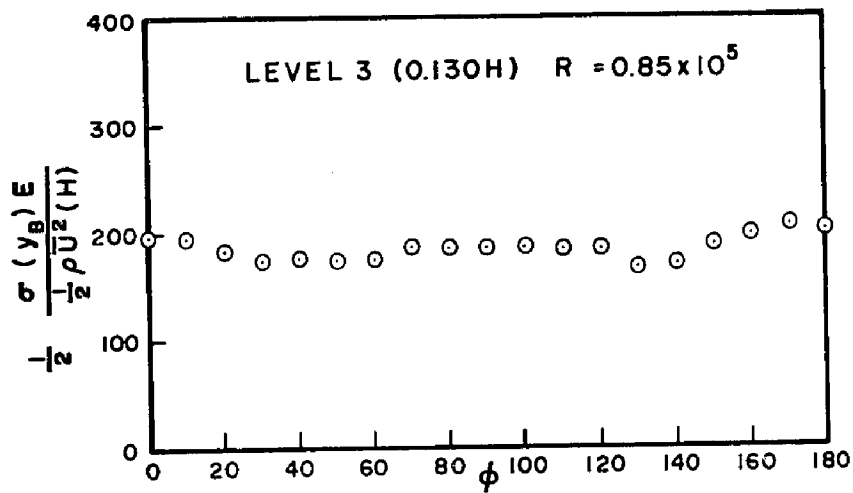


FIG. 6.25 RMS MERIDIONAL STRAIN -
CIRCUIT B

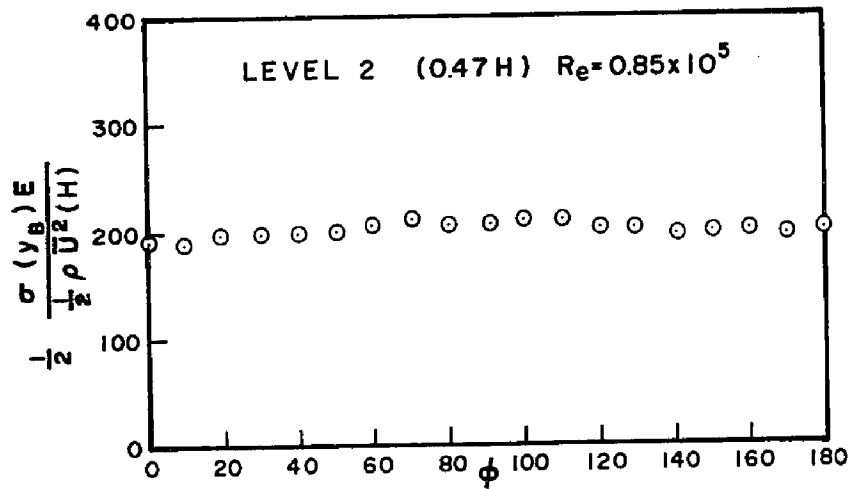


FIG. 6.26 RMS MERIDIONAL STRAIN -
CIRCUIT B

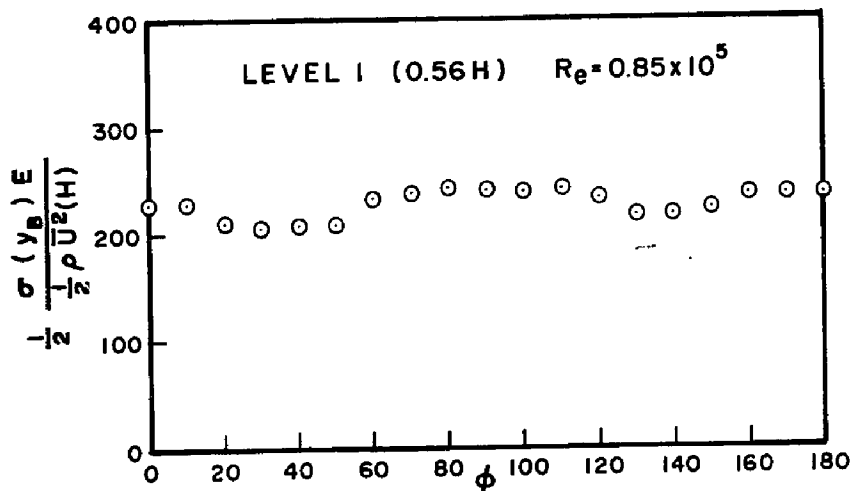


FIG. 6.27 RMS MERIDIONAL STRAIN -
CIRCUIT B

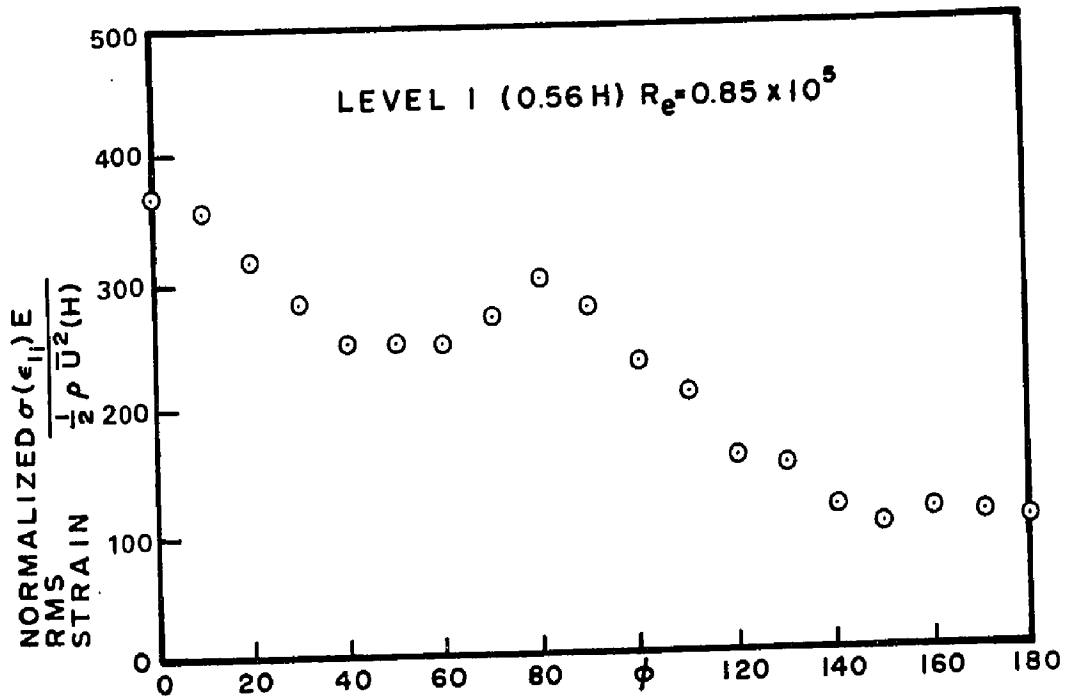


FIG. 6.28 TOTAL RMS MERIDIONAL STRAIN ON INSIDE SURFACE OF MODEL

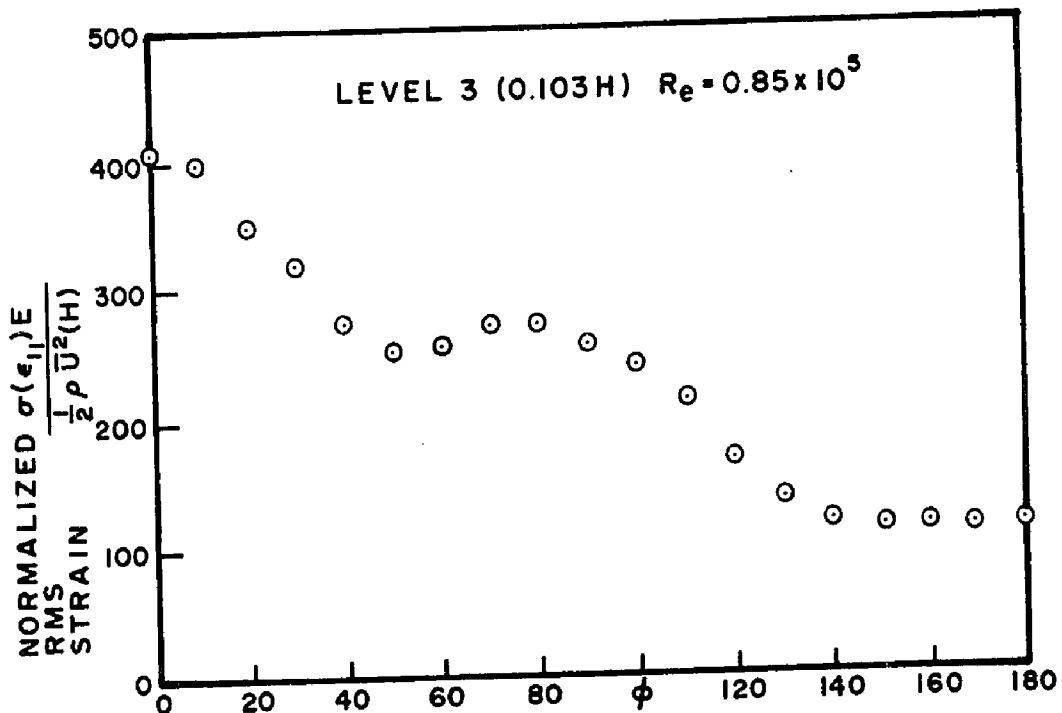


FIG. 6.29 TOTAL RMS MERIDIONAL STRAIN ON INSIDE SURFACE OF MODEL

to 6.27 respectively. The output of this circuit contains the contributions of all the odd harmonics only. The results shown in Figs. 6.25 to 6.27 indicate that the output of circuit B is made up of several harmonics. The contribution of some of these harmonics could possibly contain more than one mode. In view of the absence of any strong contribution of any mode relative to the others, no attempt was made to determine the individual contribution of each mode. Rather, the response of each mode was obtained theoretically. The individual contributions of various modes were then summed up and compared with the experimental measurements in Chapter 7.

Although the mode separation procedure was not entirely satisfactory herein, some important conclusions could be deduced from the results. It is found that the odd harmonics produce significant contribution to the shell response. Their total contribution is of the same order as the contribution of harmonic $m=2$, which is the only significant one of all even harmonics. The anti-symmetric components of the response of odd harmonics are as important as the symmetric components. Their contribution is even greater at level 2.

Measurements of the standard deviation of the total response were also obtained for the meridional strain on the inside surface of the shell. Its variation around the shell circumference at levels 1 and 3 is shown in

Figs. 6.28 and 6.29 respectively. At both levels the standard deviation attains its largest value at the stagnation point ($\phi=0$). As ϕ increases, the standard deviation decreases until a minimum is reached near $\phi = 45^\circ$; just to start increasing to reach another peak near $\phi = 80^\circ$ after which it drops rapidly as the wake region is approached. In the wake region, the standard deviation is fairly small and is characterized by an almost constant value across the region. Note the similarities between the variation of the intensity of the response fluctuations around the shell and that of the pressure fluctuations described in Chapter 5.

By comparing results of the total and modal response, it was found that harmonic $m=2$ contributes over 50% of the largest variance of shell response attained at $\phi = 0$ and about 75% of its standard deviation. The predominance of harmonic $m=2$ was also observed in the mean response measurements. The remaining part of the response variance comes from odd harmonics as the response of all other even harmonics is very small. Further inspection of the results given in Figs. 6.21 to 6.29 shows the significance of coupling between different harmonics.

The standard deviation of the total shell response at $\phi = 0$ at the base is about 23% of its mean value. The peak dynamic response is about 3.5 to 4 times the standard deviation (17). Hence, the total peak response

is about 1.81 to 1.92 times the mean response at that point.

6.7.2 Power Spectral Density

The purpose of the present section is to present the results for the power spectra of the response of the cooling tower model to turbulent wind loading. The power spectra for the generalized coordinates, $q_{m,i}(t)$ and $q'_{m,i}(t)$ or their combinations were obtained along with the power spectrum of the total meridional strain on the inside surface of the shell at some selected points. An attempt is made to define the power spectra of the generalized forces, $p_{m,i}(t)$ and $p'_{m,i}(t)$ for the significant harmonics.

In the previous section, it was found that the output of circuit A, Fig. 6.2a, is made up almost solely from the contribution of harmonic $m=2$ at levels 1 and 3 with very little contribution from higher harmonics, $m = 6, 10, \dots$. Therefore, it was possible to obtain the power spectra of both the symmetric and anti-symmetric components of the response of these harmonics directly from the experiments.

The power spectra of the output of circuit A at level 1 for $\phi_0 = 0$ and 45° are shown in Figs. 6.30 and 6.31 respectively. The power spectra of the symmetric and anti-symmetric components of the generalized coordinates for $m=2$ could be adequately obtained from:

$$\frac{Sq'_{2,1}q'_{2,1}(f)}{q'^2_{2,1}(t)} \approx \frac{Sy_A(s, \phi_0=0, f)}{y_A^2(s, \phi_0=0, t)} \quad (6.24)$$

$$\frac{Sq'_{2,1}q'_{2,1}(f)}{q'^2_{2,1}(t)} \approx \frac{Sy_A(s, \phi_0=45^\circ, f)}{y_A^2(s, \phi_0=45^\circ, t)} \quad (6.25)$$

Figs. 6.30 and 6.31 show that the shell response in these modes is caused mainly by background turbulence. The natural frequencies of the model are far removed from the frequency range in which the energy of the pressure fluctuations is concentrated. The resonance contribution to the variance of the symmetric component of shell response is very small; being less than 10%. Thus an error of less than 5% would be expected if the standard deviation is computed assuming quasi-static conditions. Results for the anti-symmetric component, shown in Fig. 6.31, indicate that the relative proportion of resonance is even smaller. The resonance contributes less than 5% to the total dynamic response. The single resonant peak observed in Figs. 6.30 and 6.31 at $f \approx 300$ cps corresponds to the fundamental mode of $m=2$.

The power spectra of the output of circuit A at level 3 are shown in Figs. 6.32 and 6.33 for $\phi_0=0$ and $\phi_0=45^\circ$ respectively. Two resonant peaks are observed at $f \approx 260$ and 300 cps. These peaks belong to the fundamental modes of harmonics $m = 6$ and 2 respectively.

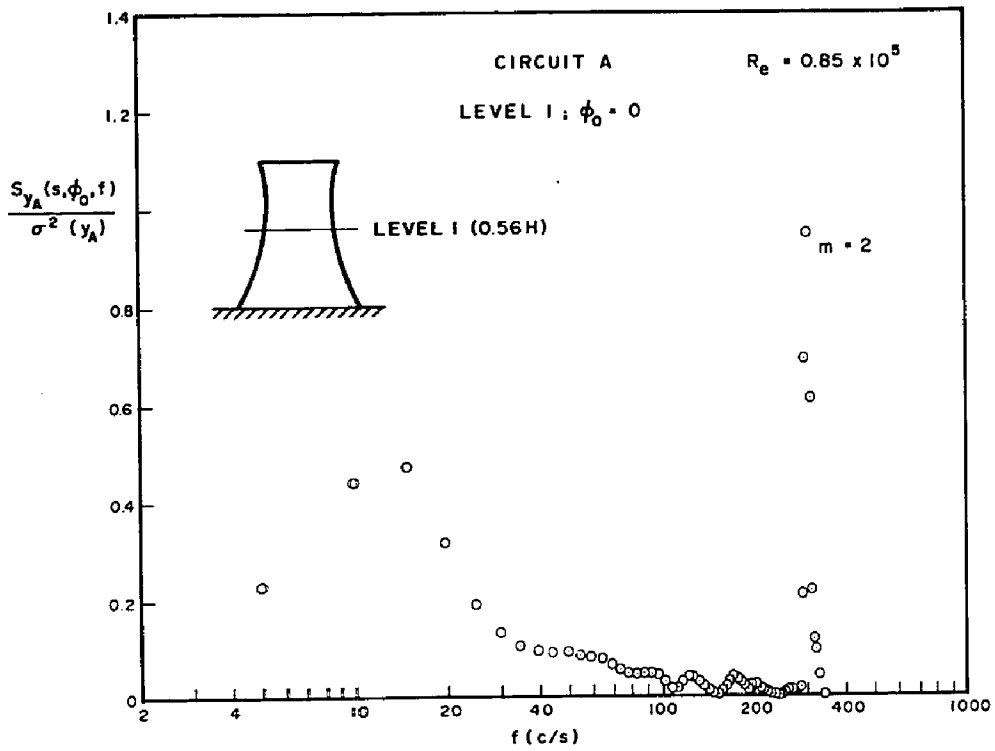


FIG. 6.30 POWER SPECTRA OF MODAL STRAIN - CIRCUIT A OUTPUT; $\phi_0 = 0$, LEVEL I (0.56H)

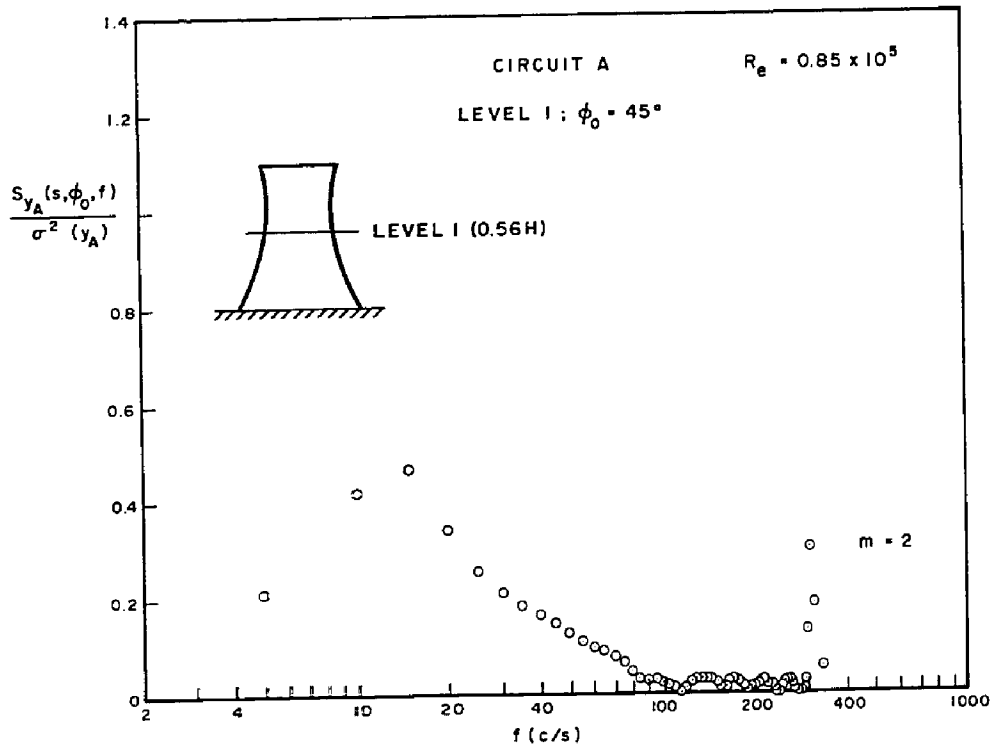


FIG. 6.31 POWER SPECTRA OF MODAL STRAIN - CIRCUIT A OUTPUT; $\phi_0 = 45^\circ$, LEVEL I (0.56H)

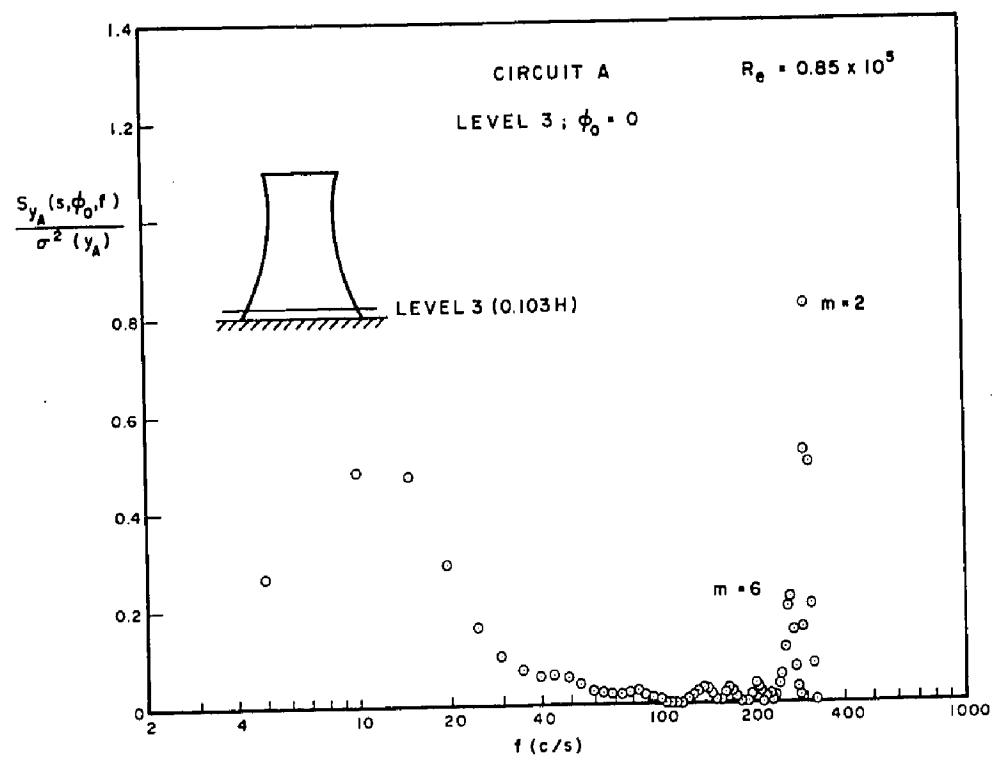


FIG. 6.32 POWER SPECTRA OF MODAL STRAIN - CIRCUIT A OUTPUT ; $\phi_0 = 0$, LEVEL 3 (0.103H)

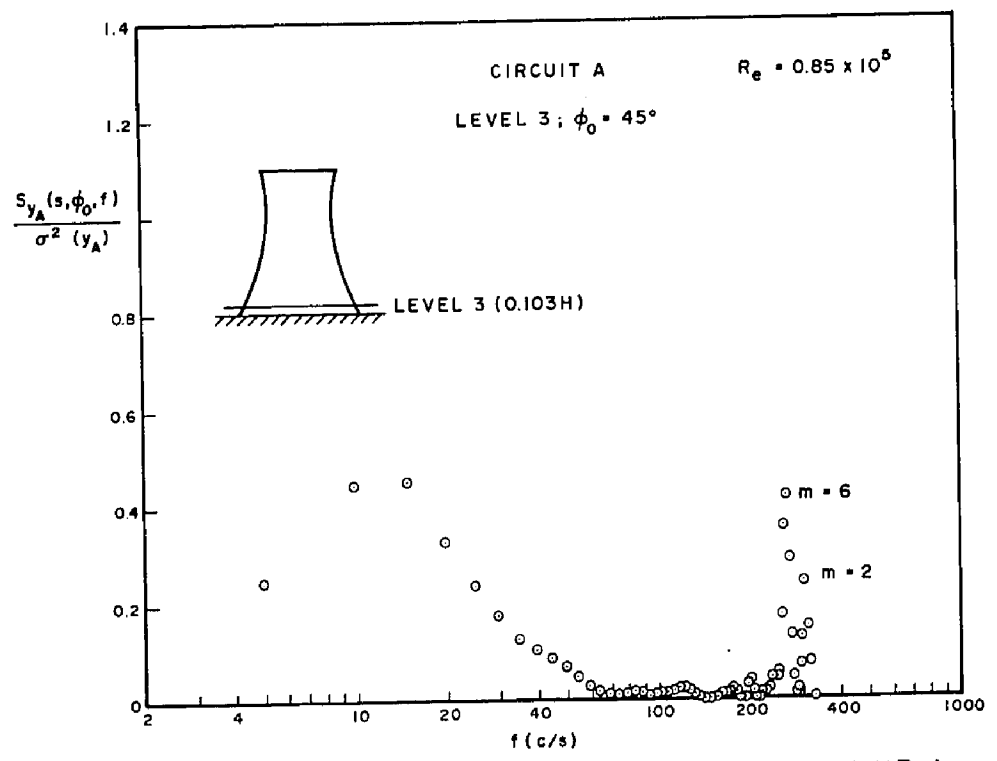


FIG. 6.33 POWER SPECTRA OF MODAL STRAIN - CIRCUIT A OUTPUT ; $\phi_0 = 45^\circ$, LEVEL 3 (0.103H)

The resonant peak of harmonic $m=6$ is comparable to the peak of harmonic $m=2$. The total variance of the former (quasi-static + resonance) is expected to be much smaller than the latter (see Section 6.7.1). The combined resonant response of harmonics $m=2$ and 6 is much smaller than their combined quasi-static response.

The mode separation procedure has thus been employed successfully to isolate the power spectra of harmonic $m=2$ and to provide a qualitative understanding of the contribution of harmonic $m=6$. This was not the case, however, when attempting to isolate the individual response of the odd harmonics using circuit B, Fig. 6.2b.

The power spectra of the output of circuit B for the meridional strain on the inside surface of the shell at levels 1 and 3 are given in Figs. 6.34 to 6.37 for $\phi_o=0$ and 90° . The response at $\phi_o=0$ includes the symmetric components only of all the odd harmonics, while that at $\phi_o=90^\circ$ contains the anti-symmetric components. In Figs. 6.34 to 6.37 several response peaks are observed. The corresponding harmonic and mode numbers are given thereon. By far, the strongest peak is associated with the swaying harmonic, $m=1$. Some resonant peaks detected at level 3 were not evident at level 1 as the corresponding mode shapes have their nodal point at this level (see Fig. 6.4).

The total resonant response of all odd harmonics contributes about 10% only of their total dynamic

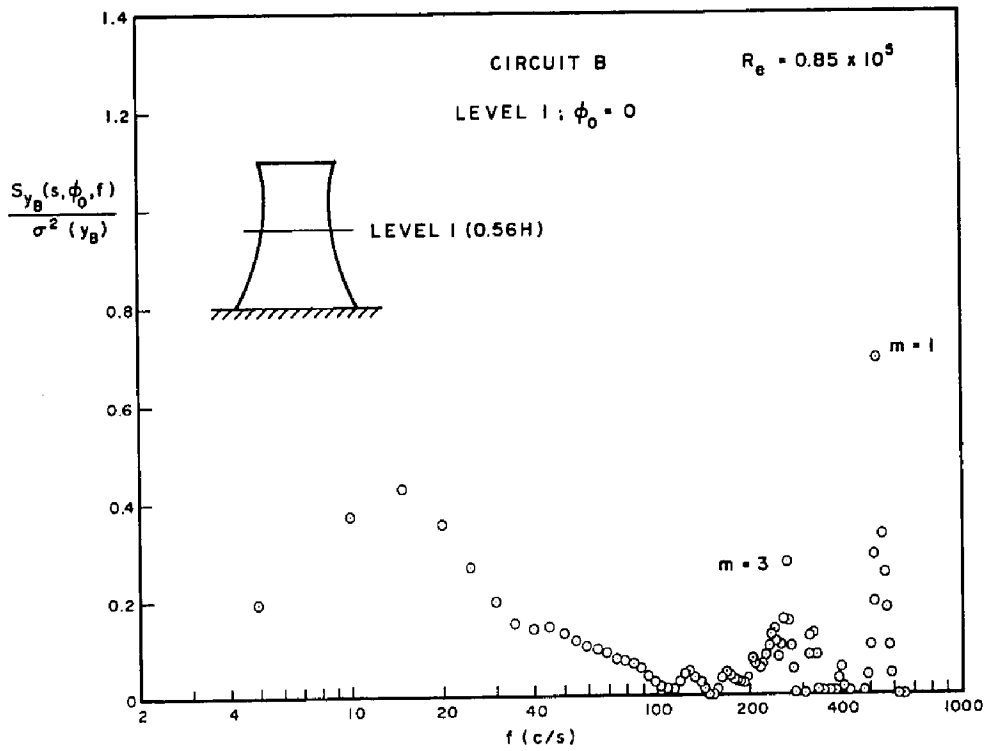


FIG. 6.34 POWER SPECTRA OF MODAL STRAIN - CIRCUIT B OUTPUT; $\phi_0 = 0$, LEVEL I (0.56H)

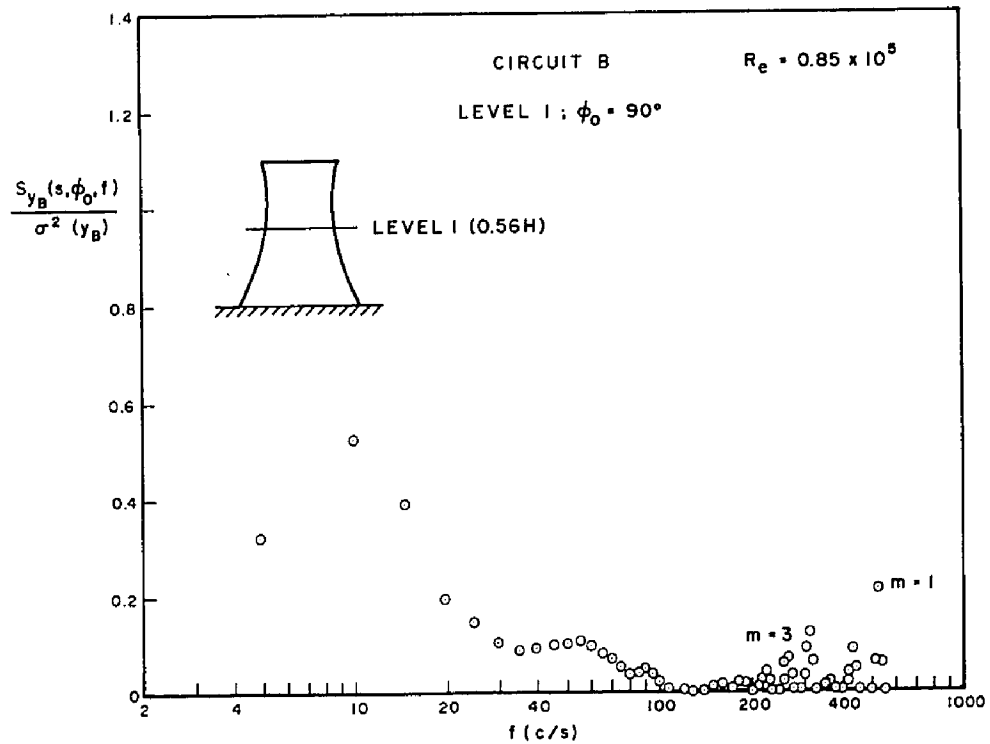


FIG. 6.35 POWER SPECTRA OF MODAL STRAIN - CIRCUIT B OUTPUT; $\phi = 90^\circ$, LEVEL I (0.56H)

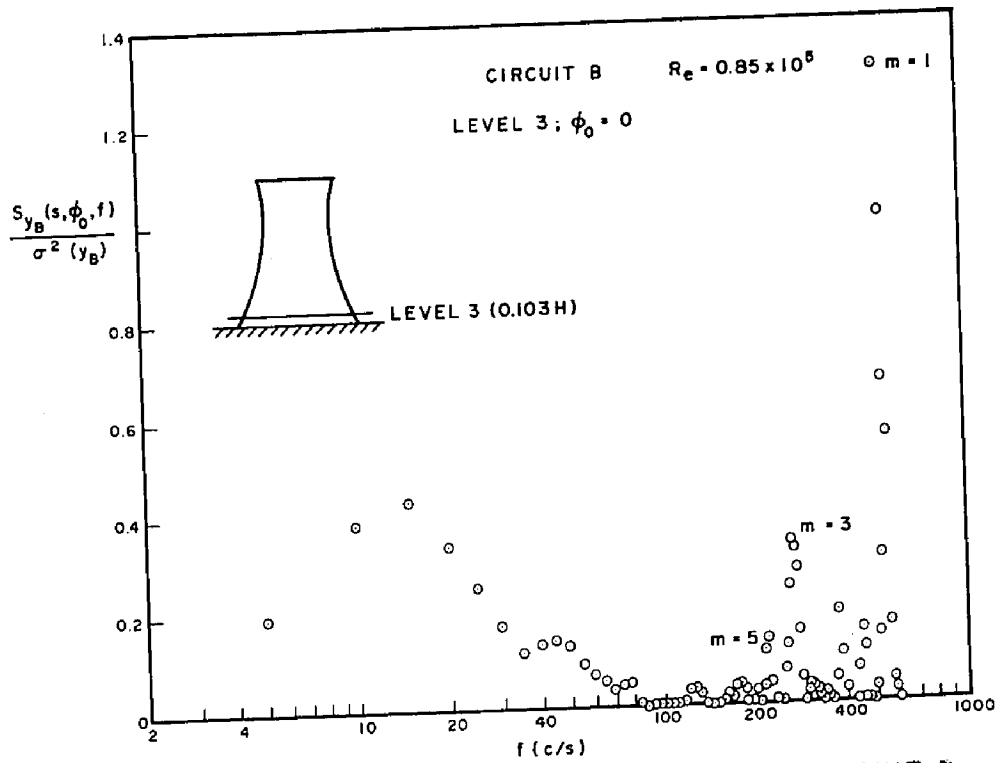


FIG. 6.36 POWER SPECTRA OF MODAL STRAIN - CIRCUIT B OUTPUT; $\phi_0 = 0$, LEVEL 3 (0.103H)

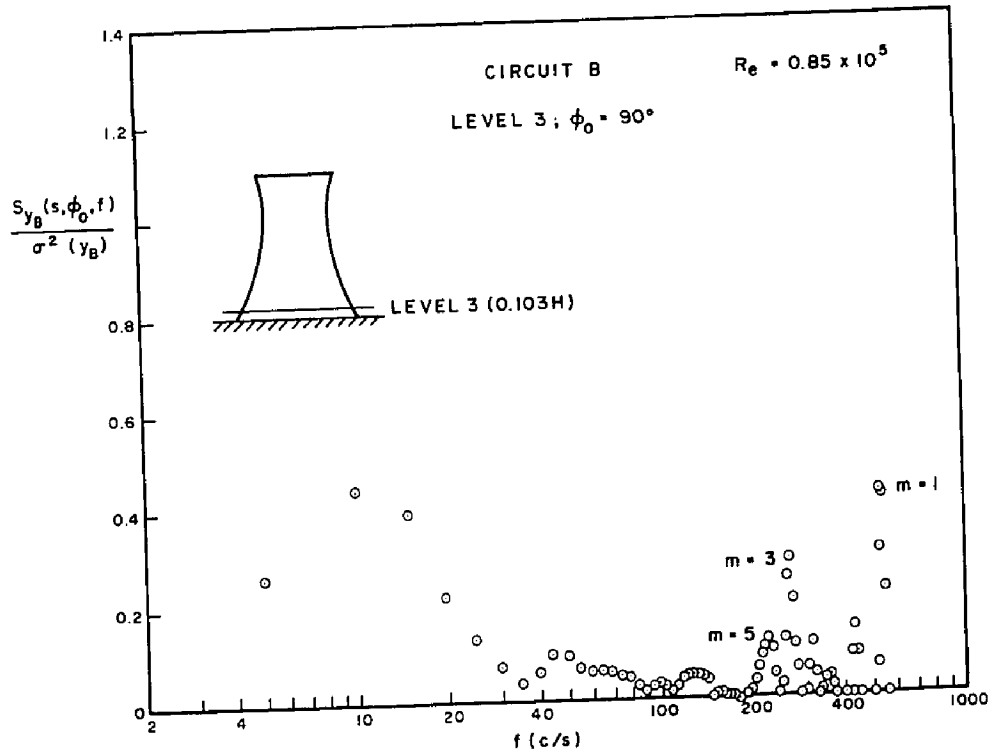


FIG. 6.37 POWER SPECTRA OF MODAL STRAIN - CIRCUIT B OUTPUT; $\phi_0 = 90^\circ$, LEVEL 3 (0.103H)

response. Here again, the resonance proportion of the anti-symmetric modes is much smaller than that of the symmetric modes.

Measurements of the power spectra of the total meridional strain on the inside surface of the shell were obtained at levels 1 and 3 for $\phi=0$ and 90° . The results are shown in Figs. 6.38 to 6.41. When compared with Figs. 6.30 to 6.37, it is found that the general characteristics of the power spectra of the total dynamic response are similar to those of its modal components. Most of the shell response resides in the low frequency range. The resonant response is very small and its relative proportion is less than 10% of the total dynamic response. It is further found that coupling between modes at the natural frequencies is very small.

The insignificance of resonance is attributable to the high stiffness of hyperbolic shells of revolution. The fundamental natural frequencies of hyperbolic cooling towers are considerably higher than those of similar upright structures (e.g. cylinders, cone-toroids,.. etc.) with same overall dimensions. The significance of resonance for cooling tower structures increases as the wind velocity increase and/or if the effective shell stiffness is reduced (e.g. increased height, flexibility of supports, etc.).

Some of the previous results of the modal response

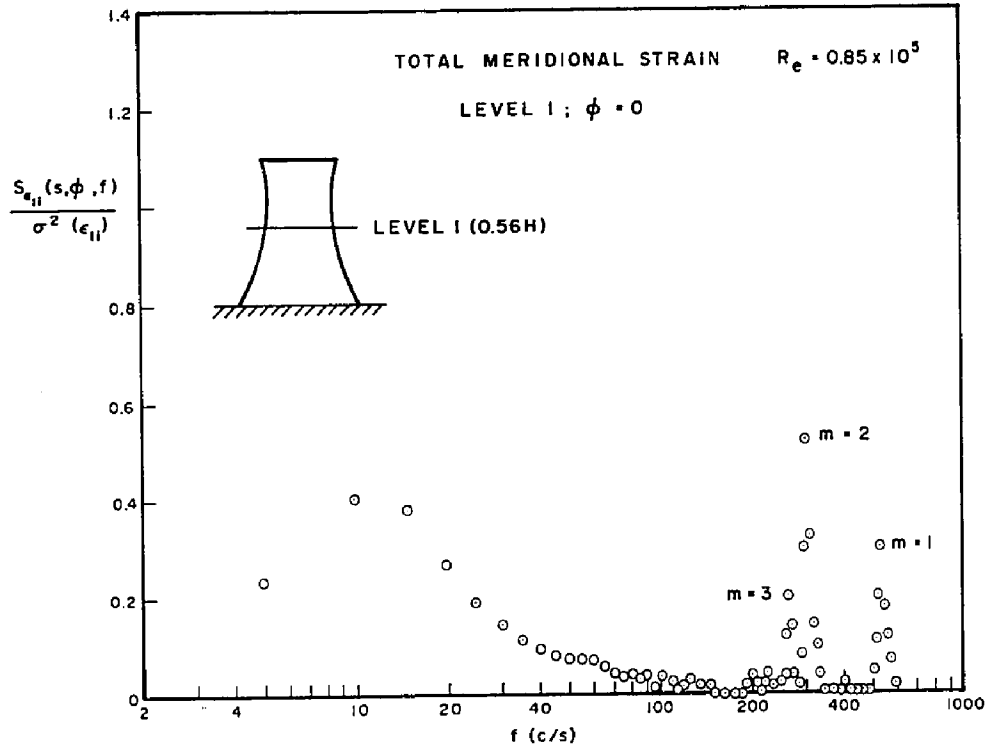


FIG. 6.38 POWER SPECTRA OF TOTAL MERIDIONAL STRAIN

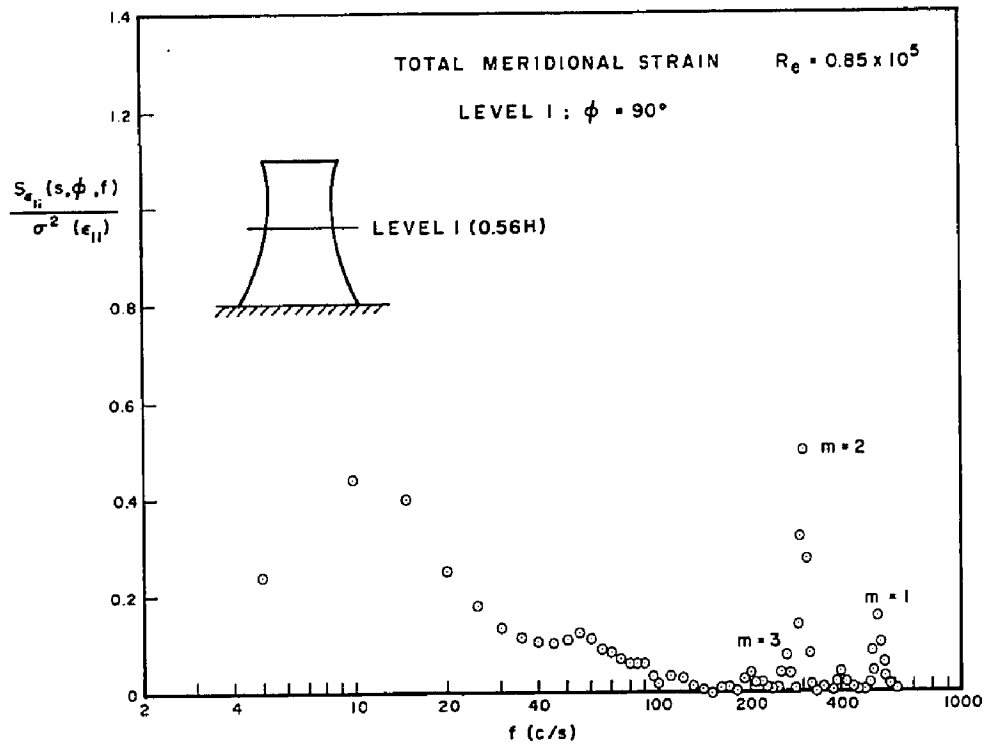


FIG. 6.39 POWER SPECTRA OF TOTAL MERIDIONAL STRAIN

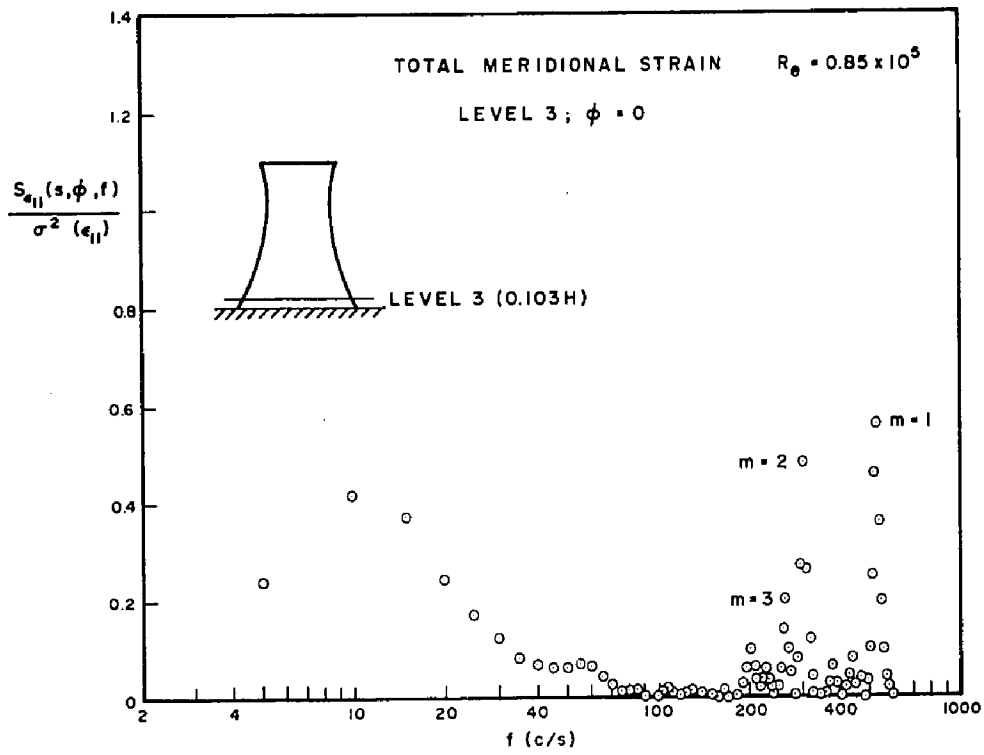


FIG. 6.40 POWER SPECTRA OF TOTAL MERIDIONAL STRAIN

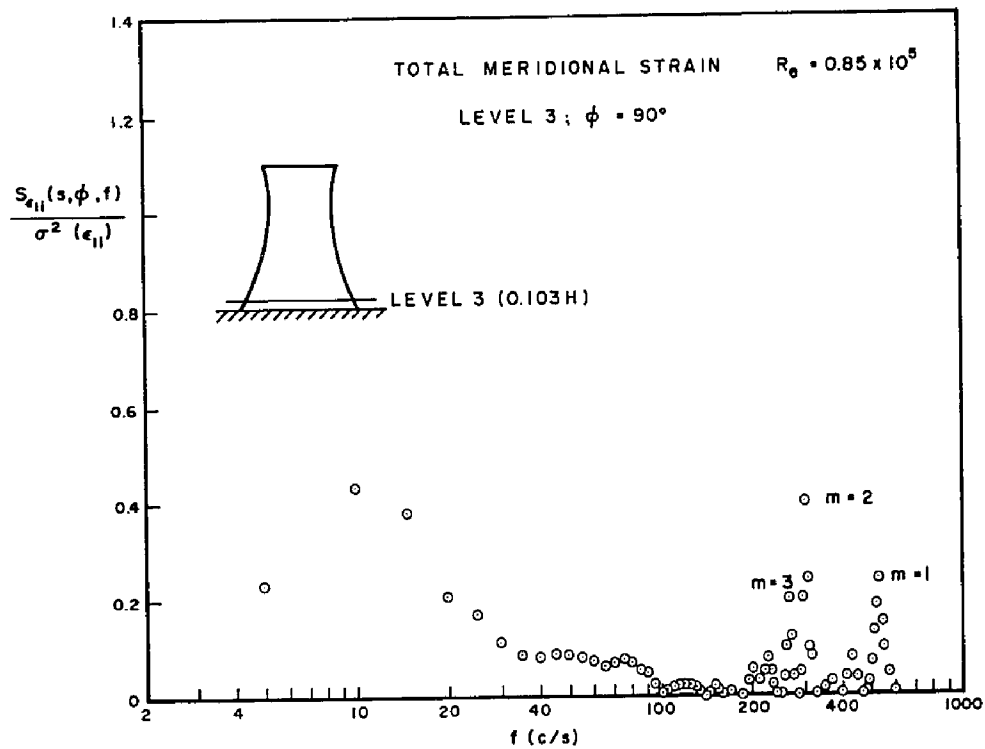


FIG. 6.41 POWER SPECTRA OF TOTAL MERIDIONAL STRAIN

could be used to compute the statistical properties of the generalized forces experienced by the individual modes of vibration. This could help to extend the present experimental measurements of shell response to other geometrically similar structures or nearly so, but otherwise with different structural or vibration characteristics.

For hyperbolic cooling towers with marginal geometric differences, it is reasonable to assume that neither the statistical properties of the wind pressure fluctuations nor the mode shapes of the shell displacement will not be altered significantly. For such towers, the function, $\tilde{S}_{p_m, i p_n, j}(\tilde{f})$, could be considered as a universal representation of the cross-spectra of the generalized forces, where,

$$\tilde{S}_{p_m, i p_n, j}(\tilde{f}) = \frac{S_{p_m, i p_n, j}(\tilde{f})}{s_o^4 \left(\frac{1}{2} \rho \bar{U}^2\right)^2} \quad (6.26)$$

in which, $\tilde{f} = \frac{fd}{U}$, d = typical tower dimension taken as throat diameter, $p_{m, i}(t)$ = generalized force of the i th mode associated with harmonic wave number m and s_o = total meridional length.

The power spectra of the generalized forces $S_{p_m, i p_n, j}(\tilde{f})$, could be easily obtained from equation (3.56) if the power spectra of the generalized co-ordinates are known. The covariance of the generalized forces, $\overline{p_{m, i}(t) p_{n, j}(t)}$, could then be obtained. If resonance is small and could be neglected, then it could be shown that,

$$\overline{p_{m,i}(t)p_{n,j}(t)} = \frac{q_{m,i}(t)q_{n,j}(t)}{16\pi^4 f_{m,i}^2 f_{n,j}^2 M_{m,i} M_{n,j}} \quad (6.27)$$

in which $M_{m,i}$ is defined by equation (3.16).

The computation of $Sp_{m,i}p_{n,j}(f)$ using equation (3.56) requires knowledge of: a - natural frequencies and mode shapes, b - total (mechanical and aerodynamic) damping, for various modes of interest. The natural frequencies and mode shapes of the shell model are given in Table 6.2 and Fig. 6.4 respectively. The total critical damping ratio could be obtained from the time records of the modal response for various modes.

The critical damping ratio η_{cr} of lightly damped single degree of freedom system, subject to white-noise excitation, could be obtained from the envelope of autocorrelation function of the response given by:

$$R(\tau) = \pm e^{-\eta_{cr}\omega_o\tau} \quad (6.28)$$

in which ω_o = natural frequency and τ = time-lag.

This equation could be used directly to determine the critical damping ratios of the cooling tower model from the modal response signals by isolating the resonant response using a narrow-band filter. Errors resulting from approximating the spectra of wind excitation, across the band-width, by a band-width limited white-noise spectra are expected to be small. Estimates of the

critical damping ratio, thus obtained, are given in Table 6.4 for the fundamental mode of harmonics $m=1, 2$ and 3. The difference between these results and the estimates of the mechanical damping ratio given in Table 6.3 gives the aerodynamic damping ratio.

Thus, we have all the data necessary to compute the generalized force spectra from the spectra of the modal response using equation (3.56). The power spectra of the symmetric and anti-symmetric components of the generalized force for the fundamental mode of harmonic $m=2$ are shown in Figs. 6.42 and 6.43. Because of the difficulties experienced in the separation of the response spectra of other harmonics, no attempt was made to compute the corresponding spectra of the generalized forces. These, however, were obtained from the analytical approach and are presented in the next chapter.

TABLE 6.4

m	1	2	3
$\eta_{cr} \%$	1.15	0.93	1.04

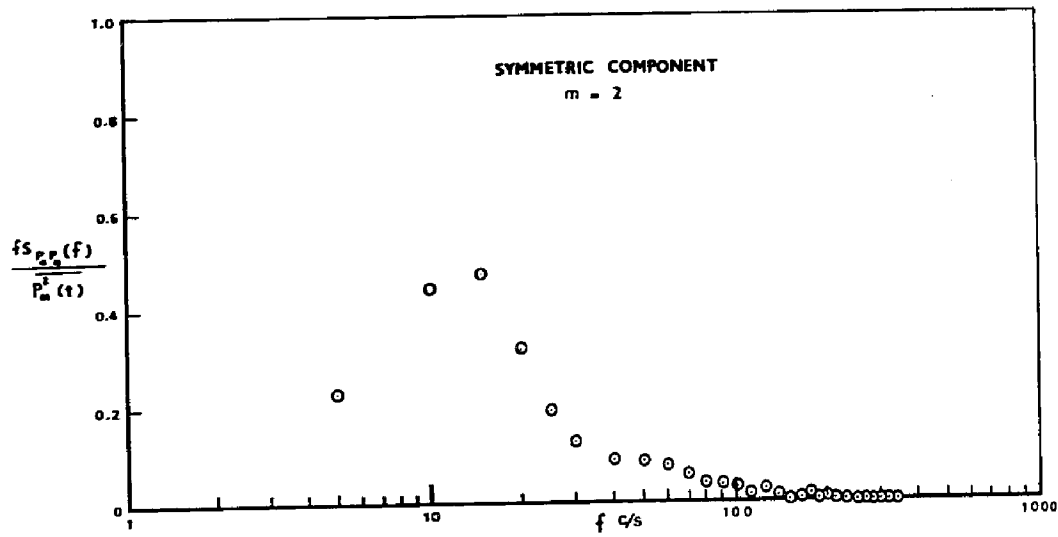


FIG.6.42 POWER SPECTRUM OF THE SYMMETRIC COMPONENT OF THE GENERALIZED FORCE FOR HARMONIC m=2

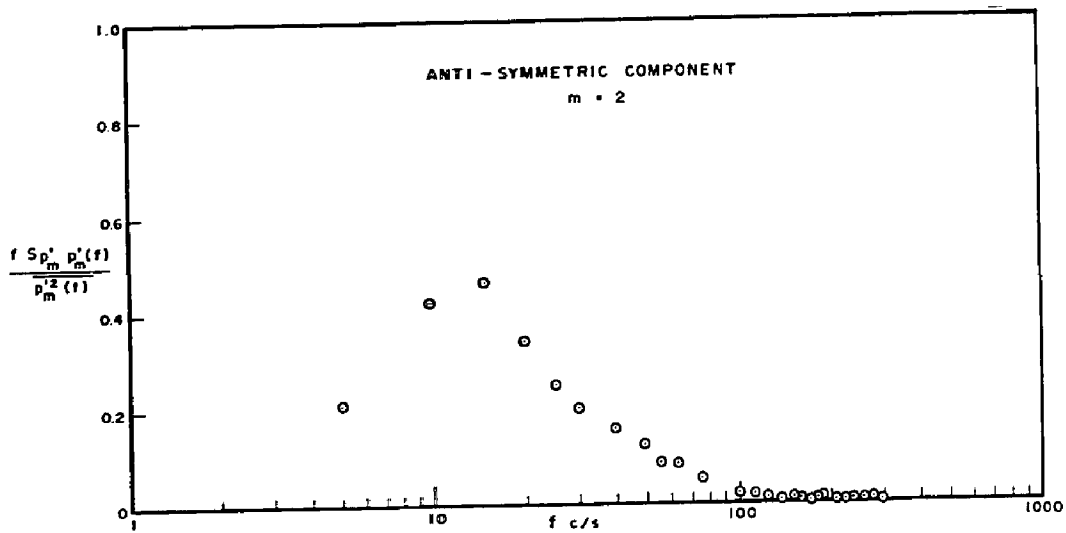


FIG.6.43 POWER SPECTRUM OF THE ANTI-SYMMETRIC COMPONENT OF THE GENERALIZED FORCE FOR HARMONIC m = 2

CHAPTER 7

APPROACHES TO THE PREDICTION OF DYNAMIC RESPONSE

7.1 Introduction

One of the main aims of the present work is to establish a reliable procedure for the prediction of the response of hyperbolic cooling towers to turbulent wind loading. Such a procedure should take into consideration the random nature of the wind loading and the dynamic response characteristics of the structure.

For a linear analysis, the wind response of cooling towers could be conveniently divided into two components; a mean and a dynamic (fluctuating) component. Both components could be treated separately and then superimposed to produce the final shell response.

Two formulations for the prediction of the mean wind response based on the modified finite difference method have been presented in Chapter 2. Both formulations allow for variations in geometry, variable wall thickness, variable shell stiffnesses, column supports, flexible foundations, top ring beam, and a number of possible combinations of boundary conditions. Their accuracy is

well established as shown by comparisons with previous work for a variety of problems (see Appendix II). Other approaches utilizing the finite element method (1), numerical integration technique (2) and the conventional finite difference formulation (3) have been used for comparison.

In this chapter, two approaches to the prediction of the dynamic component of the wind response will be developed. The first approach, a simplified one, is based on a quasi-static analysis of the shell response. The second is a more rigorous approach.

The quasi-static approach neglects any resonant response. There are many situations in which this is the case. In fact, where the soil conditions are favourable, the cooling tower shell could be designed in such a manner as to avoid any significant resonant response. This could be achieved by a careful choice of the geometric profile, adequate reinforcement, and a well proportioned column support system. Nevertheless, there will be other situations in which the resonance can not be effectively suppressed without paying a high penalty in cost. The quasi-static approach is, therefore, less general. It may also be necessary in the final design stage to apply a rigorous dynamic analysis.

The fundamental equations relevant for the quasi-static and the rigorous dynamic approaches could be

deduced from the general formulation of the response of shells of revolution to turbulent wind loading developed earlier in Chapter 3. These are described briefly in Sections 7.2.1 and 7.3.1 respectively. In the presentation, some simplifying assumptions based on experimental evidence are introduced. The relevant statistical properties of the wind pressure fluctuations are also underlined.

Both approaches are used to predict the dynamic response of two sample cooling tower models. The statistical properties of the wind pressure fluctuations required for the analysis were obtained from wind tunnel tests and are reported in Chapter 5. Comparisons are made with experimental measurements of the shell response wherever possible.

An investigation of the influence of possible variations in the statistical properties of the wind pressure fluctuations are carried out. Three main quantities were considered for this study. These are: a/ point of flow separation, b/ cross correlation coefficient for meridional and circumferential separations, and c/ standard deviation of the pressure fluctuations.

Comments on the reliability of the two approaches and the adequacy of the underlying assumptions are given. Some possible refinements in the analysis are also suggested.

7.2 Quasi-Static Approach

7.2.1 Theory

The dynamic response of structures to gusty wind could be generally separated into two parts. First, the response due to the low frequency components of the wind pressure fluctuations commonly referred to as quasi-static response. The second part comprises the resonant response components. The dominance of one part or the other depends mainly on the natural frequencies of the structure, the critical damping ratio, and the frequency range in which most of the energy of the wind pressure fluctuations are contained.

The present quasi-static approach is based on the premise that the lowest natural frequency of the cooling tower is sufficiently high such that the resonance could be neglected. Experimental (4) and theoretical investigations (2,4,5) of the free vibration of cooling towers have shown that the natural frequencies of typical towers are fairly high. A 500 ft. high hyperbolic cooling tower could have its lowest frequency higher than 1 cps.

The fundamental assumptions underlying the shell theory are outlined in Appendix I. In regard to the wind load, it will be assumed that the wind pressure fluctuations constitutes a stationary random process (6).

Let $y(s, \phi, t)$ be the instantaneous value of any of the response functions of the shell (displacement, stress, etc.) at position (s, ϕ) . As in equation (3.1), $y(s, \phi, t)$ can be expanded in terms of the mode shapes of vibration as follows:

$$y(s, \phi, t) = \sum_m \sum_i \{q_{m,i}(t) \cos m\phi + q'_{m,i}(t) \sin m\phi\} y_{m,i}(s) \quad (7.1)$$

in which, $y_{m,i}(s)$ is the i th meridional mode for the m th circumferential wave number and $q_{m,i}(t)$ and $q'_{m,i}(t)$ are time-dependent generalized coordinates.

The variance of $y(s, \phi, t)$ is given by:

$$\overline{y^2(s, \phi, t)} = \sum_m \sum_i \sum_n \sum_j \{ \overline{q_{m,i}(t) q_{n,j}(t) \cos m\phi \cos n\phi + q'_{m,i}(t) q'_{n,j}(t) \sin m\phi \sin n\phi} + 2 \overline{q_{m,i}(t) q'_{n,j}(t) \cos m\phi \sin n\phi} \} y_{m,i}(s) y_{n,j}(s) \quad (7.2)$$

in which n and j are alternative values of m and i respectively.

Following equation (3.56) and neglecting the resonance contribution, expressions for the covariance of the generalized coordinate $\overline{q_{m,i}(t) q_{n,j}(t)}$ could be related to the covariance of the generalized forces $\overline{p_{m,i}(t) p_{n,j}(t)}$ by,

$$\overline{q_{m,i}(t)q_{n,j}(t)} = \frac{1}{16\pi^4 f_{m,i}^2 f_{n,j}^2 M_{m,i} M_{n,j}} \overline{p_{m,i}(t)p_{n,j}(t)} \quad (7.3)$$

Expressions for $\overline{q'_{m,i}(t)q'_{n,j}(t)}$ and $\overline{q_{m,i}(t)q'_{n,j}(t)}$ can be similarly obtained.

Expressions for the covariance of the generalized forces given by equation (3.32) could be put in simple form if the correlation coefficient, $C(l, \phi, l', \phi')$ is replaced by,

$$C(l, \phi, l', \phi') = C_v(l, l') C_f(\phi, \phi') \quad (7.4)$$

in windward region, and by

$$C(l, \phi, l', \phi') = C_w(l, l') C_r(\phi, \phi') \quad (7.5)$$

in wake region, and that the standard deviation of pressure $\sigma_p(l, \phi)$ is replaced by:

$$\sigma_p(l, \phi) = \sigma_p(l_p, \phi_1) f_1(l) f_2(\phi) \quad (7.6)$$

in which (l_1, ϕ_1) is a reference point.

Experimental evidence supporting this decomposition is given in Chapter 5. Expressions for the covariance of the generalized coordinates thus reduce to,

$$\overline{p_{m,i}(t)p_{n,j}(t)} = s_o^4 \sigma_p^2(l_1, \phi_1) A_1 B_1 \quad (7.7)$$

$$\overline{p'_{m,i}(t)p'_{n,j}(t)} = s_o^4 \sigma_p^2(l_1, \phi_1) A_1 B_2 \quad (7.8)$$

$$\overline{p_{m,i}(t)p'_{n,j}(t)} = s_o^4 \sigma_p^2(l_1, \phi_1) A_1 B_3 \quad (7.9)$$

in which

$$A_1 = \int_0^1 \int_0^1 C_v(l, l') f_1(l) f_1(l') w_{m,i}(l) w_{n,j}(l') \gamma_2(l) \gamma_2(l') dl dl' \quad (7.10)$$

$$B_1 = \int_{-\phi_s}^{+\phi_s} \int_{-\phi_s}^{+\phi_s} C_f(\phi, \phi') f_2(\phi) f_2(\phi') \cos m\phi \cos n\phi' d\phi d\phi' + \int_{-\phi_s}^{+\phi_s} \int_{-\phi_s}^{+\phi_s} C_r(\phi, \phi') f_2(\phi) f_2(\phi') \cos m\phi \cos n\phi' d\phi d\phi' \quad (7.11)$$

$$B_2 = \int_{-\phi_s}^{+\phi_s} \int_{-\phi_s}^{+\phi_s} C_f(\phi, \phi') f_2(\phi) f_2(\phi') \sin m\phi \sin n\phi' d\phi d\phi' + \int_{-\phi_s}^{+\phi_s} \int_{-\phi_s}^{+\phi_s} C_r(\phi, \phi') f_2(\phi) f_2(\phi') \sin m\phi \sin n\phi' d\phi d\phi' \quad (7.12)$$

$$B_3 = \int_{-\phi_s}^{+\phi_s} \int_{-\phi_s}^{+\phi_s} C_f(\phi, \phi') f_2(\phi) f_2(\phi') \cos m\phi \sin n\phi' d\phi d\phi' + \int_{-\phi_s}^{+\phi_s} \int_{-\phi_s}^{+\phi_s} C_r(\phi, \phi') f_2(\phi) f_2(\phi') \cos m\phi \sin n\phi' d\phi d\phi' \quad (7.13)$$

and s_0 = total meridional length, $l=s/s_0$, $\gamma_2=r(s)/s_0$,
 ϕ = circumferential angle measured clockwise from the
 upstream stagnation line, $w_{m,i}(l)$ = mode shape of the
 normal displacement in the meridional direction, and $\phi_s =$
 angle of flow separation.

The covariance of the generalized forces defined by
 equations (7.7 to 7.9), describe in a simple manner the
 effective forces experienced by each single mode of
 vibration. In effect, they summarize a great deal of
 information regarding the wind pressure fluctuations
 exerted on the exterior surface of the shell in a neat
 and precise form.

Equations (7.1 to 7.13) describe all the necessary
 relations governing the quasi-static approach. The
 statistical properties of the wind pressure fluctuations
 relevant to this approach are:

- a) The standard deviation: $\sigma_p(l_1, \phi_1), f_1(l)$ and $f_2(\phi)$
- b) The correlation coefficient: $c_v(l, l'), c_f(\phi, \phi')$
 and $c_p(\phi, \phi')$.

Measurements of these variables across the shell
 surface obtained from wind tunnel tests are described in
 Chapter 5.

7.2.2 Application of Quasi-Static Approach

The accuracy of the quasi-static approach could be verified from comparisons with experimental measurements of cooling towers response to wind. To the author's knowledge, there is not as yet any published results in this regard. The only reported measurements have been obtained from wind tunnel tests.

Davenport and Isyumov (7) have used a 1/200 aeroelastic model of the 375 ft. high cooling tower of the Muskingum River power station to measure the total dynamic response in turbulent boundary layer flow. In Chapter 6, a 1/400 aeroelastic model of the same tower was used for the measurements of the modal and total dynamic response.

The quasi-static approach will be used in this section to predict the response of the two cooling tower models. Comparisons with experiments will be made where possible. The 1/200 scale model will be referred to as Model I and the 1/400 scale model as Model II.

7.2.2.1 Model I

The geometry of the model is illustrated in Fig. 7.1. It is geometrically identical to the rigid model used in the present study for the measurements of the wind pressure characteristics, Chapter 5, except for the wall thickness. The physical properties of the model material are given in Table 7.1.

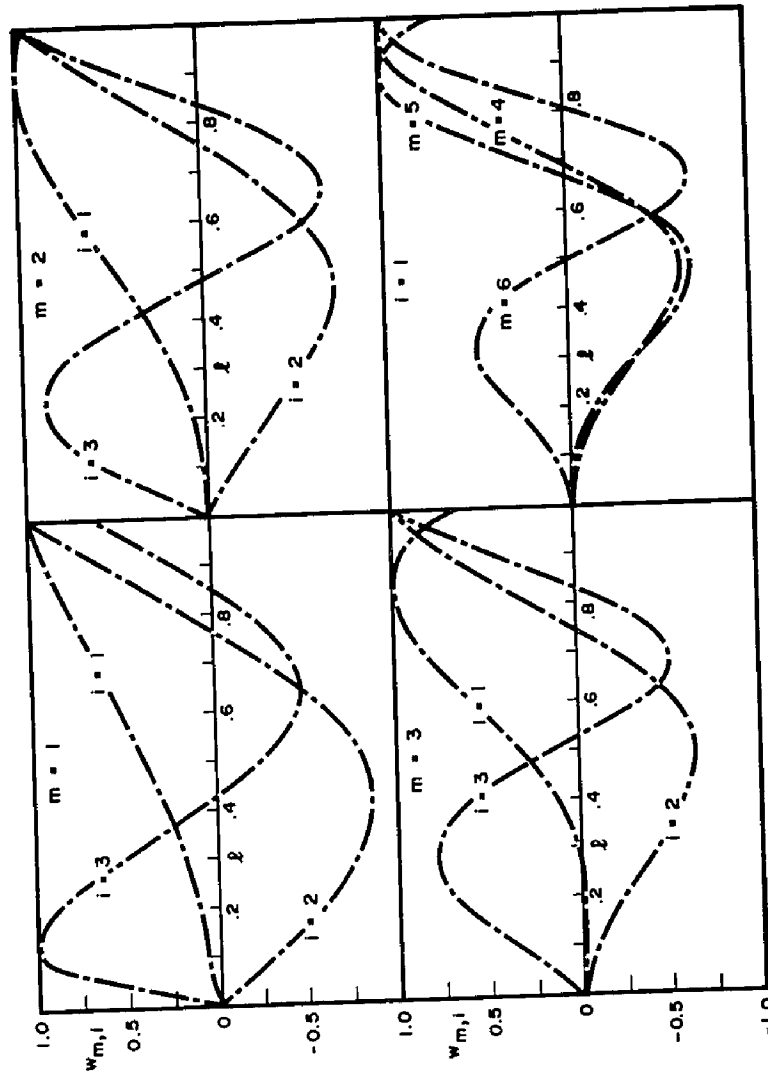


FIG. 7.2 MODAL DISPLACEMENTS ($w_{m,l}$) FOR HARMONICS $m=1$ TO 6

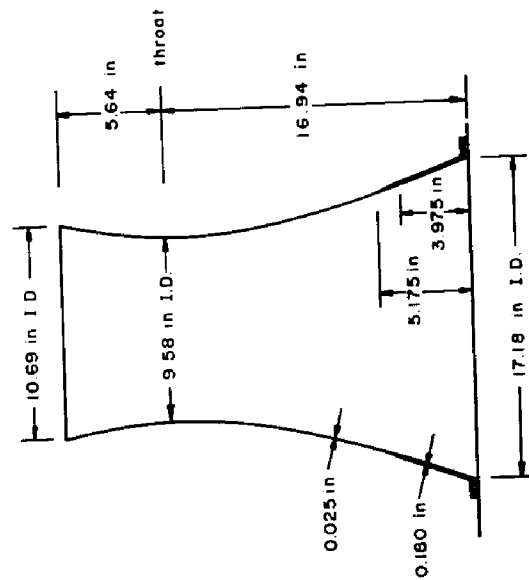


FIG. 7.1

The natural frequencies of the shell model, obtained using the modified finite difference method, are listed in Table 7.2. These results have been verified experimentally in Ref. (4). The modal configurations, in the meridional direction of the normal displacement w are shown in Fig. 7.2 for the first three modes of harmonics $m=1$ to 3 and for the fundamental modes of harmonics $m=4$ to 6. From equation (3.16), the generalized masses for various modes were obtained using the mode shapes for the three displacement components u , v , and w .

The next step is to compute the covariance of the generalized forces experienced by each mode of vibration. The relevant statistical properties of pressure fluctuations were obtained experimentally from wind tunnel measurements using a geometrically identical model. The results are reported in detail in Chapter 5.

The symmetric, anti-symmetric and cross-product components of the covariance of the generalized forces were computed for different modes of vibration using equations (7.7 to 7.9). For all modes considered, it was found that the covariance of the cross-product of the symmetric and anti-symmetric components of the generalized forces $\overline{p_{m,i}(t)p'_{n,j}(t)}$ is very small relative to $\overline{p_{m,i}(t)p_{n,j}(t)}$ and $\overline{p'_{m,i}(t)p'_{n,j}(t)}$. Therefore, $\overline{p_{m,i}(t)p'_{n,j}(t)}$ is set to zero.

TABLE 7.1 Physical Properties of Model I Material (Ref. 7)

Young's Modulus	0.738×10^6 psi
Shear Modulus	0.301×10^6 psi
Poisson's Ratio	0.23
Specific Gravity	2.23
Density	140 lb./ft. ³

TABLE 7.2 Natural Frequencies - Model I

<i>m</i> \ <i>i</i>	1	2	3
1	340	756	1005
2	197	392	763
3	170	208	464
4	129		
5	122		
6	142		
7	160		
8	216		
9	225		

Values of $\overline{p_{m,i}(t)p_{n,j}(t)}$ computed for the fundamental mode ($i=1$) of harmonics $m=1$ to 9 are given in Table 7.3. By far, the generalized forces experienced by harmonics $m=1$ to 3 are the most important ones. Recalling the Fourier representation of the mean wind pressures, the same three harmonics were also the most significant ones. Measurements of the wind pressure fluctuations have revealed similar characteristics to those of the mean wind pressures. Details are given in Chapter 5.

Table 7.4 shows also that the covariances of the generalized forces for different harmonics are of the same order as the variances of the individual harmonics and are, therefore, equally important.

Turning now to the anti-symmetric components of the pressure fluctuations, the covariances of the corresponding generalized forces were obtained using equation (7.8). The computed values for $\overline{p'_{m,i}(t)p'_{n,j}(t)}$ for the fundamental modes of harmonics $m=1$ to 9 are given in Table 7.4. The general remarks noted for the symmetric component are also observed here. Furthermore, the covariances of the anti-symmetric component of the generalized forces are of the same order as those for the symmetric components. Out of the three significant harmonics for both components, $m=1$, 2, and 3, the largest force component resides in harmonic $m=2$.

A breakdown of the results in Tables 7.3 and 7.4 to

TABLE 7.3 $p_{m,i}(t)p_{n,j}(t) / s_{op}^2(s_1, \phi_1) \times 100$

$n \backslash m$	1	2	3	4	5	6	7	8	9
1	0.934	0.811	0.050	-0.0001	-0.009	0.012	0.052	-0.012	-0.007
2		6.831	2.161	0.006	-0.0005	0.165	-0.134	0.031	0.203
3			2.105	-0.0007	-0.0017	0.059	-0.008	0.016	0.071
4				0.232	-0.039	0.014	-0.027	-0.004	0.040
5					0.054	-0.0008	0.004	0.003	-0.005
6						0.026	-0.027	0.001	0.027
7							0.075	-0.005	-0.044
8								0.005	0.002
9									0.058

TABLE 7.4 $P_{m,i}^i(t)P_{n,j}^j(t)/s_0^2 \sigma^2(S_1, \phi_1) \times 100$

$n \backslash m$	1	2	3	4	5	6	7	8	9
1	1.655	0.738	0.204	0.003	-0.019	0.098	-0.009	-0.053	0.091
2		4.047	1.530	0.003	-0.025	0.077	0.052	-0.030	0.073
3			2.380	0.0007	-0.057	0.098	0.067	-0.065	0.106
4				0.119	0.004	0.005	-0.003	0.0005	0.005
5					0.095	0.004	0.003	0.013	0.018
6						0.028	0.004	-0.010	0.022
7							0.025	-0.006	0.007
8								0.014	-0.009
9									0.039

Symmetric

contributions made from the pressure fluctuations in the windward and wake regions revealed an interesting feature. The contributions of the pressure fluctuations in the wake region to the covariances of the generalized coordinates were found to be much smaller than those from the windward region. For instance, their effective contribution to the variance of the symmetric components of harmonics $m=1, 2$, and 3 makes up for about 12, 1 and 2% of the respective variance. For the anti-symmetric components, the corresponding contributions are about 6.5, 0 and 1% respectively.

The results presented so far have been concerned with the fundamental modes only of various harmonics. Results for the second and third modes were also obtained. These are given in Tables 7.5 and 7.6 for the symmetric and anti-symmetric components respectively. Therein, results are given only for harmonics $m=1$ to 3 since other harmonics were barely significant. While the covariances of the generalized forces decrease in general, with increasing mode number (i), their magnitudes over the first three modes remain of the same order.

Having defined the covariances of the generalized forces, the covariances of the generalized coordinates of the shell response could be obtained in a straightforward manner using equation (7.3). The variance of the shell response could then be easily obtained by summing up

TABLE 7.5 $\frac{P_{m,i}(t)P_{n,j}(t)/s_0^4\sigma_p^2(s_1,\phi_1)}{X 100}$

	$i=1$			$i=2$			$i=3$			
	$m=1$	$m=2$	$m=3$	$m=1$	$m=2$	$m=3$	$m=1$	$m=2$	$m=3$	
$j=1$	$n=1$	0.934	0.811	0.050	-0.597	-0.296	-0.012	0.299	0.285	0.025
	$n=2$		6.831	2.161	-0.511	-2.464	-0.500	0.250	2.348	1.073
	$n=3$			2.104	-0.030	-0.741	-0.453	0.014	0.700	1.002
$j=2$	$n=1$				0.856	0.459	0.023	-0.517	-0.398	-0.029
	$n=2$					2.408	0.617	-0.274	-2.034	-0.761
	$n=3$						0.500	-0.014	-0.502	-0.562
$j=3$	$n=1$							0.382	0.278	0.019
	$n=2$								2.039	0.743
	$n=3$									0.868

Symmetric

contributions from different modes as shown in equation (7.2). The summation will be carried out over harmonics $m=1$ to 3 only since contributions from other harmonics were found to be small.

Because of the significance of the generalized forces experienced by higher modes, Table 7.5 and 7.6, it was felt necessary to study the convergence of the contribution to the shell response of each of the individual harmonics. The response is obtained in terms of the meridional strain on the inside surface of the shell. Figs. 7.3 to 7.5 show the variation with height at $\phi=0$ and 90° of the successive summation of modal contributions, up to $i=3$, for harmonics $m=1$ to 3, respectively.

The fundamental mode is shown to provide a good approximation to the total contribution of harmonic $m=1$. However, this is not the case for other harmonics, as the number of modes required increases with increasing m . This is mainly due to the fact that as m increases, the mode shape in the meridional direction becomes more rapidly varying. While the first two modes approximate fairly well the contribution of harmonic $m=2$, three modes are required to describe the contribution to the response of harmonic $m=3$. It is generally observed, that the convergence near the shell base is much slower than that at the rest of the shell. These remarks regarding the convergence of different harmonics have to be considered

VARIATION OF MODAL RESPONSE OF HARMONICS $m=1&2$ WITH HEIGHT

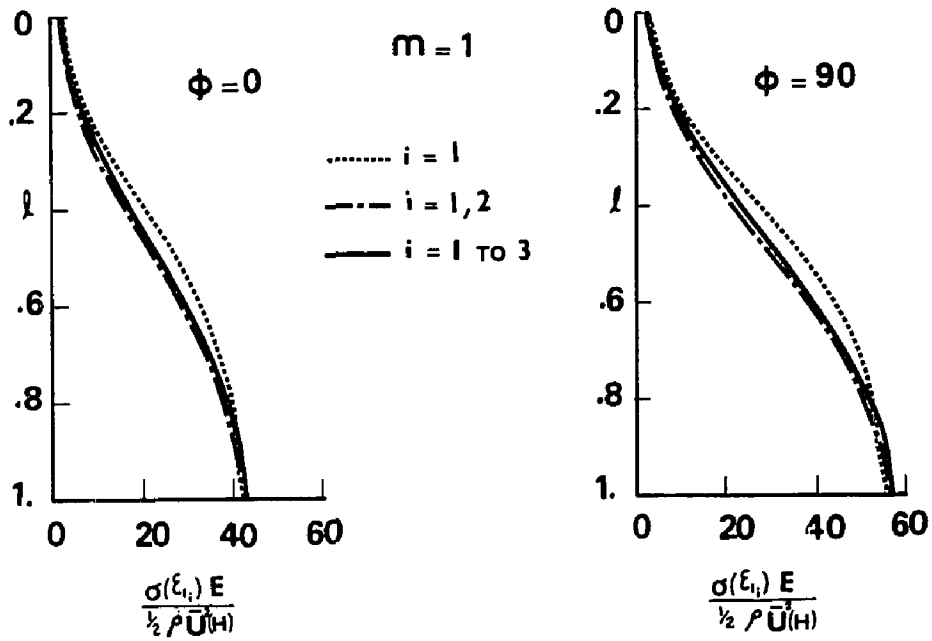


FIG. 7.3

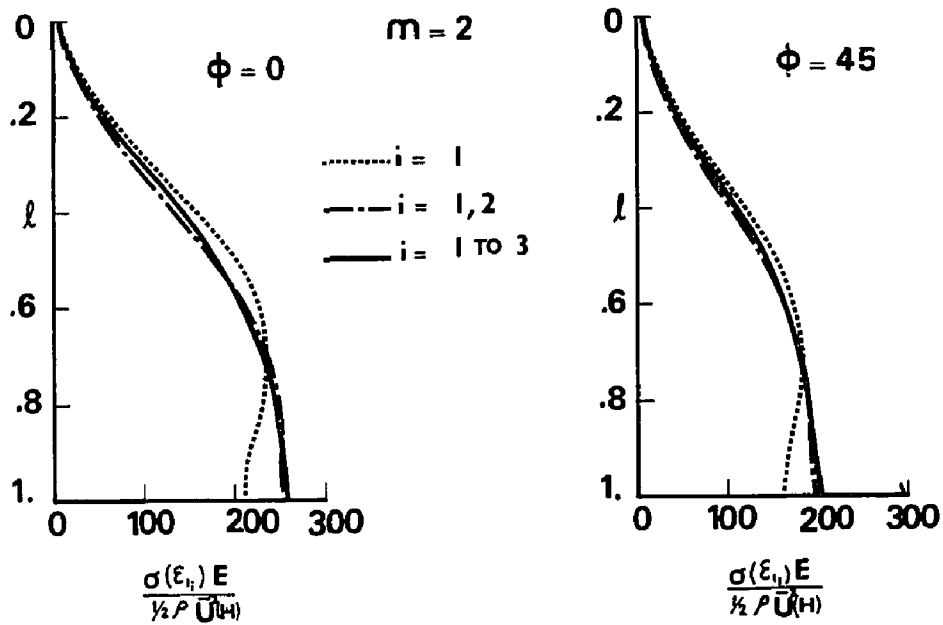


FIG. 7.4

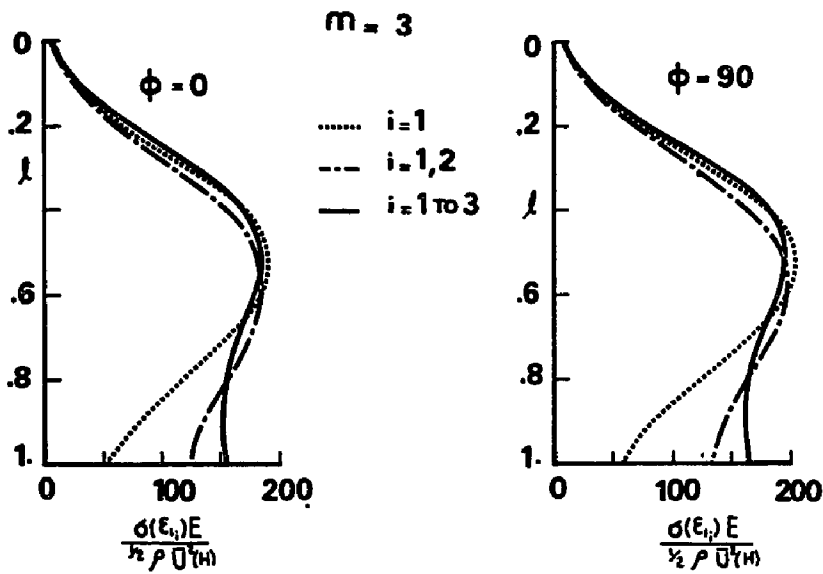


FIG. 7.5 VARIATION OF MODAL RESPONSE OF HARMONIC $m=3$ WITH HEIGHT

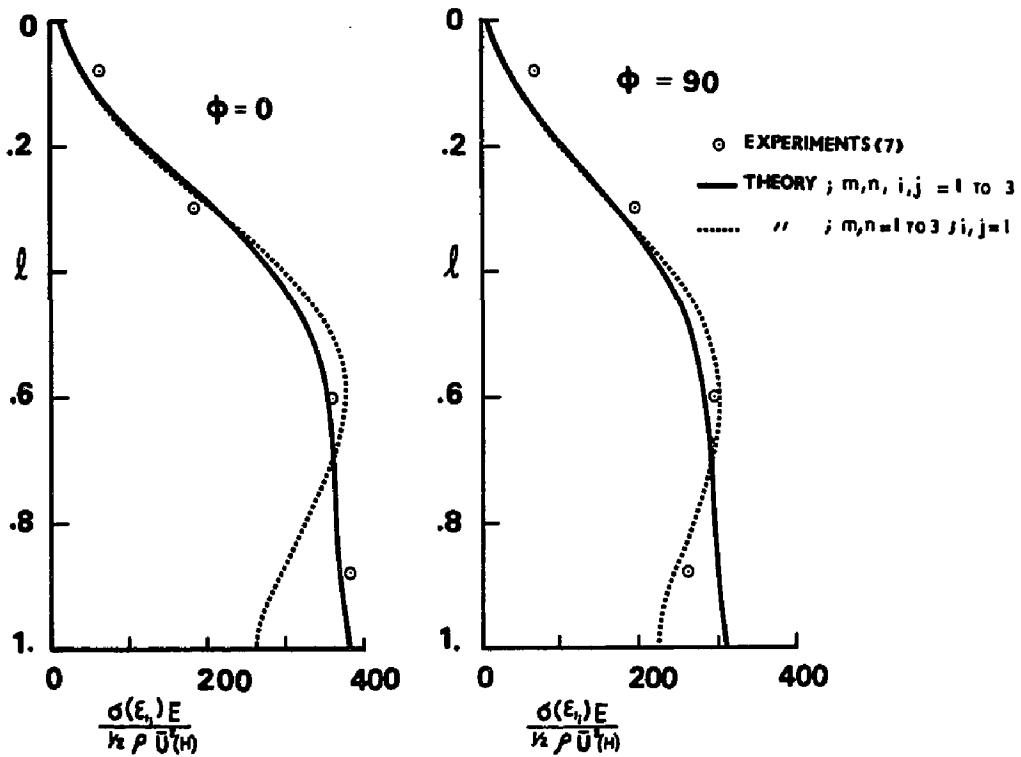


FIG. 7.6

FIG. 7.7

VARIATION OF TOTAL RESPONSE WITH HEIGHT

with some reservation when predicting the response of other towers with different geometries or boundary conditions since the mode shapes could change considerably.

The total response of the shell can now be obtained by the summation of the modal response components. Figs. 7.6 & 7.7 show the vertical distribution of the standard deviation of the meridional strain on the inside surface of the shell at $\phi=0$ and 90° . The horizontal distributions of the response at four levels, $0.27H$, $0.5H$, $0.75H$, and $0.94H$ are also shown in Figs. 7.8 to 7.11 respectively. Comparisons are made with experimental results by Davenport and Isyumov (7) from wind tunnel tests.

In general, the predicted response is in good agreement with the experimental measurements. It also indicates that the present approach could predict, with sufficient accuracy, the response at regions of largest strain and correspondingly largest stress. As mentioned earlier, this results when the resonant response, similar to the present sample problem (8) is very small relative to the response due to background turbulence.

The agreement between theory and experiment in the wake region is only fair as shown in Figs. (7.8 to 7.11). Even by including higher harmonics up to $m=8$ in the summation of equation (7.2), the discrepancy between both results still persists. The inclusion of resonance contribution will not improve the situation since it will

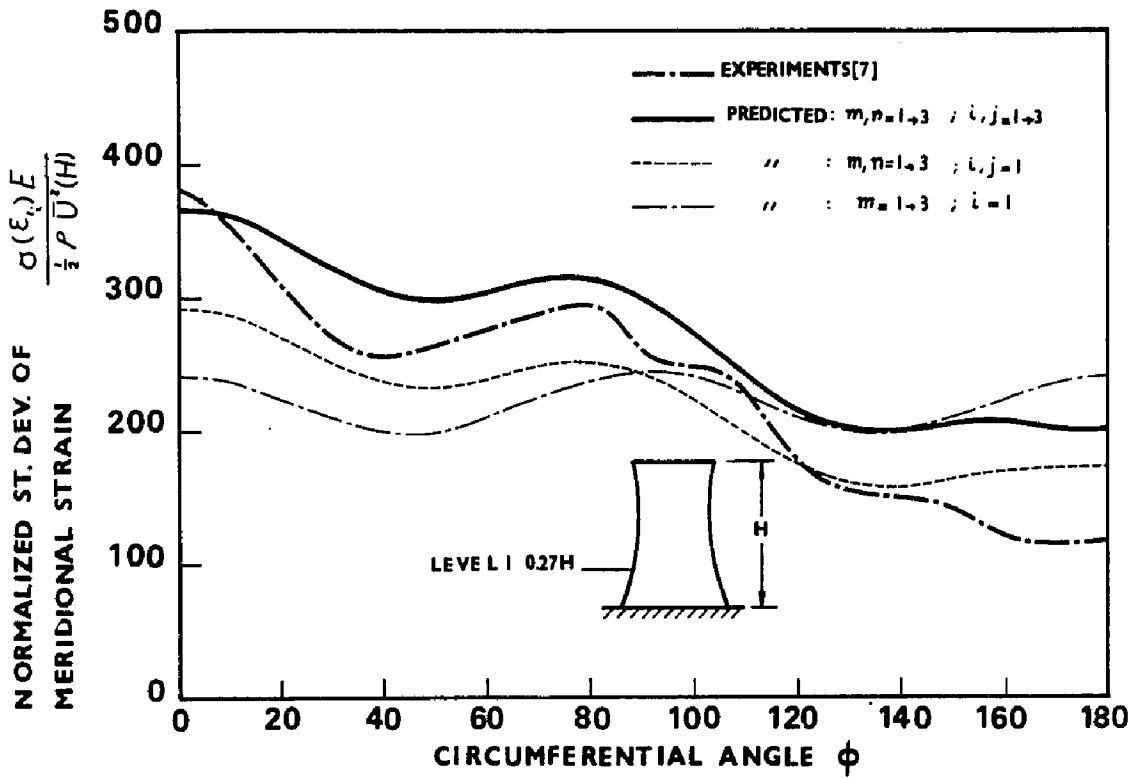


FIG. 7.8

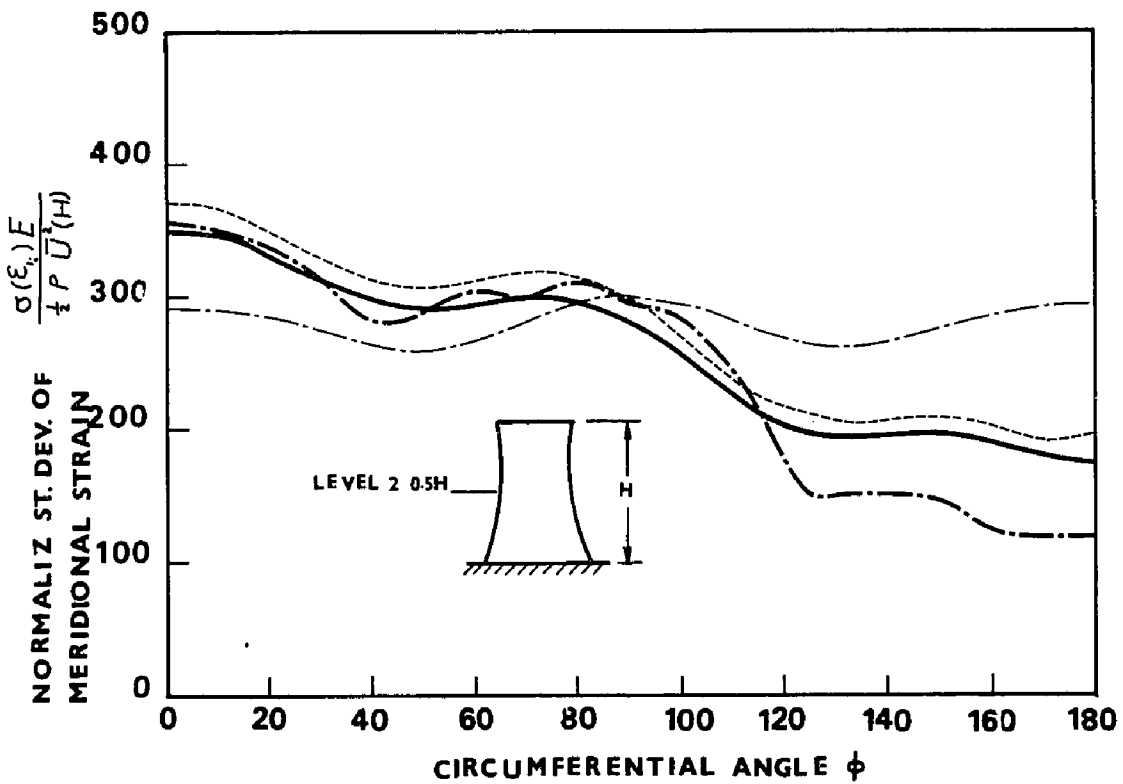


FIG. 7.9

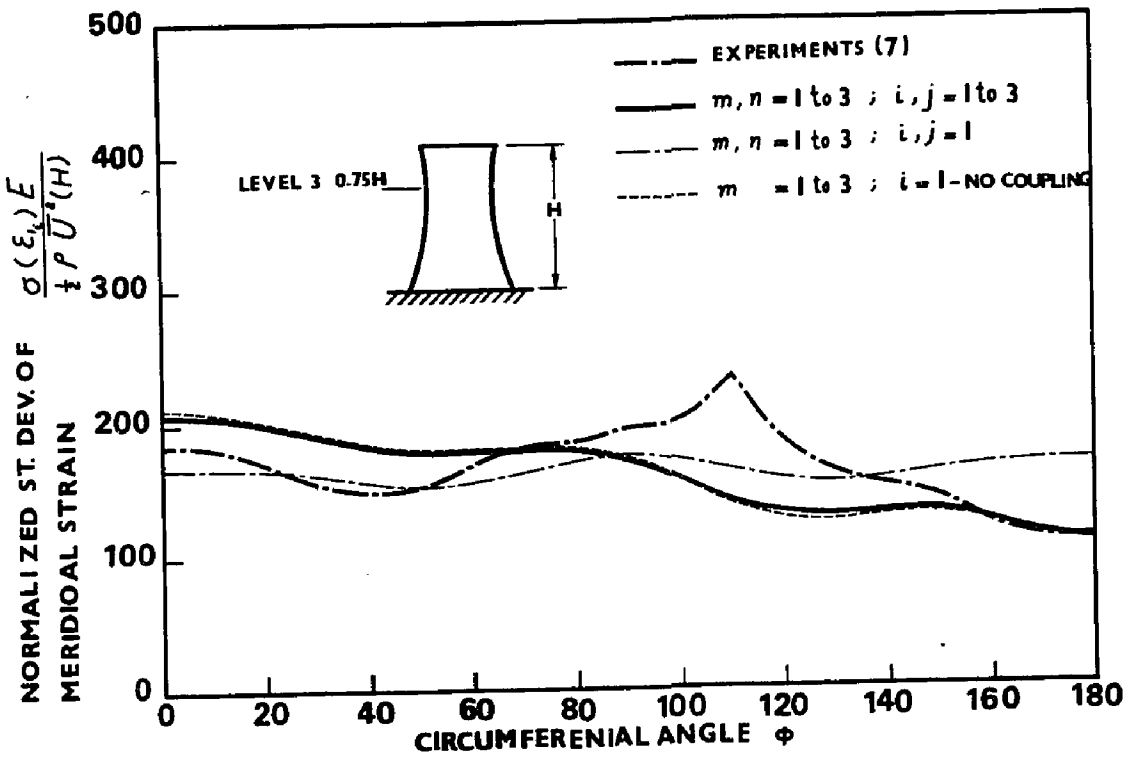


FIG. 7.10

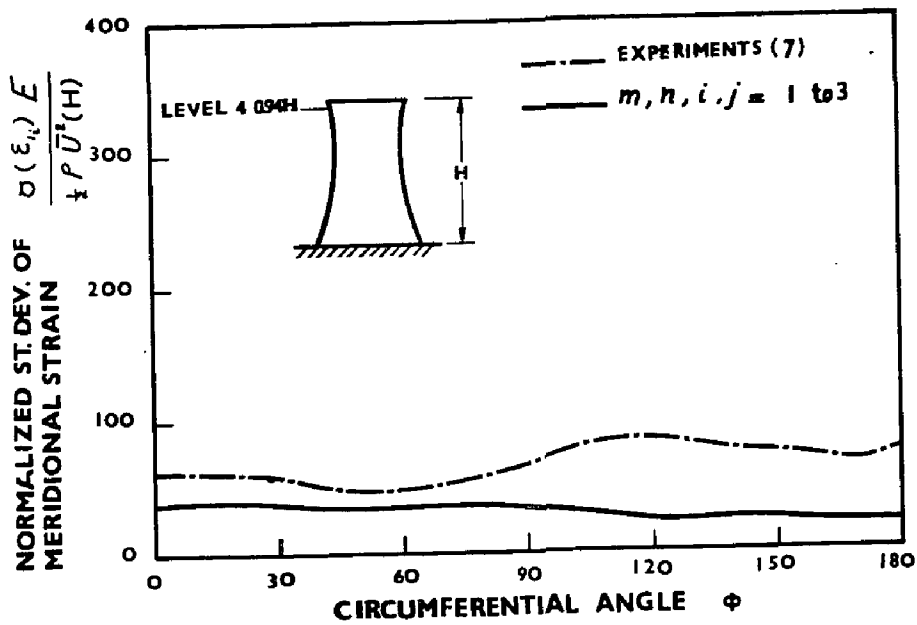


FIG. 7.11

simply add to the quasi-static response thus increasing the margin of discrepancy. Therefore, it is not a problem of convergence or resonance contribution but rather due to some deficiency in the description of the wind pressure input, experimental errors in response measurements, and/or the severity of some of the assumptions underlying the theory. The significance of this is reduced by the fact that stresses in this region are much smaller than the windward region, which is usually the design criteria.

The good agreement between experimental and theoretical results at mid-height in the windward region could be attributed to the fact that the end effects on the pressure field, which were not incorporated in the theoretical analysis, did not significantly influence the response there. However, these end effects would certainly have contributed to the poor agreement near the top (0.94H). Also, experimental measurements reported in Ref. (9) suggest that resonance near the top of the model is much more significant than at the rest of the shell. The theoretical analysis of the dynamic response including resonance, presented in Section 7.3, shows that at this level (0.94H) the resonance contribution probably exceeds the quasi-static response. While the end effects might have contributed to the poor agreement between theory and experiment near the top, the single most important

reason for the errors comes from neglecting the resonance contribution.

To explore the significance of the coupling between different modes, the cross-product terms of equation (7.2) were dropped out. The corresponding final response contributions excluding coupling are shown in Figs. 7.8 to 7.10. The obvious symmetry of all distributions at $\phi = \pm 90^\circ$ results from the way in which random functions are added and the fact that \sin^2 and \cos^2 terms are both symmetric about $\phi = \pm 90^\circ$. Thus, it becomes clearly evident that the response predicted by neglecting coupling is not adequate. Coupling terms must, therefore, be included.

7.2.2.3 Model II

The geometry of Model II is described in Fig. 6.1 and its material properties are given in Section 6.2.2. This model was used in the experimental study of the shell dynamic response described in Chapter 6. Therein, the modal response contributions of individual or certain combinations of harmonics along with the total dynamic response are reported.

The natural frequencies for different harmonics are listed in Table 6.3. The corresponding modal configurations for the normal displacement and the meridional strain at the inside surface of the shell are shown in Figs. 6.3 and 6.4 respectively.

The covariance of the generalized forces could now be computed using equations (7.7 to 7.9). The relevant statistical properties of the wind pressure fluctuations were assumed to be the same as those for Model I. However, the experimental measurements of Model II response were carried out at $R_e \approx 0.85 \times 10^5$, while the pressure measurements on Model I were conducted at $R_e \approx 1.8 \times 10^5$. This difference in R_e may influence the characteristics of the wind pressure fluctuations. Experimental measurements of the mean wind pressure distribution (7), in this range of Reynolds number, indicate that the peak suction at $R_e \approx 0.85 \times 10^5$ is reduced by about 15 to 20%.

For brevity, detailed results of the covariance of the generalized forces will not be given here, as they exhibit similar behaviour to those of Model I.

The covariances of the generalized coordinates were then obtained from equation (7.3) by direct substitution of the computed covariances of the generalized forces. These were used to determine the individual response of harmonics $m=1, 2, \text{ and } 3$.

The predicted contribution of harmonic $m=2$ to the total shell response at levels 1 and 3 (0.56H and 0.103H) are compared with the experimental results in Figs. 7.12 and 7.13 respectively. The predicted results contain the first three modes of this harmonic ($i=1$ to 3). Coupling between modes is included.

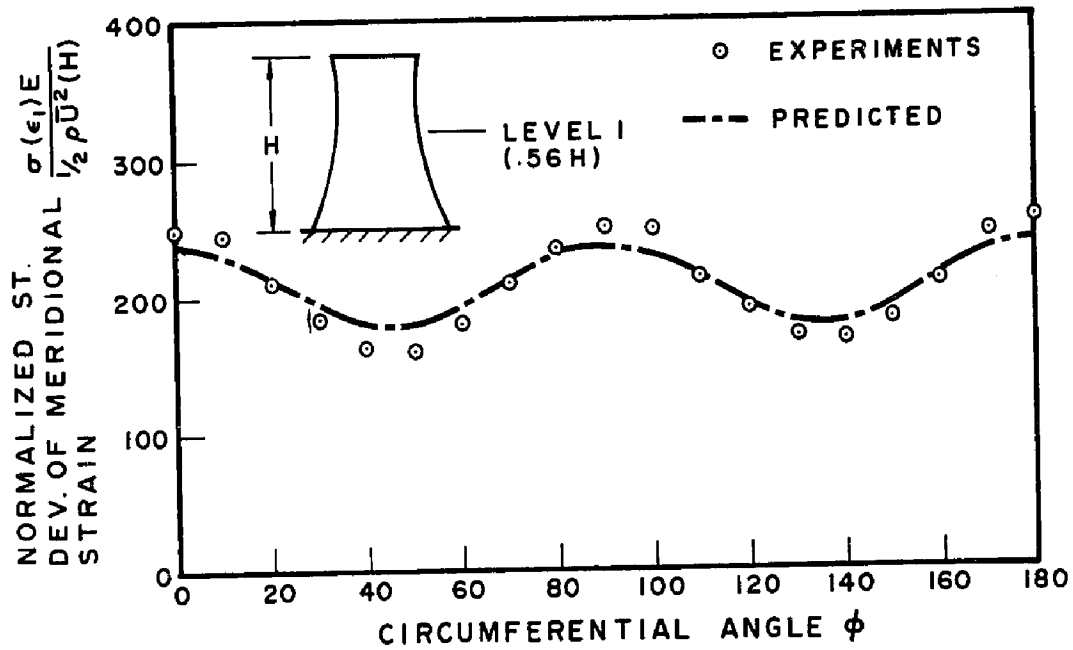


FIG. 7.12 VARIATION OF MODAL RESPONSE OF HARMONIC $m = 2$

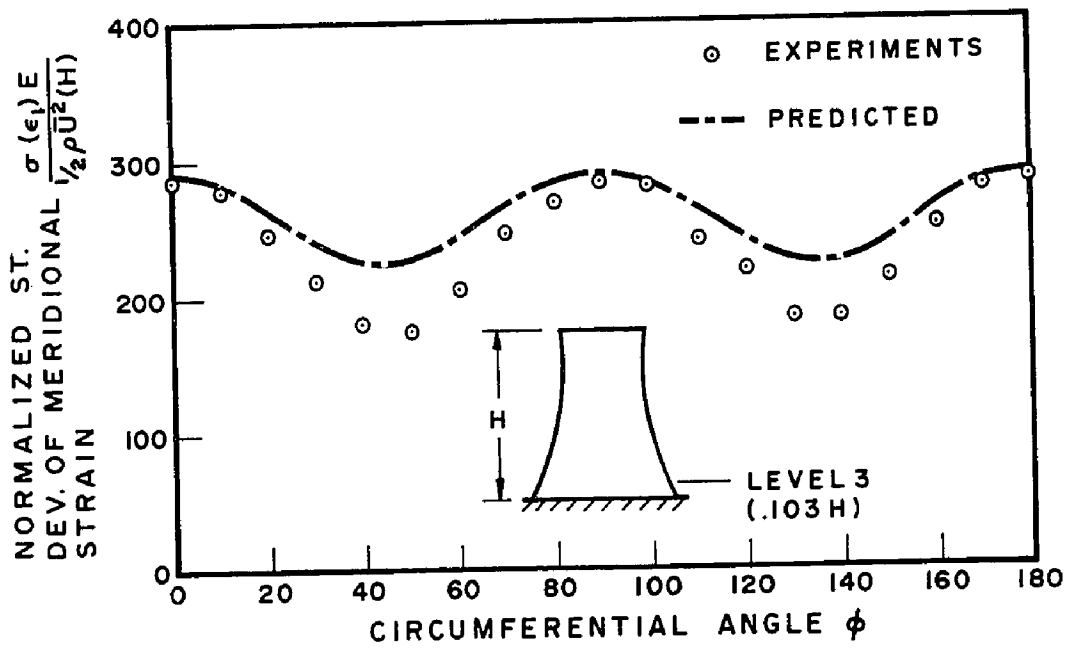


FIG. 7.13 VARIATION OF MODAL RESPONSE OF HARMONIC $m = 2$

Figs. 7.12 and 7.13 show that the theoretical results compare fairly well with the experiments. The agreement between both results would not have been as good had the resonant response been significant. As shown in Figs. 6.30 and 6.31, the resonant response is about 5% only of the total standard deviation of this harmonic.

It is observed, however, that the quasi-static approach tends to over-estimate somewhat the anti-symmetric component of the response of harmonic $m=2$. This is not a problem of convergence since the first three modes have proved to be enough as shown in Table 7.7. No specific reason for this over-estimate could be singled out with certainty in view of the multiplicity of the parameters required for the analysis. One of these is the difference between the actual properties of the wind pressure fluctuations and that adopted in the analysis.

In the modal response measurements of Chapter 6, it was not possible to isolate the individual response of the odd harmonics. Rather, their combined response was obtained. Using the present quasi-static analysis, it was found that the response of harmonics $m \geq 5$ is very small compared to that of $m=1$ to 3 and could be neglected.

The predicted combined response of harmonics $m=1$ to 3 is compared with the experimental results in Figs. 7.14 to 7.16. As shown, the agreement between both results is only fair with errors of the order of 20%. The

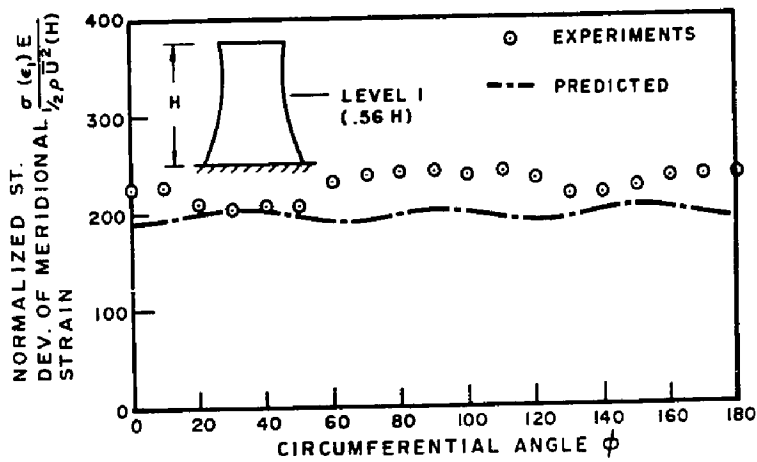


FIG. 7.14 VARIATION OF MODAL RESPONSE OF HARMONICS $m = 1$ AND 3 AROUND SHELL CIRCUMFERENCE

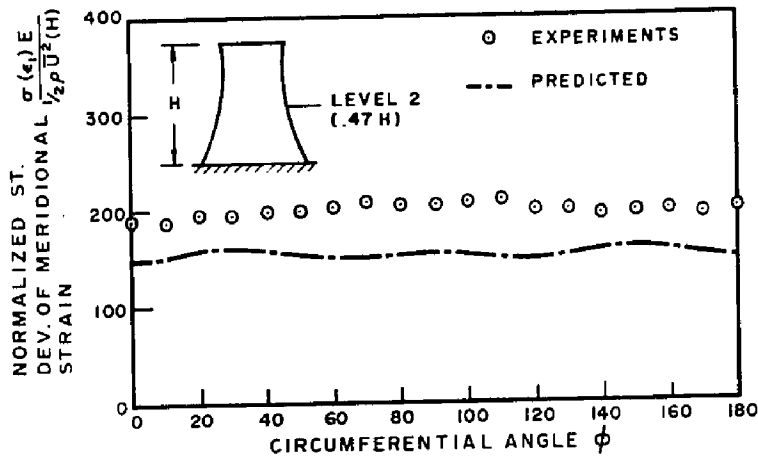


FIG. 7.15 VARIATION OF MODAL RESPONSE OF HARMONICS $m = 1$ AND 3

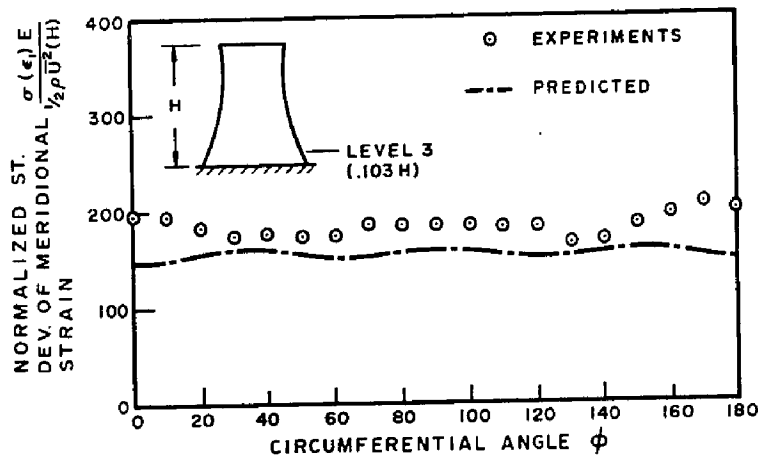


FIG. 7.16 VARIATION OF MODAL RESPONSE OF HARMONICS $m = 1$ AND 3

TABLE 7.7 Convergence of the Contribution of $m=2$ vs.Mode Number i

Number of Modes in Summation i	Normalized St. Dev. of Meridional Strain $\frac{\sigma(\epsilon_1)_i E}{\frac{1}{2}\rho\bar{U}^2 (H)}$			
	$\phi=0$		$\phi=45$	
	Level 1 (0.56H)	Level 3 (0.103H)	Level 1 (0.56H)	Level 3 (0.103H)
1	251	249	193	191
2	227	285	175	220
3	234	289	180	222

TABLE 7.8 Convergence of the Contribution of $m=1+3$ vs.Mode Number i

Number of Modes in Summation i	Normalized St. Dev. of Meridional Strain $\frac{\sigma(\epsilon_1)_i E}{\frac{1}{2}\rho\bar{U}^2 (H)}$					
	$\phi=0$			$\phi=90$		
	Level#1	Level#2	Level#3	Level#1	Level#2	Level#3
1	54.8	41.6	131	64	55.3	145
2	179	155	129	187	162	140
3	190	149	149	196	153	158

significance of these errors on the total response calculation is considerably reduced because of the predominance of the response of $m=2$ and the way in which random functions are added. The estimated errors are of the order of 7% at $\phi=0$.

The individual response contributions of harmonics $m=1$ and 3 are given in Table 7.8. The convergence of each component is also shown by successive summation over higher modes.

7.2.3 Parametric Study

The prediction of the dynamic wind response of cooling towers requires adequate knowledge of the appropriate statistical properties of the wind pressure fluctuations. Wind tunnel measurements at $Re=1.8 \times 10^5$ are now available (see Chapter 5). Reported full scale measurements are very scarce.

While the general features of the pressure characteristics as measured from the model tests are not expected to vary greatly from full scale behaviour, their details could vary significantly. Therefore, it is useful to study the influence of the possible variations in the statistical properties of the wind pressure fluctuations of the wind response of cooling towers.

The measured wind pressure characteristics are also liable to experimental errors. These errors may be

grouped in two main categories: a) instrument errors, and b) statistical errors encountered in the analysis of the wind pressure records. From repeated test measurements, it is estimated that the collective amount of errors in the results of wind pressure characteristics, presented in Chapter 5, could range between $\pm 5\%$. Therefore, the parametric study would help to establish the sensitivity of the predicted shell response to errors commonly encountered in the experimental measurements.

Three main parameters of the wind pressure characteristics will be subject to the present parametric study.

These are:

1. Angle of flow separation; by far the most important.
2. Shape functions of the correlation coefficients for circumferential and meridional separations; $C_y(l, l')$, $C_f(\phi, \phi')$, and $C_r(\phi, \phi')$.
3. Distribution of the standard deviation in the horizontal direction.

The point of flow separation, ϕ_s , exhibits considerable variations with varying flow conditions. Results from model tests, at $R_e = 1.8 \times 10^5$, indicate that the flow separation takes place at $\phi_s = 120^\circ$. At high Reynolds numbers, however, the point of flow separation moves forward accompanied by progressive widening of the wake region. Values of ϕ_s obtained from full scale tests at

$R_e = 6.53 \times 10^7$ (9) and from model tests at $R_e = 7.4 \times 10^6$ (10) were found to be about 95° and 92° respectively. Accordingly, the points of flow separation tested in the parametric analysis were chosen to be in the range $\phi_s = 90^\circ$ to 120° .

The available wind pressure characteristics, however, were obtained for $\phi_s = 120^\circ$ only. But since the main objective is to study the influence of ϕ_s on the shell response alone, the pressure characteristics for all values of ϕ_s were assumed to be the same as for $\phi_s = 120^\circ$. Hence, the circumferential angles in the windward region were reduced by a factor of $\phi_s/120$ and in the wake region were increased by a factor of $180 - \phi_s/60$, in the processing of the standard deviations and the correlation coefficients of the wind pressure fluctuations.

In the analysis of shell response (equations 7.1 to 7.13), it is seen that the only quantities affected by ϕ_s are B_1 , B_2 , and B_3 . The latter quantity, representing the correlation between the symmetric and anti-symmetric components of the generalized forces, was found to be very small and, therefore, will not be considered here.

The variations of B_1 and B_2 with ϕ_s for harmonics $m=1$ to 3 are shown in Figs. 7.17 and 7.18 respectively. The harmonic component $m=2$ shows, by far, the strongest dependence on ϕ_s for both B_1 and B_2 . It is also shown that for $m=1$, both B_1 and B_2 exhibit slight variations only

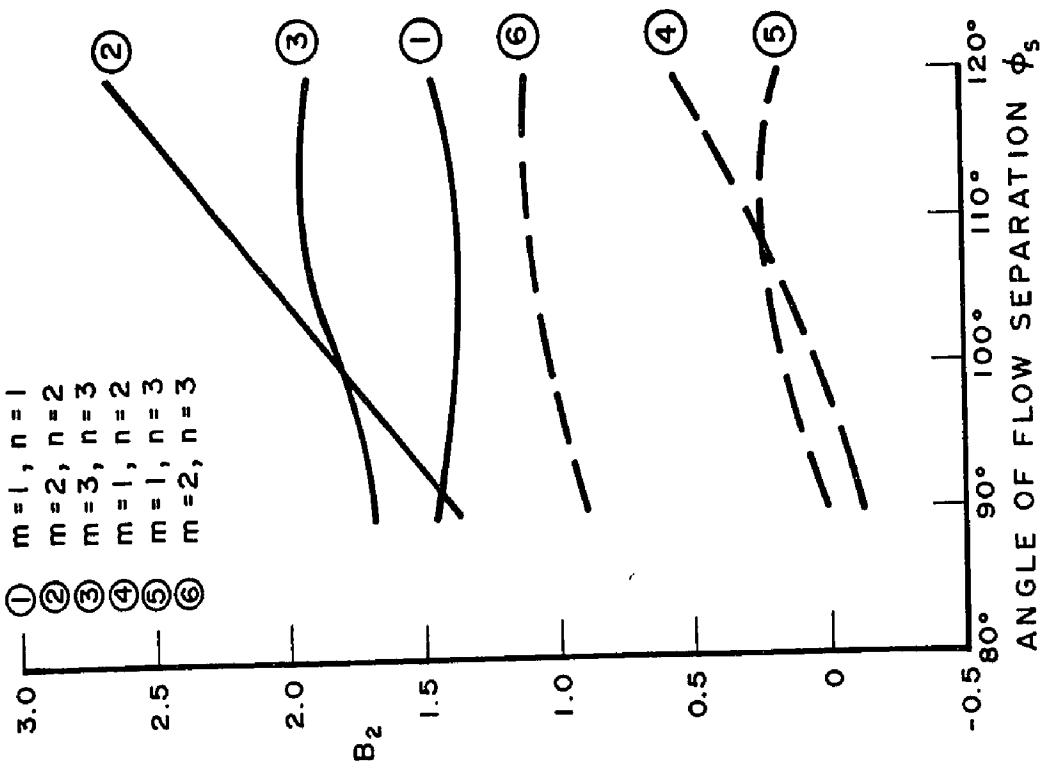


FIG. 7.18 DEPENDENCE OF B_2 ON ϕ_s

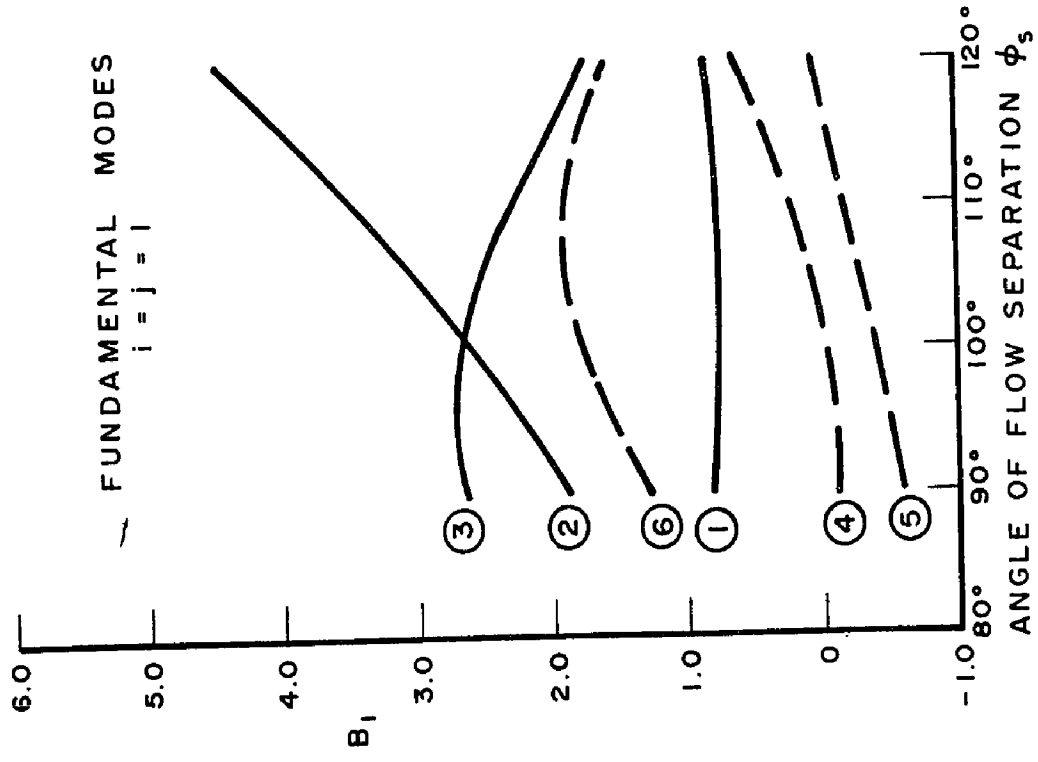


FIG. 7.17 DEPENDENCE OF B_1 ON ϕ_s

with ϕ_s . The results further indicate that while B_1 decreases with ϕ_s , for $m=3$, B_2 displays completely the opposite trend. Using these results for B_1 and B_2 , it could be shown that, in general, the total shell response will gradually decrease as the points of separation moves forward. This indicates that wind tunnel measurements of response may be an over-estimate of the full scale response. Note also that this behaviour is somewhat similar to the influence of ϕ_s on the static wind stresses.

The influence of small variations in the correlation coefficient for horizontal separations was also investigated. The three distributions of $C_f(\phi, \phi')$ and $C_r(\phi, \phi')$ considered are shown in Fig. 7.19. The corresponding values for B_1 and B_2 for harmonics $m=1$ to 3 are given in Tables 7.9 and 7.10 respectively. Here again, the components of B_1 and B_2 for harmonic $m=2$ were found to be the most sensitive to changes in the distribution of the correlation coefficients. On the other hand, harmonics $m=1$ and 3 show little change for the same variations in $C_f(\phi, \phi')$ and $C_r(\phi, \phi')$. The cross-product terms involving $m=2$ are also sensitive to small variations in the correlation coefficients.

The variation of $C_v(l, l')$ and its effect on A_1 (equation 7.10) is also examined. In the experimental measurements of Chapter 5, it was found that $C_v(l, l')$ could be adequately represented by the following expres-

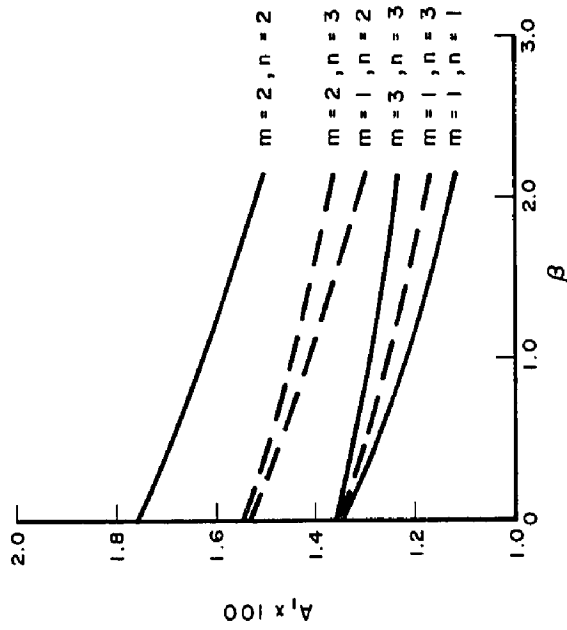


FIG. 7.20 DEPENDENCE OF A_1 ON β

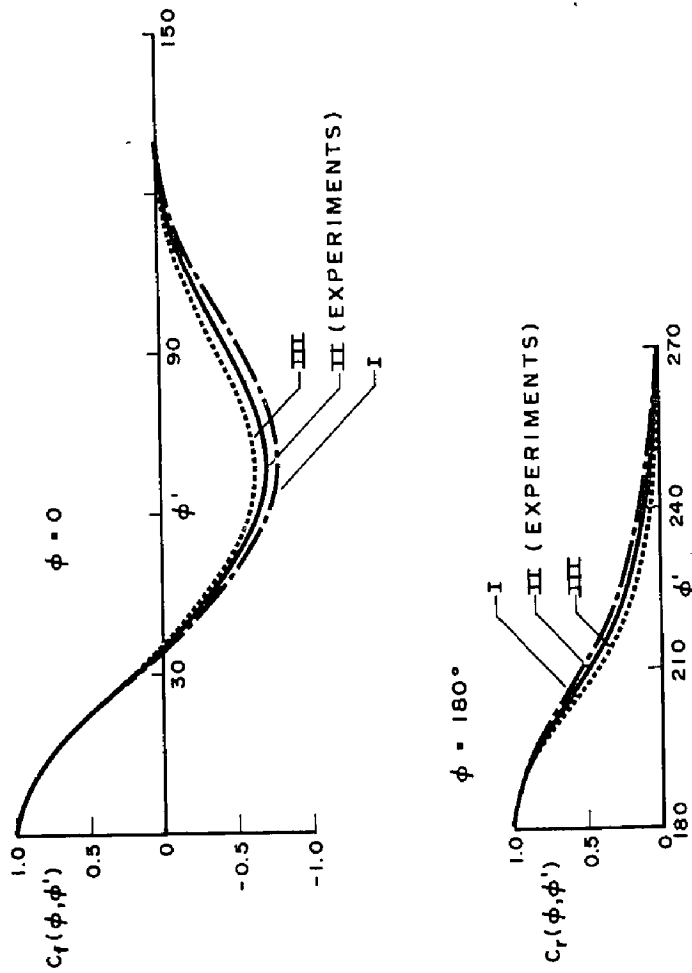


FIG. 7.19 VALUES OF CORRELATION COEFFICIENTS $C_r(\phi, \phi')$, $C_r(\phi, \phi')$

TABLE 7.9 Variations in B_1 due to Small Variations in the Details of $C_h(\phi, \phi')$

Case No. (Fig. 7.19)	$B_1 = \int_0^{2\pi} \int_0^{2\pi} C_h(\phi, \phi') f_2(\phi) f_2(\phi') \cos m\phi \cos n\phi' d\phi d\phi'$					
	$m=1, n=1$	$m=2, n=2$	$m=3, n=3$	$m=1, n=2$	$m=1, n=3$	$m=2, n=3$
I	0.786	4.781	1.688	0.643	0.088	1.667
II	0.823	4.455	1.686	0.613	0.042	1.564
III	0.858	4.127	1.685	0.321	-0.004	1.454

TABLE 7.10 Variations in B_1 due to Small Variations in the Details of $C_h(\phi, \phi')$

Case No. (Fig. 7.19)	$B_2 = \int_0^{2\pi} \int_0^{2\pi} C_h(\phi, \phi') f_2(\phi) f_2(\phi') \sin m\phi \sin n\phi' d\phi d\phi'$					
	$m=1, n=1$	$m=2, n=2$	$m=3, n=3$	$m=1, n=2$	$m=1, n=3$	$m=2, n=3$
I	1.226	2.761	1.874	0.515	0.343	1.115
II	1.451	2.638	1.906	0.558	0.172	1.102
III	1.676	2.516	2.000	0.550	-0.001	1.059

sion, irrespective of the circumferential location,

$$C_v(l, l') = e^{-\beta \Delta l^2} \quad (7.14)$$

in which, $\beta = 1.85$ and $\Delta l = |l - l'|$.

In the analysis, values of β were varied from 0 to 2.2. $\beta = 0$ represents the case where there is no loss of correlation irrespective of the meridional separation. The computed results of A_1 for the fundamental modes of harmonics $m=1$ to 3 are shown in Fig. 7.20. For all harmonics, the value of A_1 decreases gradually as the loss of correlation, represented by increasing values of β increases. The results further indicate that experimental errors in the estimation of β in the order of $\pm 5\%$ will produce errors in the range ± 1.5 to 2% only; thus, indicating the insensitivity of A_1 to usual experimental errors in β . It is not likely that model measurements of $C_v(l, l')$ are very different from full scale.

Finally the influence of the variations in the standard deviation of the pressure fluctuations around the shell circumference $\sigma_p(s, \phi)$, will be discussed. For this purpose, two different distributions of $\sigma_p(s, \phi)$ are considered. The first is obtained from the experimental measurements of Chapter 5 (distribution I). Distribution II was obtained by Davenport and Isyumov (7) for the same model and flow conditions but with a surface roughness of $\frac{k_s}{d} \approx 5 \times 10^{-3}$.

Distributions I and II are compared with the predicted results for full scale conditions in Fig. 7.21. The predicted results were computed from equation (5.7) assuming quasi-steady conditions. The mean wind pressure distribution reported by Niemann (9), from full scale measurements was used in the analysis.

The values of B_1 and B_2 , computed for the fundamental modes of harmonics $m=1$ to 3 are shown in Table 7.11 for both distributions (I and II). In general, it is found that the contributions of all modes for distribution I are considerably different from those obtained for distribution II. The most striking difference occurs for the component of B_1 associated with harmonic wave number $m=2$. The value of this component for distribution II is almost one third of that obtained if distribution I is considered instead.

Since the modal shell response is directly related to the modal components of B_1 and B_2 , then it would be expected that the final response of the shell for distribution II will be somewhat less than 50% of the response expected if distribution I is considered.

The values of B_1 and B_2 for the predicted distribution of $\sigma_p(s, \phi)$, using a two-dimensional quasi-steady theory, could be deduced approximately from Figs. 7.17 and 7.18 for $\phi_s \approx 95^\circ$.

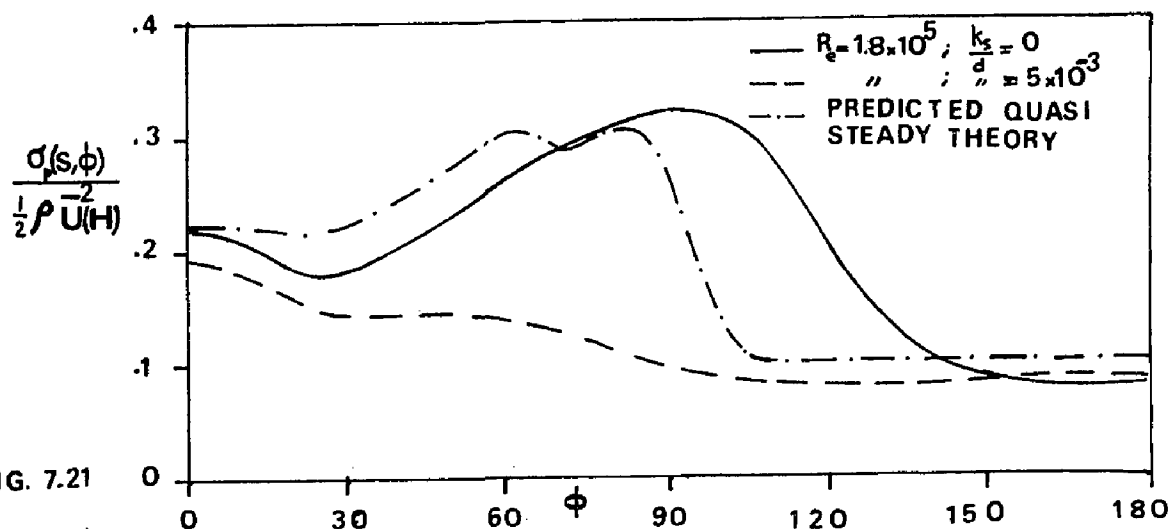
TABLE 7.11 Dependence of B_1 and B_2 on the St. Dev. of the Wind Pressure Fluctuations

m	n	B_1		B_2	
		Distr. I	Distr. II	Distr. I	Distr. II
1	1	0.823	0.624	1.451	0.569
2	2	4.455	1.588	2.638	1.270
3	3	1.686	0.942	1.906	0.918
1	2	0.613	0.475	0.558	0.539
1	3	0.042	0.387	0.172	0.423
2	3	1.564	0.930	1.102	0.722

7.2.4 Comments on the Adequacy of the Quasi-Static Approach

Approach

The adequacy of the quasi-static approach is now established in the light of the comparisons between predicted results and experimental measurements. Although the approach was applied only to cooling tower models, it is believed that it will be useful for full scale towers,



provided that the appropriate properties of the wind pressure fluctuations are defined correctly.

The approach could be as reliable as a more rigorous dynamic approach only if the natural frequencies of the cooling tower are high enough such that the resonant response contributions could be disregarded.

In practice, it is always favourable to suppress the resonance if possible since this will help to reduce the wind induced stresses in the structure. In many other upright structures like chimneys, skyscrapers, etc. this is not always possible without paying a high penalty on costs. Because of this, resonant response must be at times taken into account. In contrast, cooling towers with relatively high stiffness and accordingly high frequencies could be built without significant increase in costs. As shown in Chapter 4, the natural frequencies of hyperbolic cooling towers are strongly dependent on the shell geometry. Most important is the meridional curvature. Increased meridional curvature is associated with an increase in frequency besides reducing the surface area of the tower. Therefore, a sound design of cooling towers could possibly suppress any significant resonant response even in strong wind conditions. In such a case, the quasi-static approach would be most useful as well as reliable.

On the other hand, there are situations in which

significant resonant response is sometimes unavoidable. For example, in the case of cooling towers built on poor soil, it might be very expensive or even impossible to provide rigid foundations. Instead, one has to contend with a flexible foundation which could reduce considerably the stiffness of the structure (4,5). Also, with increasing demands on cooling, towers with heights exceeding 500 ft., are now under construction (11). If the present trend continues, higher towers could be built in the near future. Since the natural frequencies are inversely proportional to height, increasing heights could lead to increasing resonant response. Moreover, imperfections in the construction of the cooling tower shell and cracking due to tensile stresses caused by shrinkage effects, thermal stresses, etc. could produce significant reductions in the overall shell stiffness.

Under such conditions, the quasi-static approach will no longer be sufficient to predict the wind response of the structure. Instead a more rigorous approach capable of predicting both the quasi-static and resonant response with sufficient accuracy will be needed. This will be the subject of the next section.

7.3 Rigorous Dynamic Approach

7.3.1 Theory

The present approach provides a complete statistical treatment of the dynamic response of cooling towers to gusty winds on realistic basis. In effect, the approach takes into account the random nature of the wind pressure fluctuations as well as the dynamic characteristics of the structure.

The general formulation of the dynamic response of shells of revolution to random loads together with the underlying assumptions is given in detail in Chapter 3. For convenience, the procedure and the governing equations as applicable to cooling tower shells, subjected to wind loading, will be summarized briefly herein. The relevant statistical properties of the wind pressure fluctuations and the structural and dynamic characteristics of the structure required for the analysis will also be defined.

Let $y(s, \phi, t)$ be the instantaneous response at position (s, ϕ) on the shell surface. Its time-average will be set to zero. $y(s, \phi, t)$ can be expanded in terms of its mode shapes as follows:

$$y(s, \phi, t) = \sum_m \sum_i \{q_{m,i}(t) \cos m\phi + q'_{m,i}(t) \sin m\phi\} y_{m,i}(s) \quad (7.15)$$

Expressions for the symmetric and anti-symmetric components of the generalized forces, experienced by each mode of vibration, are given by:

$$p_{m,i}(t) = \int_0^{s_0} \int_0^{2\pi} p(s, \phi, t) w_{m,i}(s) \cos m\phi r(s) d\phi ds \quad (7.16)$$

$$p'_{m,i}(t) = \int_0^{s_0} \int_0^{2\pi} p(s, \phi, t) w_{m,i}(s) \sin m\phi r(s) d\phi ds \quad (7.17)$$

in which, $r(s)$ = radius of the parallel circle at position (s, ϕ) . Following equations (7.16 and 7.17) expressions for the cross-spectra of the generalized forces were found to be,

$$S_{p_{m,i} p_{n,j}}(f) = \int_0^{s_0} \int_0^{s_0} \int_0^{2\pi} \int_0^{2\pi} S_p(s, \phi, s', \phi', f) w_{m,i}(s) w_{n,j}(s') \cos m\phi \cos n\phi' r(s) r(s') d\phi d\phi' ds ds' \quad (7.18)$$

$$S_{p'_{m,i} p'_{n,j}}(f) = \int_0^{s_0} \int_0^{s_0} \int_0^{2\pi} \int_0^{2\pi} S_p(s, \phi, s', \phi', f) w_{m,i}(s) w_{n,j}(s') \sin m\phi \sin n\phi' r(s) r(s') d\phi d\phi' ds ds' \quad (7.19)$$

$$S_{p_{m,i} p'_{n,j}}(f) = \int_0^{s_0} \int_0^{s_0} \int_0^{2\pi} \int_0^{2\pi} S_p(s, \phi, s', \phi', f) w_{m,i}(s) w_{n,j}(s') \cos m\phi \sin n\phi' r(s) r(s') d\phi d\phi' ds ds' \quad (7.20)$$

$$S_{p'_{m,i} p_{n,j}}(f) = \int_0^{s_0} \int_0^{s_0} \int_0^{2\pi} \int_0^{2\pi} S_p(s', \phi', s, \phi, f) w_{m,i}(s') w_{n,j}(s) \sin m\phi' \cos n\phi r(s') r(s) d\phi' d\phi ds' ds \quad (7.21)$$

in which $S_p(s, \phi, s', \phi', f)$ is the cross-spectrum of the pressure fluctuations at points (s, ϕ) and (s', ϕ') .

$S_p(s, \phi, s', \phi', f)$ is generally a complex function; i.e.

$$S_p(s, \phi, s', \phi', f) = G(s, \phi, s', \phi', f) + iQ(s, \phi, s', \phi', f) \quad (7.22)$$

in which G and Q are referred to as the co-spectrum and quadrature spectrum respectively.

Experimental measurements of $S_p(s, \phi, s', \phi', f)$, presented earlier in Chapter 6, enable us to introduce some simplifying assumptions regarding the variation of $S_p(s, \phi, s', \phi', f)$ across the shell surface. First, it will be assumed that there is no correlation between pressure fluctuations in the windward region and the wake region. $S_p(s, \phi, s', \phi', f)$ can be conveniently represented by:

a/ Windward region

$$S_p(s, \phi, s', \phi', f) = R_v(s, s', f) R_f(\phi, \phi', f) \sqrt{S_p(s, \phi, f) S_p(s', \phi', f)} \quad (7.23)$$

b/ Wake region

$$S_p(s, \phi, s', \phi', f) = R_v(s, s', f) R_f(\phi, \phi', f) \sqrt{S_p(s, \phi, f) S_p(s', \phi', f)} \quad (7.24)$$

in which $R_v(s, s', f)$ is a shape function of $S_p(s, \phi, s', \phi', f)$ for vertical separations. Similarly, $R_f(\phi, \phi', f)$ and $R_r(\phi, \phi', f)$ are shape functions for horizontal separations in the windward and wake regions respectively.

It will be assumed that $R_v(s, s', f)$ is invariant with circumferential location ϕ and that $R_f(\phi, \phi', f)$ and $R_r(\phi, \phi', f)$ are invariant with height. It will be assumed further that $S_p(s, \phi, f)$ is independent of height. As such, it will be only a function of ϕ and f only.

By introducing the above assumptions, equations (7.18 to 7.21) become,

$$S_{p_m, i p_n, j}(f) = s_o^4 \sigma_p^2(s_1, \phi_1) J_o(f) J_1(f) \quad (7.25)$$

$$S_{p'_m, i p'_n, j}(f) = s_o^4 \sigma_p^2(s_1, \phi_1) J_o(f) J_2(f) \quad (7.26)$$

$$S_{p_m, i p'_n, j}(f) = s_o^4 \sigma_p^2(s_1, \phi_1) J_o(f) J_3(f) \quad (7.27)$$

$$S_{p'_m, i p_n, j}(f) = s_o^4 \sigma_p^2(s_1, \phi_1) J_o(f) J_4(f) \quad (7.28)$$

in which

$$J_o(f) = \int_0^1 \int_0^1 R_v(l, l', f) f_1(l) f_1(l') w_{m, i}(l) w_{n, j}(l') \gamma_2(l) \gamma_2(l') dl dl' \quad (7.29)$$

$$\begin{aligned}
 J_1(f) &= \int_{-\phi_s}^{+\phi_s} \int_{-\phi_s}^{+\phi_s} R_f(\phi, \phi', f) \frac{\sqrt{S_p(\phi, f) S_p(\phi', f)}}{\sigma_p(\phi) \sigma_p(\phi')} f_2(\phi) f_2(\phi') \\
 &\cos m\phi \cos n\phi' d\phi d\phi' + \int_{+\phi_s}^{-\phi_s} \int_{+\phi_s}^{-\phi_s} R_r(\phi, \phi', f) \frac{\sqrt{S_p(\phi, f) S_p(\phi', f)}}{\sigma_p(\phi) \sigma_p(\phi')} \\
 &f_2(\phi) f_2(\phi') \cos m\phi \cos n\phi' d\phi d\phi' \quad (7.30)
 \end{aligned}$$

$$\begin{aligned}
 J_2(f) &= \int_{-\phi_s}^{+\phi_s} \int_{-\phi_s}^{+\phi_s} R_f(\phi, \phi', f) \frac{\sqrt{S_p(\phi, f) S_p(\phi', f)}}{\sigma_p(\phi) \sigma_p(\phi')} f_2(\phi) f_2(\phi') \\
 &\sin m\phi \sin n\phi' d\phi d\phi' + \int_{+\phi_s}^{-\phi_s} \int_{+\phi_s}^{-\phi_s} R_r(\phi, \phi', f) \frac{\sqrt{S_p(\phi, f) S_p(\phi', f)}}{\sigma_p(\phi) \sigma_p(\phi')} \\
 &f_2(\phi) f_2(\phi') \sin m\phi \sin n\phi' d\phi d\phi' \quad (7.31)
 \end{aligned}$$

$$\begin{aligned}
 J_3(f) &= \int_{-\phi_s}^{+\phi_s} \int_{-\phi_s}^{+\phi_s} R_f(\phi, \phi', f) \frac{\sqrt{S_p(\phi, f) S_p(\phi', f)}}{\sigma_p(\phi) \sigma_p(\phi')} f_2(\phi) f_2(\phi') \\
 &\cos m\phi \sin n\phi' d\phi d\phi' + \int_{+\phi_s}^{-\phi_s} \int_{+\phi_s}^{-\phi_s} R_r(\phi, \phi', f) \frac{\sqrt{S_p(\phi, f) S_p(\phi', f)}}{\sigma_p(\phi) \sigma_p(\phi')} \\
 &f_2(\phi) f_2(\phi') \cos m\phi \sin n\phi' d\phi d\phi' \quad (7.32)
 \end{aligned}$$

$$\begin{aligned}
 J_4(f) &= \int_{-\phi_s}^{+\phi_s} \int_{-\phi_s}^{+\phi_s} R_r(\phi', \phi, f) \frac{\sqrt{S_p(\phi', f) S_p(\phi, f)}}{\sigma_p(\phi') \sigma_p(\phi)} f_2(\phi') f_2(\phi) \\
 &\sin m\phi' \cos n\phi d\phi d\phi' + \int_{+\phi_s}^{-\phi_s} \int_{+\phi_s}^{-\phi_s} R_r(\phi', \phi, f) \frac{\sqrt{S_p(\phi', f) S_p(\phi, f)}}{\sigma_p(\phi') \sigma_p(\phi)} \\
 &f_2(\phi') f_2(\phi) \sin m\phi' \cos n\phi d\phi d\phi' \quad (7.33)
 \end{aligned}$$

in which ϕ is the circumferential angle measured clockwise

from the upstream stagnation line and ϕ_s = angle of flow separation.

The cross-spectra of the generalized coordinates of the shell response are related to those for the generalized forces by means of the following relations:

$$S_{q_{m,i}q_{n,j}}(f) = \frac{1}{16\pi^4 f_{m,i}^2 f_{n,j}^2 M_{m,i} M_{n,j}} \chi_{m,i}^*(if) \chi_{n,j}(if)$$

$$S_{p_{m,i}p_{n,j}}(f) \quad (7.34)$$

in which

$$\chi_{m,i}(if) = \left\{ \left(1 - \frac{f^2}{f_{m,i}^2} \right) + 2i \operatorname{in}_{cr} \left(\frac{f}{f_{m,i}} \right) \right\}^{-1} \quad (7.35)$$

Similar expressions for $S_{q'_{m,i}q'_{n,j}}(f)$, $S_{q_{m,i}q'_{n,j}}(f)$ and $S_{q'_{m,i}q_{n,j}}(f)$ could be obtained.

Having defined the spectra of the generalized coordinates, the power spectra of the total shell response at position (s, ϕ) could be obtained from:

$$S_y(s, \phi, f) = \sum_m \sum_i \sum_n \sum_j \{ S_{q_{m,i}q_{n,j}}(f) \cos m\phi \cos n\phi + S_{q'_{m,i}q'_{n,j}}(f) \sin m\phi \sin n\phi + S_{q_{m,i}q'_{n,j}}(f) \cos m\phi \sin n\phi + S_{q'_{m,i}q_{n,j}}(f) \sin m\phi \cos n\phi \} y_{m,i}(s) y_{n,j}(s) \quad (7.36)$$

Its standard deviation is given by:

$$\sigma_y(s, \phi, f) = \int_0^{\infty} S_y(s, \phi, f) df \quad (7.37)$$

Equations (7.15 to 7.37) describe all the necessary relations required for a complete statistical analysis of the dynamic response of hyperbolic cooling towers subject to turbulent wind loading. To carry out the analysis, the following statistical properties of the wind pressure fluctuations and their variations around the shell have to be defined:

1. Standard deviation.
2. Power-spectral density function.
3. Cross-spectral density function.

7.3.2 Application

The present approach will be used to predict the dynamic response of the hyperbolic cooling tower model referred to earlier as Model I. The geometry, material properties, and vibration characteristics of the model were given in Section 7.2.2.1. According to Ref. (7), the critical damping ratio of the model is about 0.9%. The relevant statistical properties of the wind pressure fluctuations are described in Chapter 5.

Comparisons between theory and experimental measurements of shell response will be made wherever possible.

7.3.2.1 Statistical Properties of Generalized Forces

The first step in the present analysis is to define the statistical properties of the generalized forces. Equations (7.25 to 7.28) provide the necessary relations required to compute the cross-spectra of the various components of the generalized forces. In these equations, the cross-spectra of the pressure fluctuations are represented by $R_y(l, l', f)$, $R_f(\phi, \phi', f)$ and $R_x(\phi, \phi', f)$. In general, these are complex functions. Their real components represent the co-spectral density while their imaginary components represent the quadrature spectra.

Both components of the cross-spectra of the wind pressure are described in Chapter 5. There, it was found that, contrary to the co-spectral density, the significance of the quadrature spectra increases as the frequency increases and is only significant for large horizontal separations. For vertical separations, the quadrature spectra is hardly significant. Moreover, the quadrature spectra for horizontal separations is, in general, much smaller than the co-spectral density. Only when the co-spectral density itself is small, do they become comparable.

Therefore, for the sake of simplicity, the quadrature-spectral component of the cross-spectra will be neglected. That is,

$$S_p(s, \phi, s', \phi', f) \approx G(s, \phi, s', \phi', f) \quad (7.38)$$

Accordingly, the real part of the shape functions $R_v(l, l', f)$, $R_f(\phi, \phi', f)$ and $R_p(\phi, \phi', f)$ will be only considered. This would considerably reduce the computational effort.

If a more accurate estimate of the generalized forces is desired, the complex part of the cross-spectra of the generalized forces could be considered separately in a similar manner to the real part. However, our present limited knowledge of full scale behaviour does not justify the additional burden of the computational effort.

Experimental results of the real part of $R_v(l, l', f)$, $R_f(\phi, \phi', f)$ and $R_p(\phi, \phi', f)$ are shown in Figs. (5.71 to 5.73). The variation of $S_p(s, \phi, f)$ around the shell circumference at the throat, which is taken as the reference height, is shown in Figs. (5.39 to 5.45). Also, the variation of the standard deviation $\sigma_p(s, \phi)$ around the shell circumference is shown in Figs. (5.17 to 5.23). Using these results, the generalized force functions, $J_0(f)$, $J_1(f)$, $J_2(f)$ and $J_3(f)$ were evaluated for various modes of vibration by means of equations (7.29 to 7.32).

Experimental measurements of the spectra and cross-spectra of the pressure fluctuations were limited to frequencies up to 125 cps. The values of these functions

at higher frequencies were projected by a simple extension of the results. Therefore, confidence in the results beyond $f = 125$ cps has to be viewed with caution.

The cross-spectra of the product of the symmetric and anti-symmetric components of the generalized forces, represented by the product $J_0(f) J_3(f)$ was found to be very small in comparison to $J_0(f) J_1(f)$ and $J_0(f) J_2(f)$. In other words, the correlation between both components of the generalized forces could be ignored. Similar conclusions are drawn from the previous quasi-static analysis regarding the covariance of the product of both components, $\overline{p_{m,i}(t)p'_{n,j}(t)}$.

The computed results of $J_0(f)$ for the fundamental modes of harmonics $m=1$ to 3 are shown in Fig. 7.22, including those involving the cross-product of different harmonics. In all cases, it was found that $J_0(f)$ consistently decreases with increasing frequency. A close examination of the results revealed an interesting feature when they were normalized by $J_0(0)$. From equation (7.29).

$$J_0(0) = \int_0^1 \int_0^1 f_1(l) f_1(l') w_{m,i}(l) w_{n,j}(l') \gamma_2(l) \gamma_2(l') dl dl' \quad (7.39)$$

since $R_v(l, l', 0) = 1.0$.

The resulting curves for the normalized results,

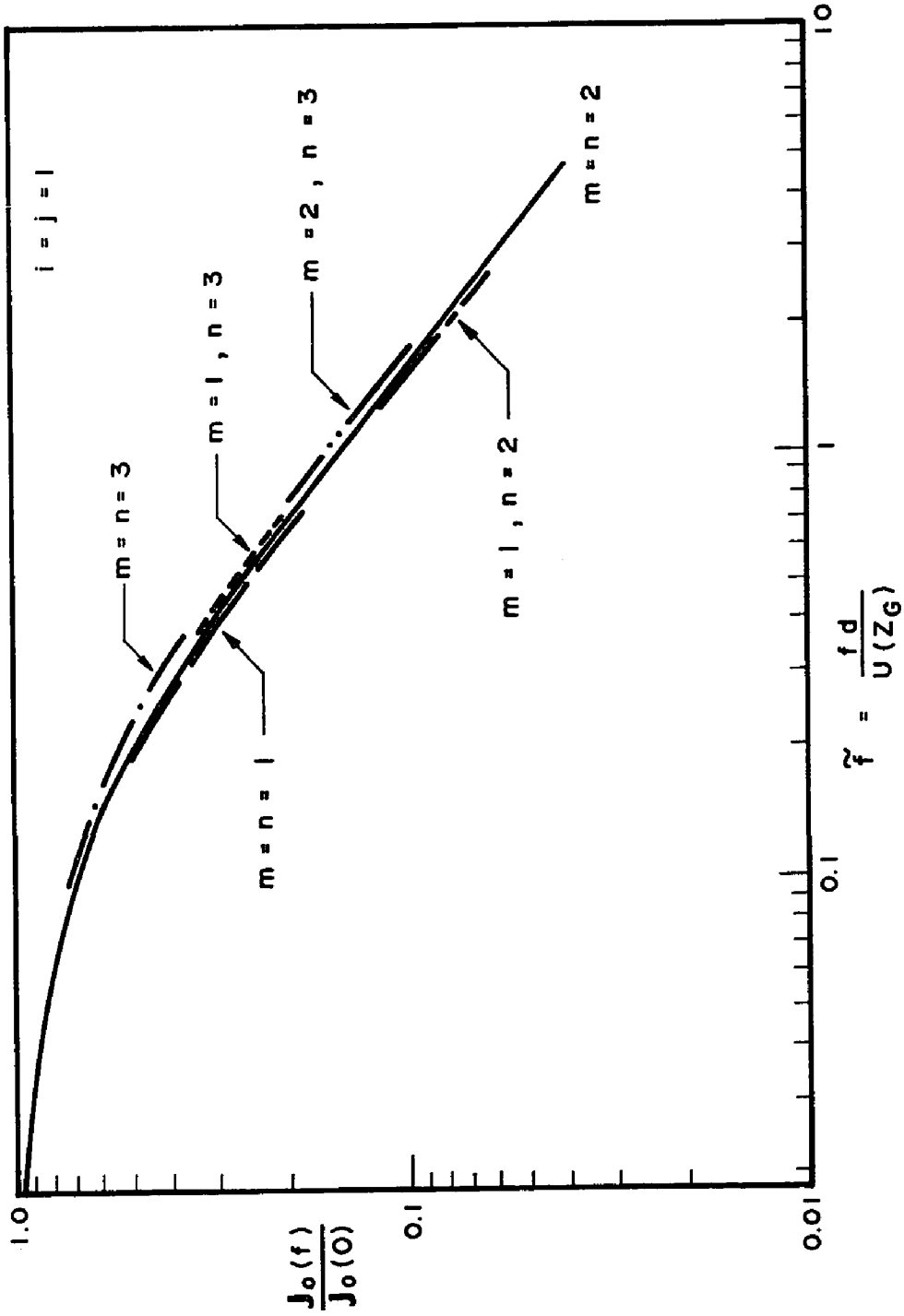


FIG. 7.22 VALUES OF $J_0(f)$ FOR HARMONICS
 $m = 1$ TO 3

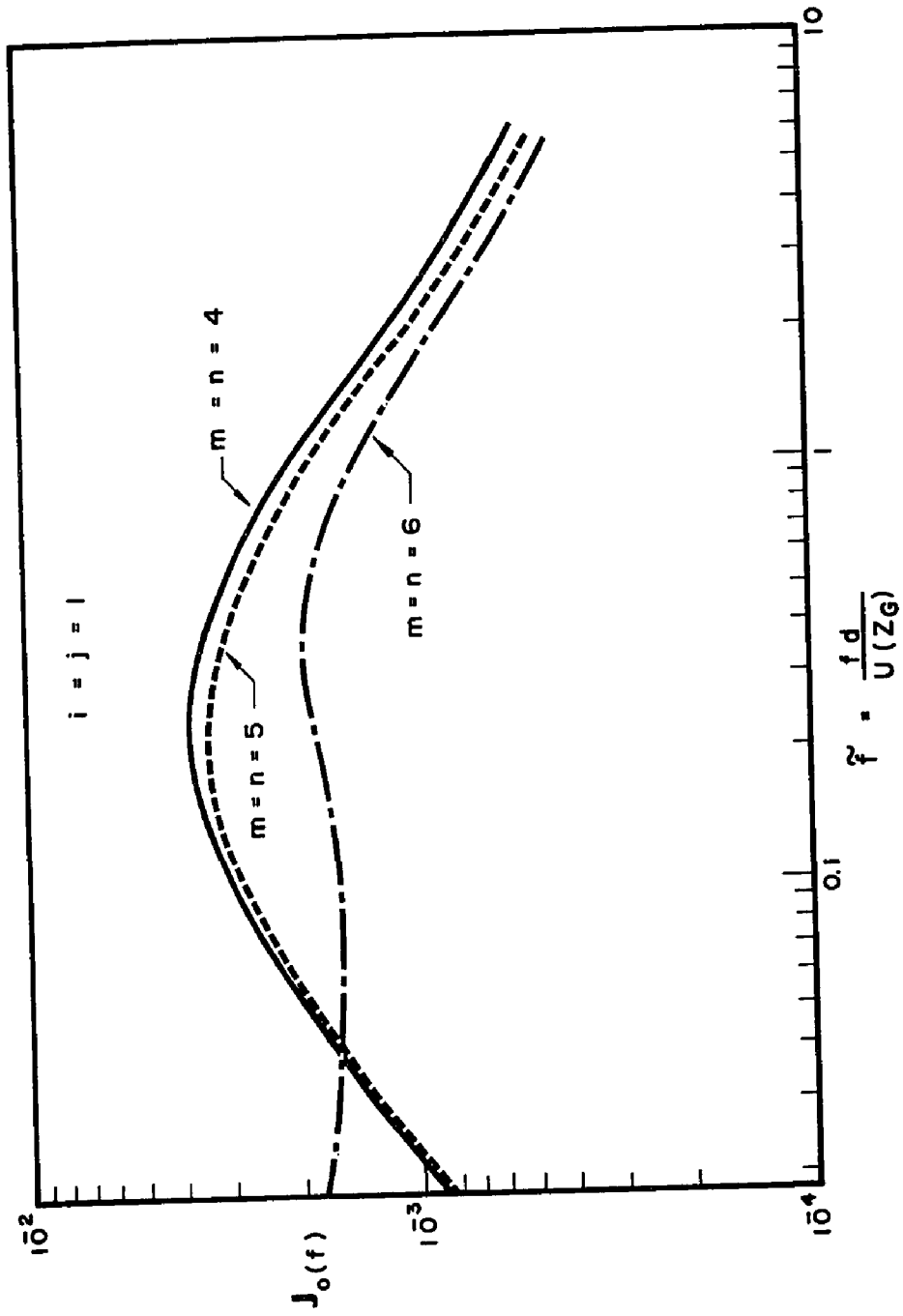


FIG. 7.23 VALUES OF $J_0(f)$ FOR HARMONICS
 $m = 4$ to 6

$J_0(f)/J_0(0)$, for all the three individual harmonics and the cross-products involving pairs of different harmonics, could be practically represented by a single curve with errors of the order of about $\pm 5\%$. Such a universal curve could not be extended to cover modes other than the fundamental ones for harmonics $m=1$ to 3 . Neither was it found to be representative of the fundamental modes associated with harmonic wave number $m>3$. This is evident from the computed results of $J_0(f)$ for harmonics $m=4$ to 6 shown in Fig. 7.23. This rather abrupt change in the character of $J_0(f)$ is due to the variation of the normal displacement, w , with height for various harmonics. These are shown in Fig. 7.2. The fundamental mode shapes of $m=1$ to 3 do not change sign along the height of the shell unlike the case for $m>3$.

Results for the real part of $J_1(f)$ and $J_2(f)$ were also computed, using equations (7.30 and 7.31). For brevity, sample results only will be given here. These are shown in Figs. 7.24 to 7.26. It should be noted that the variations of $J_1(f)$ and $J_2(f)$ with the circumferential wave number m is significant and cannot be neglected.

On the basis of the computed results for $J_0(f)$, $J_1(f)$ and $J_2(f)$, the power spectra and co-spectra of the generalized forces were obtained for the fundamental modes of harmonics $m=1$ to 6 . Sample results are shown

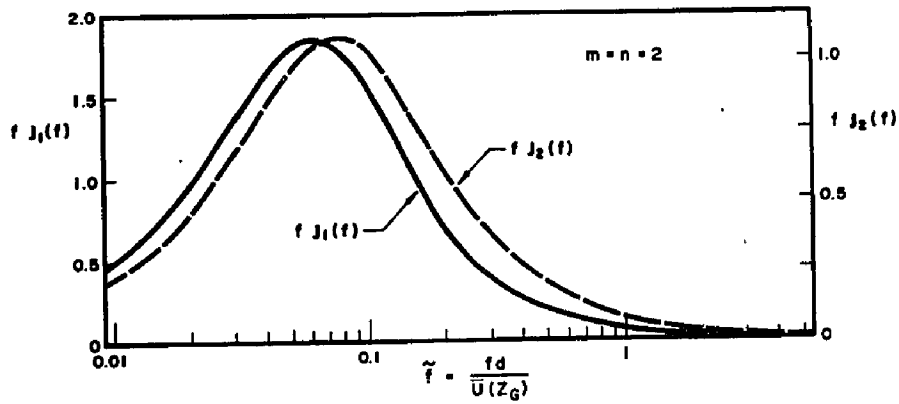


FIG. 7.24 VARIATION OF $J_1(f)$ AND $J_2(f)$ WITH FREQUENCY FOR HARMONIC $m = 2$

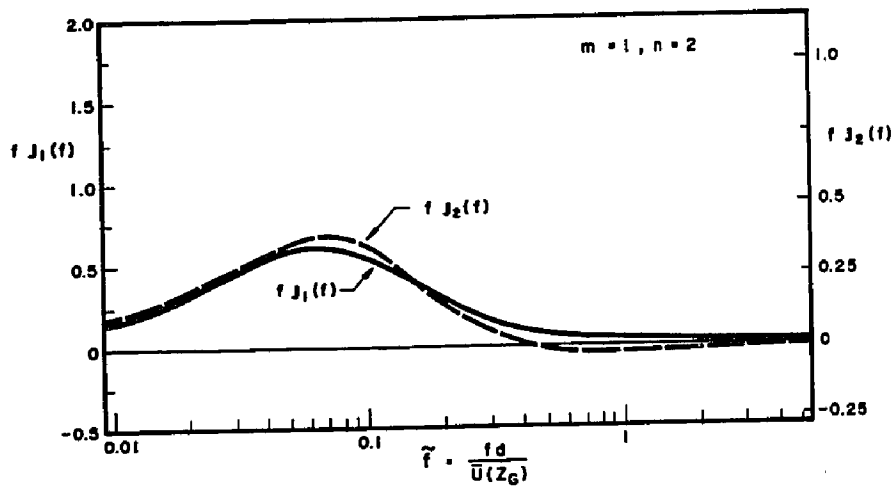


FIG. 7.25 VARIATION OF $J_1(f)$ AND $J_2(f)$ WITH FREQUENCY FOR THE CROSS-PRODUCT OF HARMONICS $m = 1$ AND 2

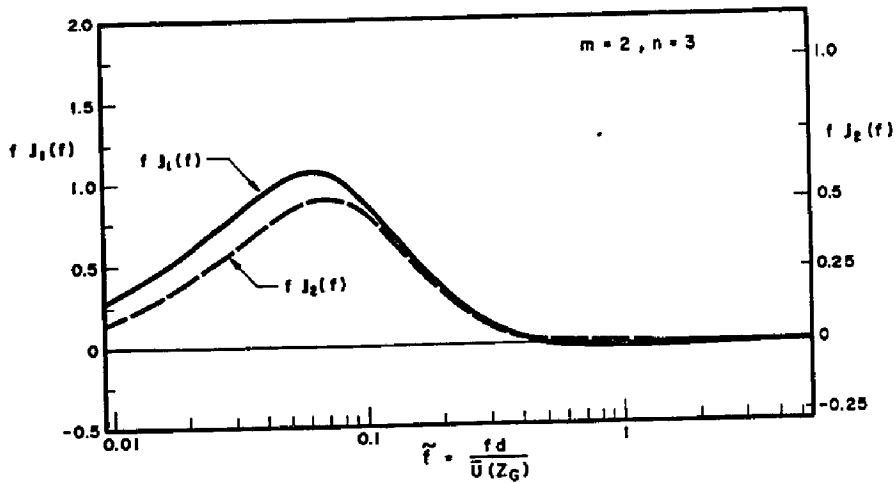


FIG. 7.26 VARIATION OF $J_1(f)$ AND $J_2(f)$ WITH FREQUENCY FOR THE CROSS-PRODUCT OF HARMONICS $m = 2$ AND 3

in Figs. 7.27 to 7.29. The results were adequately fitted with fairly simple function of the reduced frequency \tilde{f} , ($\tilde{f} = \frac{fd}{\bar{U}(z_G)}$, d = throat diameter, and $\bar{U}(z_G)$ = wind velocity at gradient height), as shown in Table 7.12. At high frequencies ($f > 15$ cps) it was found that:

$$S_{p_{m,i} p_{n,j}}(f) \propto \tilde{f}^{-\beta_1}$$

$$S_{p'_{m,i} p'_{n,j}}(f) \propto \tilde{f}^{-\beta_2}$$

in which β_1 and β_2 varies between 2.8 to 3.45 depending on the harmonic wave number.

In Chapter 6 the power spectra of the symmetric and anti-symmetric components of the generalized force for harmonic $m=2$ were obtained from the modal response measurements. The results were obtained using Model II, Fig. 6.1, and are given in Figs. 6.42 and 6.43. These results include contributions from all modes of $m=2$. However, the participation of the fundamental mode is predominant (see Section 7.2.2). The theoretical results obtained for the fundamental mode of $m=2$ are compared with the experimental results in Fig. 7.27. Both results are in good agreement. The observed differences could be due, in part, to the differences in the integral length scale of turbulence to shell diameter ratio (12,13). This ratio for Model II is about 1/2 that of Model I.

TABLE 7.12 EXPRESSIONS FOR THE POWER SPECTRA OF THE GENERALIZED FORCES

m	$S(\bar{f}) = \frac{A_1 \tilde{f}^{A_2}}{(A_3 + \tilde{f}^{A_4})^{A_5}}$					$\bar{f} = \frac{f d}{\bar{U} \langle Z_G \rangle}$				
	SYMMETRIC COMPONENT					ANTI SYMMETRIC COMPONENT				
	A ₁	A ₂	A ₃	A ₄	A ₅	A ₁	A ₂	A ₃	A ₄	A ₅
1	0.000230	0.0	0.04199	1.5953	2.10	0.00016	0.0	0.01579	1.9117	1.70
2	0.000046	0.0	0.00321	2.2333	1.50	0.000125	0.0	0.00341	2.3486	1.30
3	0.001505	0.0	0.00387	2.2307	1.30	0.000095	0.0	0.01151	2.0294	1.70
4	0.000607	1.0	0.0396	1.5185	2.70	0.00134	1.0	0.07089	1.3448	2.90
5	0.00226	1.0	0.1019	1.3448	2.90	0.00130	1.0	0.0585	1.4074	2.70

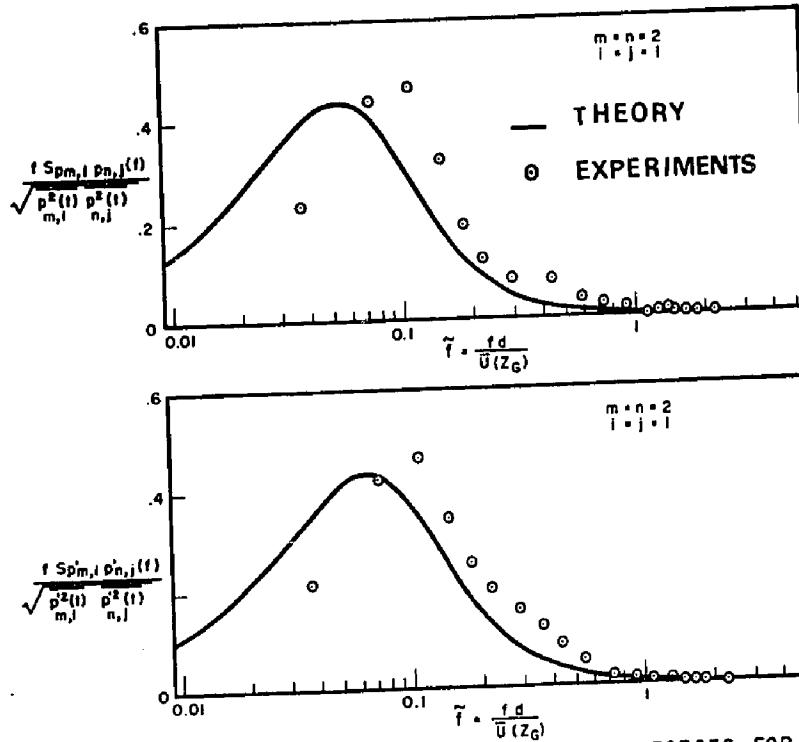


FIG. 7.27 POWER-SPECTRA OF THE GENERALIZED FORCES FOR $m = 2$

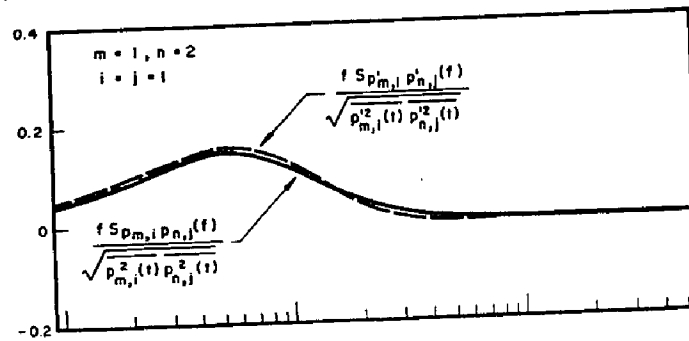


FIG. 7.28 POWER-SPECTRA OF THE CROSS-PRODUCT OF THE GENERALIZED FORCES FOR HARMONICS $m = 1$ AND 2

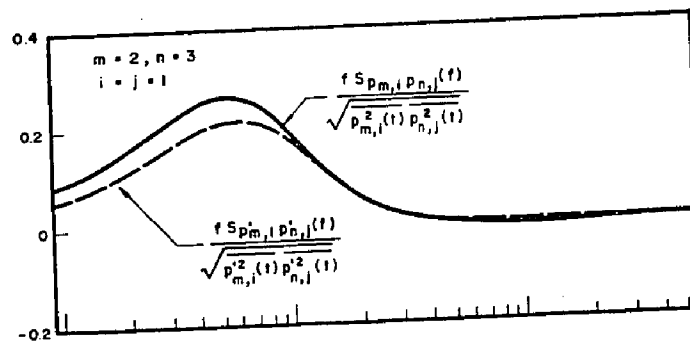


FIG. 7.29 POWER-SPECTRA OF THE CROSS-PRODUCT OF THE GENERALIZED FORCES FOR HARMONICS $m = 2$ AND 3

7.3.2.2 Dynamic Response

On the basis of the previous results, the dynamic response of the shell can now be determined. First, the cross-spectra of the generalized coordinates of the shell response could be directly obtained from equation (7.34). The total dynamic response at any location on the shell surface could then be obtained by summing up the individual contributions of various modes of vibration, equation (7.36).

During the analysis, the following two important observations were consistently noted:

1. The total dynamic response at low frequencies, commonly referred to as the quasi-static response, is dominated by contributions made from harmonics $m=1$ to 3 , with $m=2$ producing the highest contribution.
2. The only significant contributions to the total resonant response of the shell are associated with harmonic wave numbers $m=3, 4, 5$, and 6 .

For harmonics $m>6$, neither the quasi-static nor the resonant response components were of any significance. Therefore, the summation of the modal contributions to the shell response were carried up to $m=6$ only.

On this basis, the power spectra of the total shell

response, in terms of the meridional strain on the inside surface of the shell, was computed. Figs. 7.30 to 7.33 show the variation of the response power spectra, along the upstream stagnation line, at levels 0.94H, 0.75H, 0.50H and 0.27H respectively. The response power spectra at $\phi = 120^\circ$ and $\phi = 180^\circ$, at level 0.27H, is also shown in Figs. 7.34 and 7.35 respectively.

In Fig. 7.33, comparisons are made with the experimental measurements reported in Ref. (8). The experimental results were obtained from wind tunnel measurements at almost the same flow conditions under which the statistical properties of the wind pressure fluctuations were obtained for the purpose of the present study.

On the whole, the experimental results compare fairly well with the experiments. For the quasi-static response alone, the agreement between both results is excellent. However, the resonant response does not compare as well. Noting that, the measurements of the wind pressure characteristics used in the theoretical model have been limited to frequencies below 125 cps because of the frequency response of the pressure tubes, and that the results above that frequency are just a simple extension of the prevailing trend, the main reason for the discrepancy between theory and experiments at high frequencies becomes obvious. It is also worth mentioning that the total area under the resonant peaks from the theoretical results compares well

POWER SPECTRA OF SHELL RESPONSE

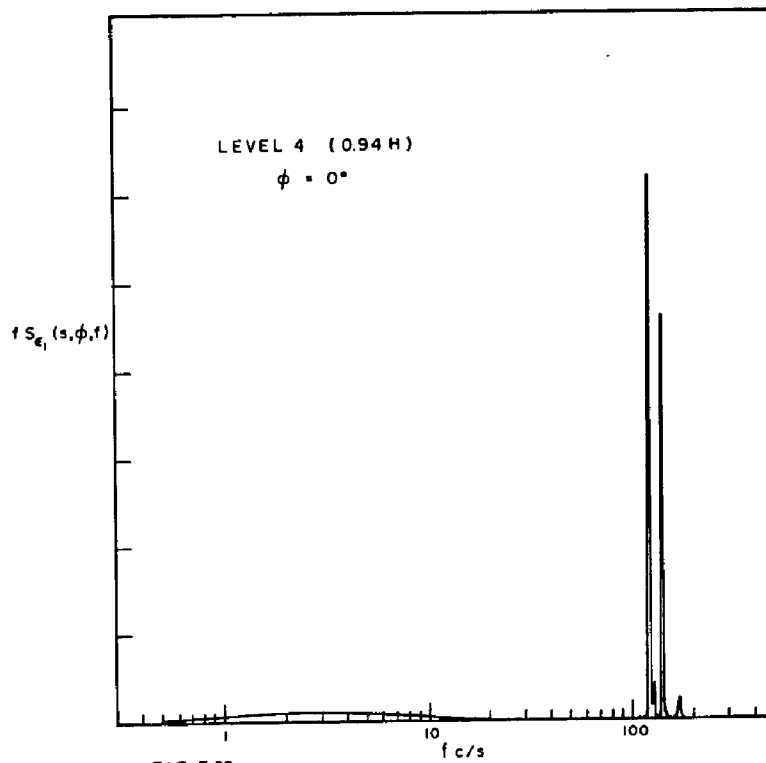


FIG. 7.30

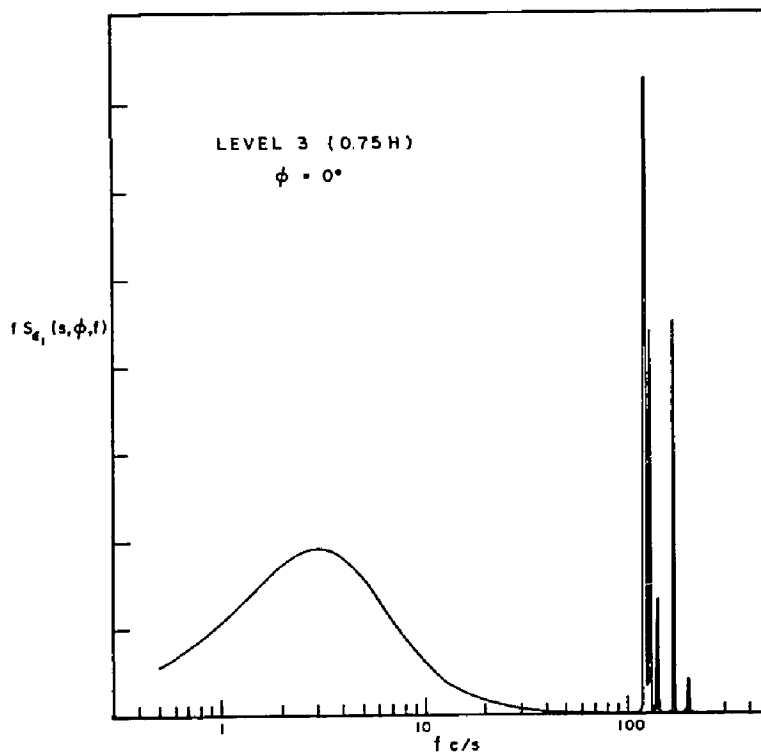


FIG. 7.31

POWER SPECTRA OF SHELL RESPONSE

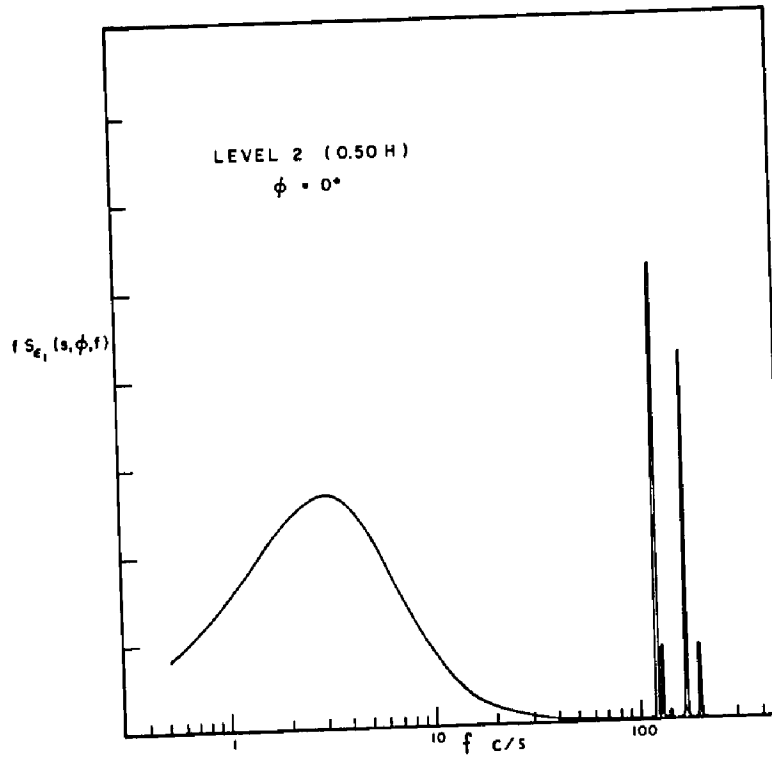


FIG. 7.32

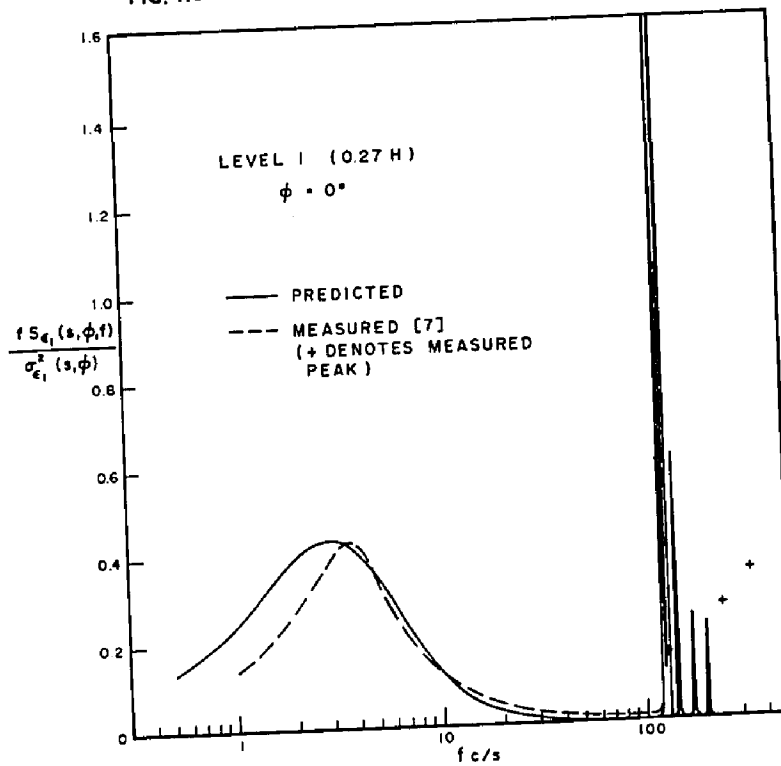


FIG. 7.33

POWER SPECTRA OF SHELL RESPONSE

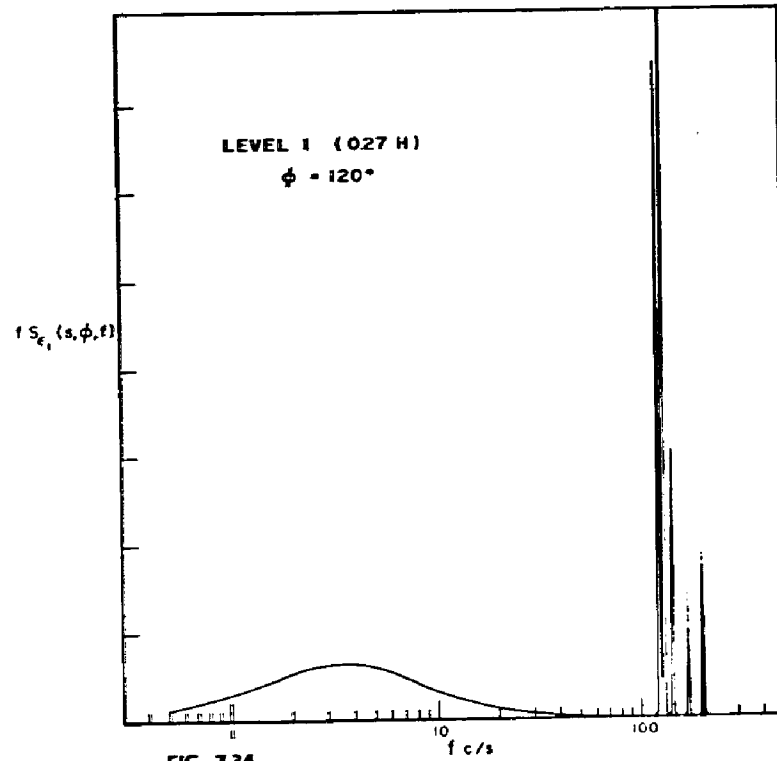


FIG. 7.34

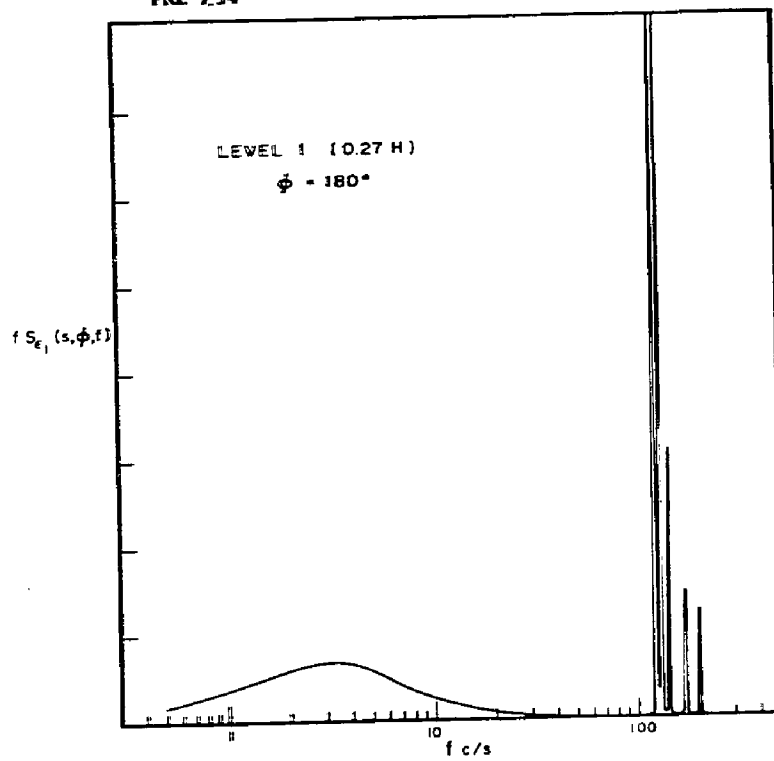


FIG. 7.35

with that from the experimental measurements. Both results confirm the conclusion that the contribution of resonance to the total shell response at this location is relatively small in comparison with the quasi-static portion.

Figs. 7.32 to 7.33 indicate that the resonance portion of the total dynamic response in the lower half of the shell is fairly small. However, their relative proportion increases as height above ground increases. In Fig. 7.30 it is observed that the resonant response is actually much more predominant than the quasi-static response. The variation of the relative contribution of resonance with height could be explained from the modal response contributions of various modes. The quasi-static response is largely concentrated in harmonics $m=1$ to 3 whose modal amplitudes near the top are very small and increase gradually downwards. On the other hand, most of the resonant response resides in harmonics $m=4$ to 6 whose amplitudes near the top are of the same order of magnitude as the rest of the shell.

The relative contribution of resonance to the total response varies also with circumferential location ϕ , as shown in Figs. 7.33 to 7.35. The percentage of resonance in the wake region is higher than that in the upwind face of the tower. Noting that, both components (quasi-static and resonance) of the individual contribution of each

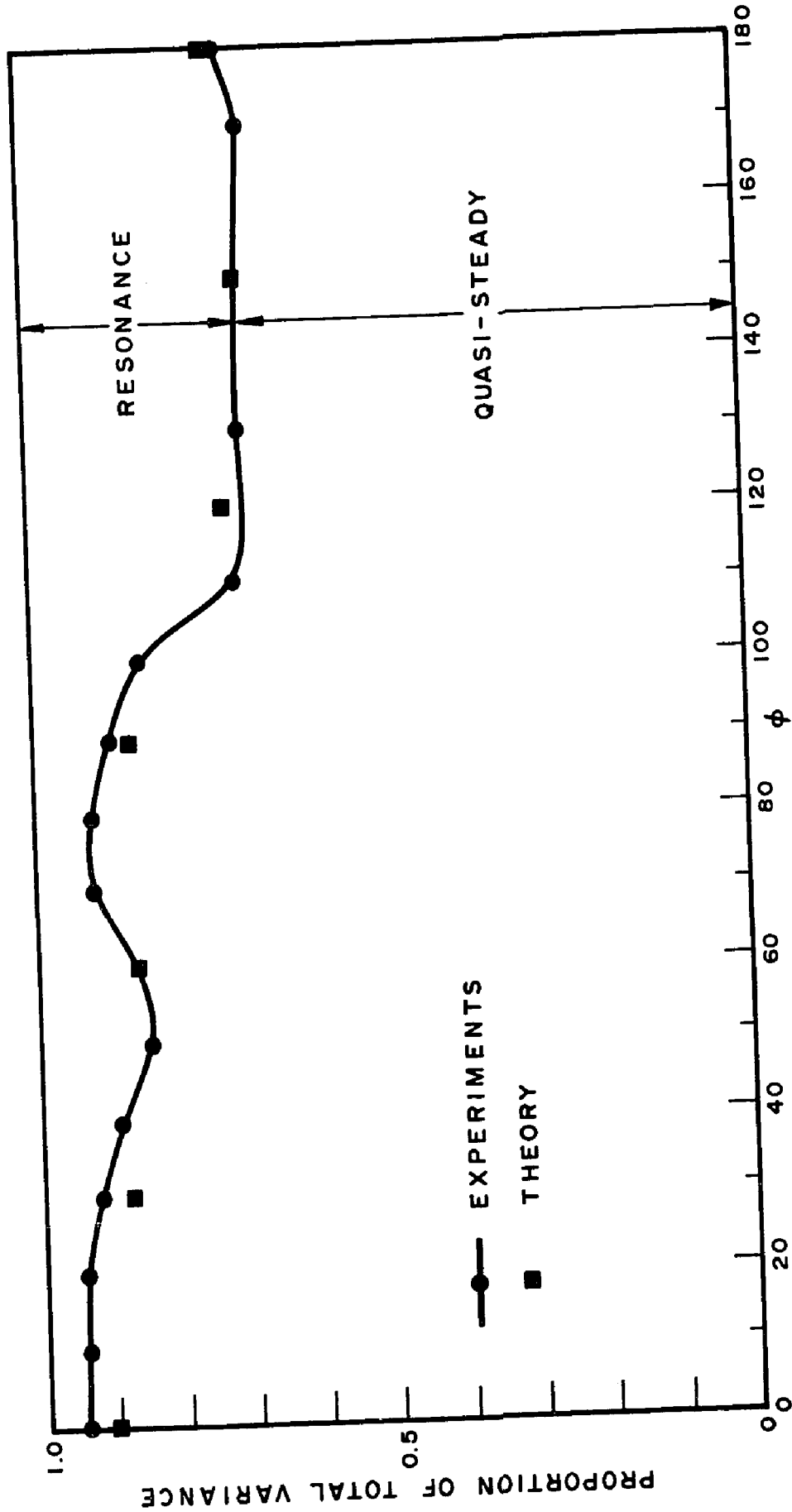


FIG. 7.36

harmonic is symmetric about $\phi = \pm 90^\circ$, then it could be only concluded that the change of the relative proportion of resonance with ϕ must be due solely to the coupling between different modes of vibration. But since the coupling between different modes at resonance was found to be insignificant, then the increased relative proportion of resonance in the wake region is caused mainly by the reduction in the quasi-static response due to coupling between different modes.

The variation of the percentage proportion of resonance around the circumference was computed at level 1 (0.27H) and the results are shown in Fig. 7.36. Comparisons are made with experimental measurements reported in Ref. (8). As seen, the agreement between both results is very satisfactory.

7.3.3 Comments

In the preceding sections, the formulation of a rigorous dynamic approach to the prediction of wind stresses in hyperbolic cooling towers is presented.

The approach was applied to predict the dynamic response of a sample cooling tower model. Comparisons with experimental measurements were made wherever possible. On the whole, the accuracy of the predicted results was satisfactory.

The good agreement between the predicted results and experimental measurements further supports the adequacy of various assumptions introduced in the analysis. Some more simplifying assumptions could still be introduced on the basis of a sensitivity study of various parameters entering the analysis.

In the formulation of the governing equations, the relevant statistical properties of the wind pressure fluctuations were clearly defined. This should prove to be very useful in future measurements of wind pressure characteristics. The assumptions introduced in the analysis regarding the variation of the statistical properties of the pressure fluctuations across the shell surface could be helpful in reducing the amount of experimental measurements.

In the analysis of the sample problem, the quadrature component of the cross-spectra of the wind pressure was ignored. Apparently, its influence on the final response results is not significant as evident from comparisons with experimental results. However, they could be included as a possible refinement of the dynamic analysis of shell response.

The analysis of the sample problem was based on experimental measurements of the statistical properties of the wind pressure fluctuations obtained at a low value of Reynolds number (1.8×10^5). Therefore, the application

of the cited conclusions to full scale behaviour should be approached carefully. The prediction of shell response on the basis of the present model measurements of the wind pressure fluctuations is expected to produce an over-estimate of the actual full scale response.

Future full scale measurements of wind pressure characteristics are most desired. Using the present approach with data from full scale tests, universal curves for the covariance, cross-spectra, etc. of the generalized forces could be obtained. Further wind tunnel tests for a sensitivity analysis of the statistical properties of the generalized forces are also desirable. Universal curves for the generalized forces, thus obtained, can be applied with confidence, to predict the dynamic response of cooling towers with varying profiles and structural and dynamic properties.

Until now, there has not been any reported full scale measurements of the critical damping ratio of reinforced concrete cooling towers. In situations where resonance is significant, an accurate estimate of the critical damping ratio is of prime importance. Future measurements of damping should, therefore, prove invaluable.

Finally, in contrasting the rigorous dynamic approach with the quasi-static approach, the various advantages of the former over the latter become obvious.

However, the rigorous approach has two main drawbacks. First, the amount of data required for the statistical description of the wind pressure fluctuations is much larger. Second, the computational effort is increased by a factor of $2N$ or more, where N is the number of frequency intervals of the response power spectra. These two problems will certainly be encountered in the initial use of the dynamic approach. However, once the wind pressure characteristics of full scale towers become well defined, the required data could then be reduced considerably in a compact and useful form in terms of the statistical characteristics of the generalized forces.

CHAPTER 8

CONCLUSIONS AND DESIGN CONSIDERATIONS

8.1 General

In this thesis an attempt has been made to establish a rationale for the prediction of the wind-induced stresses in hyperbolic cooling towers.

The general theory of the linear response of shells of revolution to turbulent wind loading is formulated. The theory takes into account the random variations of the wind loads, in both the space and time domains, as well as the vibration characteristics of the structure. The basic assumptions regarding the wind loads and the state of stress in the shell were outlined. The theory could be applied to the analysis of shells of revolution whose natural modes of vibration could be readily defined.

Based on the general formulation, two approaches were developed for the analysis of the dynamic wind stresses in hyperbolic cooling towers. The first, a simplified one, is based on the premise that the resonant response is small and can be neglected. The analysis is then carried out on a quasi-static basis. The second, a rigorous approach, is capable of predicting both the quasi-static and resonant components of the shell dynamic response.

In the formulation of both the quasi-static and the rigorous

approaches, the necessary statistical properties and joint-properties of the pressure fluctuations were clearly identified. An extensive experimental program was carried out to determine these properties. The experiments were conducted in the Boundary Layer Wind Tunnel. The simulated flow represents the flow of natural wind over a moderately rough terrain.

On the basis of experimental observations, some simplifying assumptions regarding the variation of the statistical properties of the wind pressure fluctuations over the shell surface were introduced. These were then incorporated in both the quasi-static and the rigorous dynamic approaches; thus rendering the analysis more tractable.

The accuracy of both approaches was verified by comparisons with previous and present experimental measurements of the shell dynamic response. Comparisons were only possible with results from model tests due to the absence of full-scale measurements.

In the experimental measurements of the shell response, the statistical properties of the total response and its constituent modal components were obtained. A technique was developed for the separation of the individual modal response. An attempt was made to deduce the statistical properties of the generalized forces experienced by different modes of vibration. The obtained results were compared with theory.

In view of the uncertainties surrounding the full-scale behaviour of cooling towers in natural wind, a sensitivity

analysis of the important parameters that affect the shell dynamic response was carried out. The analysis was restricted to ranges of practical significance.

The mean response component was also given due consideration. Experimentally, the modal components of shell response were measured and then summed up to produce the total mean response. Theoretically, two numerical procedures for the solution of the governing shell equations were described. Comparisons were made with previous results.

A parameteric study of the static wind stresses in cooling towers, was conducted. Emphasis was placed on parameters of direct significance in design. These include the variation of wind pressure with height and around the shell circumference, base flexibility, top ring beam and the shell meridional profile.

8.2 General Conclusions

From the theoretical and experimental investigations of the various aspects of the wind response of hyperbolic cooling towers, the following conclusions are made:

A - Wind Pressure

1. The standard deviation of the wind pressure fluctuations over the shell surface could be predicted with reasonable accuracy using a two-dimensional quasi-steady theory, if the mean wind pressure distribution is known. That is:

$$\sigma_p(s, \phi) = \frac{1}{2} \rho \bar{U}^2(Z) \left\{ 4 \left[\frac{\sigma_u}{\bar{U}} c_p(s, \phi) \right]^2 + \left[\frac{\sigma_v}{\bar{U}} \frac{d c_p(s, \phi)}{d\phi} \right]^2 \right\}^{1/2} \quad (8.1)$$

This does not apply at the shell boundaries where the pressure characteristics are influenced by end effects. The intensity of the pressure fluctuations along the upstream stagnation line is about twice the turbulence intensity, and σ_p is given approximately by

$$\sigma_p(s, 0) = 2 \sigma_u(Z) \bar{U}(Z) \quad (8.2)$$

2. The variation of the pressure fluctuations in the frequency domain exhibits some similar characteristics to the turbulence in the incoming flow; especially in the vicinity of the upstream stagnation line. In the windward region, most of the energy of the pressure fluctuations is concentrated in the low frequency range; i.e. at $\tilde{f} = \frac{fd}{\bar{U}(Z_G)} \leq 0.25$. At high frequencies, the intensities of the pressure fluctuations attenuate more rapidly than the velocity fluctuations. It is found that, at $\tilde{f} \geq 0.2$, the pressure fluctuations decay as,

$$S_p(s, \phi, f) \propto \tilde{f}^{-\beta}$$

where β varies between 2 and 2.5 depending on the circumferential location. For turbulence spectrum the value of β is about 5/3. In the leeward region, the vortices

shed in the wake of cooling tower were found to be weak, disorganized and spread over a broad range of frequencies.

3. There is no or little correlation between the pressure fluctuations acting in the windward region and those acting in the wake region. The correlation between the pressure fluctuations at different points along a shell meridian consistently decreases as separation increases in a similar manner to line-like structures. Its dependence on the actual location of the points is small. For horizontal separations in the windward region, the character of the correlation function is complex, and is strongly dependent on both the circumferential locations and the angular separations. The quadrature component of the cross-spectrum is generally small, if compared to the co-spectrum. It becomes slightly important for large separations and/or at high frequencies.
4. When resolved into its modal components, it was found that most of the energy of the pressure fluctuations resides in modes with low harmonic wave numbers; $m = 1, 2$ and 3 . The components of the force associated with harmonic $m = 2$ are predominant. This is similar to the modal components of the mean wind pressure. Each mode of vibration is subjected to a symmetric as well as an anti-symmetric force components, about the mean wind direction. Both components are equally significant. However, there is no or little correlation between the symmetric and anti-symmetric force components.

At high frequencies ($\tilde{f} \geq 0.25$), the power spectra of the generalized forces decay according to

$$S_{p_{m,i}}(f) \propto \tilde{f}^{-\beta}$$

where β varies between 2.8 to 3.45 depending on the harmonic wave number.

B Shell Response

1. On the basis of the comparisons made with experimental results, it was found that, the dynamic response of cooling towers could be predicted theoretically, with reasonable accuracy, using a quasi-static approach if resonance is negligible. Both the quasi-steady and resonance components of the shell response could be predicted with reasonable accuracy using the rigorous dynamic approach. Errors are estimated to be of the same order as those inherent in the measurements of the wind pressure characteristics.

The adequacy of the basic assumptions used in the theoretical approaches for the prediction of the shell response is established in the light of the good agreement obtained between predicted and measured results. More reliable evaluation of the functions used in the analysis could be introduced on the basis of full-scale measurements.

2. Measured and predicted results of the shell response indicate that the dynamic wind stresses are of the same order as the static wind stresses and both share some of the basic characteristic features (if resonance is negligible). In regions of largest meridional stress, the

dynamic response is about 85% of the mean response if resonance is small. This proportion is bound to increase if resonance becomes significant. In certain situations, it is likely that the dynamic response could possibly exceed the mean response.

In general, the distribution of the resonance contribution is almost uniform around the shell circumference. However, its relative contribution to the total response in the wake region is much higher than in the windward region. The resonance proportion of the total response increases gradually with height and is largest in the uppermost portion of the shell. Resonance contributions increase rapidly as the wind speed increases and/or the natural frequency decreases.

3. When resolved into its constituent modal components, it was found that most of the shell response at low frequencies (quasi-static), resides in modes associated with low harmonic wave number m ; particularly $m = 1, 2$ and 3 . Similar to the generalized force components, the contribution of harmonic $m = 2$ is predominant. The number of modes in the meridional direction, required to describe the response, increases with the harmonic wave number. However, for a typical calculation of the quasi-static response, it is sufficient to include one mode for $m = 1$, two for $m = 2$ and three for $m = 3$. Most of the resonant contribution to the shell dynamic response resides in

modes with lowest natural frequency, irrespective of the harmonic wave number. For the example given in the text, these were found to be the fundamental modes of harmonics $m = 4, 5$ and 6 .

Both the symmetric and anti-symmetric components of the modal response are equally significant. There is no or little correlation between both components. Coupling between modes for quasi-static response is very significant and can not be ignored; especially those including the cross product of harmonics $m = 2$ and 1 , and $m = 2$ and 3 .

The individual contributions of different modes of vibration could be measured directly from experiments using the present procedure for separation of modes. This could help reduce the amount of experimental measurements in future research.

4. The shell response is, in general, much more sensitive to variations in the statistical properties of the wind pressure fluctuations in the circumferential direction than in the meridional direction; most important is the position of flow separation ϕ_s . Mode $m = 2$ is particularly sensitive to these variations.
5. With a suitable choice of the shell meridional shape and appropriate proportioning of column supports, resonance could be effectively suppressed for towers with reasonable heights. While this might be difficult to achieve

for exceptionally high towers (over 500 ft.), resonance could still be considerably reduced.

C Shell Stiffness

1. The shell resistance to deformation under applied loads originates from two sources; membrane and bending actions. The effective membrane stiffness is particularly sensitive to variations in the meridional curvature and the constraints on the meridional displacements. The effective bending stiffness is almost insensitive to these variations. The membrane energy decreases rapidly with increasing m while the bending energy increases gradually. Since most of the wind response (static and dynamic) resides in low harmonics, conditions for the predominance of the membrane action must therefore be maintained.
2. The increase in shell thickness as a means of increasing the effective shell stiffness is not, in general the best solution; especially in cases where membrane action and quasi-static response predominate. It may be useful, however, in situations where resonance is significant, as it is generally associated with harmonics whose effective bending stiffness is significant.
3. A stiffening ring beam at top has little effect on the overall shell stiffness. The increases in the natural frequencies due to the presence of the beam are only marginal.

4. The natural frequencies for modes with low harmonics are very sensitive to variations in the stiffnesses of the column supports.
5. The shell stiffness is strongly dependent on the meridional curvature. An increase in the curvature parameter ($k_0 = a/b$) results in a considerable increase in the effective shell stiffness.

8.3 Design Considerations

For modern cooling towers in strong wind conditions, the wind-induced stresses are generally of the same order as the stresses due to self-weight. Small errors in the estimation of the wind-induced stresses could produce large differences in the net tensile stresses. This fact was emphasized by the collapse of the Ferrybridge cooling towers in England in 1965. An accurate estimation of the design wind stresses, on realistic basis, should therefore be given due consideration.

The main parameters required for the prediction of the mean component of the design wind loads are:

1. Mean design wind speed
2. Variation of mean wind speed with height
3. Mean pressure distribution around the shell circumference.

One of the most critical factors in design is to determine the design mean hourly wind speed. A rational approach to this problem should be based on the statistics of the largest

annual mean hourly wind speed, the anticipated life-time of the structure and the acceptable risk [1].

The variation of mean wind speed with height varies considerably with ground roughness. Some typical profiles have been suggested by Davenport [1]. For a given tower, the appropriate profile may vary with wind direction. Critical conditions could be defined from topographic wind tunnel models of the cooling tower site.

The choice of an appropriate distribution of the wind pressure coefficients, from available results is not a simple matter and further measurements, especially from full-scale tests, are still necessary. Evidence available at present suggest that, possible ranges of the main parameters of the mean wind pressure distribution are as follows:

1. Peak suction = $- 1.30 \pm 0.10$
2. Angle of flow separation = $95^{\circ} \pm 3^{\circ}$
3. Base pressure coefficient = $- 0.45 \pm 0.05$

Having defined the mean wind loads, the static component of the shell response \bar{y} , could be determined following the procedure described in Chapter 2.

Let us now turn to the dynamic component of the shell response $y(t)$. In Chapter 7, it is shown that, for a comprehensive treatment of $y(t)$, the following characteristics of the pressure fluctuations have to be defined:

1. Standard deviation
2. Correlation coefficient

3. Power spectral density function
4. Cross-spectral density function

At present, the only available measurements of these quantities were obtained from model tests at low Reynolds number ($R_e \approx 1.8 \times 10^5$). As yet, there exists some uncertainties as to their correspondence to full-scale behaviour. A sensitivity analysis of the functions employed to describe the pressure fluctuations proved valuable in this regard; but should not be considered as a substitute for full-scale measurements.

The dynamic response of the shell is composed of a quasi-static and a resonant component. It is instructive to examine the variation of both components in the light of the dynamic analysis given in Chapter 7.

Denoting the variance of the quasi-static response of mode (m, i) by $Q_{m, i}$ and the variance of the resonant response by $R_{m, i}$, then if all parameters are kept constant except for the wind speed, it could be shown that,

$$Q_{m, i} \propto \left\{ \frac{1}{2} \rho \bar{U}^2(z_G) \right\}^2 \quad (8.3)$$

and

$$R_{m, i} \propto \left\{ \frac{1}{2} \rho \bar{U}^2(z_G) \right\}^2 \tilde{S}_{p_{m, i} p_{m, i}}(\tilde{f}_{m, i}) \quad (8.4)$$

in which, $\tilde{S}_{p_{m, i} p_{m, i}}(\tilde{f}) = \frac{S_{p_{m, i} p_{m, i}}(\tilde{f})}{p_{m, i}^2(t)}$, $\tilde{f}_{m, i} = \frac{f_{m, i}^d}{\bar{U}(z_G)}$

and $\bar{U}(z_G)$ = gradient wind speed.

Previous results of the power spectra of the generalized forces $\tilde{S}_{p_{m,i}p_{m,i}}(\tilde{f})$, given in Chapter 7, indicate that,

$$\tilde{S}_{p_{m,i}p_{m,i}}(\tilde{f}) \propto \tilde{f}_{m,i}^{-2.8} \text{ to } \tilde{f}_{m,i}^{-3.45} \quad (8.5)$$

at high frequencies ($\tilde{f}_{m,i} > 0.25$), depending on the specific mode of vibration considered. Some typical results for the fundamental mode ($i = 1$) of harmonics $m = 2$ and 4 for Model I are shown in Fig. 8.1. At high frequencies, equation (8.4), thus, reduces to

$$R_{m,i} \propto \left(\frac{1}{2} \rho \bar{U}^2\right)^2 \left(\frac{\bar{U}}{f_{m,i} d}\right)^{2.9 \text{ to } 3.45} \quad (8.6)$$

By comparing equations (8.3 and 8.6), it is found that,

$Q_{m,i}$ is proportional to the fourth order of the wind velocity, while $R_{m,i}$ is approximately proportional to $(\bar{U})^{6.8 \text{ to } 7.45}$.

Also, for a given wind speed but with a varying natural frequency, it is found that, $Q_{m,i} \propto \tilde{f}_{m,i}^{-4}$ and $R_{m,i} \propto \tilde{f}_{m,i}^{-6.8 \text{ to } -7.45}$.

Therefore, a small increase in wind speed or a reduction in natural frequency could result in a considerable increase in the relative proportion of the resonant response. A somewhat similar conclusion, obtained experimentally, was pointed out by Armitt (3) who found that $R \propto (\bar{U})^8$.

If the static and dynamic components of the response are known, the peak response of mode (m, i) , $\hat{y}_{m,i}$, could be

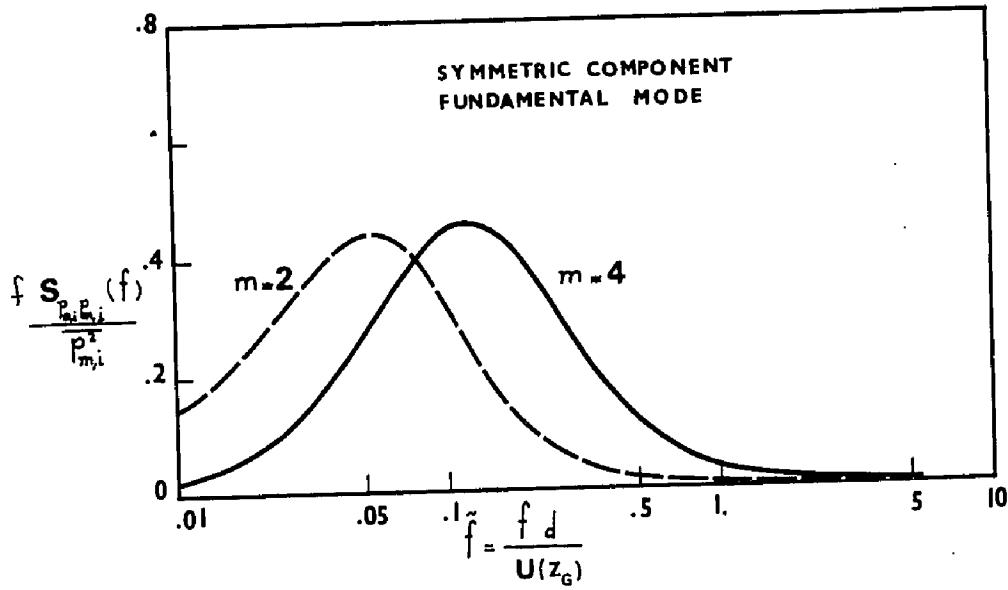


FIG.8.1 POWER SPECTRA OF THE GENERALIZED FORCES FOR MODEL I

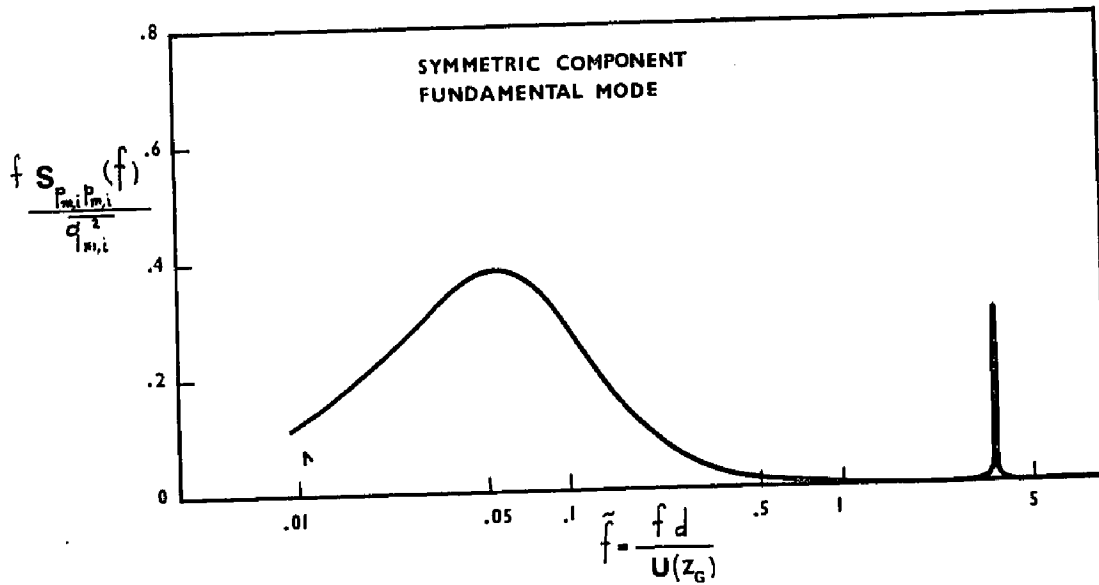


FIG.8.2 POWER SPECTRUM OF THE RESPONSE OF HARMONIC $m=2$

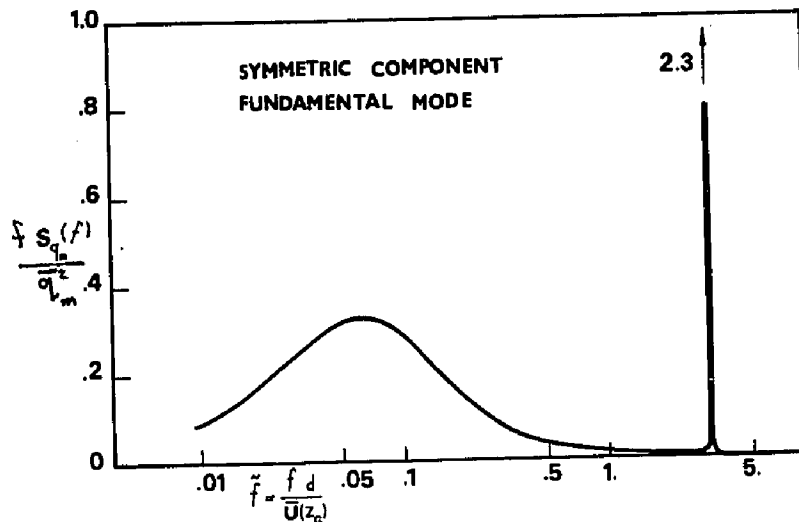


FIG.8.3 POWER SPECTRUM OF THE RESPONSE OF HARMONIC $m=3$

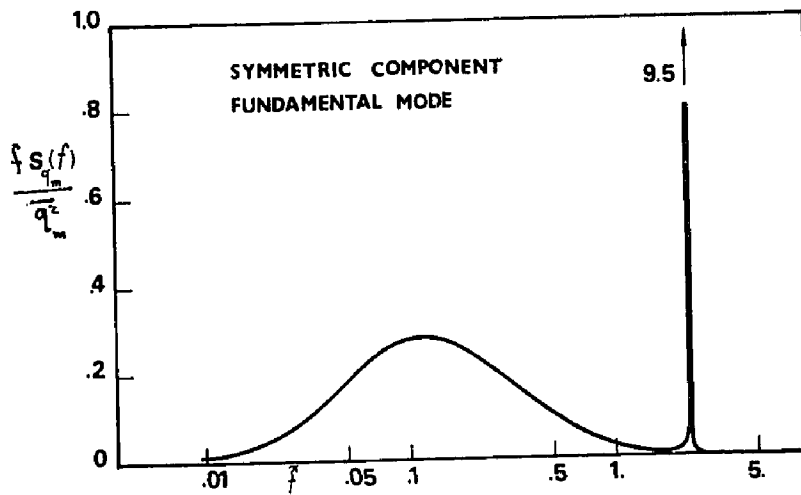


FIG.8.4 POWER SPECTRUM OF THE RESPONSE OF HARMONIC $m=4$

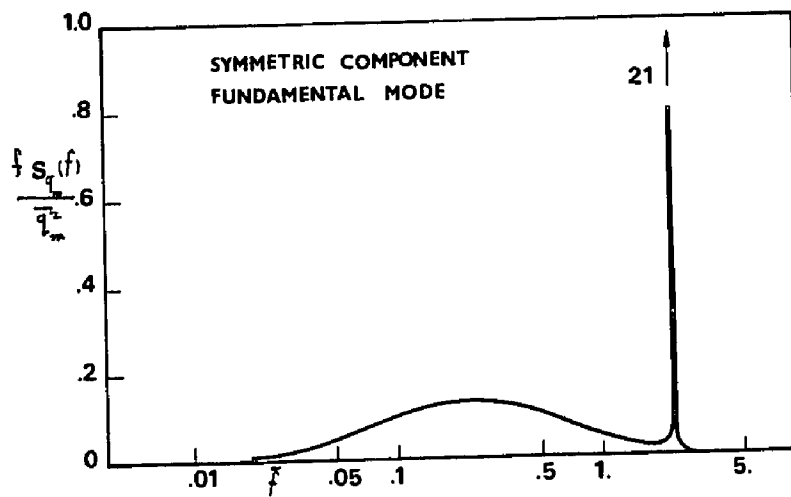


FIG.8.5 POWER SPECTRUM OF THE RESPONSE OF HARMONIC $m=5$

obtained as follows [2],

$$\hat{y}_{m,i} = \bar{y}_{m,i} + g_{m,i} \sigma(y_{m,i}) \quad (8.7)$$

in which, $g_{m,i}$ is a peak factor defined by [2],

$$g_{m,i} = \frac{0.577}{\sqrt{2 \log_e \bar{v}_{m,i}^T}} \quad (8.8)$$

and

$$\bar{v}_{m,i} = \left\{ \frac{\int_0^\infty f_{m,i}^2 S_{y_{m,i}}(f) df}{\int_0^\infty S_{y_{m,i}}(f) df} \right\}^{1/2} \quad (8.9)$$

In cases where resonance is predominant, \bar{v} is approximately equal to $f_{m,i}$. For cooling towers, resonance is generally small and the integrations of equation (8.9) have to be carried out to determine \bar{v} . As an example, the values of \bar{v} are computed herein for the 1/200 scale model (Model I) described in section 1.2.2.

Figs. 8.2 to 8.5 show the power spectra of the modal response for the fundamental mode shapes of harmonics $m = 2$ to 5. The computed values of $\bar{v}_{m,i}$ are given in Table 8.1 for $m = 1$ to 6.

The peak factor $g_{m,i}$, computed from equation (8.8) assuming $T = 40$ seconds, is also given in Table 8.1. It is found to vary between 3.84 and 4.25 depending on the mode of vibration considered. The value of $g_{m,i}$ increases as resonance increases.

It might be useful to extend the experimental and theoretical results of the dynamic response for the 1/200 scale model, described in section 7.2.2 to a typical cooling tower. The geometry and material properties of the tower are given in Fig. 8.6. The natural frequencies of the fundamental modes of harmonics $m = 1$ to 5 are given in Table 8.2. The dynamic response of the tower was extrapolated from the model response results.* The percentages of resonance of the modal response at gradient wind speeds of 60 and 95 mph are shown in Table 8.2. Note that for $U(Z_G) = 95$ mph, the resonant response is predominant for all modes except $m = 2$.

The variation of the peak dynamic response (just above the base ring at $\phi = 0$), with wind speed, is depicted in Fig. 8.7. Also shown in this figure are the mean wind and dead weight stresses. For this tower it is found that at gradient wind speeds over 50 mph, the dynamic response exceeds the static component. At $U(Z_G) = 75$ mph, the wind stresses start to overcome the self weight of the shell; beyond this speed the net tensile stresses increase very rapidly with wind speed.

The results given above are meant only to illustrate the order of magnitude of the peak wind stresses (relative to self weight stresses) and their variation with wind speed. A comprehensive analysis could be carried out as described in Chapter 7.

* For $\phi_s = 95^\circ$.

Table 8.1 Peak Factors for Model I

m	$f(\text{cps})$	$\tilde{f} = \frac{fd}{\bar{U}(z_G)}$	$\frac{\text{Resonance}}{\text{Modal Response}} \%$	$\bar{v}_{m,i}$ cps	$g_{m,i}$
1	340	6.0	3.0	57	4.08
2	197	3.5	2.0	22	3.84
3	170	3.1	7.5	46	4.03
4	129	2.3	31.0	73	4.14
5	122	2.15	65.0	100	4.21
6	142	2.5	64.0	114	4.25

Table 8.2 Resonance Contribution for a Full-Scale Tower ($H = 400 \text{ ft.}$)

m	f	$\bar{U}(z_G) = 90 \text{ ft/sec. (60 mph)}$		$\bar{U}(z_G) = 140 \text{ ft/sec. (95 mph)}$	
		\tilde{f}	% Resonance	\tilde{f}	% Resonance
1	1.78	3.14	17.8	2.03	60.0
2	1.29	2.30	6.9	1.48	21.6
3	0.99	1.75	30.8	1.13	62.5
4	0.92	1.62	57.0	1.05	78.5
5	1.02	1.80	75.5	1.16	92.0

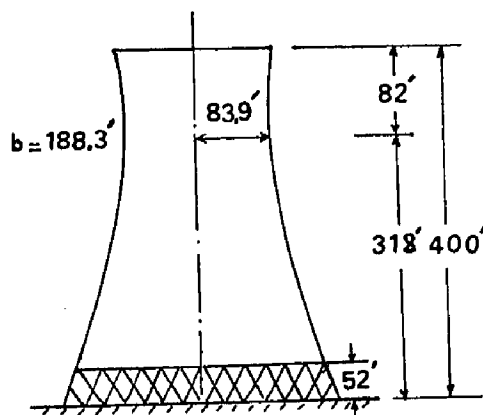


FIG. 8.6

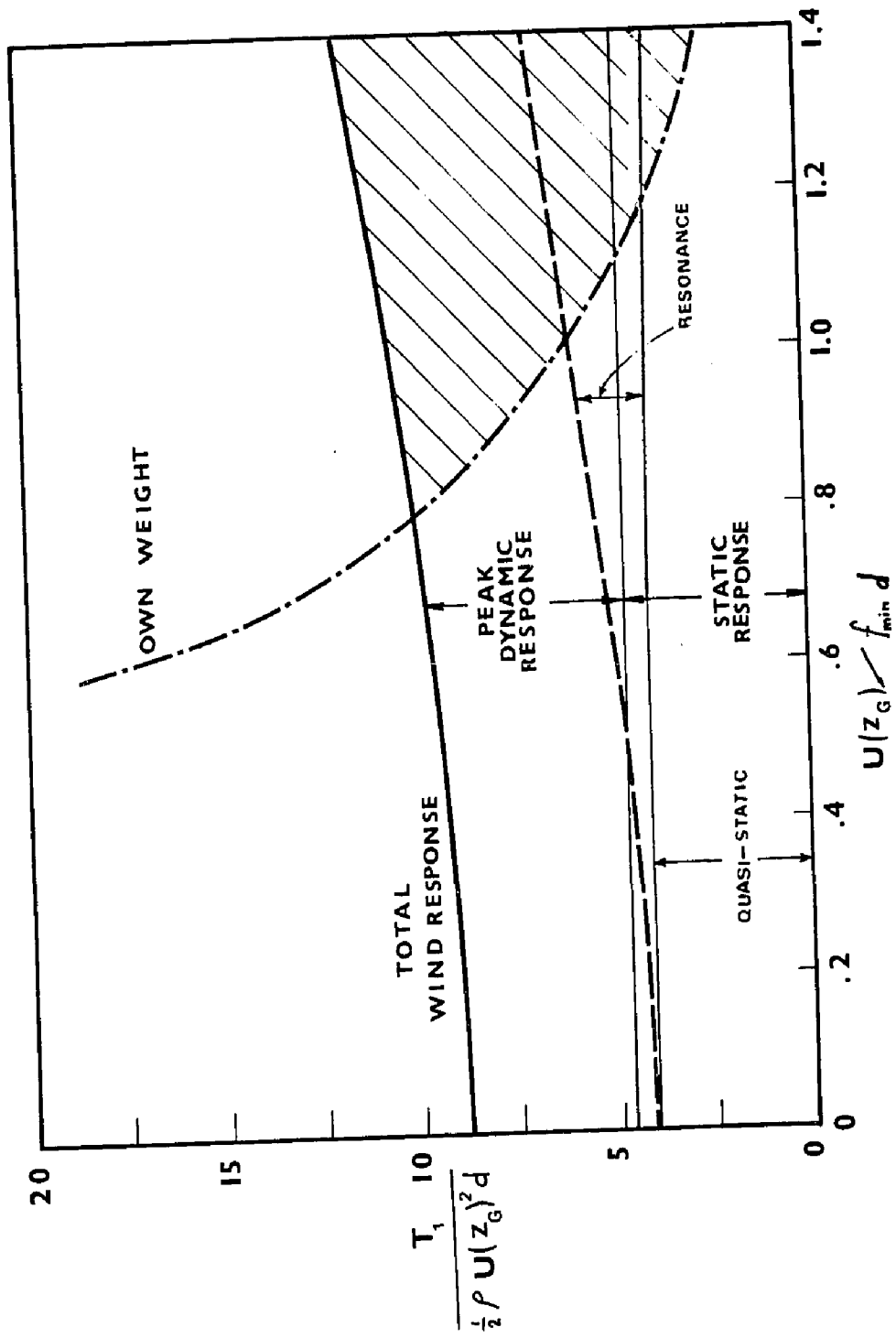


FIG. 8.7 VARIATION OF WIND- AND NET TENSILE STRESSES WITH WIND SPEED

8.4 Recommendations for Future Research

1. Full-scale measurements of mean pressure distribution and the statistical properties of the wind pressure fluctuations with emphasis on their variations around the shell circumference.
2. The investigation of the relationship between velocity and pressure fluctuations.
3. The study of the influence of shell surface roughness on the pressure characteristics at high Reynolds numbers ($\approx 10^8$).
4. The investigation of proximity effects of nearby structures on the flow of wind around the cooling tower.
5. Full scale measurements of the damping characteristics.
6. An extension of the present sensitivity analysis of the wind response and its dependence on the aerodynamics, structural and geometrical parameters. An attempt could be made to simplify the rigorous approach to the prediction of the shell dynamic response.

APPENDIX I

I.1 Shell Geometry

The geometry of the generating curve, for a hyperboloid of revolution, Fig. 2.1, is given by:

$$r^2 = a^2 \left\{ 1 + \frac{z^2}{b^2} \right\} \quad (\text{I-1})$$

in which r = radius of parallel circle, z = axial coordinate, Fig. 2.1, a = throat radius, and b = curvature parameter.

For our purpose, the geometric characteristics of the shell will be described by the following non-dimensional parameters:

$$\begin{aligned} \bar{h} &= h/h_0 & \gamma_0 &= \cos\theta \\ \gamma_1 &= h_0/r & \gamma_2 &= r/s_0 \\ \gamma_3 &= s_0/r_1 & \gamma_4 &= s_0/r_2 \\ \lambda &= s/s_0 \end{aligned} \quad (\text{I-2})$$

in which h = shell thickness, h_0 = a reference thickness, θ = angle between the z -axis and the normal to the shell surface, r_1 and r_2 = principal radii of curvature in the meridional and circumferential directions respectively,

s = meridional coordinate measured from shell base, and
 s_0 = total meridional length.

From equation (I-1), it could be shown that:

$$\theta = \arctan\left(\frac{b^2}{a^2} \frac{r}{z}\right) \quad (\text{I-3})$$

$$r_1 = - \frac{a^2 b^2}{(a^2 \sin^2 \theta - b^2 \cos^2 \theta)^{3/2}} \quad (\text{I-4})$$

$$r_2 = \frac{a^2}{(a^2 \sin^2 \theta - b^2 \cos^2 \theta)^{1/2}} \quad (\text{I-5})$$

$$s_0 \approx \left\{ \left(1 + \frac{a^2}{2b^2}\right) z - \frac{a^2}{2b} \arctan\left(\frac{z}{b}\right) \right\}_{z_t}^{z_b} \quad (\text{I-6})$$

in which, z_t and z_b are the values of z at top and bottom edges respectively.

I.2 Displacement and Mixed Formulations of the Fundamental Shell Equations

On the basis of Novozhilov (1) general equations for thin shells, the fundamental equations for thin shells are presented in two forms:

1. Displacement scheme: 3 differential equations of the eighth order in terms of shell displacements u , v , and w .
2. Mixed scheme: 8 first order differential equations in terms of the eight fundamental variables that appear in the natural boundary conditions.

Herein,, the underlying assumptions and the Fourier representation of shell variables are described, followed by the presentation of the displacement and mixed schemes.

I.2.1 Assumptions

The following assumptions are made:

1. The shell is thin; i.e. maximum (thickness/radius) ratio $\leq \frac{1}{50}$.
2. The shell material is elastic, homogeneous, and obeys Hooke's law.
3. Shell displacement everywhere is small compared to shell thickness.
4. The normals to the middle surface before deformation remain so after deformation and do not undergo any change in length.

I.2.2 Fourier Representation of Shell Variables

Due to the fact that hyperbolic cooling towers are complete in the circumferential direction (no boundary), it is possible to introduce periodic solutions of the form,

$$f(s, \phi) = \sum_{m=0}^{\infty} f_m(s) \begin{cases} \cos m\phi \\ \sin m\phi \end{cases} \quad (\text{I-7})$$

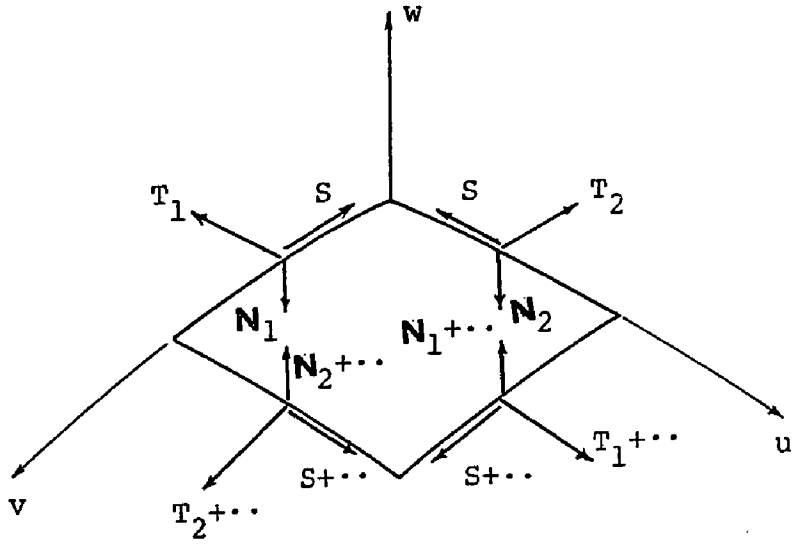


Fig. I.1a

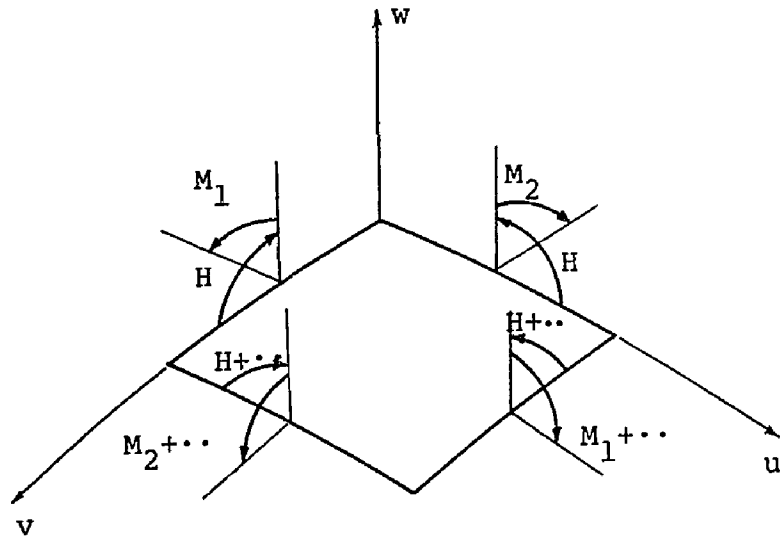


Fig. I.1b

in which m = harmonic wave number.

Furthermore, the function $f_m(s)$ could be represented in terms of the mode shapes of vibration in the meridional direction as follows:

$$f_m(s) = \sum_{i=1}^{\infty} a_{m,i} f_{m,i}(s) \begin{cases} \cos m\phi \\ \sin m\phi \end{cases} \quad (\text{I-8})$$

in which i = mode number.

Equation (I-7) thus becomes:

$$f(s, \phi) = \sum_{m=0}^{\infty} \sum_{i=1}^{\infty} a_{m,i} f_{m,i}(s) \begin{cases} \cos m\phi \\ \sin m\phi \end{cases} \quad (\text{I-9})$$

I.2.3 Force - Displacement Relations

Fig. I-1 shows the forces and moments acting on a typical shell element. Expressed as forces or moments per unit coordinate length, T_1 and T_2 are the normal forces in the meridional and circumferential directions, T_{12} and T_{21} are the in-plane shear forces, N_1 and N_2 are the out-of-plane shear forces, M_1 and M_2 are the bending moments around the circumferential and the meridional coordinates, and M_{12} and M_{21} are the twisting moments. The positive directions of shell displacement components are also shown in Fig. I-1.

For thin elastic shells, the force-displacement relations obtained on the basis of Novozhilov (1) stress-strain relations are as follows:

$$T_1 = C_o \left\{ S_1 \left(\frac{\partial u}{\partial s} + \frac{w}{r_1} \right) + \mu S_2 \left(\frac{\partial v}{r \partial \phi} + \frac{\gamma_o u}{r} + \frac{w}{r_2} \right) \right\} \quad (7-10)$$

$$T_2 = C_o \left\{ S_3 \left(\frac{\partial v}{r \partial \phi} + \frac{\gamma_o u}{r} + \frac{w}{r_2} \right) + \mu S_4 \left(\frac{\partial u}{\partial s} + \frac{w}{r_1} \right) \right\} \quad (I-11)$$

$$S = \frac{1}{2} C_o (1-\mu) S_5 \left\{ r \frac{\partial}{\partial s} \left(\frac{v}{r} \right) + \frac{1}{r} \frac{\partial v}{\partial \phi} \right\} \quad (I-12)$$

$$M_1 = D_o \left\{ S_6 \left(-\frac{\partial^2 w}{\partial s^2} + \frac{\partial}{\partial s} \left(\frac{u}{r_1} \right) \right) + \mu S_7 \left(-\frac{\partial^2 w}{r^2 \partial \phi^2} + \frac{\partial v}{r r_2 \partial \phi} - \frac{\gamma_o}{r} \left(\frac{\partial w}{\partial s} - \frac{u}{r_1} \right) \right) \right\} \quad (I-13)$$

$$M_2 = D_o \left\{ S_8 \left(-\frac{\partial^2 w}{r^2 \partial \phi^2} + \frac{\partial v}{r r_2 \partial \phi} - \frac{\gamma_o}{r} \left(\frac{\partial w}{\partial s} - \frac{u}{r_1} \right) \right) + \mu S_9 \left(-\frac{\partial^2 w}{\partial s^2} + \frac{\partial}{\partial s} \left(\frac{u}{r_1} \right) \right) \right\} \quad (I-14)$$

$$H = D_o (1-\mu) S_{10} \left\{ -\frac{1}{r} \left(\frac{\partial^2 w}{\partial \phi \partial s} - \frac{\gamma_o}{r} \frac{\partial w}{\partial \phi} \right) + \frac{\partial u}{r r_1 \partial \phi} + \frac{1}{r_2} \left(\frac{\partial v}{\partial s} - \frac{\gamma_o v}{r} \right) \right\} \quad (I-15)$$

in which

$$S = T_{12} - \frac{M_{21}}{r_2} = T_{21} - \frac{M_{12}}{r_1} \quad (I-16)$$

$$H = \frac{1}{2} (M_{12} + M_{21}) \quad (I-17)$$

$$C_o = \frac{Eh}{1-\mu^2} = \text{shell extensional stiffness}$$

$$D_o = \frac{Eh^3}{12(1-\mu^2)} = \text{shell bending stiffness}$$

E = Young's modulus, and μ = Poisson's ratio.

S_1 to S_{10} = non-dimensional factors introduced to allow

for possible variations in shell stiffnesses.

I.2.4 Equilibrium Equations

According to Novozhilov (1), the equilibrium equations for shells of revolution are:

$$\frac{1}{r} \frac{\partial r T_1}{\partial s} + \frac{1}{r} \frac{\partial T_{21}}{\partial \phi} - \frac{\cos \theta}{r} T_2 + \frac{N_1}{r_1} = -p_1 \quad (\text{I-18})$$

$$\frac{1}{r} \frac{\partial r S}{\partial s} + \frac{1}{r} \frac{\partial T_2}{\partial \phi} + \frac{\cos \theta}{r} T_{21} + \frac{N_2}{r_2} = -p_2 \quad (\text{I-19})$$

$$\frac{T_1}{r_1} + \frac{T_2}{r_2} - \frac{1}{r} \frac{\partial r N_1}{\partial s} - \frac{1}{r} \frac{\partial N_2}{\partial \phi} = p_3 \quad (\text{I-20})$$

$$\frac{1}{r} \frac{\partial r M_1}{\partial s} + \frac{1}{r} \frac{\partial M_{21}}{\partial \phi} - \frac{\cos \theta}{r} M_2 - N_1 = 0 \quad (\text{I-21})$$

$$\frac{1}{r} \frac{\partial r M_{12}}{\partial s} + \frac{1}{r} \frac{\partial M_2}{\partial \phi} + \frac{\cos \theta}{r} M_{21} - N_2 = 0 \quad (\text{I-22})$$

$$T_{12} - T_{21} + \frac{M_{12}}{r_1} - \frac{M_{21}}{r_2} = 0 \quad (\text{I-23})$$

in which p_1 , p_2 and p_3 are the components of the applied loads in the meridional, circumferential, and normal directions.

I.2.5 Displacement Scheme

In this section, the fundamental equations of the theory of thin shells of revolution are reduced to 3-differential equations in terms of shell displacements u , v , and w . This is carried out by substituting from equation (I-7), equations (I-10 to I-17), and equations (I-21 to I-23) into equations (I-18 to I-20). For each harmonic wave number m the resulting equations can be presented in a non-dimensional form as follows:

$$\begin{aligned}
 & \frac{1}{(1-\mu)^2 \gamma_2} \frac{d}{d\bar{l}} \{ \gamma_2 \bar{h} S_1 \left(\frac{dU}{d\bar{l}} + \gamma_3 W \right) + \mu \bar{h} S_2 (mV + \gamma_0 U + \gamma_2 \gamma_4 W) \} + \\
 & \frac{m}{2(1+\mu) \gamma_2} S_5 \bar{h} \left\{ \gamma_2 \frac{d}{d\bar{l}} \left(\frac{V}{\gamma_2} \right) - m \frac{U}{\gamma_2} \right\} - \frac{\gamma_0}{(1-\mu)^2 \gamma_2} \left\{ \frac{\bar{h} S_3}{\gamma_2} (mV + \gamma_0 U + \gamma_2 \gamma_4 W) + \right. \\
 & \left. \mu \bar{h} S_4 \left(\frac{dU}{d\bar{l}} + \gamma_3 W \right) \right\} + \frac{\gamma_1^2 \gamma_2 \gamma_3}{12(1-\mu)^2} \frac{d}{d\bar{l}} \left\{ -\gamma_2 \bar{h}^3 S_6 \frac{d}{d\bar{l}} \left(\frac{dW}{d\bar{l}} - \gamma_3 U \right) + \right. \\
 & \left. \mu \bar{h}^3 S_7 \left(\frac{1}{\gamma_2} (m^2 W + m \gamma_2 \gamma_4 V) - \gamma_0 \left(\frac{dW}{d\bar{l}} - \gamma_3 U \right) \right) \right\} - \frac{\gamma_0 \gamma_1^2 \gamma_2 \gamma_3}{12(1-\mu)^2} \\
 & \left\{ \bar{h}^3 S_8 \left(\frac{1}{\gamma_2} (m^2 W + m \gamma_2 \gamma_4 V) - \frac{\gamma_0}{\gamma_2} \left(\frac{dW}{d\bar{l}} - \gamma_3 U \right) \right) - \mu \bar{h}^3 S_9 \frac{d}{d\bar{l}} \left(\frac{dW}{d\bar{l}} - \gamma_3 U \right) \right\} \\
 & + \frac{m \gamma_1^2 \gamma_2 \gamma_3}{6(1+\mu) \bar{h}} S_{10} \left\{ \frac{m}{\gamma_2} \left(\frac{dW}{d\bar{l}} - \frac{\gamma_0}{\gamma_2} W - \gamma_3 U \right) + \gamma_4 \left(\frac{dV}{d\bar{l}} - \frac{\gamma_0}{\gamma_2} V \right) \right\} = - \frac{P_1^s}{E h_0}
 \end{aligned}
 \tag{I-24}$$

$$\frac{1}{2(1+\mu) \gamma_2} \frac{d}{d\bar{l}} \left\{ S_5 \bar{h} \left(\gamma_2 \frac{d}{d\bar{l}} \left(\frac{U}{\gamma_2} \right) - mU \right) \right\} - \frac{m \bar{h}}{(1-\mu)^2 \gamma_2} \left\{ \frac{S_3}{\gamma_2} (mV + \gamma_0 U + \gamma_2 \gamma_4 W) \right\}$$

$$\begin{aligned}
& + \mu S_4 \left(\frac{dU}{d\tau} + \gamma_3 W \right) + \frac{\gamma_0 \bar{h} S_5}{2(1+\mu)\gamma_2} \left\{ \gamma_2 \frac{d}{d\tau} \left(\frac{V}{\gamma_2} \right) - \frac{U}{\gamma_2} \right\} + \frac{m\gamma_1^2 \gamma_2 \gamma_4}{12(1-\mu^2)} \\
& \left\{ \bar{h} S_8 \left(-\frac{m^2 W}{\gamma_2} - m \frac{\gamma_4}{\gamma_2} V + \frac{\gamma_0}{\gamma_2} \left(\frac{dW}{d\tau} - \gamma_3 U \right) \right) + \mu \bar{h}^3 S_9 \frac{d}{d\tau} \left(\frac{dW}{d\tau} - \gamma_3 U \right) \right\} \\
& + \frac{\gamma_1^2 \gamma_2 \gamma_4}{6(1+\mu)} \frac{d}{d\tau} \bar{h}^3 S_{10} \left\{ m \left(\frac{dW}{d\tau} - \frac{\gamma_0}{\gamma_2} W - \gamma_3 U \right) + \gamma_2 \gamma_4 \left(\frac{dV}{d\tau} - \frac{\gamma_0}{\gamma_2} V \right) \right\} \\
& + \frac{\gamma_0 \gamma_1^2 \gamma_2 \gamma_3}{6(1+\mu)} \bar{h}^3 S_{10} \left\{ \frac{m}{\gamma_2} \left(\frac{dW}{d\tau} - \frac{\gamma_0}{\gamma_2} W - \gamma_3 U \right) + \gamma_4 \left(\frac{dV}{d\tau} - \frac{\gamma_0}{\gamma_2} V \right) \right\} = -\frac{F_2^S \epsilon_0}{E \bar{h}_0} \\
\end{aligned} \tag{I-25}$$

$$\begin{aligned}
& - \frac{1}{1-\mu} \left\{ \bar{h} (\gamma_3 S_1 + \mu \gamma_4 S_4) \left(\frac{dU}{d\tau} + \gamma_3 W \right) + \frac{\bar{h}}{\gamma_2} (\gamma_4 S_3 + \mu \gamma_3 S_2) (mV + \gamma_0 U + \gamma_2 \gamma_4 W) \right\} \\
& - \frac{\gamma_1^2 \gamma_2}{12(1-\mu^2)} \frac{d^2}{d\tau^2} \bar{h}^3 \gamma_2 \left\{ S_6 \frac{d}{d\tau} \left(\frac{dW}{d\tau} - \gamma_3 U \right) - \frac{\mu}{\gamma_2} S_7 \left((m^2 W + m\gamma_2 \gamma_4 V) \right. \right. \\
& \left. \left. - \gamma_0 \gamma_2 \left(\frac{dW}{d\tau} - \gamma_3 U \right) \right) \right\} - \frac{m\gamma_1^2 \gamma_2}{12(1+\mu)} \frac{d}{d\tau} \bar{h}^3 S_{10} \left\{ \frac{m}{\gamma_2} \left(-\frac{dW}{d\tau} + \frac{\gamma_0}{\gamma_2} W + \gamma_3 U \right) \right. \\
& \left. - \gamma_4 \left(\frac{dV}{d\tau} - \frac{\gamma_0}{\gamma_2} V \right) \right\} + \frac{\gamma_1^2 \gamma_2}{12(1-\mu^2)} \frac{d}{d\tau} \left\{ -\frac{\gamma_0 \bar{h}^3 S_8}{\gamma_2} \left(\frac{1}{\gamma_2} (m^2 W + m\gamma_2 \gamma_4 V) \right. \right. \\
& \left. \left. - \gamma_0 \left(\frac{dW}{d\tau} - \gamma_3 U \right) \right) + \mu \gamma_0 \bar{h}^3 S_9 \frac{d}{d\tau} \left(\frac{dW}{d\tau} - \gamma_3 U \right) \right\} - \frac{m\gamma_1^2}{12(1+\mu)} \frac{d}{d\tau} \bar{h}^3 \\
& S_{10} \left\{ \left(-m \frac{dW}{d\tau} + m \frac{\gamma_0}{\gamma_2} W + m\gamma_3 U \right) - \gamma_2 \gamma_4 \left(\frac{dV}{d\tau} - \frac{\gamma_0}{\gamma_2} V \right) \right\} + \frac{m^2 \gamma_1^2}{12(1-\mu^2)} \\
& \left\{ -\frac{\bar{h}^3 S_8}{\gamma_2} (m^2 W + m\gamma_2 \gamma_4 V - \gamma_0 \gamma_2 \left(\frac{dW}{d\tau} - \gamma_3 U \right)) + \mu \bar{h}^3 S_9 \frac{d}{d\tau} \left(\frac{dW}{d\tau} - \gamma_3 U \right) \right\} \\
& - \frac{m\gamma_0 \gamma_1^2}{12(1+\mu)} \bar{h}^3 S_{10} \left\{ \frac{m}{\gamma_2} \left(-\frac{dW}{d\tau} + \frac{\gamma_0}{\gamma_2} W + \gamma_3 U \right) - \gamma_4 \left(\frac{dV}{d\tau} - \frac{\gamma_0}{\gamma_2} V \right) \right\} = -\frac{F_3^S \epsilon_0}{E \bar{h}_0} \\
\end{aligned} \tag{I-26}$$

in which $U = u/s_0$, $V = v/s_0$, and $W = w/s_0$.

I.2.6 Mixed Scheme

The fundamental equations of the theory of thin shells of revolution are represented, herein, by a set of eight-first-order ordinary differential equations in terms of the eight fundamental variables that appear in the natural boundary conditions. These variables are: the displacement components u , v , and w , angle of rotation β , and the stress resultants T_1 , M_1 , \bar{S} and \bar{N}_1 , where,

$$\bar{S} = S + 2H/r_2 \quad (\text{I-27})$$

$$\bar{N}_1 = N_1 + \frac{1}{r} \frac{\partial M_{12}}{\partial \phi} \quad (\text{I-28})$$

In the formulation of the governing equations, the stress resultants associated with harmonic wave number m are replaced by non-dimensional quantities defined by:

$$\begin{aligned} \tilde{T}_1 &= rT_1/Es_0^2; & \tilde{M}_1 &= rM_1/Es_0^3 \\ \tilde{S} &= r\bar{S}/Es_0^2; & \tilde{N}_1 &= r\bar{N}_1/Es_0^3 \end{aligned} \quad (\text{I-29})$$

and the displacement components u , v , and w are replaced by:

$$\tilde{W} = w/s_0; \quad \tilde{V} = v/s_0; \quad \tilde{U} = u/s_0 \quad (\text{I-30})$$

and the external loads are replaced by:

$$\tilde{p}_1 = -\frac{p_1\gamma_2}{E} \quad \tilde{p}_2 = -\frac{p_2\gamma_2}{E} \quad \tilde{p}_3 = -\frac{p_3\gamma_2}{E} \quad (\text{I-31})$$

The following non-dimensional ratios are also introduced,

$$\begin{aligned} \gamma_5 &= \gamma_1 \gamma_2 \gamma_4; & \gamma_6 &= s_5 + \frac{\gamma_5^2}{3} s_{10} \\ \gamma_7 &= \frac{1}{1-\mu^2} \{s_3 - \mu^2 s_2 s_4/s_1\} \\ \gamma_8 &= \frac{1}{1-\mu^2} \{s_8 - \mu^2 s_7 s_9/s_1\} \end{aligned} \quad (\text{I-32})$$

The shell equations are formulated following the procedure described in (2,3). The formulation proceeds as follows: the first, second, and seventh equations are obtained by expressing T_1 , M_1 , and \bar{S} , in terms of u , v , w , and β , equations (I-10, I-11, and I-27). The third to sixth equations are obtained by rewriting the first four equilibrium equations (I-18 to I-21) in terms of the eight fundamental variables. The last equation is,

$$\beta = \frac{\partial w}{\partial s} + \frac{w}{r_1} \quad (\text{I-33})$$

In the eight equations, the dependence of the shell variables on the circumferential direction is eliminated by means of equation (I-7).

In a non-dimensional form, the eight first order differential equations are presented in matrix form as follows:

$$(A)\{x\} + (B)\left\{\frac{dx}{d\ell}\right\} = \{p\} \quad (\text{I-34})$$

in which A and B are coefficient matrices,

$$\{x\}^T = \{\tilde{T}_1, \tilde{M}_1, V, W, U, \beta, \tilde{S}, \tilde{N}_1\} \quad (\text{I-35})$$

$$\{p\}^T = \{0, 0, \tilde{p}_2, \tilde{p}_3, \tilde{p}_1, 0, 0, 0\} \quad (\text{I-36})$$

The non-zero elements of matrix A are given by:

$$\begin{aligned} A_{1,1} &= - (1-\mu^2)/\gamma_1\gamma_2^2 \\ A_{1,3} &= \mu m S_2/\gamma_2 \\ A_{1,4} &= \gamma_3 S_1 + \mu \gamma_4 S_2 \\ A_{1,5} &= \mu \gamma_0 S_2/\gamma_2 \\ A_{2,2} &= -12(1-\mu^2)/\gamma_1^3 \gamma_2^4 \\ A_{2,3} &= \mu m \gamma_4 S_7/\gamma_2 \\ A_{2,4} &= \mu m^2 S_7/\gamma_2^2 \\ A_{2,6} &= \mu \gamma_0 S_7/\gamma_2 \\ A_{3,1} &= \mu m S_4/\gamma_2 S_1 \\ A_{3,2} &= \mu m \gamma_4 S_9/\gamma_2 S_6 \\ A_{3,3} &= m^2 \gamma_1 (\gamma_7 + \gamma_8 \gamma_5^2/12) \\ A_{3,4} &= m \gamma_5 (\gamma_7 + m^2 \gamma_1^2 \gamma_8/12) \\ A_{3,5} &= m \gamma_0 \gamma_1 \gamma_7 \\ A_{3,6} &= m \gamma_0 \gamma_1^3 \gamma_2^2 \gamma_4 \gamma_8/12 \\ A_{3,7} &= -\gamma_0/\gamma_2 \\ A_{4,1} &= \gamma_3 + \mu \gamma_4 S_4/S_1 \\ A_{4,2} &= \mu m^2 S_9/\gamma_2^2 S_6 \\ A_{4,3} &= A_{3,4} \\ A_{4,4} &= \gamma_7 \gamma_5^2/\gamma_1 + m^4 \gamma_1^3/12 + m^2 S_{10} \gamma_0^2 \gamma_1^3 (1 - \frac{\gamma_5^2 S_{10}}{3 \gamma_6})/6(1+\mu) \end{aligned}$$

$$\begin{aligned}
A_{4,5} &= \gamma_0 \gamma_5 \{ \gamma_7 - m^2 \gamma_1^2 S_5 S_{10} / 6 \gamma_6 (1+\mu) \\
A_{4,6} &= \frac{m^2 \gamma_0 \gamma_1^3 \gamma_2}{12} \{ \gamma_8 + 2 S_{10} (1 - S_{10} \gamma_5^2 / 3 \gamma_6) / (1+\mu) \} \\
A_{4,7} &= - m \gamma_0 \gamma_1 \gamma_5 S_{10} / 3 \gamma_2 \gamma_6 \\
A_{5,1} &= \mu \gamma_0 S_4 / \gamma_2 S_1 \\
A_{5,3} &= A_{3,5}; \quad A_{5,4} = A_{4,5} \\
A_{5,5} &= \gamma_0^2 \gamma_1 \gamma_7 + m^2 \gamma_1 \gamma_5^2 S_5 S_{10} / 6 \gamma_6 (1+\mu) \\
A_{5,6} &= - m^2 \gamma_1^2 \gamma_2 \gamma_5 S_5 S_{10} / 6 \gamma_6 (1+\mu) \\
A_{5,7} &= - m S_5 / \gamma_2 \gamma_6 \\
A_{5,8} &= - \gamma_3 \\
A_{6,2} &= \mu \gamma_0 S_9 / \gamma_2 \gamma_6 \\
A_{6,3} &= A_{3,6}; \quad A_{6,4} = A_{4,6}; \quad A_{6,5} = A_{5,6} \\
A_{6,6} &= \frac{\gamma_1^3 \gamma_2^2}{12} \{ \gamma_0^2 \gamma_8 + 2 m^2 S_{10} (1 - \gamma_5^2 S_{10} / 3 \gamma_6) / (1+\mu) \} \\
A_{6,7} &= - m \gamma_1 \gamma_5 S_{10} / 3 \gamma_6 \\
A_{6,8} &= 1.0 \\
A_{7,3} &= A_{3,7}; \quad A_{7,4} = A_{4,7} \\
A_{7,5} &= A_{5,7}; \quad A_{7,6} = A_{6,7} \\
A_{7,7} &= -2(1+\mu) / \gamma_1 \gamma_2^2 \gamma_6 \\
A_{8,5} &= A_{5,8}; \quad A_{8,6} = A_{6,8}
\end{aligned}$$

1.3 Boundary Conditions

Hyperbolic cooling tower shells are bounded by two parallel circles, top and bottom edges. The solution of shell equations requires the definition of the boundary conditions at both edges. In this section, the boundary conditions for free, simply-supported, fixed, ring stiffened, and column-supported edges are presented.

I.3.1 Free Edge

$$T_1 = M_1 = \bar{S} = \bar{N}_1 = 0 \quad (\text{I-37})$$

I.3.2 Simply-Supported Edge

$$w = v = T_1 = M_1 = 0 \quad (\text{I-38})$$

I.3.3 Fixed Edge

$$w = v = u = \beta = 0 \quad (\text{I-39})$$

I.3.4 Ring-Stiffened Edge

Hyperbolic cooling tower shells are, sometimes, stiffened with a ring beam at top edge. In a comprehensive treatment of the beam joint-action with the shell, the author (4) have shown that the beam-boundary equations in terms of shell variables, at top edge, are given by:

$$\begin{aligned} & \frac{\beta_1}{\gamma_2} \{-m^2 V - (\beta_6 \cos \beta_0 + \beta_7 \sin \beta_0) (m^3 W + m^2 V) - m W \sin \beta_0 + m U \cos \beta_0 \\ & + m \beta_2 \beta_7 \frac{dW}{dl}\} + \beta_3 \beta_5 \left(\frac{\gamma_1}{\gamma_2}\right)^2 \{-m^3 W \sin \beta_0 + m^3 U \cos \beta_0 + m^3 \gamma_2 \beta_7 \frac{dW}{dl} \\ & + m W \sin \beta_0 - m U \cos \beta_0 - m \gamma_2 \beta_7 \frac{dW}{dl} - m^2 V - (\beta_6 \cos \beta_0 + \beta_7 \sin \beta_0) \\ & (m^3 W + m^2 V)\} + (1 - \beta_5 \beta_6) \frac{\gamma_1}{2 \gamma_2 (1 + \mu)} \bar{S} + \frac{\gamma_1}{\beta_5 \gamma_2 E r_t} \left(X_0 + \frac{M y_0}{r_b}\right) = 0 \end{aligned} \quad (\text{I-40})$$

$$\begin{aligned}
& -\beta_2 \beta_5 \left(\frac{\gamma_1}{\gamma_2}\right)^2 \left\{ m^2 \gamma_2 \frac{dW}{dL} + m^4 U \sin \beta_0 + m^4 W \cos \beta_0 - m^4 \beta_6 \gamma_2 \frac{dW}{dL} \right\} \\
& -\beta_4 \beta_5 \left(\frac{\gamma_1}{\gamma_2}\right)^2 \left\{ m^2 \gamma_2 \frac{dW}{dL} - m^2 U \sin \beta_0 - m^2 W \cos \beta_0 + m^2 \gamma_2 \beta_6 \frac{dW}{dL} \right\} \\
& + m \beta_5 \beta_7 \frac{\gamma_1}{2\gamma_2(1+\mu)} \bar{S} + \frac{\gamma_1}{\gamma_2(1-\mu)^2} \sin \beta_0 T_1 + \frac{\gamma_1^3 \cos \beta_0}{12(1-\mu)^2} \bar{N}_1 \\
& + \frac{\gamma_1}{\beta_5 \gamma_2 E r_t} \left(Y_0 - \frac{M z_0}{r_t} \right) = 0 \tag{I-41}
\end{aligned}$$

$$\begin{aligned}
& \beta_3 \beta_5 \left(\frac{\gamma_1}{\gamma_2}\right)^2 \left\{ -m^4 \sin \beta_0 W + m^4 \cos \beta_0 U + m^4 \gamma_2 \beta_7 \frac{dW}{dL} \right. \\
& \left. + m^2 W \sin \beta_0 - m^2 U \cos \beta_0 - m^2 \gamma_2 \beta_7 \frac{dW}{dL} - m^3 V - (\beta_6 \cos \beta_0 + \beta_7 \sin \beta_0) \right. \\
& \left. (m^4 W + m^3 V) - \frac{\beta_1}{\gamma_2} \{ mV - (\beta_6 \cos \beta_0 + \beta_7 \sin \beta_0) (-m^2 W - mV) \right. \\
& \left. + W \sin \beta_0 - U \cos \beta_0 - \gamma_2 \beta_7 \frac{dW}{dL} \right\} - \beta_5 \beta_6 \frac{m \gamma_1}{2\gamma_2(1+\mu)} \bar{S} + \frac{\gamma_1^3 \sin \beta_0}{12(1-\mu)^2} \bar{N}_1 \\
& - \frac{\gamma_1}{\gamma_2(1-\mu)^2} \cos \beta_0 T_1 + \frac{\gamma_1}{\beta_5 \gamma_2 E r_t} \left(Z_0 + \frac{M y_0}{r_t} \right) = 0 \tag{I-42}
\end{aligned}$$

$$\begin{aligned}
& \beta_4 \left(\frac{\gamma_1}{\gamma_2}\right)^2 \left\{ m^2 \gamma_2 \frac{dW}{dL} - m^2 U \sin \beta_0 - m^2 W \cos \beta_0 + m^2 \gamma_2 \beta_6 \frac{dW}{dL} \right\} + \beta_2 \left(\frac{\gamma_1}{\gamma_2}\right)^2 \\
& \left\{ \gamma_2 \frac{dW}{dL} + m^2 U \sin \beta_0 + m^2 W \cos \beta_0 - m^2 \gamma_2 \beta_6 \frac{dW}{dL} \right\} + \frac{\gamma_1}{\gamma_2(1-\mu)^2} (\beta_7 \cos \beta_0 \\
& - \beta_6 \sin \beta_0) T_1 - (\beta_7 \sin \beta_0 + \beta_6 \cos \beta_0) \frac{\gamma_1^3}{12(1-\mu)^2} \bar{N}_1 - \frac{\gamma_1^3}{12\gamma_2(1-\mu)^2} M_1 \\
& - \frac{\gamma_1}{\gamma_2} \frac{r_b}{r_t} M_{x0} = 0 \tag{I-43}
\end{aligned}$$

in which, the ratios $\beta_1 \dots \beta_7$ define the elastic and geometric properties of the beam as follows:

$$\beta_1 = E_b A_b / E h r_t; \quad \beta_2 = E_b I_z / E h^3 r_t$$

$$\beta_3 = E_b I_y / E h^3 r_t; \quad \beta_4 = G_b J_b / E h^3 r_t$$

$$\beta_5 = r_t / r_b; \quad \beta_6 = b' / s r_t$$

$$\beta_7 = d' / 2 r_t$$

and A_b = beam cross-sectional area.

E_b, G_b = Young's and shear moduli of beam material respectively,

x, y, z = beam coordinates (Fig. I.2),

I_y, I_z = beam flexural moments of inertia,

J_b = effective torsional moment of inertia of the beam,

r_b = beam radius,

r_t = shell radius at top,

β_0 = angle between shell tangent and the horizontal axis of the beam (z -axis) measured clockwise,

ρ_b = mass density of beam material,

$X_0, Y_0, Z_0, M_{x_0}, M_{y_0}$, and M_{z_0} = external forces and moments acting on the beam, Fig. I.2.

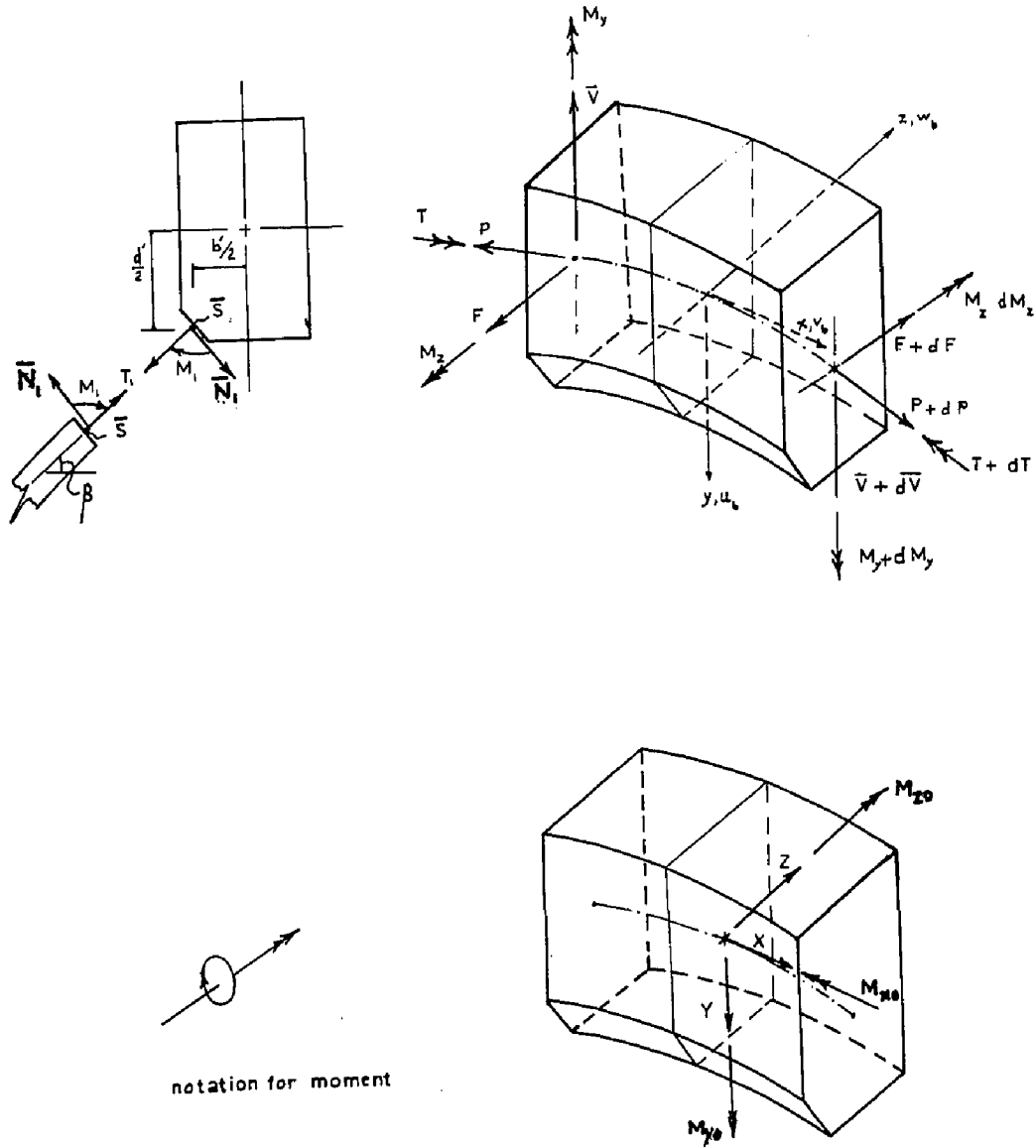


FIG. I.2

Expressions of beam displacements u_b , v_b , and w_b in terms of shell displacements, were found to be (4,5):

$$u_b = u \sin \beta + w \cos \beta - \frac{b'}{2} \frac{\partial w}{\partial s} \quad (\text{I-44})$$

$$v_b = v - \left(\frac{b'}{2} \cos \beta + \frac{d'}{2} \sin \beta \right) \left(\frac{\partial w}{r_t \partial \phi} - \frac{v}{r_t} \right) \quad (\text{I-45})$$

$$w_b = w \sin \beta - u \cos \beta - \frac{d'}{2} \frac{\partial w}{\partial s} \quad (\text{I-46})$$

The beam forces and moments are related to beam displacements by (4,5):

$$P = E_b A_b \left(\frac{\partial v_b}{r_b \partial \phi} + \frac{w_b}{r_b} \right) \quad (\text{I-47})$$

$$M_z = E_b I_z \left(- \frac{\partial w}{r_b \partial s} + \frac{\partial^2 u_b}{r_b^2 \partial \phi^2} \right) \quad (\text{I-48})$$

$$M_y = E_b I_y \left(- \frac{w_b}{r_b} - \frac{\partial^2 w_b}{r_b^2 \partial \phi^2} + \frac{\partial v_b}{r_b^2 \partial \phi} \right) \quad (\text{I-49})$$

$$T = G_b J_b \left(- \frac{1}{r_b} \frac{\partial^2 w}{\partial \phi \partial s} + \frac{\partial u_b}{r_b^2 \partial \phi} \right) \quad (\text{I-50})$$

1.3.5 Column-Supported Edge

Cooling towers are usually supported by a deep ring beam resting on a system of closely spaced column supports.

Abu-Sitta (6) has shown that the column support system could be treated as an extension of the shell but with reduced stiffnesses. The equiva-

lent uniform stiffnesses were found to be:

$$1. \text{ Membrane force } T_1; C_1 = E \frac{b_c d_c \sin^3 \alpha_o (1-\mu^2)}{l_c \cos \alpha_o} \quad (\text{I-51})$$

$$2. \text{ Membrane shear } S; C_{12} = E \frac{b_c d_c \sin \alpha_o \cos \alpha_o (1-\mu^2)}{l_c} \quad (\text{I-52})$$

$$3. \text{ Bending moment } M_1; D_1 = E \left\{ \frac{I}{l_c} \frac{\sin^3 \alpha_o}{\cos \alpha_o} + 4 \frac{i}{l_c} \frac{\sin \alpha_o \cos \alpha_o}{(1+\mu)} \right\} \quad (\text{I-53})$$

$$4. \text{ Torsion, } H; D_{12} = E \left\{ \frac{4I}{l_c} \sin \alpha_o \cos \alpha_o + \frac{8}{(1+\mu)} \frac{i}{l_c} \right\} \quad (\text{I-54})$$

in which, $i = (d_c b_c^3 / 12)$, $I = (b_c d_c^3 / 12)$, C_1 and C_{12} = membrane meridional and shear stiffnesses and D_1 and D_{12} = flexural meridional and torsional stiffnesses.

In the circumferential direction M_2 and T_2 are assumed zero, since there is no continuity in the circumferential direction.

APPENDIX II

COMPARISONS WITH PREVIOUS RESULTS

In Appendix I, the shell equations are presented in two forms; displacement and mixed schemes. For both schemes, solution of the shell differential equations was obtained by means of the modified finite difference method described in Chapter 2.

Both the displacement and mixed modified finite difference schemes were used in the analysis of several static and free vibration problems [1 to 5]. Some selected results follow.

II.1 Static Response

The displacement and mixed modified finite difference schemes are used to determine the static wind stresses in a hyperbolic cooling tower, shown in Fig. II.1, which has the same over-all dimensions as the Ferrybridge cooling towers which failed in England in 1965. Young's modulus of the shell material is 3×10^6 psi and its Poisson's ratio is 0.15. Fixed-free edge conditions are assumed at bottom and top boundaries of the shell respectively. The wind pressure considered is given in Ref. [6]. The wind pressure along the upstream stagnation line is assumed to be invariant with height and is set to unity (1 lb/ft^2). In the finite difference solutions, equal intervals were used and

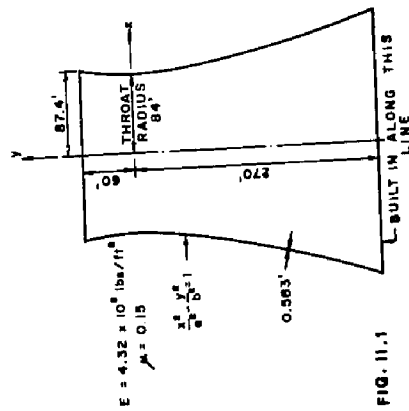
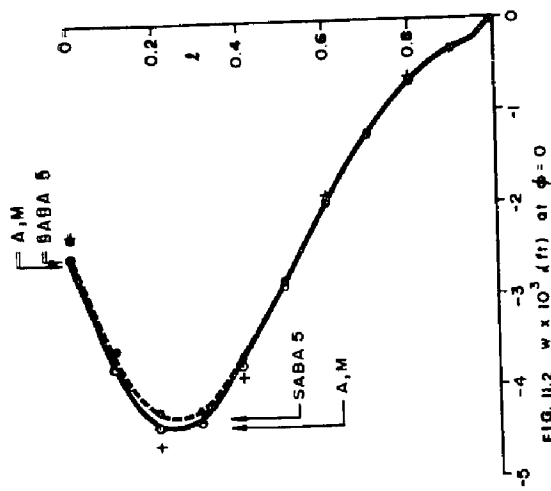
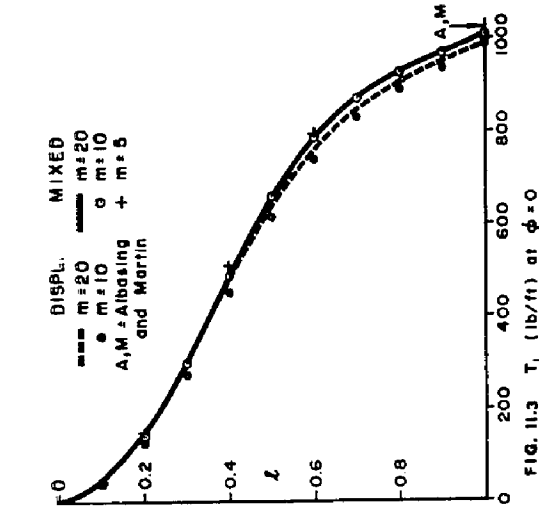


FIG. 11.1

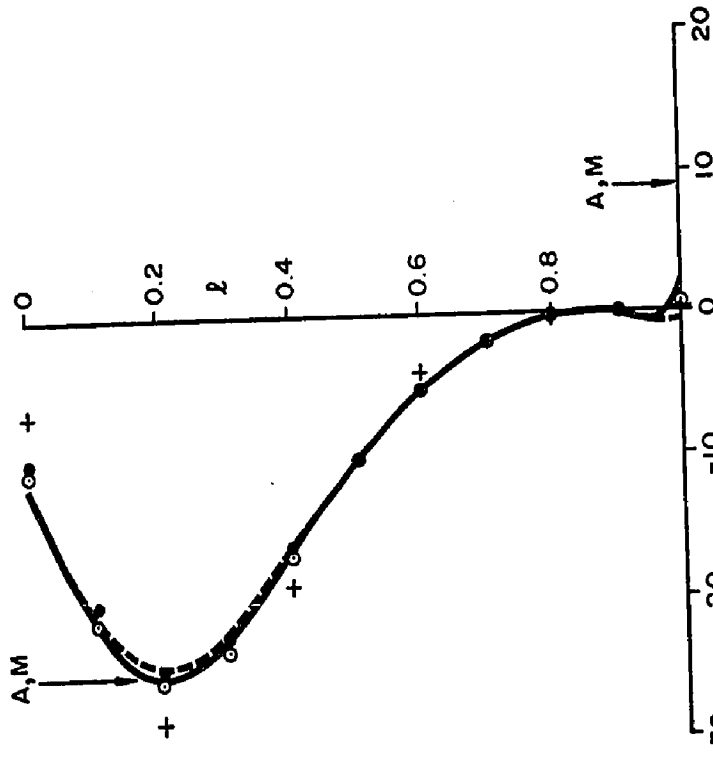


FIG. II.5 M_2 (lb.ft/ft) at $\phi = 0$

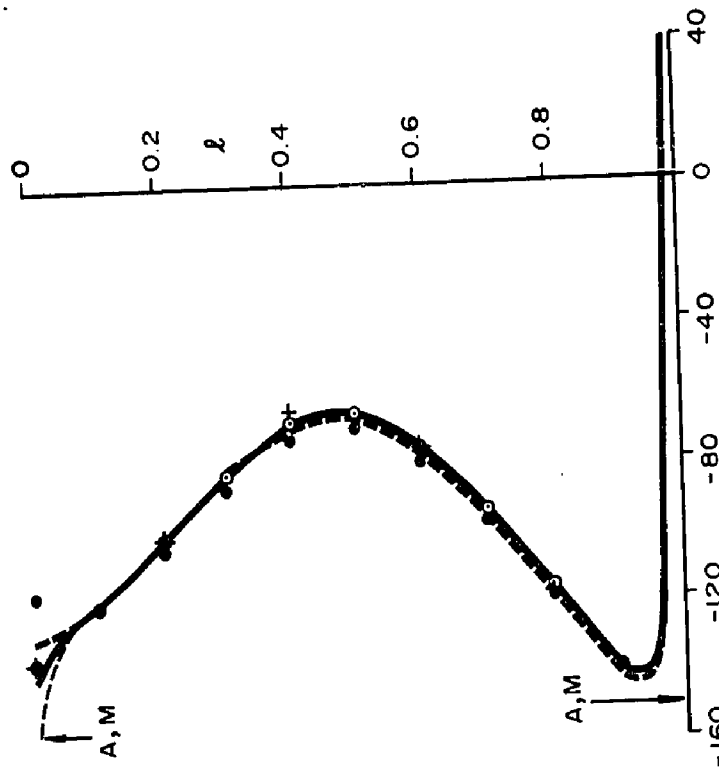


FIG. II.4 T_2 (lb/ft) at $\phi = 0$

the number of grid intervals varied from 5 to 20.

Figs. II.2 to II.5 show the variation with height, at $\phi = 0$, of the normal displacement w , the meridional force T_1 , the circumferential force T_2 and the circumferential moment M_2 respectively. The results are compared with the conventional finite difference solution by Albasiny [6] and the finite difference solution by Chan and Firmin [7]. In the finite difference solution 162 unequal intervals were used; very fine at the boundary. In the finite element solution, the shell was divided into five unequal elements, with nine degrees of freedom at each node; these are, three displacements u, v and w , and their first and second derivatives. For clarity, only maximum values are compared.

It is observed that the mixed modified finite difference scheme compares well with more complex or large schemes, even for as few as five equal intervals. Discrepancy at the shell boundary can be easily eliminated by using unequal intervals.

For the same number of intervals, the mixed scheme is superior than the displacement scheme. However, for same number of equations, both schemes have almost the same accuracy.

II.2 Free-Vibration

The displacement modified finite difference scheme is

applied, herein, to determine the natural frequencies of a fixed-free hyperboloid. The shell basic dimensions and material properties are:

Total height	$H = 330.67 \text{ ft.}$
Throat radius	$a = 84.00 \text{ ft.}$
Curvature parameter	$b = 209.67 \text{ ft.}$
Height above throat	$z_t = -61.00 \text{ ft.}$
Height below throat	$z_b = 269.67 \text{ ft.}$
Shell thickness	$h = 0.417 \text{ ft.}$
Young's modulus	$E = 3 \times 10^6 \text{ psi}$
Material density	$= 150.111 \text{ lb/ft}^3$
Poisson's ratio	$= 0.15$

The lowest natural frequency of the shell, associated with harmonic wave number $m = 5$, was computed using different numbers of grid intervals. The results are depicted in Fig. II.7. Comparisons are made with the mixed modified finite difference solution by Noor and Schnobrich [8] and the conventional finite difference solution by Budiansky and Radkowski quoted in Ref. [8]. The marked superiority of the modified - over the conventional finite difference solutions is clearly evident. Accuracy in the order of 1% can be obtained with as few as ten equal intervals using the modified schemes. The lowest natural frequencies for harmonics $m = 1$ to 7, computed using 50 equal intervals are shown in Table II.1 and compared with results given by Carter, et al [8] using a numerical integration technique, Noor and

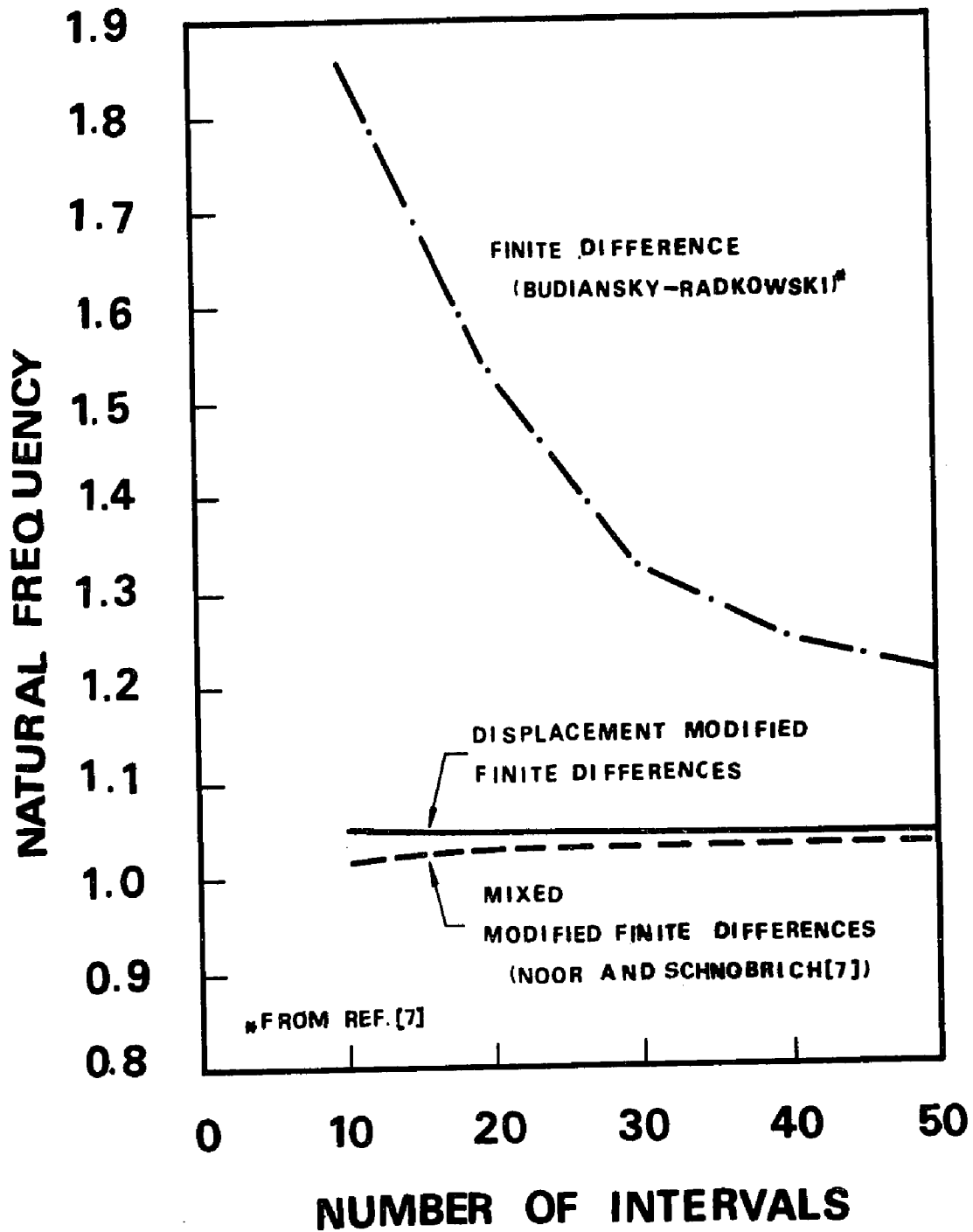


FIG. II.6

Table II.1 Natural Frequencies for a Sample Cooling Tower

Harmonic Wave Number m	Displacement Modified Finite Difference	Numerical Integration [9]	Mixed Modified Finite Difference [8]	Finite Element [10]	Partition Method [11]
1	3.3345	3.2884	-	3.286	-
2	1.7848	1.7654	1.7653	-	1.766
3	1.3929	1.3749	1.3751	1.375	1.383
4	1.2003	1.1808	1.1793	1.181	1.201
5	1.0441	1.0348	1.0325	1.034	1.077
6	1.1544	1.1467	1.1473	1.148	1.208
7	1.3055	1.3014	1.3018	1.303	-

Schnobrich [8] using the mixed modified finite difference method, Lashkari, et al [10] using the finite element method and Stoneking [11] using the partition method. Except for the results of Ref. [11], the differences between all solutions range between 1 to 2% only.

The influence of a top ring beam on the natural frequencies of hyperbolic cooling towers was investigated by the author [2] using the modified finite difference scheme. The percentage increase in frequency due to the presence of the ring beam, for the sample problem described above, is shown in Table II.2 for the fundamental modes of harmonics $m = 0$ to 7. The results are compared with those obtained by Weingarten, et al [12] using the finite element method. Both results are in good agreement.

Table II.2 Influence of Top Ring Beam
on the Natural Frequency

Harmonic Wave Number m	% Increase in Fundamental Frequency due to Ring Beam	
	Modified Finite Difference [2]	Finite Element [12]
0	0	-
1	1.2	0
3	2.0	1.6
4	15.9	14.4
5	14.7	15.7
6	0.0	2.0
7	6.1	6.0

APPENDIX III
1/400 AEROELASTIC MODEL

III.1 Model Material

As mentioned earlier in Chapter 6, correct aeroelastic modeling of the cooling tower requires that the material density and critical damping ratios be the same for both model and prototype. Young's modulus of model material E , is related to that of the prototype structure by,

$$E_m = E_p \frac{U_m^2}{U_p^2}$$

in which subscripts m and p refer to model and prototype structures respectively. Since the maximum wind speed that could be attained in the available wind tunnel facility is about 50 ft/sec., a material with a very low Young's modulus was therefore required.

A plastic steel material with the trade name of Devcon A was found to meet these requirements. The Devcon material contains approximately 80% steel, 20% epoxy resins and modifiers. This material is similar to putty and modeling clay in consistency and has a dark grey colour. According to the manufacturer, the material has a density of 156 lb/ft³ and a Young's modulus of 0.85×10^6 psi. These properties could be changed considerably by the use of different hardeners. The Devcon Flex, for example, can be used instead of

the regular hardener to make the Devcon material more flexible; i.e. to reduce its modulus of elasticity. This property was taken into advantage to reduce the Young's modulus without altering the other properties significantly. The following different mixes were tested for this purpose.

Mix A: Regular hardener = no Devcon Flex

Mix B: Devcon Flex/Devcon A ratio = 1/9 by weight

Mix C: Devcon Flex/Devcon A ratio = 1/4 by weight

Four beam specimens ($\frac{1}{2}$ " \times $\frac{1}{4}$ " \times 10") were made of each mix and tested to determine its physical properties. The average values are:

	<u>Mix A</u>	<u>Mix B</u>	<u>Mix C</u>
Young's Modulus - 10^6 psi	0.820	0.680	0.507
Mass Density lb/ft ³	152	142	127
Critical Damping Ratio	0.75%	0.9%	1.1%

Mix C was therefore most convenient for manufacturing the aeroelastic model.

III.2 Model Construction

The model was built at the Engineering Machine Shop of the University of Western Ontario. The process of manufacturing the shell model is depicted in Plate III-1. As shown the model was turned on a lathe fitted with special tools to generate the required hyperbolic profile.

To form the model an aluminium core was made to the rough shape of the model. The core consisted of two parts fastened together at the throat. The external diameters of

the aluminium core were about $\frac{1}{2}$ in. less than the internal diameter of the model. The core was coated with a thin layer of paraffin wax, above which a thick layer of rigidax was applied. A final coat of paraffin wax was applied and machined to the correct shape of the inside surface of the cooling tower model. The model was then coated with the Devcon material (Mix C). The Devcon layer was machined, after hardening, to the correct external profile of the shell model and was left for one week for full cure. The model was then coated with oil to prevent rust. The aluminium core was heated with steam till it dropped out at approximately 127°F. The model, with the wax layers still attached to it, was submerged in warm water for about (3 hours and 15 minutes) to remove the rigidax. Finally the paraffin wax was dissolved by submerging the model in turpentine for about 24 hours.

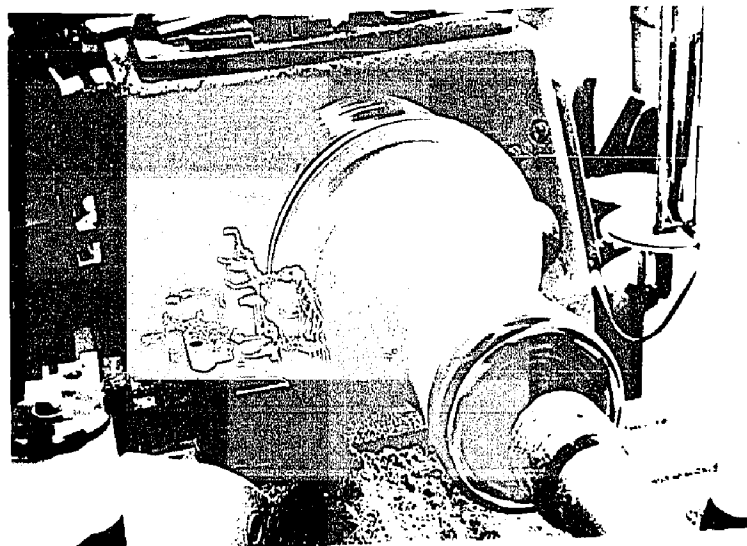
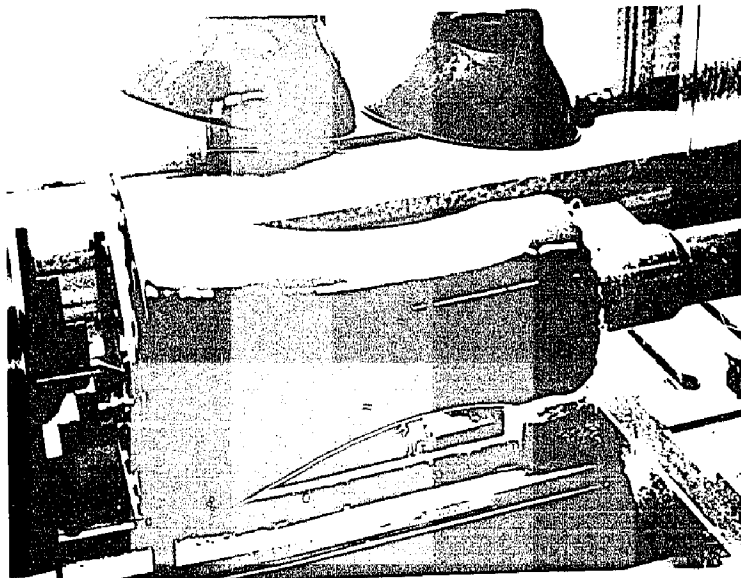
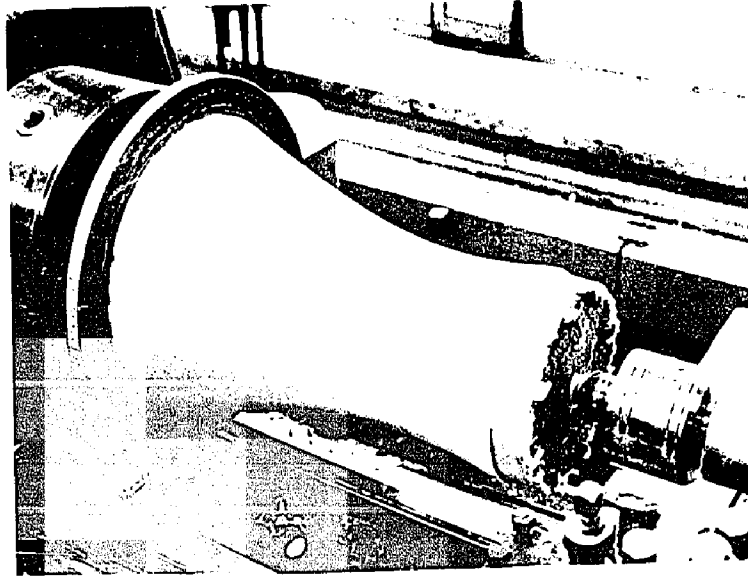


PLATE II.1

REFERENCES

CHAPTER 1

1. Central Electricity Generating Board. Report of the Committee of Inquiry into Collapse of Cooling Towers at Ferrybridge, 1 November 1965.
2. Jameson, R.M. and Adkins, G.G., "Waste Heat Disposal in Power Plants", Chemical Engineering Progress, July 1971, pp. 64 - 67.
3. McKelvey, K.K. and Brooke, M., The Industrial Cooling Tower, Amsterdam, New York, Elsevier Publ. Co., 1959.
4. "Cooling Towers", Power Special Reports, March 1963 and 1973.
5. Van Iterson, F.K. TH, "Stresses in Thin Shells of Circular Section", Engineering, Nov. 1919, pp. 640 - 642.
6. Van Iterson, F.K. TH, "Hyperboloidal Cooling Towers "Korinkl. Ned. Akad. Wetenschap, Proc. 49, 1946, pp. 114.- 122.
7. Cole, P.R., "Hyperbolic Natural Draft Evaporative Cooling Towers", Dept. of Civil and Geological Engineering Research Report No. 72 - SM 2, July, 1972.
8. Cowdrey, C.R., and O'Neill, P.G.G., "Report of Tests on a Model Cooling Tower for the C.E.A. Pressure Measurements at High Reynolds Numbers," NPL Aero Report 3.16A, 1956.

9. Davenport, A.G. and Isyumov, N., "The Dynamic and Static Action of Wind on Hyperbolic Cooling Towers", BLWT-1-66, Faculty of Engineering Sc., The University of Western Ontario, London, Canada.
10. Armitt, J., "The Effects of Surface Roughness and Free Stream turbulence on the Flow around a Model Cooling Tower at Critical Reynolds Numbers", Proc. Symp. on Wind Effects on Build. and Struct., Loughborough, 1968.
11. Niemann, H.J., Zur stationaren Windbelastung rotations symmetrischer Bauwerke im Bereich transkritischer Reynoldszahlen. Techn-wissensch. Mitt., Institut fur Konstr. Ing.-bau, Ruhr-Universitat Bochum, Mitt. Nr. 71-2, 1971.
12. Isyumov, N., Abu-sitta, S.H., and Davenport, A.G., "Approaches to the Design of Hyperbolic Cooling Towers against the Dynamic Action of Wind and Earthquake", Bulletin of the IASS, N. 48, January 1972.
13. Armitt, J., "Vibration of Cooling Towers", Int. Symp., Vibration Problems in Industry, 10 - 12 April, 1973, Keswick, England.
14. Martin, D.W. and Scriven, W.E., "The calculation of Membrane Stresses in Hyperbolic Cooling Towers", Proceedings, Institution of Civil Engineering, London, Vol. 19, 1961, pp. 503 - 513.
15. Martin, D.W., Maddock, J.S. and Scriven, W.E., "Membrane Displacement in Hyperbolic Cooling Towers

- due to Wind and Dead-Loading", Proceedings, Institution of Civil Engineering, London, Vol. 28, 1964, pp. 327 - 337.
16. Lee, S.L. and Gould, P.L., "Hyperbolic Cooling Towers Under Wind Load", Journal of the Structural Division, ASCE, Vol. 93, No. ST5, Proc. Paper 5532, Oct. 1967, pp. 487 - 514.
 17. Abu-Sitta, S.H., "A Finite Difference Solution of the General Novozhilov Equations", IASS Int. Colloquium, Madrid, Sept. - Oct. 1969.
 18. Albasiny, E.L. and Martin, D.W., "Bending and Membrane Equilibrium in Cooling Towers", Journal of the Engineering Mechanics Division, ASCE, Vol. 93, No. EM3, June 1967, pp. 1 - 13.
 19. Carter, R.L., Robinson, A.R. and Schnobrich, W.C., "Free Vibrations of Hyperboloidal Shells of Revolution", Journal of the Engineering Mechanics Division, ASCE, Vol. 95, No. EM5, Proc. Paper 6808, October 1969, pp. 1033 - 1052.
 20. Chan, A.S.L. and Firmin, A., "The Analysis of Cooling Towers by the Matrix Finite Element Method", Aeronautical Journal, V. 74, Part I, Oct. 1970.
 21. Hashish, M.G., and Abu-Sitta, S.H., "Free Vibration of Hyperbolic Cooling Towers", Journal of Engineering Mech. Div., ASCE, 97, No. EM2, Paper 8037, April 1971.
 22. Noor, A.K., and Schnobrich, W.C., "On Improved Finite Difference Discretization Procedures", Int.

Symp., Variational Methods in Engineering,
Southampton Univ., Sept. 1972.

23. Yeh, C.H., "Non-linear Dynamic Analysis of Cooling Tower", Journal of Power Div., ASCE, PO1, Paper 8983, June 1972.
24. Langhaar, H.L., and Boresi, A.P., "Periodic Response of a Viscoelastic Cooling Tower", Nuclear Engineering and Design, 22, 1972, pp. 75 - 94.

CHAPTER 2

1. Novozhilov, V.V., "The Theory of Thin Shells", Noordhoff Ltd., Croningen, The Netherlands, 1959.
2. Flügge, W., Stresses in Shells, Berlin, Springer, 1960.
3. Krauss, H., Thin Elastic Shells, John Wiley & Sons, Inc., New York, 1967.
4. Martin, D.W., and Scriven, W.E., "The Calculations of Membrane Stresses in Hyperbolic Cooling Towers", Proceedings, Institution of Civil Engineering, London, Vol. 19, 1961, pp. 503 - 513.
5. Timoshenko, S., Theory of Plates and Shells, New York, McGraw-Hill, 1959.
6. Martin, D.W., Maddock, J.S., and Scriven, W.E., "Membrane Displacements in Hyperbolic Cooling Towers due to Wind-and Dead-Loading", Proc., Inst. of Civil Engineering, London, Vol. 28, 1964, pp. 327 - 337.

7. Lee, S.L. and Gould, P.L., "Hyperbolic Cooling Towers under Wind Load", J. of the Struct. Div., ASCE, Vol. 93, No. ST5, Oct. 1967.
8. Croll, J.G.A., "The influence of Shape on the Stresses in Cooling Towers", Proceedings, Institution of Civil Engineering, London, 1969.
9. Albasiny, E.L. and Martin, D.W., "Bending and Membrane Equilibrium in Cooling Towers", Journal of the Engineering Mechanics Division, ASCE, Vol. 93, No. EM3, June 1969, pp. 1 - 17.
10. Abu-Sitta, S.H., "A Finite difference Solution of the General Novozhilov Equations", IASS, Int. Colloquium, Madrid, Spain, Sept. - Oct. 1969.
11. Schroblich, W.C. and Melin, J.W., "Model Analogue for Cylindrical Shells", World Conference on Shell Structures, 1962.
12. Hashish, M.G., "Free Vibration of Hyperbolic Cooling Towers", Faculty of Engineering Sc., Research Report No. ST-1-70, The University of Western Ontario, London, Canada, August 1970.
13. Noor, A.K., and Schnobrich, W.C., "On Improved Finite Difference Discretization Procedures", Int. Symp., Variational Methods in Engineering, Southampton University, Sept. 1972.
14. Hashish, M.G. and Abu-Sitta, S.H., "Mixed and Displacement Finite Difference Schemes For Hyperbolic

- Cooling Towers", Proceedings, Fourth Canadian Congress of Applied Mech., Montreal, Canada, 1973.
15. Chan, A.S.L. and Firmin, A., "The Analysis of Cooling Towers by the Matrix Finite Element Method", Aeronautical Journal, V. 74, Part I, Oct., 1970.
 16. Gould, P.L., Szabo, B.A., and Suryoutomo, H.B., "Curved Rotational Shell Elements by the Constraint Method", Int. Symp., Variational Methods in Engineering, Southampton, Sept., 1972.
 17. Abu-Sitta, S.H., "Cooling Towers Supported on Columns", J. Struct. Div., ASCE, Vol. 96, No. ST12, Paper 7753, Dec., 1970.
 18. Gould, P.L. and Lee, S.L., "Hyperboloids of Revolution Supported on Columns", J. Engineering Mech. Div., ASCE., Vol. 95, EM5, Oct., 1969.
 19. Hashish, M.G. and Abu-Sitta, S.H., "Ring-Stiffened Hyperbolic Cooling Towers under Static Wind Loading", Buid. Sc., Vol. 7, 175 - 181, Pergamon Press, 1972.
 20. Cowdrey, C.F. and O'Neill, P.G.G., "Report of Tests on a Model Cooling Tower for the C.E.A. Pressure Measurements at High Reynolds Numbers", NPL Aero Report 3.16A, 1956.
 21. Davenport, A.G. and Isyumov, N., "The Dynamic and Static Action of Wind on Hyperbolic Cooling Towers", BLWT-1-66, Faculty of Engineering Science, The University of Western Ontario, London, Canada.

22. Armitt, J., "The Effects of Surface Roughness and Free Stream Turbulence on the Flow around a Model Cooling Tower at Critical Reynolds Numbers", Proc., Symp. on Wind Effects on Build. and Struc., Loughborough, 1968.
23. Paduart, A., "Stabilite des Tours de Refrigeration", Le Genie Civil - T, Part 2, 145 No. 2, February, 1968.
24. Scruton, C., "Effects of Wind on Stacks, Towers and Masts with Special Reference to Wind Excited Oscillations", Proc. IASS Symp. on Tower Shaped Steel and Reinf. Conc. Struct., Bratislava, Czechoslovakia, 1966.
25. Niemann, H.J., "Stationary Wind Force on Natural Draft Cooling Towers", Colloquium on Recommendations for the struct. Design of Hyperbolic or Other Similarly Shaped Cooling Towers, IASS, Brussels, May, 1971.
26. Niemann, H.J., Zur stationaren Wind belastung rotations symmetrischer Bauwerke in Bereich transkritischer Reynoldszahlen. Technisch-wissenschaftliche Mitteilung Nr. 71-2 des Instituts fur Konstruktiven Ingenieurbau der Ruhr-Universitat Bochum.
27. Proceedings, IASS Symposium on Hyperbolic Cooling Towers, Brussels, May, 1971.
28. Chan, A.S.L. and Firmin, A., "The Analysis of Cooling Towers by the Matrix Finite Element Method", Part ii, Aeronautical Journal, Vol. 74, Oct., 1970.

29. Love, A.E.H., A Treatise on the Mathematical Theory of Elasticity, 4th ed., New York, Dover Publications, 1944.
30. Proceedings, First IUTAM Symp. on the Theory of Thin Elastic Shells, Delft, 1959.
31. Proceedings, Second IUTAM Symp. on the Theory of Thin Elastic Shells, Copenhagen, 1969.
32. Proceedings, IASS, International Colloquium Madrid, Spain, Sept. - Oct., 1969.
33. Noor, A.K., Stephens, W.B., and Fulton, R.E., "An Improved Numerical Process for Solution of Solid Mechanics Problems", National Symp., Computerized Structural Analysis and Design, George Washington University, March, 1972.
34. Gilles, D.C., "The Use of Interlacing Nets for the Application of Relaxation Methods to Problems Involving Two Dependent Variables", Proc., Royal Society of London, 1948, pp. 407 - 433.
35. Martin, R.S., and Wilkinson, J.H., "Solution of Symmetric and Unsymmetric Band Equations and the Calculation of Eigenvectors of Band Matrices", Numerische Mathematik, 9, 1967, pp. 279 - 301.
36. Isyumov, N., Abu -Sitta, S.H. and Davenport, A.G., "Approaches to the Design of Hyperbolic Cooling Towers Against the Dynamic Action of Wind and Earthquake", IASS Bulletin, N. 48, pp. 3 - 22, 1972.

37. Goldstein, S., "Modern Developments in Fluid Dynamics", Vol. I and II, Dover Publication, New York, 1965.
38. Engineering Sciences, Data, "Fluid Forces Acting on Circular Cylinders for Application in General Engineering, Part I: Long Cylinders in Two-Dimensional Flow", Item No. 70013, 1970.
39. Engineering Sciences Data, "Fluid Forces Acting on Circular Cylinders for Application in General Engineering, Part II: Finite Length Cylinders", Item No. 70014, 1970.
40. Fage, A., and Falkner, V.M., "The Flow around a Circular Culinder", ARC R & M 1369, Feb., 1931.
41. Roskhko, A., "Experiments on the Flow Past a Circular Cylinder at Very High Reynolds Number", J. Fluid Mechanics, Vol. 10, pp. 345 - 356, 1961.
42. Flachsbart O., 1929, From an article by Roshko, A., J. Fluid Mech., Vol. 10, pp. 345 - 356, 1961.
43. Achenbach, E., "Influence of Surface Roughness on the Cross-Flow Around a Circular Cylinder", J. Fluid Mech., Vol. 46, Part 2, pp. 321 - 335, 1971.
44. Batham, J.P., "Pressure Distributions on Circular Cylinders at Critical Reynolds Numbers", J. Fluid Mech., Vol. 57, Part 2, pp. 209 - 228, 1973.
45. Parkinson, G.V. and Jandali, T., "A Wake Source Model for Bluff Body Potential Flow", J. Fluid Mech.,

Vol. 40, Part 3, 1970, Pp. 557 - 594.

46. Davenport, A.G., et al, "New Approaches to Design Against Wind Action", Seminar Notes, ASCE Committee on Continuing Education, 1972.
47. Scruton, C., "The Problems of Estimating Wind Loading on Structures with Special Reference to Cooling Towers", Proceedings, Natural Draft Cooling Towers - Ferrybridge and After, ICE, London, 1967.
48. Central Electricity Generating Board, Report of the Committee of Inquiry into Collapse of Cooling Towers at Ferrybridge, Nov. 1, 1965.
49. Canadian Structural Design Manual, Supplement No. 4 to the National Building Code of Canada, 1970.
50. Abu-Sitta, S.H., "An Approximate Theory for Shells of Revolution", IASS Bulletin, No. 45, pp. 23 - 33, 1972.
51. Hannah, I.W., Proceedings, Natural Draft Cooling Towers - Ferrybridge and After, ICE, London, 1967.
52. Chilver, A.H., "Structural Design Philosophy", Proceedings, Natrual Draft Cooling Towers - Ferrybridge and After, ICE, London, 1967.
53. Hashish, M.G. and Abu-Sitta, S.H., "Free Vibration of Hyperbolic Cooling Towers", J. Eng. Mech. Div., ASCE, 97, No. EM2, paper 8037, April 1971.
54. Walser, A., and Curfinkel, G., "Structural Design of Hyperbolic Cooling Towers", IASS, Proceedings,

Shell Structures and Climatic Influences, Calgary, Canada, 1972.

CHAPTER 3

1. Davenport, A.G., "The Application of Statistical Concepts to the Wind Loading of Structures", Proceedings, Inst. of Civil Engineers, Vol. 19, pp. 449 - 472, London, England, 1961.
2. Davenport, A.G., "Response of Slender, Line-Like Structures to Gusty Winds", Journal of Inst. of Civil Engineers, Vol. 23, Nov. , 1962.
3. Davenport, A.G., "Gust Loading Factors", Journal of Struct. Div., Proceedings, ASCE, pp. 11 - 34, June, 1967.
4. Etkin, B., "Theory of Response of a Slender Vertical Structure to a Turbulent Wind with Shear", NASA Conf., Ground Wind Loads on Launch Vehicles, Langley Res. Centre, June, 1966.
5. Velozzi, J., "Gust Response Factors", Journal, Structural Div., Proc. ASCE, Vol. 94, No. ST6, 1968.
6. Vickery, B.J., "On the Reliability of Gust Loading Factors", Wind Loads on Buildings and Structures, Bldg., Sc. Series 30, NBS, Nov., 1970.
7. Vickery, B.J. and Kao, K.H., "Drag or Along Wind Response of Slender Structures", ASCE National Struct. Eng. Meeting, Baltimore, Maryland, April, 1971.

8. Crandall, S.H. and Mark, W.D., Random Vibrations in Mechanical Systems, Academic Press, New York, 1963.
9. Robson, J.D., An Introduction to Random Vibrations, Edinburgh Univ. Press, Elsevier Publishing Co., 1964.
10. Lin, Y.K. Probabilistic Theory of Structural Dynamics, McGraw-Hill Book Company, 1967.
11. Novozhilov, V.V., The Theory of Thin Shells, Noordhoff Ltd., Groningen, The Netherlands, 1959.
12. Davenport, A.G., "Note on the Distribution of the Largest Values of a Random Function with Application to Gust Loading", ICE, V. 28, 1964, pp. 187-196.
13. Hurty, W. and Rubinstein, M., Dynamics of Structures, Prentice Hall, 1964.

CHAPTER 4

1. Carter, R.L., Robinson, A.R. and Schnobrick, W.C., "Free Vibrations of Hyperboloidal Shells of Revolution", Journal of the Eng. Mech. Div., ASCE, Vol. 95, No. EM5, Proc. Paper 6808, Oct., 1969, pp. 1033 - 1052.
2. Hashish, M.G., and Abu-Sitta, S.H., "Free Vibration of Hyperbolic Cooling Towers", Journal of Engineering Mech. Div., ASCE, 97, No. EM2, Proc. Paper 8037, April 1971.
3. Noor, A.K., and Schnobrick, W.C., "On Improved Finite Difference Discretization Procedures", Int. Symp., Variational Methods in Eng., Southampton Univ., Sept., 1972.
4. Lashkari, M., Weingarten, V.I. and Magolias, D.S., "Vibrations of Pressure Loaded Hyperboloidal Shells",

- Journal of Eng. Mech. Div., ASCE, Vol. 98, No. EM5,
Proc. Paper 9230, Oct., 1972.
5. Neal, B.G., "Natural Frequencies of Cooling Tower Shells", Journal of Strain Analysis, The Inst. of Mech. Engineers, London, Vol. 2, No. 2, 1967, pp. 127 - 133.
 6. Hashish, M.G., "Free Vibration of Hyperbolic Cooling Towers", Faculty of Engineering Sc. Research Report No. ST-1-70, The Univ. of Western Ontario, London, Canada, August, 1970.
 7. Abu-Sitta, S.H., "An Approximate Theory for Shells of Revolution", IASS Bulletin, No. 45, pp. 23 - 33, 1972.
 8. Abu-Sitta, S.H. and Davenport, A.G., "Earthquake Design of Cooling Towers", J. Struct. Div., ASCE, 96, No. ST5, Paper 7524, Sept., 1970.
 9. Weingarten, V.I., Masri, S.F., Lashkari, M., and Kahyai, K., "Effect of Gravity Loading on the Earthquake Response of Cooling Towers", Fifth World Conference on Earthquake Engineering, Rome, 1973.

CHAPTER 5

1. Davenport, A.G. and Isyumov, N., "The Dynamic and Static Action of Wind on Hyperbolic Cooling Towers",

- BLWT-1-66, Faculty of Eng. Sc., The Univ. of Western Ontario, London, Canada.
2. Isyumov, N., Abu-Sitta, S.H. and Davenport, A.G., "Approaches to the Design of Hyperbolic Cooling Towers against the Dynamic Action of Wind and Earthquake", Bulletin of the IASS, N. 48, January 1972.
 3. Armit, J., "Vibration of Cooling Towers", Int. Symp., Vibration Problems in Industry, 10 - 12, April, 1973, Keswick, England.
 4. Davenport, A.G. and Isyumov, N., "The Application of the Boundary Layer Wind Tunnel to the Prediction of Wind Loading", The Int. Research Seminar on: Wind Effects on Building and Structures, Ottawa, 1967.
 5. Davenport, A.G., "The Relationship of Wind Structure to Wind Loading", Symp. on Wind Effects on Build. and Struct., NPL, 1963.
 6. Harris, R.I., "The Nature of Wind", Paper No. 3, C.I.R.I.A. Seminar on the Modern Design of Wind Sensitive Structures, Inst. of Civil Eng., June, 1970.
 7. Tunstall, M.J., "Measurements of the Wind Loading on Fawley Generating Station Chimney", CERL, Lab. Note No. RD/L/N 6/72.
 8. Teunissen, H.W., "Characteristics of the Mean Wind and Turbulence in the Planetary Boundary Layer", Institute for Aerospace Studies, Univ. of Toronto,

UTIAS Review No. 32, Oct., 1970.

9. Tunstall, M.J., "Fluctuating Pressures on Circular Cylinders in Uniform and Turbulent Flows", CERL, Lab. Note No. RD/L/N 45/70.
10. Kao, K.H., "Measurements of Pressure/Velocity Correlation on a Rectangular Prism in Turbulent Flow", Univ. of Western Ontario, Faculty of Eng. Sc., Research Report No. BLWT-2-70.
11. Hunt, J.C.R., "A Theory for Fluctuating Pressures on Bluff Bodies in Turbulent Flow", Symp. on Flow-Induced Struct. Vibrations, Karlsruhe, Germany, August, 1972.
12. Bearman, P.W., "Some Measurements of the Distortion of Turbulence Approaching a Two-Dimensional Body", J. Fluid Mech., Vol. 53, Part 3, 1972, pp. 451 - 467.
13. Davenport, A.G., "A Statistical Approach to the Treatment of Wind Loading on Tall Masts and Suspension Bridges", Ph.D. Thesis, Univ. of Bristol, 1961.
14. Vickery, B.J. and Kao, K.H., "Drag or Along-Wind Response of Slender Structures", ASCE National Struct. Meeting, Baltimore, Maryland, April, 1971.

CHAPTER 6

1. Davenport, A.G. and Isyumov, N., "The Dynamic and Static Action of Wind on Hyperbolic Cooling Towers", BLWT-1-66, Faculty of Eng. Sc., The Univ. of Western

- Ontario, London, Canada.
2. Isyumov, N., Abu-Sitta, S.H. and Davenport, A.G.,
"Approaches to the Design of Hyperbolic Cooling
Towers against the Dynamic Action of Wind and Earth-
quake", Bulletin of the IASS, N. 48, January, 1972.
 3. Armit, J., "Vibration of Cooling Towers", Int. Symp.,
Vibration Problems in Industry, 10 - 12 April, 1973.
 4. Williams, J.J., "Vibration of Cooling Tower Shells",
Inst. of Civil Eng. Symp.: Natural Draft Cooling
Towers -- Ferrybridge and After, June 1967.
 5. Hashish, M.G., "Free Vibration of Hyperbolic Cooling
Towers", Faculty of Eng. Sc. Research Report No. ST-1-70,
The Univ. of Western Ontario, London, Canada, August,
1970.
 6. Davenport, A.G. and Isyumov, N., "The Application of
the Boundary Layer Wind Tunnel to the Prediction of
Wind Loading", Int. Res. Seminar on Wind Effects on
Buildings and Structures, Ottawa, Canada, 1967.
 7. Whitbread, R.F., "Model Simulation of Wind Effects
on Structures", NPL Int. Conf. on Wind Effects on
Build. and Struct., NPL, 1963.
 8. Scruton, C., "On the Wind-Excited Oscillations of
Stacks, Towers and Masts", Proc. of Symp. on Wind
Effects on Buildings and Structures, NPL, 1963.
 9. Isyumov, N., "Wind Tunnel Methods for Evaluating Wind
Effects on Buildings and Structures", Proceedings of

- the Int. Symp. on Experimental Mechanics, Univ. of Waterloo, 1972, pp. 40 - 1 to 40 - 20.
10. Vickery, B.J., "On the Aeroelastic Modelling of Structures in Wind", Conference on the Struct. Models, Univ. of Sydney, Australia, May 1972.
 11. Jensen, M., "The Model Law for Phenomena in Natural Wind", *Ingenioren*, Int. Ed. 2, (4), 1958.
 12. Weingarton, V.I., Masri, S.F., Lashkari, M., and Kahyai, K., "Effect of Gravity Loading on the Earthquake Response of Cooling Towers", Fifth World Conf. on Earthquake Eng., Rome, 1973.
 13. Armit, J., "The Effects of Surface Roughness and Free Stream Turbulence on the Flow Around a Model Cooling Tower at Critical Reynolds Numbers", Proc. Symp. on Wind Effects on Build. and Struct., Loughborough, 1968.
 14. Hashish, M.G. and Abu-Sitta, S.H., "Free Vibration of Hyperbolic Cooling Towers", *J. Eng. Mech. Div.*, ASCE, 97, No. EM2, Proc. Paper 8037, April 1971.
 15. Abu-Sitta, S.H., "A Finite Difference Solution of the General Novozhilov Equations", IASS, INT. Colloquium, Madrid, Spain, Sept. - Oct., 1969.
 16. Abu-Sitta, S.H., "Finite Difference Solutions of the Bending Theory of the Elliptic Paraboloid", IASS Bulletin, No. 20, Dec. 1964.
 17. Davenport, A.G., "Note on the Distribution of the

Largest Values of a Random Function with Application to Gust Loading", Proc., Inst. of Civil Eng., Vol. 28, 1964, pp. 187 - 196.

CHAPTER 7

1. Chan, A.S.L. and Firmin, A., "The Analysis of Cooling Towers by the Matrix Finite Element Method", Aeronautical Journal, V. 74, Part I., Oct. 1970.
2. Carter, R.L., Robinson, A.R. and Schnobrich, W.C., "Free Vibrations of Hyperboloidal Shells of Revolution", J. of the Eng. Mech. Div., ASCE, Vol. 95, No. EM5, Proc. Paper 6808, Oct. 1969, pp. 1033 - 1052.
3. Albasiny, E.L. and Martin, D.W., "Bending and Membrane Equilibrium in Cooling Towers", J. of the Eng. Mech. Div., ASCE, Vol. 93, No. EM3, June 1967, pp. 1 - 17.
4. Hashish, M.G., "Free Vibration of Hyperbolic Cooling Towers", Faculty of Eng. Sc. Research Report No. ST-1-70, The Univ. of Western Ontario, London, Canada, August 1970.
5. Hashish, M.G. and Abu-Sitta, S.H., "Free Vibration of Hyperbolic Cooling Towers", J. Eng. Mech. Div., ASCE, 97, No. EM2, Proc. Paper 8037, April 1971.
6. Davenport, A.G., et. al., "New Approaches to Design Against Wind Action", Seminar Notes, ASCE Committee on Continuing Education, 1972.
7. Davenport, A.G. and Isyumov, N., "The Dynamic and

- Static Action of Wind on Hyperbolic Cooling Towers", .
BLWT-1-66, Faculty of Eng. Sc., The Univ. of Western
Ontario, London, Canada.
8. Isyumov, N., Abu-Sitta, S.H., and Davenport, A.G.,
"Approaches to the Design of Hyperbolic Cooling Towers
against the Dynamic Action of Wind and Earthquake",
Bulletin of the IASS, N. 48, January 1972.
 9. Niemann, H.J., Zur Stationaren Windbelastung
rotationssymmetrischer Bauwerke im Bereich transkrit-
ischer Reynoldszahlen. Techn-Wissensch, Mitt.,
Institut fur Konstr. Ing., - bau, Ruhr - Universitat
Bochum, Mitt. Nr. 71-72, 1971.
 10. Cowdrey, C.F. and O'Neill, P.G.G., "Report of Tests
on a Model Cooling Tower for the C.E.A. Pressure
Measurements at High Reynolds Numbers", NPL Aero
Report 3.16A, 1956.
 11. Cole, P.P., "Hyperbolic Natural Draft Evaporative
Cooling Towers", Dept. of Civil and Geological
Eng. Res. Report No. 72-SM2, July 1972.
 12. Hunt, J.C.R., "A Theory for Fluctuating Pressures
on Bluff Bodies in Turbulent Flow", Symp. of Flow-
Induced Struct. Vibrations, Karlsruhe, Germany,
August, 1972.
 13. Hunt, J.C.R., "A Theory of Turbulent Flow over Bodies",
to be published in J. Fluid Mech.

CHAPTER 8

1. Davenport, A.G., et. al., "New Approaches to Design Against Wind Action", Seminar Notes, ASCE Committee on Continuing Education, 1972.
2. Davenport, A.G., "Note on the Distribution of the Largest Values of a Random Function with Application to Gust Loading", Proc., Inst. of Civil Eng. Vol. 28, 1964, pp. 187 - 196.
3. Armit, J., "Vibration of Cooling Towers", Int. Symp., Vibration Problems in Industry, 10 - 12, April 1973, Keswick, England.

Appendix I

1. Novozhilov, V.V., The Theory of Thin Shells, Noordhoff Ltd., Croningen, The Netherlands, 1959.
2. Krauss, H., Thin Elastic Shells, John Wiley & Son Inc., New York, 1967.
3. Noor, A.K., Discussion on "Free Vibration of Hyperbolic Cooling Towers", J. of the Eng. Mech. Div., ASCE, Vol. 98, No. EM1, Feb. 1972.
4. Hashish, M.G., Free Vibration of Hyperbolic Cooling Towers, Faculty of Eng. Sc. Res. Report No. ST-1-70, The Univ. of Western Ontario, London, Canada, August 1970.
5. Hashish, M.G., and Abu-Sitta, S.H., "Ring-Stiffened Hyperbolic Cooling Towers under Static Wind Loading", Build. Sc., Vol. 7, 175 - 181, Pergamon Press, 1972.
6. Abu-Sitta, S.H., "Cooling Towers Supported on Columns", J. Struct. Div., ASCE., Vol. 96, No. ST12, Paper 7753, Dec. 1970.

Appendix II

1. Abu-Sitta, S.H., "A Finite Difference Solution of The General Novozhilov Equations", Proc. Int. IASS Symp., Madrid, 1969.
2. Hashish, M.G., "Free Vibration of Hyperbolic Cooling Towers", Engineering Science Research Report No. ST-1-70, The University of Western Ontario, London, Canada, August 1970.

3. Hashish, M.G. and Abu-Sitta, S.H., "Free Vibration of Hyperbolic Cooling Towers", Eng. Mech. Div., ASCE, Vol. 97, No. EM2, April 1971.
4. Hashish, M.G. and Abu-Sitta, S.H., "Ring-Stiffened Hyperbolic Cooling Towers under Static Wind Loading", Building Science, Vol. 7, pp. 175 - 181, Pergamon Press, 1972.
5. Hashish, M.G. and Abu-Sitta, S.H., "Mixed and Displacement Finite Difference Schemes for Hyperbolic Cooling Towers", Proc., Fourth Canadian Congress of Applied Mechanics, Montreal, Canada, July, 1973.
6. Abasiny, E.L. and Martin, D.W., "Bending and Membrane Equilibrium in Cooling Towers", Proc. ASCE, Eng. Mech. Div., June 1967.
7. Chan, A.S.L. and Firmin, A., "The Analysis Of Cooling Towers by the Matrix Finite Element Method", Aeronautical Journal, Vol. 74, Part I, Oct. 1970.
8. Noor, A.K. and Schnobrich, W.C., "On Improved Finite Difference Discretization Procedures", Int. Symp., Variational Methods in Engineering, Southampton Univ., Sept. 1972.
9. Carter, R.L., Robinson, A.R. and Schnobrich, W.C., "Free Vibrations of Hyperboloidal Shells of Revolution", Journal of Eng. Mech. Div., ASCE, Vol. 95, No. EM5, Oct. 1969.
10. Lashkari, M., Weingarten, V.I. and Marolias, D.S., "Vibrations of Pressure Loaded Hyperboloidal Shells",

J. Eng. Mech. Div., ASCE, Vol. 98, No. EM5,
Oct. 1972.

11. Stoneking, J.E., "Free Vibrations of Shells of Revolution with Variable Thickness", Nuclear Engineering and Design, V24, 1973, pp. 314 - 321.
12. Weingarten, V.I., Masri, S.F., Lashkari, M. and Kahyai, K., "Effect of Gravity Loading on Earthquake Response of Cooling Towers", Fifth World Conf. on Earthquake Eng., Rome, 1973.